Mechanics and Mechanotransduction of Adherent Cells

A Compendium of Atomic Force Microscopy Studies

Kristina M. Haase

A thesis submitted to the Faculty of Graduate and Postdoctoral Studies in partial fulfillment of the requirements for the degree of Doctor of Philosophy in Physics.

Department of Physics
Faculty of Science
University of Ottawa
Ottawa, Canada

Abstract

Mechanical cues have been recognized to be critically important in the regulation of cells. A myriad of cellular processes including differentiation, proliferation, and gene expression are all affected by physical forces from the extra- and intra-cellular microenvironments. Despite recent advances in nano-technologies, many questions still surround how cells sense and respond to forces. Through a series of studies, we demonstrate how both the structure and inherent mechanical properties of the cell affect their response to mechanical cues. We first develop a methodology to mechanically manipulate cells while simultaneously characterizing their deformations. Using combined atomic force and confocal microscopy techniques and through systematic examination we demonstrate the role of the cytoskeleton and nucleus in the deformability and shape change of epithelial cells. Mechanical properties have been used in recent years to identify diseased states, including cancer. With this in mind, we used HeLa cells as a model and characterized significant deformability of their plasma membrane and underlying cortex. Importantly, we demonstrate and characterize their ability to recover from large shape changes, which we also observed in other epithelial cells. Shape recovery is shown to be rapid and reliant upon the actin cytoskeleton and intracellular fluid flow. Although the nucleus does not contribute significantly to the deformation and recovery of HeLa cells, the importance of nuclear mechanics cannot be forgone. In vitro studies have shown that mechanical forces transmitted through the cell's cytoskeleton critically affect nuclear mechanics and gene transcription processes. Many others have used simple models and isolated nuclei in an attempt to characterize nuclear properties. Thus, in a subsequent study, we examine the nucleus within intact cells. Nuclear shape change, in response to force, is shown to be complex and cannot be well-characterized by isotropic mechanical properties. Characterization of the mechanics of the cell, as demonstrated through our findings, is crucial in the field of biological physics. The aforementioned studies, written as scientific articles, are presented in the body of this thesis (Chapters 2-5). A review article that focuses on mechanotransduction and relevant examples using AFM as a tool for its examination acts as an introductory chapter.

Résumé

Les signaux mécaniques sont reconnus pour jouer un rôle essentiel dans la régulation des cellules. Une multitude de processus cellulaires, dont la différentiation, la prolifération et l'expression des gènes, sont affectés par des forces physiques provenant du microenvironnement cellulaire interne et externe. Malgré les récentes avancées dans le domaine des nanotechnologies, les processus par lesquels les cellules détectent de telles forces et y répondent soulèvent toujours de nombreuses questions. A travers plusieurs études, nous démontrons que la structure et les propriétés mécaniques de la cellule affectent sa réponse aux signaux mécaniques. Nous développons d'abord une méthodologie pour manipuler les cellules mécaniquement et caractériser simultanément les déformations résultantes. Par l'utilisation combinée des microscopies à force atomique et confocale et grâce à des études systématiques, nous démontrons l'influence du cytosquelette et du noyau cellulaire sur la déformabilité et le changement de forme des cellules épithéliales. Les propriétés mécaniques des cellules ont été utilisées ces dernières années pour l'identification d'anomalies cellulaires, notamment le cancer. Dans cette optique et en utilisant des cellules HeLa pour modèle, nous avons caractérisé un degré important de déformabilité de la membrane plasmique et du cortex sous-jacent. Surtout, nous démontrons et caractérisons leur habileté à retrouver leur forme initiale à la suite de déformations importantes, ce qui a également été observé pour d'autres types de cellules épithéliales. Le retour à la forme initiale est rapide et dépend du cytosquelette d'actine et de l'échange de fluide intracellulaire. Bien que le noyau cellulaire ne contribue pas significativement à la déformation et à la capacité des cellules HeLa à rétablir leur forme, l'importance de la mécanique du noyau ne doit pas être négligée. Des études *in vitro* ont montré que les forces mécaniques transmises par le cytosquelette influencent de manière significative la mécanique du noyau et le processus de transcription de gènes. Néanmoins, pour caractériser les propriétés des noyaux, de nombreuses études les isolent et utilisent des modèles simplifiés. Par conséquent, dans une étude supplémentaire, nous examinons le noyau dans des cellules intactes. La déformation du noyau en réponse à l'application d'une force apparaît comme étant complexe et ne pouvant être adéquatement caractérisée par des propriétés mécaniques isotropes. Comme nos résultats le démontrent, la caractérisation de la mécanique cellulaire est fondamentale dans le domaine de la physique biologique. Les études mentionnées ci-dessus, qui ont été écrits comme étant des articles scientifiques, sont présentées dans le corps de cette thèse (chapitres 2 à 5). L'introduction consiste en un article de revue, mettant l'emphase sur la mécanotransduction et présentant des exemples pertinents basés sur la microscopie à force atomique.

Author's note

Knowledge surrounding cellular phenomena is crucial towards our understanding of life, death, and disease. This thesis, through an exploratory experimental approach, attempts to shed light on the interplay between cellular mechanics and the influence of the physical environment in directing cellular responses. The majority of work performed herein employs a human cancerous cell line which has become notorious for its use in labs [1], and has even gained attention in mainstream popular culture [2]. HeLa cells were the first-ever successfully immortalized human cell culture line, and as such they have paved the way for many scientific discoveries, notably the development of the polio vaccine and discovery of human teleromase. Much controversy has surrounded the use of HeLa cells, as they were first obtained from a cervical biopsy of Henrieta Lacks in 1951, by Dr. George O. Gey, at John Hopkins Hospital, without patient consent. Recently, the genomic sequence of HeLa cells has been re-released following an agreement with the family of the late Henrietta whom have consented to the use of the data for biomedical research on a case by case basis [3]. The widespread use and accessibility of HeLa, and its genome, brings to light many ethical questions. With this in mind, we can gain an appreciation for this ubiquitous and inspiring cell line, which has encouraged this work amongst innumerable others.

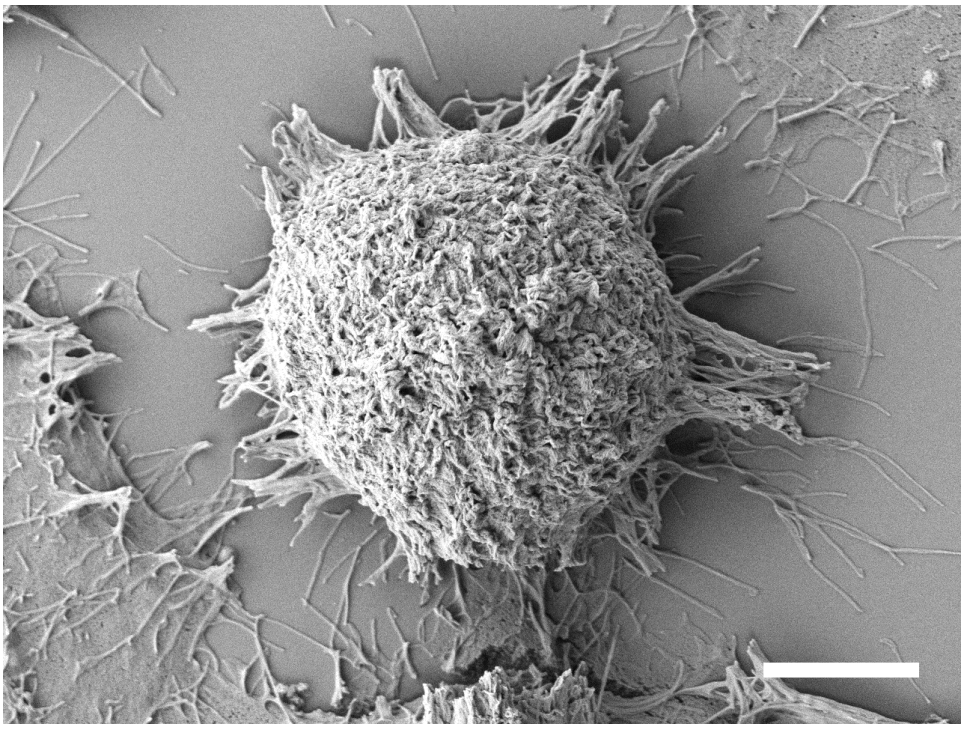

Figure 0.1 SEM image of a HeLa cell.
A scanning electron microscopy (SEM) image is presented for the purpose of demonstrating the complex surface structures (cilia) observable on the apical and peripheral regions of the plasma membrane of a HeLa cell with rounded morphology. Preparation of HeLa cells for SEM imaging was performed according to the protocol presented in reference [4]. I would like to thank Daniel Modulevsky for assistance with sample preparation, and Dr. Yun Liu for assistance with SEM imaging. Scale bar is 5µm.

Statement of Originality

To the best of the author's knowledge, this thesis and work is entirely original. Research and manuscripts were prepared under the supervision of Dr. Andrew E. Pelling, in the Centre for Interdisciplinary Nanophysics laboratories in the Department of Physics at the University of Ottawa. This thesis consists of a review paper, which acts as an introductory chapter, as well as subsequent experimental research manuscripts (Chapter 2-5), which have been published, submitted or prepared for peer-reviewed scientific journals. A contribution of co-authors is presented prior to each experimental manuscript, along with a brief overview of the motivation, hypothesis and objective of the chapter. Following the presentation of scientific results, we discuss future directions of this work (Chapter 6). Lastly, we outline protocols for the experiments performed in a technical note (Chapter 7).

Manuscripts included in this thesis:

- Haase, K. & Pelling, A.E. "Poking and prodding our understanding of cell mechanics," *Journal of the Royal Society Interface*, Submitted Aug. 29th, 2014.
- Haase, K. & Pelling, A.E. "Resiliency of the Plasma Membrane and Actin Cortex to Large-Scale Deformation." *Cytoskeleton,* 70, p. 494-514, Published Sept. 3rd, 2013.
- Haase, K. & Pelling, A.E. "The Role of the Actin Cortex in Maintaining Cell Shape," *Communicative &Integrative Biology*, 6, e26714, Published Oct. 9th, 2013.
- Haase, K., Shendruk, T.N., Slater, G.W., Pelling, A.E. "Rapid dynamics of the membrane and actin cortex in response to local deformations", *In preparation for Nature Materials*, 2014.
- Haase, K., Macadangdang, J.K.L., Cuerrier, C.M., Hadjiantoniou, S., Harden, J.L., Skerjanc, I.S., Pelling, A.E. "Extracellular forces cause the nucleus to deform in a highly controlled and anisotropic manner," *PNAS,* Submitted Aug. 1st, 2014.

This work has also been presented at the following conferences & workshops:

- Haase, K., Gullekson, C., Pelling, A.E. "The force is strong in these *cells*", *Cell Dynamics Workshop*, Keene, Ontario, 2014. (Talk)
- Haase, K., Shendruk, T., Slater, G., Pelling, A.E. "The Role of the Cortex & the Cytoplasm in Deformations of the Plasma Membrane ". BPS. San Francisco, California, 2014. (Poster)
- Haase, K. & Pelling, A.E. "Membrane Resiliency Following Large-Scale Local Deformations Using an AFM". *AFM-Based Nanoscopies in the Life Sciences*. M&M. Indianapolis, Indiana, 2013. (Talk)
- Haase, K., & Pelling, A.E. "Nano-forces reveal cell resiliency via the membrane and cytoskeleton", *Cell Dynamics Workshop*, Keene, Ontario, 2013. (Talk)
- Haase, K. & Pelling, A.E. "Mechanotransduction through the Plasma Membrane". *Cytoskeleton and Bioemechanics – Biochemical Mechanisms*. APS. Boston, Massachusetts, 2012. (Talk)
- Haase, K., Pelling, A.E. "Nano-forces reveal cell resiliency via the membrane and cytoskeleton", *Cell Dynamics Workshop*, Keene, Ontario, 2012. (Poster)

Other Contributions

Over the course of the work and preparation of this thesis, I have also contributed to other publications with other members of the Pelling lab, as listed below. Other on-going projects have involved collaborators within the biology department (Dr. Micheal G. Jonz and M.Sc. student Benjamin Campbell), wherein seasonal effects on the mechanics of primary cells are under investigation.

Contributions to other manuscripts:

- Modulevsky, D.J., Lefebvre, C., **Haase, K.**, Al-Rekabi, Z. & Pelling, A.E. "Apple Derived Cellulose Scaffolds for 3D Mammalian Cell Culture ." *Plos One,* **9,** e97835, 2014
- Al-Rekabi, Z., **Haase, K.** and Pelling, A.E. "Microtubules mediate changes in membrane nanomechanics during contractile activation." *Experimental Cell Research*,322, 21, 2014
- Bukoreshtliev, N.V., **Haase, K.** & Pelling, A.E. "Mechanical Cues in Cellular Signalling and Communication." *Cell and Tissue Research,* 352, 77, 2013
- Guolla, L., Bertrand, M., **Haase, K.** & Pelling, A.E. "Force Transduction and Strain Dynamics in Actin Stress Fibres in Response to Nanonewton Forces." *Journal of Cell Science,* 125, p. 603-13, 2012

Book chapters:

- **Haase, K.**, Al-Rekabi, Z., Pelling, A.E. "Mechanical cues direct focal adhesion dynamics", Sanjay, K and Engler, A. ed. *Molecular Mechanism of Mechanotransduction.* Elsevier, 2014.
- **Haase, K.**, Tremblay, D., Pelling, A.E. "Mechanotransduction: Probing its Mechanisms at the Nanoscale using the Atomic Force Microscope", Takeyasu, K. ed. *Atomic Force Microscopy in Nanobiology.* Pan Stanford Publishing, 2014.
- Al-Rekabi, Z., Tremblay, D., **Haase, K.**, Leask, R.L., Pelling, A.E. "Computational and Experimental Approaches to Cellular and Subcellular Tracking at the Nanoscale". Musa, S.M. ed. *Computational Nanotechnology: Modeling and Applications with MATLAB.* New York: CRC Press, pp.333-361, 2011.

Statement of Contributions

I, Kristina M. Haase, contributed the large majority of the work presented in this thesis. The work involved includes cell culture, molecular biology, experimental design, experimentation using atomic force and confocal microscopy techniques, image and data analysis, and statistical analysis. Background research on mechanotransduction and the mechanics of cells was completed and compiled as a review paper. As well, I wrote two book chapters as a first author, one involving mechanotransduction and the other involving focal adhesions as sensors. Both chapters are directly related to the topics in the thesis and involve discussion of relevant atomic force microscopy studies. These however, have not been included here in an effort to limit the length of the thesis. I was also the first author and primarily wrote the scientific manuscripts included here (Chapters 2-5), including any revisions.

Other researchers have also contributed to this work and are outlined prior to the manuscripts presented in the thesis. Dr. Andrew E. Pelling contributed to the direction and editing of all manuscripts, and performed some experiments/analysis for the nuclear strain paper (Chapter 5). Dr. Tyler Shendruk, as a Ph.D. student in Dr. Gary W. Slater's lab, developed theoretical models in an effort to simulate the shape recovery processes observed following cell deformation experiments (Chapter 4). Joan Karla Macadangdang, a previous Master's student in the Pelling lab, performed the preliminary experiments regarding nuclear strain (Chapter 5) and recorded these findings in her thesis. Following a change in the focus of the manuscript and experiments performed by myself, I re-wrote the manuscript and consecutive drafts. Dr. Charles M. Cuerrier, a post-Doc, provided me with primary cells that I used in nuclear deformation experiments. Sebastian Hidjiantoniou, a Ph.D. candidate, provided me with cultured embryonic stem cells for experiments that originally came from the lab of Dr. Ilona S. Skerjanc. Dr. James L. Harden has provided advice on modelling and assisted in editing of the nuclear strain paper. Corinne Gullekson, a Ph.D. candidate, developed preliminary Matlab models discussed in the future directions chapter.

Acknowledgements

First, and foremost, I would like to thank Dr. Andrew E. Pelling for giving me the opportunity to work in his lab. I count myself extremely lucky to have been given the chance to work in an exploratory-driven environment under the supervision of a great mentor. Overall, the physics department has been extremely welcoming. In particular I would like to thank Dr. James Harden and Dr. Béla Joos for continual inspiration and encouragement. Of course, all of the members of the Pelling lab, both past and present, have been very supportive and encouraging throughout the years. I am happy to call you my friends, and so glad we were brought together as colleagues. To all of you, I sincerely thank you.

Thank you to my supportive network of family and friends. I am lucky to have you all. Special thanks go to my parents, brother, and grandparents, for always believing that I will “reach the light at the end of the tunnel”.

Most importantly, thanks to Dave, you stood by with me through the challenges and triumphs. For that, I cannot thank you enough.

List of Abbreviations

- α – anisotropic strain ratio
- ADF – actin depolymerizing factor
- AFM – atomic force microscopy
- ATP – adenosine triphosphate
- CCD – charge coupled device
- CHO – Chinese hamster ovary cell
- CytD - Cytochalasin D (inhibitor)
- DiD – long-chain dialkyl carbocyanine dye
- Dmd – Duchenne muscular dystrophy
- DMEM - Dulbecco's Modified Eagle's medium
- DMSO – dimethylsulfoxide
- DNA – deoxyribonucleic acid
- ECM – extracellular matrix
- E – elastic or Young's modulus
- EDTA – Ethylenediaminetetraacetic acid
- EGFP – enhanced green fluorescent protein
- f - frequency
- FA – focal adhesion
- F-actin – filamentous actin
- FAK – focal adhesion kinase
- FBS – fetal bovine serum
- FC – focal complex
- FE – finite element
- fps – frames per second
- G – shear modulus
- G-actin – globular actin
- GDP – guanosine diphosphate
- GEF- guanine neucleotide exchange factor
- GFP – green fluorescent protein
- GPCR - G-protein coupled receptor
- GTP – guanosine triphosphate
- HFF – Human foreskin fibroblast (cell line)
- ICA – intensity correlation analysis
- ICQ – intensity correlation quotient
- IF – intermediate filaments
- LF2K – Lipofectamine 2000 (reagent)
- LIF – leukemia inhibitory factor (reagent)
- LIMK – LIM domain kinase
- LINC - Linker of Nucleoskeleton and Cytoskeleton
- LSCM - Laser scanning confocal microscopy
- LTM – laser tracking microrheology
- M – Molar mass (unit)
- MβCD – Methyl-beta-cyclodextrin
- MDCK – Madin Darby canine kidney (epithelial cell line)
- mESC – mouse embryonic stem cells
- MLC – myosin light chain
- MLCK – myosin light chain kinase
- MT – microtubules
- NA – numerical aperture
- N – Newton (unit)
- Noco – Nocodazole (inhibitor)
- P - phosphatase
- Pa – Pascal (unit)
- PBS – phosphate buffered saline
- PDMS – polydimethylsiloxane
- PFA - paraformaldehyde
- PH – plekstrin homology
- PI – propidium iodide
- PSF – point spread function
- RFP – red fluorescent protein
- RhoA – ras homolog gene family (member A)
- ROCK – Rho-associated protein kinase
- ROI – region of interest
- SEM – standard error of the mean
- SD – standard deviation
- SGR – soft glassy rheology
- SUN – Sad1p, UNC-84 (nuclear envelope protein)
- TFM – traction force microscopy
- TIRF – total internal reflection microscopy
- TSA – Trichostatin A
- TX – Triton X-100 (reagent)
- VEGF – vascular endothelial growth factor
- WGA – Wheat germ agglutinin (dye)

Table of Contents

List of Figures

List of Tables

Chapter 1| *Review manuscript*

Poking and prodding our understanding of cell mechanics

Kristina Haase[1], and Andrew E. Pelling[1,2,3]

[1]*Centre for Interdisciplinary NanoPhysics, Department of Physics, MacDonald Hall, 150 Louis Pasteur*
[2]*Department of Biology, Gendron Hall, 30 Marie Curie*
[3]*Institute for Science Society and Policy, Simard Hall, 60 University*
University of Ottawa, Ottawa, ON, K1N 6N5, Canada.

Submitted Aug. 29th 2014 to the *Journal of the Royal Society Interface*

- A condensed version of this review manuscript was submitted to the *Journal of the Royal Society Interface*.
- I, Kristina Haase, performed the majority of the work including research and preparation of this review article and its subsequent revisions.
- The presentation of the manuscript has been modified for the purposes of formatting the thesis.

Motivation |

Mechanical forces are ubiquitous *in vivo*, and are well-known to be crucial for normal cellular processes and development. However, many open questions involving cellular force transmission remain, largely due to an incomplete picture of cell rheology. Recent advances in nanotechnologies, such as atomic force microscopy (AFM), are gradually increasing our understanding of mechanotransduction through studies of cell mechanics in both the time and frequency domains. Characterization of mechanics at the sub-cellular, and cellular levels using AFM are vital in understanding force transmission.

Hypothesis & Objectives |

This review acts as an introductory chapter providing a general overview of mechanotransduction and known mechanosensors. The main focus is to highlight the importance of AFM in the context of examining cellular mechanics. We present AFM-based cellular manipulation methods through recent examples, and discuss common models used to characterize observed cellular phenomena.

1| Poking and Prodding our Understanding of Cell Mechanics

1.1 Abstract

Transmission of mechanical forces is crucial for normal cell development and functioning. However, the process of mechanotransduction cannot be studied in isolation from cell mechanics. Thus, in order to understand how cells "feel" we must first understand how they deform and recover from physical perturbations. Due to its versatility, atomic force microscopy (AFM) has become a popular tool to study intrinsic cellular mechanical properties. Used to directly manipulate and examine whole and subcellular reactions, AFM allows for top-down and reconstitutive approaches to mechanical characterization. These studies show that the response of cells and its components are complex, and largely depend on the magnitude and time-scale of loading. In this review, we generally describe the mechanotransductive process through discussion of well-known mechanosensors. We then focus on discussion of recent examples where AFM is used to specifically probe the elastic and inelastic responses observed during cellular deformation studies. We present a brief overview of classical and current models often used to characterize observed cellular phenomena in response to force. Both simple mechanistic models and complex non-linear models have been used to describe the observed cellular behaviours, however a unifying description of cell mechanics has not yet been resolved.

1.2 Introduction

Cells are exposed to and must respond to a variety of mechanical loads *in vivo* [5-7]. Primary examples include: shear fluid forces on endothelial cells [8], compressive forces on bone cells [9], and highly dynamic tensile forces experienced by epithelial cells [10]. Cells are able to deform rapidly, leading to subsequent changes in their biochemistry. They "feel" neighbouring cells, as well as respond to changes in their underlying extracellular matrix. Cells exposed to substrate stretch, for example, have been shown to realign in the direction of minimal deformation (perpendicular to the axis of strain) [11-13], whereas cells exposed to fluid shear stresses align in the direction of flow [14]. The response to mechanical stimuli is complex, and depends on both force magnitude [15] and rate [16]. Strain rate, in particular, has been shown to affect stretch-induced remodelling of F-actin [17-19]. External forces transmitted through the plasma membrane and focal adhesions are conveyed to internal load-bearing structures of the cytoskeleton [20], influencing nuclear deformations, transcription processes, and gene expression [21, 22]. Whereas, internal forces generated via molecular motors [23] and actin polymerization [24, 25] are transmitted to the substrate in order to facilitate migration [26], undergo mitosis [27], and communicate with neighbouring cells [28]. This continual process of sensing, transmission, and response, is known as mechanotransduction, and is essential for maintenance of normal cell functioning and development (Fig. 1.1).

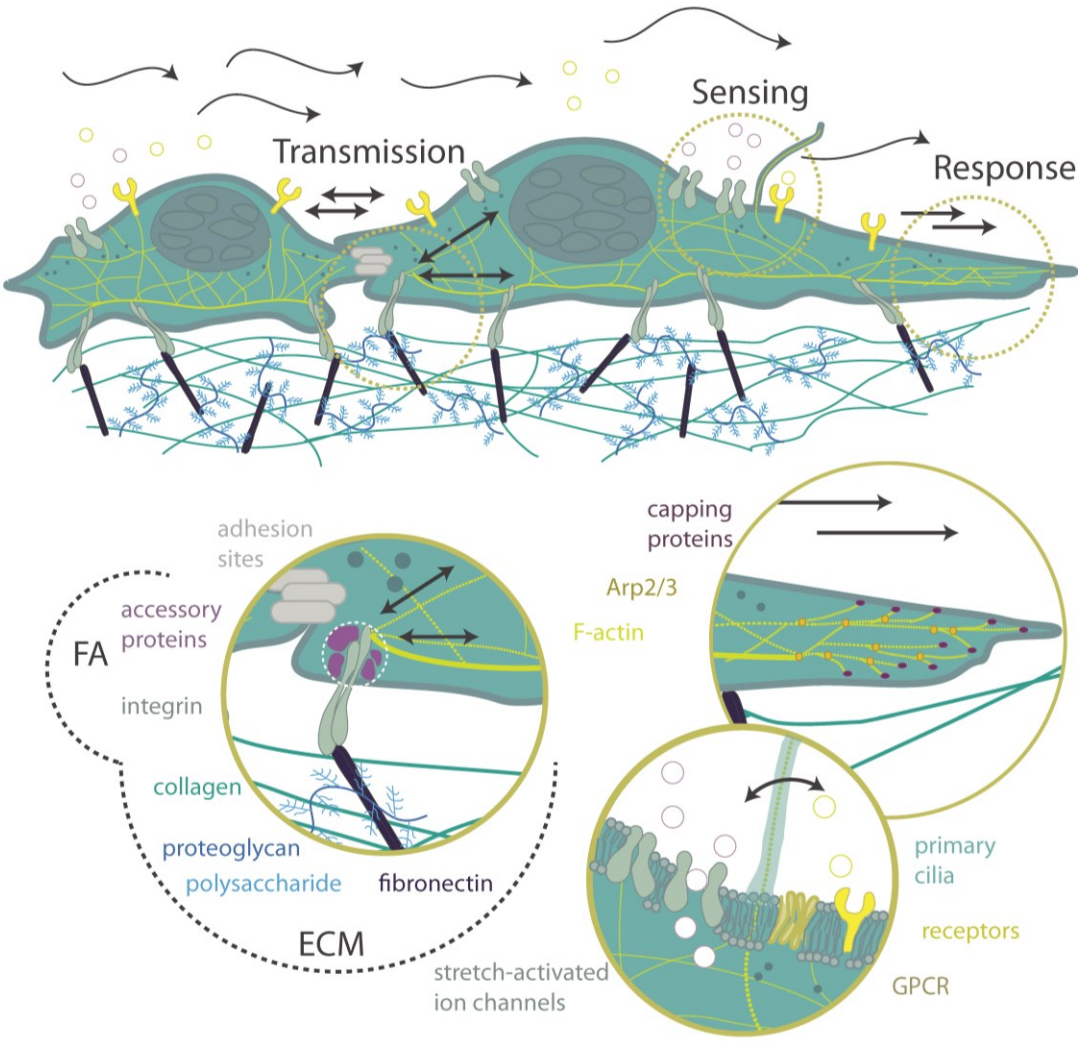

Figure 1.1 Mechanotransduction – a process of force sensing, transmission, and response.
Forces, such as tension/compression, and shear flow from the microenvironment are sensed by membrane surface receptors, such as bending of primary cilia, stretch-activated ion channels, and G-protein coupled receptors (GPCRs). Meanwhile forces from the ECM are sensed through focal adhesions (FAs) and transmitted to the inner actin cytoskeleton. Force is also transferred between adjacent cells through cell-cell junctions. Mechanical cues have been shown to elicit a variety of cellular responses, from biochemical signalling to directed migration.

Although some of the key mechanosensors, such as stretch-activated ion channels [29], integrins [30], and primary cilia [31], have been identified, how they configure themselves within the cell and how they respond to a myriad of mechanical cues has yet to be well characterized [32]. In order to understand the inner workings of mechanotransduction, we must first aim to understand the complex nature of cell mechanics. Two approaches are generally employed in order to examine cellular properties: a top-down approach involving cellular manipulation, or a bottom-up approach including biochemical and single biopolymer studies. Unfortunately, both approaches leave a gap in knowledge at the mesoscopic scale.

Renewed interest in the study of cell mechanics has come about with the emergence of passive and active nano-technologies. Internal and external laser tracking microrheology (LTM) [33-36] and two-point microrheology (TPM) [37-39] are often employed to passively measure the elastic and shear moduli of cells and their subcellular constituents. On the other hand, active measurement techniques including magnetic twisting cytometry (MTC) [40-43], uniaxial rheometry (UAR) [44], micropipette aspiration (MPA) [16, 45], and optical tweezers [46-48] direct localized or whole-cell deformations. Atomic force microscopy (AFM) in particular has become a popular tool to probe the mechanical response of cells [15, 49, 50].

Cells are often treated as linearly viscoelastic materials, as both elastic [51] and time-dependent viscous [43] responses to mechanical loading have been observed. Active measurement techniques are often used to measure these cell properties, reports of which vary widely in the literature. Young's moduli of epithelial cells have been reported between 1-100kPa, as measured by AFM alone [52-54]. Of course, results are cell-type dependent [55, 56] and reliant upon the experimental and analysis techniques employed [57, 58]. Furthermore, in the process of measurement, active techniques, such as AFM or optical tweezers, are capable of inadvertently stimulating mechanotransduction pathways [59, 60]. Nevertheless, tools such as AFM are invaluable in the efforts to elucidate the mechanics behind cellular function and response. A number of models have been proposed in an attempt to characterize and explain observed cellular behaviours. Although some models fit experimental data quite well, most do not fully describe all of the observed behaviour, and many appear contrasting in their predictions [61].

In this review, we aim to provide an overview of our current understanding of mechanotransduction, in the context of mechanosensing and force generation within cells. First, we will discuss some of the key players identified in mechanotransductive processes. As well, we will take a look at how cells respond to mechanical stimuli. We will then provide a concise overview of some of the classical and more current models used to describe cellular mechanics. A generalized model of cell mechanics remains elusive, and so characterization of cell mechanics lends important cues in our understanding of cell behaviours. Direct cell deformation experiments, such as those performed using AFM, are valuable in order to characterize cell deformation and recovery responses. Therefore, the main focus of this review involves a discussion of recent articles where AFM is used to directly probe the response of whole-cells as well as their subcellular components.

1.3 Multiple mechanosensors are at play

Cells must respond to a wide variety of forces in vivo, as mechanical cues are ubiquitous at the cellular level. Extracellular forces, such as shear fluid forces and substrate stretch, intracellular forces, from actomyosin based contractility, and intercellular forces between neighbouring cells all must be simultaneously received and processed by cells. In vitro examination has shown that these mechanical cues are responsible for directing cell proliferation, behaviour, and pathology [62-64]. This process of force-sensing, transmission, and response is referred to as mechanotransduction (Fig. 1.1). Major contributors in this process include: the extracellular matrix (ECM), adhesion sites (cell-cell and cell-ECM), the cytoskeleton, surface membrane molecules, as well as nuclear components.

In this section, we briefly discuss some of the main regulators of mechanotransduction – those involved in sensing, and transmission throughout the cell.

Tensile forces originating at the tissue level are transferred to the ECM, which acts as both a stress buffer and transmitter. The ECM is a composite substrate composed of an interstitial layer and basement membrane underlying epithelial cells. Its composition is composed of polysaccharides and a variety of proteins (i.e. fibronectin, collagen) secreted from fibroblasts, which create a dense interwoven network of filaments. Not only does the ECM provide structural support, and act as an external cell-signalling region, but its composition allows for the integration and adhesion of specific cell types. The mechanical properties of the ECM have long been known to influence cell behaviour and fate [65]. For example, fibroblasts exposed to decreased substrate stiffness result in increased lamellipodia growth and overall cell motility [66]. Moreover, culturing embryonic stem cells on polydimethylsiloxane (PDMS) substrates of varying stiffnesses demonstrated that differentiation was stiffness-dependent - stiffer substrates resulted in mainly osteogenic differentiation [67]. Sites of ECM-cell adhesion (focal adhesions) [68-70], as well as cell-cell adhesion (cadherins) [71] are also directly affected by ECM composition, and are known regions of force sensing and transmission. Moreover, cadherin-based adhesions have been shown to promote transmission of intercellular forces to the ECM via the periphery of epithelial cell colonies [72]; an example of direct mechanical coupling.

Classically, a mechanosensor was defined as a transmembrane ion channel linked via tethered networks to both intra- and extra-cellular anchors [73]. A primary example of a classical mechanosensor, stretch-activated ion channels have long been known to transduce mechanical signals into chemical ones [74-76]. Membrane and cytoskeletal tension have been shown to drive the opening of these channels, thus altering the permeability of cells to specific ions. Although most voltage- and ligand-gated channels are mechanosensitive, only some are fully activated by mechanical stresses. Sachs provides a concise review of the mechanism of opening of these mechano-sensitive channels, and discusses how uncoupling the membrane and cortex using methyl-β cyclodextrin (which depletes cholesterol) resulted in increased tension in channels, as determined by patch-clamping [29]. As proposed by the author, these mechano-sensitive channels may act as sensors in order to indicate where the cytoskeleton, which absorbs and transmits most of the structural loads within the cell, should be reinforced.

Adhesion sites, as mentioned above, are known regulators of mechanical signal transmission across the cell. In particular, focal adhesions transfer forces between the ECM and inner cell. Acting as a hub, focal adhesions direct signalling molecules towards integrins - transmembrane proteins that link the extra and intra-cellular microenvironments. Many cellular responses have been shown to be reliant upon integrin signalling alone (reviewed in [77]). External mechanical forces applied locally to the cell, either apically, or through the ECM, have a crucial impact on formation and size of focal adhesions [78, 79]. Interestingly, focal complexes (precursors to mature focal adhesions) are not reliant upon mechanical tension in order to assemble [73]. Moreover, the formation of mature focal adhesions is highly transient with disassembly occurring upon loss of mechanical stimuli, as demonstrated by a loss of actomyosin mediated contractility [80, 81]. In vitro studies have shown that mechanical activation of both integrin signalling and focal adhesion assembly results from substrate

stretching [82-84], and induced fluid shear stresses [85, 86]. These examples clearly demonstrate that mechanical forces are sensed and transmitted by several cellular components simultaneously.

The cytoskeleton spans the entirety of eukaryotic cells, providing structural support and integral tension, therefore its key role in mechanotransduction processes is unsurprising. Composed of actin, intermediate filaments, as well as microtubules, the cytoskeleton provides a dense meshwork of polymers wherein intracellular transport occurs and local forces have been shown to be widely distributed [87]. The actin network, in particular, has long been known to respond to external forces through deformation and rearrangement [15, 88-93]. Actin is the most profuse protein within the cell. By binding with adenosine triphosphate (ATP), globular actin (G-actin) polymerizes to form filamentous actin (F-actin). F-actin and microtubules, unlike intermediate filaments, are highly polarized, and deformation of these filaments occurs through a dynamic process of assembly and disassembly – a process that influences mechanical loading. Combined mechano-chemical models of actin filaments demonstrate an interaction between filament deformations and ATP hydrolysis [94]. It is only reasonable that applied force should also cause changes in the chemical make-up of the filament [95]. Mechanical cues directly affect actin formation and alignment. For example, endothelial cells exposed to fluid shear stresses, result in a significant change in the shape of the cells through remodelling of adherens junctions and the actin cytoskeleton [96]. The phenomenon of F-actin re-alignment in the direction of shear flow is dependent on tyrosine kinase activity (an enzyme that phosphorylates ATP), intracellular calcium (Ca^{2+}), and intact microtubules [14].

The cytoskeleton is also coupled with the plasma membrane via the actin cortex (reviewed in [97]). Proteins such as ezrin, radixin, and moesin (ERM) form links between the cortex and membrane, thus providing a direct interface for mechanical force transduction between the extracellular and intracellular environments. Phosphorylation of moesin, for instance, crosslinks actin filaments to membrane proteins, and is important for the initiation of cell stiffening and rounding during early stages of mitosis [98]. This interplay between the plasma membrane and underlying actin cortex has been shown to influence both cell shape [99] and function [100, 101]. Of course, intermediate filaments (reviewed in [102]), as well as compression-resistant microtubules also play a role in maintaining cell shape [103], in addition to sensing and trafficking signals to the nucleus [104].

The individual role of the plasma membrane in mechanotransduction has gained recent attention. Acting as a dynamic barrier between the external and internal environments of the cell, the plasma membrane mediates transport across lipid bilayers via passive diffusion for selective ions, active transport across ion channels, as well as endocytosis and exocytosis. The plasma membrane is host to a number of ligand-receptor binding sites and is coated by a number of proteins that encompass the glycocalyx – which itself has been recognized as a mechanosensor (reviewed in [105, 106]). The plasma membrane of endothelial cells are coated in a number of proteoglycans and glycosaminoglycans (GAGs) which have been shown to play a role in white blood cell rolling [107], red cell motion, and transendothelial transport (a review on shear flow and GAG force transduction is provided in [108]). Shear stresses arising from fluid flow may affect the structure of molecular components of the glycocalyx, or may alter the activation of enzymes. For example,

nitrous oxide (NO) production, which is activated in response to shear stress, is a homeostatic regulator of endothelial cells and the cardiovascular system [109]. By depleting specific components of the glycocalyx of bovine aortic endothelial cells, NO production is diminished by loss of heparan sulphate [110], hyaluronan, and glycosaminoglycans (all main components of the glycocalyx, excluding chondroitin sulphate) [111]. In a seminal paper by Weinbaum et al. [112], the dynamics of GAGs due to shear flow effects are described as a quasi-periodic fibre matrix model [113]. Squire et al. observed fibres on the order of 10-12nm that were spaced ~20nm apart in a mesh-like network throughout the glycocalyx, suggesting that its organization, which presented clustering effects, were driven by connections with the underlying cortex [113]. The model proposed by Weinbaum and colleagues suggests that bending rigidity (EI = 700 pn·nm^2) of this brush-like structure is adequate for providing a molecular filter for plasma membrane molecules, as well as for transducing shear forces to the underlying cytoskeleton [112].

Besides the glycocalyx, other membrane microdomains such as caveolae and lipid rafts, and membrane bound organelles such as the primary cilia, have been shown to play a role in mechanotransduction. Caveolae and lipid rafts are known to be involved in vesicular transport and cell signalling [114-116]. In particular, they have been shown to play an important role in Ca^{2+} signalling [117, 118], due to their coordination of many key proteins in a single microdomain, as reviewed and listed in [119]. Under normal circumstances, exposing cells to fluid pressure and shear forces results in subsequent activation of tyrosine kinase, extracellular signal-regulated kinase, and c-Fos (transcription factor) [120]. Through inhibition of membrane-bound cholesterol using filipin and methyl-β cyclodextrin, Ferraro et al. showed that none of the aforementioned mechanotransductive processes were initiated – validating that cholesterol-rich membrane microdomains were responsible for their activation [120]. Another membrane-bound non-motile organelle involved in mechanosensing is the primary cilia (an overview can be found in [121]). Primary cilia exist on most mammalian cells. They are composed of a microtubule-based axoneme and basal body, and rely on intraflagellar transport of protein complexes by molecular motors such as kinesin-2 and dynein. Deflection of these membrane protrusions triggers biochemical signals, the malfunction of which are associated with numerous disorders, known as ciliopathies [122]. Bending of cilia results in a build-up of stress, which causes an increase in intracellular calcium in epithelial cells [123]. In bone cells, primary cilia have also been shown to translate shear fluid forces into cellular responses, independent of Ca^{2+} flux. These include an increase in gene expression, such as up-regulation of the bone-matrix protein osteopontin, and an increase in cytokine release, such as the release of prostaglandin E2 (a metabolism regulator) in response to mechanical loading [31].

In discussing mechanotransduction, the importance of the nucleus cannot be overlooked. Acting as gene host and regulator, the nucleus is the largest organelle within the cell, and as such it must respond to mechanical forces that arise from both the extra- and intracellular microenvironments. In order for direct mechanotransduction to occur the cytoskeleton must directly interact with the nucleus [124]. Transmission of forces to and from the nucleus occurs via the Linker of Nucleoskeleton and Cytoskeleton (LINC) complex – a physical tie between SUN and nesprin proteins [125]. This mesh of transmembrane proteins connects the nuclear envelope (inner and outer

nuclear membranes and the nuclear lamina) with the actin cytoskeleton. Inner and outer nuclear membranes are coupled by nuclear pore complexes, wherein ion transport occurs. The nuclear lamina resides on the inner membrane and is mainly composed of lamin and associated proteins which connect the membranes to the inner chromatins amongst other nuclear components [126]. Despite the existence of these structural proteins within the inner nucleus, whether a force-bearing matrix exists within the nucleus remains controversial amongst researchers [127, 128]. Mutations in nuclear envelope proteins, particularly lamins, have been shown to result in altered transcription leading to a number of disease pathologies, also known as laminopathies. For example, mutations of the LMNA (lamin A/C) encoding gene results in the development of muscular dystrophy. Malfunctioning of lamins A and C also result in abnormal nuclear and chromatin structures, with loss of A-type lamins leading to reduced nuclear stiffness [129, 130]. Thus, if lamins provide structural support to the nucleus, then it is not surprising that mechanically high stressed tissues will result in cell death and ultimate failure. Interestingly, nuclear shape is highly correlated to expression of lamins. For example, human embryonic stem cells, which do not express lamin A and possess dynamic chromatin, have a very round nucleus. Only upon differentiation do these cells express noticeable levels of lamin A [131, 132]. Moreover, specialized cells such as neutrophils have irregularly shaped nuclei – lobes connected by chromatin, which are the result of reduced lamin A/C and over-expression of lamin B proteins. A thorough review on nuclear mechanics and its role in mechanotransduction can be found in [126].

Although we only have discussed the most well-known mechanotransduction constituents, many others have been documented. Despite their identification, many open questions surround exactly how mechanosensors actually sense mechanical stimuli. It is possible that applied force alters the position of molecules allowing for incorporation of other extracellular molecules. Or perhaps protein configuration is altered; proteins associated with focal adhesions such as vinculin, ERM, and fibronectin, for example, all exist in dual states of inactivity or activity [73]. Altered conformations may expose new binding sites where molecular interactions can occur. Of course, mechanical stimuli such as substrate stretch and fluid shear stresses may activate more than one response from more than one mechanosensor – and so sensors such as focal adhesions or ion channels likely act in unison.

1.4 Forces generated within the cell

Although extracellular forces have long been known to affect cell behaviour, recent studies also implicate intracellular forces in the regulation of cell and tissue fate [63, 95, 133]. Often, forces generated within the cell are responsible for the dynamics involved in morphological changes, adhesion processes, and motility. One mechanism of intracellular force generation is through ATP-driven sliding of molecular motors (Fig. 1.2 A). Hydrolysis of ATP, the unit energy of the cell, is required for movement of the cell's molecular motors, such as myosin II. This energy release allows molecular motors to slide along actin filaments, allowing for the cell to contract and expand. Contractile forces are transmitted from the actin cytoskeleton to the ECM via focal adhesions - mechanosensors of force from both the inner and external cellular microenvironments [79]. The magnitude of contractility is coupled with ECM stiffness, as demonstrated through observations using traction force

microscopy. Increased substrate stiffness results in increased focal adhesion assembly that drives increased actomyosin contractility. Increased actomyosin contractility also leads to increased focal adhesion signalling. This force-balancing act drives shape change and cell proliferation through adaptive cell adhesion. Molecular motors and their expenditure of ATP is not the only force-generating mechanism in the cell's repertoire; actin filament polymerization also directs forces along the cell membrane.

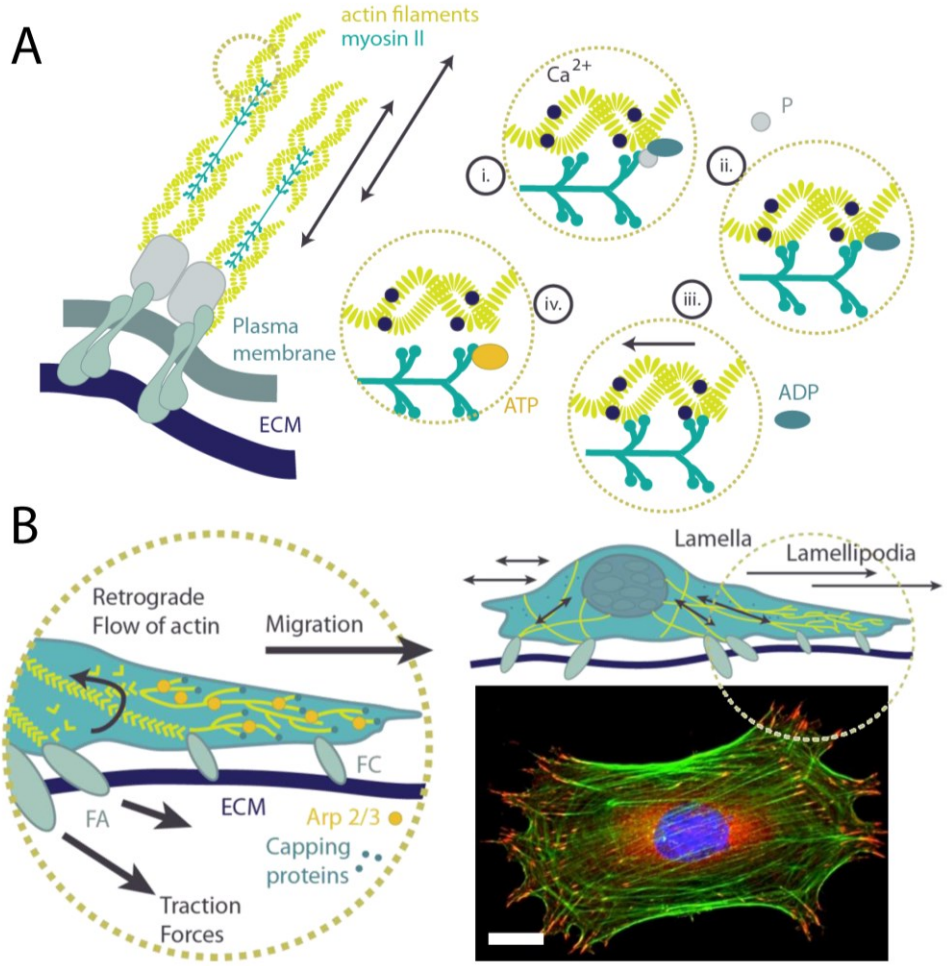

Figure 1.2 Force generation within the cell.
A) Actomyosin contractility, as proposed by Huxley and Simmons [134], generates forces transmitted through focal adhesions towards integrins and the ECM. i. In the presence of intracellular calcium (Ca2+) myosin heads hydrolyze ATP before firmly attaching to actin filaments. ii. Myosin binds to actin and forms cross-bridges. iii. Force is generated by "power stroke" as myosin cross-bridges reorient towards sarcomere center. iv. ATP binds to myosin head and it releases from actin bundle. B) Propulsive forces. Actin in the lamellipodia pushes against the plasma membrane in the direction of motion through actin branching and binding of Arp2/3. Capping proteins limit the length of polymerization. Forces are not required for the formation of focal complexes (FC) but do develop across mature focal adhesions in the lamella. Bottom right shows an immunofluorescent image of a C2C12 mouse myoblast cell stained for actin (green), an FA protein - vinculin (red), and DNA (blue). Scale bar is 10µm.

Actin polymerization is a polarized process involving continual acquisition and deposition of free monomeric polymers (G-actin). This active assembly/disassembly process generates a dynamic linear polymeric chain (F-actin), in a process known as treadmilling (Fig. 1.2 B). Formation of protrusions and their subsequent attachment to the underlying ECM are the driving factors involved in cellular motility. In motile cells, forces on the order of ~45pN are generated by branching of dendritic actin networks close to the cell's periphery [135]. These forces result in protrusions at the leading edge, which must be stiff enough to withstand significant compression and tension of the plasma membrane [136, 137]. This highly anisotropic network of actin fibres is formed by a repetitive sequence wherein surface-membrane proteins are activated, triggering the Arp2/3 complex which is involved in recruitment of G-actin monomers to mother F-actin filaments, thereby creating branches of daughter filaments [138]. The flow of actin towards the periphery is directed by the short effective radius of membrane-bound activating proteins. Capping proteins that diffuse throughout the cytoplasm are the limiting factor in actin filament elongation. Microtubules also contribute to the polarization process, and have been shown to direct migration by activating Rac1 leading to subsequent actin polymerization in lamellipodia [139, 140]. This repetitive process of initiation, branching, and elongation, which depends on this highly anisotropic network, is what drives the cell forward.

While providing integral support and stability to the cell, actin undergoes continual remodelling of key cellular features, such as lamellipodia, filopodia, and stress fibres. Actin dynamics have long been investigated in a variety of species and cell types [141]. A seminal paper by Theriot demonstrated that actin turnover in goldfish epithelial keratocytes is on the order of ~23s [142]. Measurements were made in the lamellipodia of these highly motile cells, and so it is unsurprising that actin turnover was found to be less rapid in a subsequent studying involving slower moving fibroblasts [143]. Differences in actin polymerization rates amongst cells have been hypothesized to be the result of diverse localization of ADF/cofilin, which is known to induce phosphate release [144]. The rate at which individual actin filaments elongate is on the order of ~0.3 microns per second. Actin-binding proteins such as formin and profilin have been shown to have significant effects on the rate of actin polymerization and rearrangement [145]. Although actin turnover is rapid in motile cells, actin filaments have been observed to remain stable between hours to days in striated muscle [137]. In these cases, ADF/cofilin binding is inhibited by tropomyosin. Similarly, stable stress fibres have been observed in non-muscle cells [146, 147]. A detailed review of actin dynamics in non-muscle cells can be found in [144]. While a variety of actin-binding proteins influence the polymerization rate and dissociation of actin filaments, mechanical forces have also been shown to influence both actin organization and mechanical properties.

The integration of mechanical forces and cellular mechanics dictates cellular shape and function. The interactions between actin and microtubules, for example, play a role in dictating locomotion, cell division, wound healing, and cortical flow [148]. During migration, the retrograde flow of actin at the leading edge has been directly linked to microtubule translocation to the rear of the cell. The integration of these two cytoskeletal networks has been hypothesised to direct movement through their physical links and activation of a Rho GTPase gradient [149]. Microtubule growth at the

leading edge is countered by de-polymerization at the rear of the lamellum, a region where actin converges and causes compressive disruption of microtubules. This polarized polymerization/growth interaction between actin and microtubules has been hypothesized to stimulate Rac/RhoA activation [140, 149, 150], direct signalling or membrane molecules during lamellipodia protrusions [151], or regulate focal contact interactions with the substrate [152, 153], in order to generate motility.

As discussed, cells experience a multitude of external forces that are transmitted between the outer and inner microenvironments via the cytoskeleton to inner cellular organelles, such as the nucleus. Moreover, cells themselves also generate force, through actomyosin contractility, and actin branching. Although many components involved in mechano-sensing have been identified, many questions still remain surrounding their exact mechanisms and function. For this reason, a variety of experimental tools, including AFM, have been used to probe the cellular response to force. Some of the commonly observed responses are discussed in the next section.

1.5 Nanomechanics using AFM

Nanomechanics has become a high traffic research area, wherein active (MTC, AFM, UAR, and MPA) and passive (LTM, and TPM) techniques have been used in attempt to characterize the cellular response to mechanical cues. Bulk rheological properties, typically Young's (elastic) (E), or shear (G) modulus are measured as they largely dictate the cellular response observed. Tools such as AFM, which can be used to directly apply and simultaneously measure cellular forces, are key tools in this emergent field. The advantage of AFM is that it is a multifunctional tool that can be used for imaging as well as force transmission and measurement. By altering tip geometry or chemistry a multitude of both local and whole-cell studies can be performed on living cells in their native environments (Fig. 1.3). Studies of this nature have been shown to induce a rapid response of cells through shape change, remodelling of the cytoskeleton, and calcium signalling, which all depend on frequency, duration, magnitude, and location of applied force [15, 50, 154, 155]. In the following sections, we first discuss the role of AFM as a tool to measure the mechanical properties of cells, particularly cell stiffness and viscous properties. As well, we highlight commonly observed cell behaviours in response to mechanical loading, including changes in cell geometry and internal organization. Finally, we outline some of the current techniques involving both localized and global stimulation of cell mechanics using modified cantilevers.

1.5.1 Apparent cell stiffness

The deformability of cells has been shown to affect a number of cell functions [156, 157], with increased cell stiffness correlating with differentiation [67], aging and diseased states [52, 158]. Commonly, AFM is used to measure the local elastic response of cell membranes and the underlying cytoskeleton by fitting force-indentation curves to contact models such as Hertz [159] and Sneddon [160]. Details on these methods [161] as well as Young's moduli of a variety of cell types are listed in [56]. Apparent stiffness of mammalian cells, as measured with AFM, typically range between 1 - 100's of kPa [15, 162, 163]. Apparent cell stiffness is highly correlated with the stiffness of the actin cytoskeleton, the structure and mechanics of which have all be shown to be directly influenced by mechanical forces including

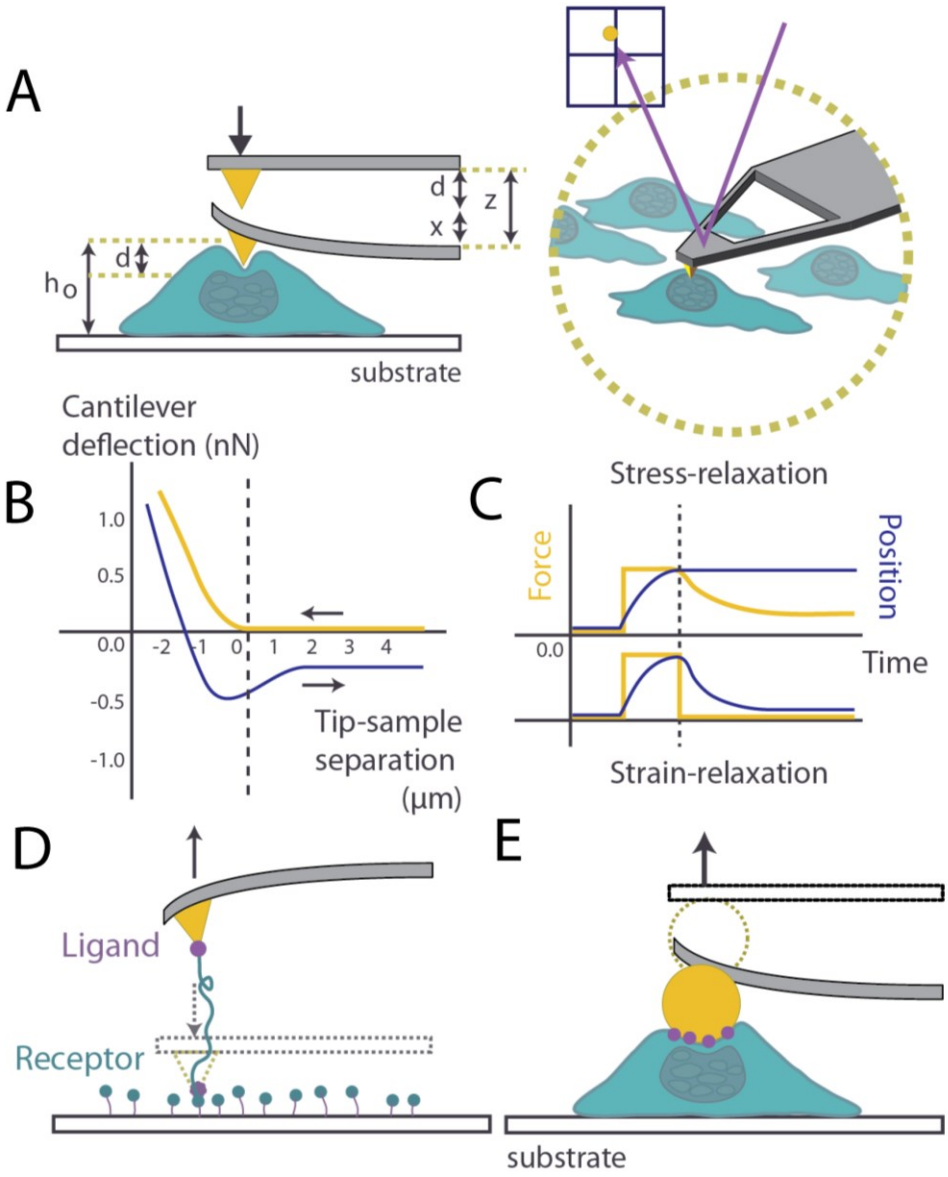

Figure 1.3 AFM modes of measurement.

A) AFM can be used to precisely apply compressive strains apically to cells within their aqueous environment. A laser deflected on the back of an AFM cantilever is measured by a photo sensitive detector (PSD). This allows for measurements of cantilever deflection to be recorded. B) AFM force-indentation curves are often used to measure cellular elasticity, by fitting the approach curve (yellow) to the Hertz model of contact mechanics. The retract curve (purple) often shows a hysteresis, and can be used to analyze adhesion. C) Stress and strain relaxation curves are often used to measure time-dependent cellular behaviours. Following an applied strain on a cell, the cantilever can be kept at a constant height, and measurements of cellular force onto the cantilever can be measured. On the other hand, following strain, the height of the cantilever as the cell relaxes can be measured. Modified cantilevers are also useful for measuring binding/unbinding forces between ligands and receptors. D) Functionalized AFM tips are often employed for single molecule interaction experiments. E) Spherical tips or other physical modifications to AFM cantilevers can also be used to measure distributed forces. This can be combined with functionalization techniques, as shown.

tension/compression [164, 165] hydrostatic and osmotic forces [53, 166]. Studies have directly demonstrated drastic reductions in stiffness with the use of actin depolymerizers, but not with depolymerizers of microtubules [50, 167, 168]. Interestingly, the elastic moduli of purified filament networks are orders of magnitude lower than whole-cell measurements, with reports of E ≈ 1Pa. While marginal increases in stiffness have been reported when cross-linkers are employed (1-100Pa), there still remains a significant difference between the apparent stiffness of reconstituted networks and that of whole-cells. Unsurprisingly, cells exposed to constant cyclic mechanical load (cardiac and muscle cells) have been shown to be stiffer than endothelial cells [55]. Mechanical cues largely regulate actin organization and growth leading to different stiffnesses between cell types [169].

It has become increasingly common to characterize and identify diseased and healthy cells using stiffness measurements [158, 170-172]. Combined AFM imaging and local force-indentation measurements have demonstrated significant differences between healthy and diseased erythrocytes [158]. Erythrocytes from patients with type 2 diabetes demonstrated significant aggregation of surface proteins, increased tip-cell adhesion, as well as increased stiffness in comparison to healthy cells [158]. Cell stiffness has also recently been proposed as a candidate for cancer cell detection, as cancerous cells are considerably softer (upwards of 70%) in comparison to healthy cells [170, 171, 173, 174]. Softness associated with cancerous cells has been linked to the deformability of the cytoskeleton which has long been known to play a role in metastasis [175]. Lekka et al. have shown that this type of characterization can also be used directly with cells from tumours and surrounding tissue samples taken from patients [170]. In comparison to normal cells, cancerous cells have been shown to have a dense elongated cellular brush, consisting of the glycocalyx and pericellular layer [173]. This brush may interfere with fitting of force curves using typical pyramidal AFM tips. Stringent statistical tests must be carried out in order for AFM analysis to be used as an effective cancer diagnostic method [170], as both substrate effects [162] and incorrect fitting of force-indentation curves can lead to deleterious reports of absolute Young's moduli.

Varied reports of cellular elasticities in the literature are in part due to the highly non-uniform cell surface. AFM generated force-maps have revealed local variations in cell height and stiffness (usually several kPa) due to the presence of internal components, such as actin bundles [163, 167] and the nucleus [155]. Moreover, stiffness measurements depend not only on cell type, but probe geometry, rate of force application, and force magnitude [56, 176]. Typical high aspect ratio conical AFM tips have radii < 30nm, and generate high local stresses which might penetrate the membrane during large magnitude force application [177]. Thus, to avoid damage and operate within the elastic deformation regime, Young's modulus measurements are generally made using low forces, in the range of 0.1 to several nN. Nawaz et al. have recently shown that only at extremely low forces (< 30 pN) and low deformations (0.2μm) do fibroblast cells present ideal linear elastic behaviour [176]. They used an optical trap method to apply these low forces, as the AFM is limited by thermal noise at forces nearing 20pN in liquid. At higher forces (> 30pN) delivered by an AFM, viscoelastic behaviour was observed, as indicated by hysteresis between the force approach-retract curves. Importantly, their work demonstrated that at very small deformations the elastic response was rate independent, and reliant upon the cortex. Considering the limited thickness of the plasma

membrane (~10nm), it is unsurprising that the underlying cortex (~200nm) will largely resist the deformation [178].

Apparent stiffness, which is generally measured using AFM, is based on the assumption that the cell behaves as an isotropic purely elastic material. Dynamic AFM experiments, on the other hand, suggest that stiffness (k) increases with increasing frequency (f), and can be described by a weak power law $(k(f) \sim f^{\alpha})$ at higher deformations. Although power laws have often been used to describe frequency-dependent rheology, there remains variability in reports of exponents (α). Elasticity measurements of this nature are generally only comparable if all experimental conditions are kept constant. In order to circumvent these concerns, stiffness measurements are often used in a relative manner rather than as absolute values [167]. The heterogeneous nature of the cell, as well as influence from the underlying substrate makes obtaining the cell's intrinsic apparent stiffness difficult to quantify. Applying shallow indentations [55] and using modified contact mechanics models [162, 179] can however alleviate these issues.

1.5.2 Stress-strain relationships

Although a cell's apparent elasticity directly influences its deformability it does not fully account for the complex behaviours observed following mechanical perturbation. Cells respond to abrupt external perturbations in a highly non-linear, time-dependent manner [180]. Many AFM studies have revealed the viscoelastic nature of cells, as witnessed by creeping deformation and relaxation behaviour following loading [16, 56, 155, 174, 181, 182]. The actin cytoskeleton alone has been shown to exhibit viscoelastic behaviours [39]. Cellular viscoelasticity is influenced by a hierarchical structure - the membrane, cortex, and cytoplasm (amongst other subcellular components) all contribute to the cell's mechanical properties. The cortex and actomyosin in particular play key roles in maintaining cell shape and function [168, 183, 184]. Organization of actin significantly impacts the cellular response to force, as seen during recruitment to the cortex which provides resistance to external forces. Tension in the plasma membrane also resists deformations, and has been shown to possess a relatively high elastic modulus [185] and a low shear modulus [186]. Membrane tension is relieved by increasing intermolecular separation and relieving undulations in order to increase its surface area during deformations [187, 188]. The mechanics of the membrane and cortex are also physically linked, and so the properties of both inherently influence one another. Recently the contributions of cytosolic flow have also been shown to influence the response to deformation [181]. Moreover, the nucleus, as the largest cellular organelle, clearly plays a large part in defining overall cell properties. Until recently, nuclear mechanics have been characterized as isotropic materials [189, 190], however recent evidence has shown that they possess much more complex behaviours [191-193]. Clearly, the complex shape and structure of the cell's inner components play a role in defining cell mechanics. With these considerations in mind, many researchers have used the AFM as a cell nano-indenter to quantify cell viscoelastic properties in the time and frequency domains [49, 56, 194-197].

A large number of studies have employed both pyramidal and spherical tips to directly deform cells (Fig. 1.4 A) which have been shown to withstand relatively large forces (within 10-20nN) *in vitro* [198, 199]. These deformations of the membrane and underlying cytoskeleton result in viscoelastic behaviours. Cellular creep and relaxation experiments, measured using AFM, have been used to

determine apparent viscosity and relaxation behaviours that are generally associated with simple models and a discreet number of time constants [16, 56, 155, 174, 181, 182, 200]. Time constants are generally associated with an elastic deformation regime, and exponentially increasing viscous creep (Fig. 1.3 C). During constant stress experiments, creep, J, can be measured as a ratio of time dependent strain over stress: $J(t) = \varepsilon(t)/\sigma_o$. On the other hand, by maintaining a constant cantilever displacement (while straining the cell), the force-feedback on the cantilever can be measured as a function of time. This type of experiment results in stress relaxation curves, from which apparent cell viscosity can be measured by fits to a time-dependent modification of the Hertz model [168]. Using this method, the relaxation behaviour of the cell is treated as a standard linear solid model (a Maxwell model in parallel with a spring). Stress-relaxation experiments have shown that the actin cytoskeleton, and not microtubules, primarily influence the cell's apparent viscosity in mouse ovarian surface epithelial cells [168].

Cellular rheology is best described by the mechanics observed across a wide range of frequencies, as well as force magnitudes. For this reason, many have used the AFM in a dynamic mode, which allows for determination of the complex elastic or shear moduli of cells [201]. For example, by operating in a high frequency (50-300Hz), low amplitude (2-5nm) oscillatory manner, the frequency-dependent viscoelastic behaviour of NIH 3T3 fibroblasts was examined [179]. Mahaffy et al. determined the elastic storage and loss moduli of living fibroblast cells by measuring the amplitude and phase shifts, and extending the Hertz model to include frequency-dependent behaviour [179]. Both elastic and adhesive properties of the cell can be examined in this oscillatory mode, however it is necessary to include appropriate models to incorporate the deformation of soft samples of finite thickness. By taking into account tip-cell contact geometry, as well as viscous drag effects of the aqueous sample, researchers have used this dynamic mode to measure the complex shear modulus $G^*(\omega)$ of cells at a range of frequencies and load magnitudes [202]. Generally, the observation that prevails is power law behaviour. At low frequencies (< 10Hz) both the storage $G'(\omega)$ and loss moduli $G''(\omega)$ follow the same behaviour, however at higher frequencies the power law exponent of the loss modulus is progressively increased. Power-law behaviours suggests that cells may not be described by distinct time constants after all [43, 44, 48, 203]. While experimental observations do appear to follow power-law behaviour; measurements are often only performed over millisecond- to second-long timescales. Limitations of both methods must be taken into consideration, including possible interactions within the cell which may lead to remodelling events and unknown binding geometries [204]. Moreover, the cell is not an inert material, the cytoskeleton undergoes constant remodelling within timescales relevant to these experiments, and so it is difficult to obtain a complete picture of overall cell mechanical properties.

1.5.3 Cellular response to force

In addition to characterizing strains, AFM deformation studies have elicited a plethora of cellular responses in vitro (Fig. 1.4 B depicts several of these responses). Cell signalling, in particular, has been demonstrated in response to forces applied using an AFM. One example demonstrated that vertically applied strains results in a transient increases in intracellular calcium in osteoblast cells – a

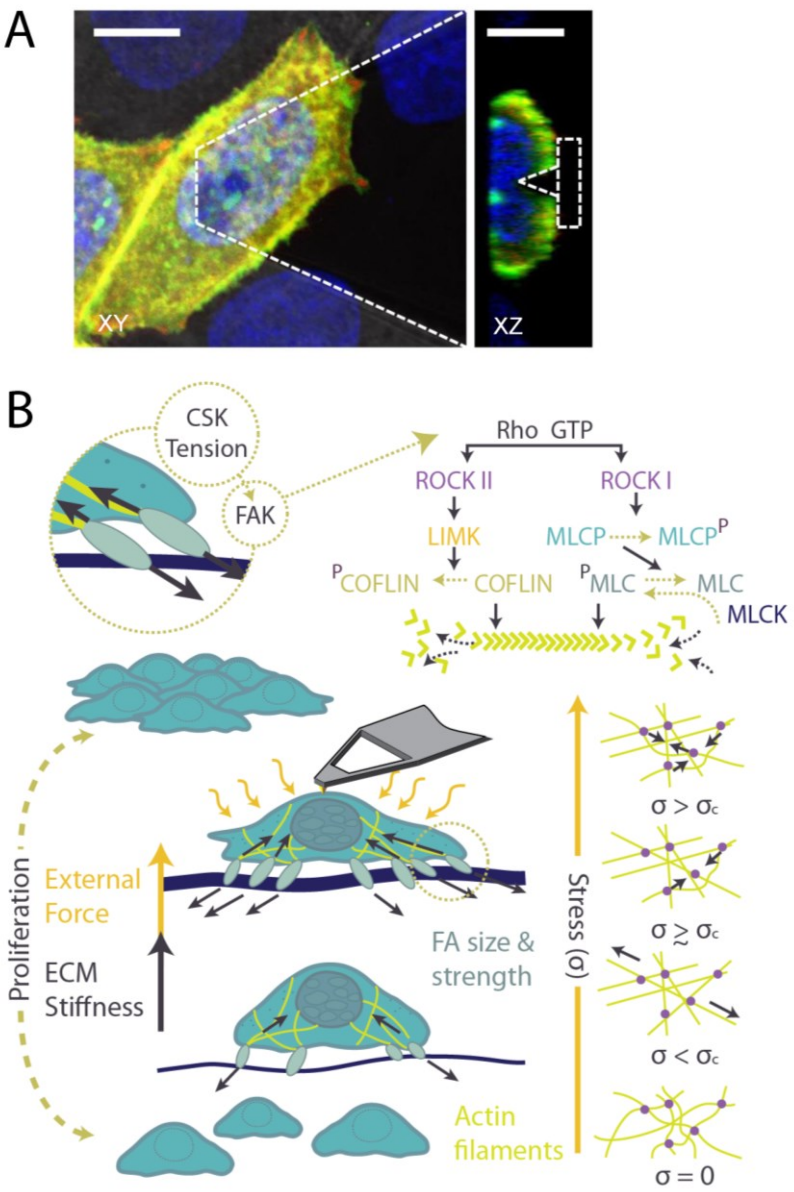

Figure 1.4 Cellular response to mechanical cues.
A) Confocal projection image of a live HeLa cell deformed by a pyramidal AFM tip. Shown is the deformation in the orthogonal XZ direction. HeLa cells shown were transfected with EGFP – Phospholipase-C- δ (a membrane marker in green), and in LifeAct Ruby (an actin RFP shown in red); nuclei were dyed with Hoescht (blue). Scale bars are 10µm. B) Both the mechanical properties of the ECM and externally applied forces, such as those from an AFM tip, have been shown to increase cell spreading, traction force magnitude, and proliferation. Tension between the ECM and cytoskeleton (CSK) activate focal adhesion kinase (FAK), which has been shown to directly activate the Rho family of GTPases. Through different pathways, ROCK has been shown to lead to both polymerization and depolymerisation of actin stress fibres. Mechanical forces have also been shown to stimulate both a stress-stiffening and softening response of actin networks. One hypothetical model explaining this paradox is shown, as in [205]. With increasing stress actin filaments elongate due to tension (stiffening), until a critical stress (σ_c) is reached, following which filaments begin to buckle (apparent softening).

response observed to be transmitted to neighbouring cells [50]. Importantly, compressive forces applied to cell nuclei have also been shown to result in altered gene expression [22, 126]. The cell actively senses and responds to changes in the surrounding environment through an interplay of actomyosin dynamics and focal adhesion remodelling. Thus, it is not surprising that mechanical tension directs the formation and remodelling of focal adhesions in vitro. Cells are particularly sensitive to changes in stiffness and actively tune the magnitude of traction forces they generate upon their substrate, as regulated by Rho, Rac, and CDC 42 GTPases [206]. Recently, AFM stiffness measurements of wild type and mutant mouse embryo fibroblasts demonstrated that focal adhesion kinase (FAK) and Cas stimulate Rac activity, promoting intracellular stiffness and a mechanosensitive feedback loop in response to ECM stiffness [207]. Compressive forces may also stimulate this feedback mechanism. Combined AFM and traction force microscopy demonstrated that external forces and substrate stiffness both direct focal adhesion size and strength [208].

Mechanisms of actin-based force generation and growth have also been investigated using nano-indenters [205, 209, 210]. By functionalizing an AFM cantilever with ActA (Listeria nucleation promotion factor), and immersing it within a liquid cytoplasmic cell extract, the Arp2/3 complex can be activated, resulting in the growth of a network of actin [209]. Force feedback measurements on the cantilever revealed three growth regimes: a development phase, a load-independent phase, and load-dependent cessation of network lengthening. Surprisingly, a decreased load applied to the network resulted in an increased growth velocity demonstrating a load-history dependent response [209]. In vitro studies have also shown that apically applied compressive forces result in highly localized non-isotropic deformations of stress fibres [15]. Myoblasts and alveolar epithelial cells are constantly exposed to quick bursts of stretch in vivo; however in vitro experimentation has shown a complex mechanical response to cyclic forces. The cellular response to stretch and compression results in a paradox: as both cytoskeletal reinforcement and fluidization have been reported [92, 211]. The same is true for reconstituted dendritic actin networks formed by a nucleating surface (an AFM cantilever). In response to a sinusoidal load, stress stiffening was observed, followed by reversible softening [205]. This behaviour has been attributed to entropic elasticity as filaments are extended, leading to a stress-stiffening regime, and reversible buckling of actin filaments at higher loads [205] (Fig. 1.4). The large elastic modulus of these anisotropically organized filaments is primed for resistance to compression – as is necessary at the leading edge of motile cells. This stress-stiffening behaviour has been observed during relatively small (< 10nN) cyclic forces applied at a constant height from an AFM to attached cells [212]. Initial increases in local tension were followed by a subsequent decrease (explained by stress-relaxation of the cortical cytoskeleton), and long-term slow increase in tension as the cycles persist (likely diffusion-limited, as in the recruitment of myosin II). Considering that tension recovery-associated factors (such as myosin II here) are recruited during each tension-compression cycle, it is not surprising that the tension recovery slows with each cycle, as binding sites are filled, and there may be less of the motor proteins in the vicinity. By inhibiting actin polymerization and myosin II contractility with the use of Cytochalasin D, and Blebbistatin, respectively, the authors verified that the acto-myosin network is responsible for the observed tension recovery following cyclical loading [212]. This study importantly shows that cells have

"memory" – they initially stiffen with regard to an external force, but then become increasingly insensitive to repeated perturbations, thus responding in an adaptive, and likely protective, manner.

1.5.4 Modified cantilevers

Biochemically modified cantilevers are often used in order to probe adhesion of whole cells, localized regions, and specific molecules (reviewed in [213]). Coatings, such as poly-L-lysine, have been used to strengthen the bond between the tip and cell allowing for membrane tethering and retraction curve analysis [214]. By microinjecting biotinylated cadherin-expressing cells onto an AFM tip coated with streptavidin, single cells can be used to form adhesions with other cells in culture [215]. Using this method, researchers have shown that the specificity of E- and N-cadherins are distinct (preferring homophilic bonds), alongside producing different adhesive and compliant bonding forces. Similarly, ligand binding to AFM tips allows for examination of specific cellular molecules and their interactions [216]. Recently, biotin/streptavidin functionalization has shown that tension regulates actin depolymerisation [217]. This technique has also been used in conjunction with force-mapping methods in order to spatially locate receptors of specific antibodies bound to the tip. For example, a specific tyrosine kinase antibody (anti-Flk-1) was used to demonstrate that clusters of vascular endothelial growth factor (VEGF) receptors exist. VEGF is known to play a role in altering permeability to extracellular macromolecules in endothelial cells, which aid in their growth. These clusters were shown to drastically alter the mechanical properties of the cell [218]. The reduced elastic modulus observed in regions of VEGF clusters, is thought to be caused by their reorganization of underlying cytoskeletal filaments in the promotion of cell growth. This is a good example demonstrating the influence of local composition and structure on cellular mechanics.

Besides biochemical functionalization, modifications to tip geometry have also resulted in numerous interesting applications. For example, ion beams have been used to etch the cantilever's tip into a thin needle-like rod (200-300nm in diameter) which researchers have used to perform cellular nano-surgery. [219]. Sharp tips have been shown to penetrate both the outer plasma membrane and inner nuclear membrane, as demonstrated by recorded spikes in force-indentation curves. This technique has allowed for delivery of proteins and chemicals to the inner cell nuclei [219], enabling single cell transfections [177]. Rather than decrease the size of the tip, others have attached spherical beads of a relatively large diameter (> 20μm) to AFM cantilevers. This approach allows for a more even distribution of compressive forces to be exerted upon cells, and is often applied to adherent cells to gain a better approximation of whole-cell rheological properties. Often tip modifications are used in unison with optical microscopy techniques. For example, Stewart et al. tracked the force feedback on a spherical tipped AFM cantilever and simultaneously tracked the cross-sectional area of a cell undergoing mitosis [220]. Cell pressure was shown to increase dramatically (3-fold in 10min) alongside a small volume change, suggesting that osmotic pressures and the actin cortex largely contribute to morphological changes in the cell [220]. Tipless cantilevers have also been employed as parallel plate compression devices by adding a wedge to the end of the cantilever to correct for the mounting angle (usually 10-12°) [221].

Combining AFM with traditional microscopy methods has become quite conventional, as it provides a means for simultaneous application of external forces, quantitative measurements, and

direct visualization of the perturbed cells. A major limitation of these combined methods is that compressive forces on the apical surface of the cell create deformations in the orthogonal planes. To visualize deformations in the axis of loading Chaudhuri et al. developed a method using a coverslip and second CCD camera used in the lateral plane [222]. Using this method they were able to examine adhesive forces between leukocytes and endothelial cells. An AFM tip coated with concavalin-A was contacted with a leukocyte forming a strong bond, after which the sample surface was moved steadily away from the cantilever causing a tension on the tip-attached leukocyte and underlying endothelial cell. Large adhesive rupture forces, attributed to delamination of the cortex and membrane, were recorded as the cells were separated followed by small non-zero rupture forces as membrane tethers (visualized by their side-view method) that had formed between the two cells came apart. AFM has also been combined with other known optical techniques, such as total internal reflection microscopy (TIRF). TIRF allows for observation of the dynamics in the basal membrane of cells, all while undergoing compression from an AFM cantilever. Using this technique, Jonas and Duschl demonstrated non-linear stress stiffening behaviour of the cytoskeleton in the basal membrane of L929 fibroblast cells following compression [223]. Importantly, images obtained using TIRF showed that actin is responsible for force transmission throughout the cell. Existing contact regions between the cell and underlying substrate increase in size, and some new regions are formed following compression. Although we do not discuss AFM imaging in this review, this technique has many important applications in cell mechanics. For example, it has been used to identify various membrane proteins, and intracellular microfilaments [224, 225]; a good review can be found in [226].

Future studies must also consider mechanics at the mesoscale, as embryonic development, morphogenesis, and tumour progression, for example, are highly dependent on cellular organization. Techniques such as modified traction force microscopy [227] and stretching devices [228, 229] have recently been used to examine coordinated cell migration and stretch, respectively. Integrated mechanical properties have been shown to supersede those of single cells [228], demonstrating the importance of characterization of multicellular mechanics. While the precision of the AFM is primed for single cell studies, perhaps, novel AFM modifications will also prove useful for future studies of mechanics at the multi-cellular scale. Integration of single cell and multicellular studies will be necessary for a comprehensive understanding of their mechanics.

1.6 Models of the cell

In an attempt to describe the observed cellular behaviours discussed, a number of models have emerged over the years (Fig. 1.5). Simple mechanical models are often used to characterize the mechanical properties of cells in the time domain. These models are generally comprised of one or more elastic and viscous components, often denoted by springs and dashpots, respectively. The downside to this simplistic approach is that reported time constants vary widely in the literature. Discrepancies associated with these models are often attributed to varying time scales and frequencies of experiments. Measurements made using passive techniques, such as LTM, tend to fall into two distinct regimes (sub- and super-diffusive regimes)[37, 89, 91], whereas active

measurements demonstrate more rheological variance when comparing frequency dependent behaviour.

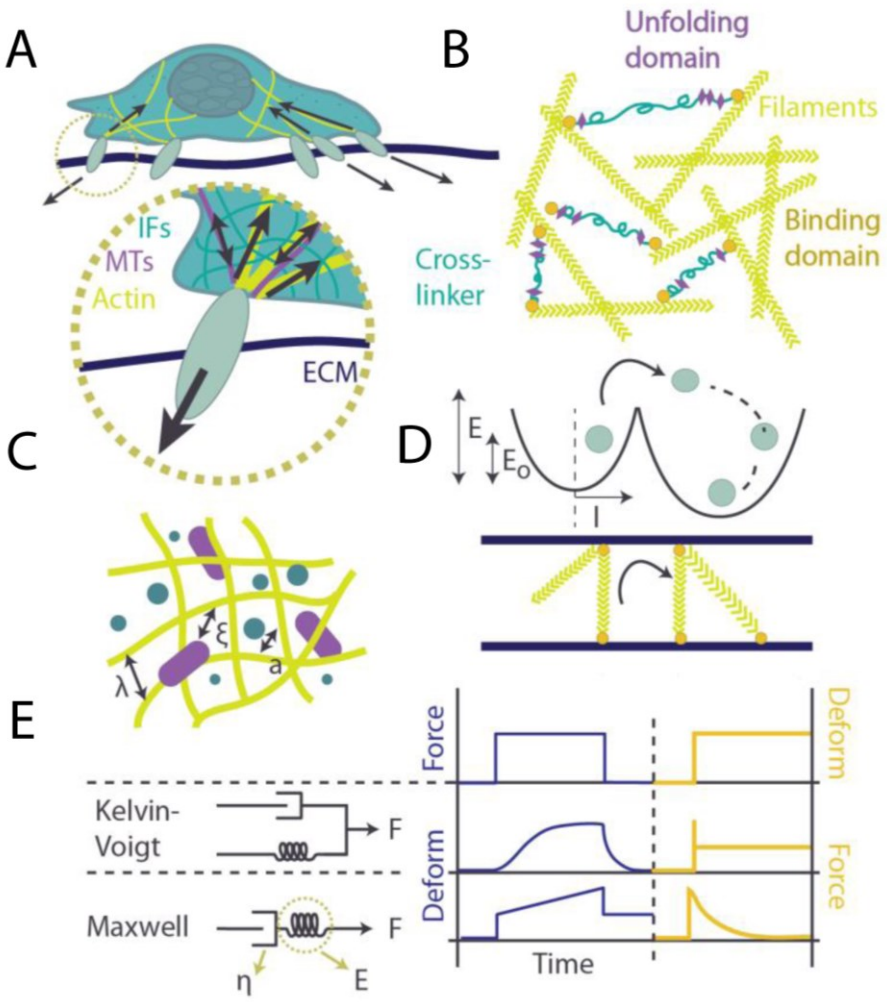

Figure 1.5 Models of cell mechanics.
A) Tensegrity model, as shown by force balancing between the cytoskeletal components and ECM. B) Active cross-linked polymer networks. C) Poroelastic model of cytosol flowing through a solid meshwork of filaments. The rate of flow is limited by filament size, and size of the macromolecules, a, and entanglement length of filaments, λ, and ξ, hydraulic pore size. Adapted from ref. [181] D) Soft glassy rheology (SGR) is shown through an image of a dynamic trap, wherein elements (myosin motors) hop between different quadratic wells or binding energies: $E = 1/2\, kl^2$. If attachment of a filament occurs at a length (l), then a force kl is generated (k is the spring constant) which results in sliding of the filament until equilibrium is reached. Adapted from ref. [230, 231] E) Commonly employed viscoelastic models. The Maxwell and Kelvin-Voigt models are shown as simple combinations of springs and dashpots, representing elastic (E) and viscous (η) components, respectively. Shown are the corresponding stress (constant force) and strain (constant deformation) creep and relaxation curves for each of the models.

Many researchers have reported power-law behaviour to describe the creep function of cells following an applied step-stress [44, 203]. Contrary to the discreet number of time constants associated with simple mechanical models, power-law behaviour implies a large number of continuous time

constants. Universality in rheological exponents appears to exist amongst the power-law form of cells' frequency-dependent behaviour, but not in its amplitude, as demonstrated during controlled changes of physical properties, particularly apparent during chemical perturbation. For example, Cytochalasin D is often employed to depolymerise actin, resulting in decreased elastic moduli of cells, however the range of values reported is quite large (100-1000's kPa). In cases of non-universality, researchers have proposed that cells were nearing a phase change and can be better represented by soft glassy rheology (SGR). Whether or not these discrepancies are due to altered interactions with the measurement probes remains an active area of research. A number of other classical models have been used to describe cellular mechanics over the years. These include, but are not limited to, the sol-gel hypothesis, tensegrity, and models of active cross-linked gels, a detailed discussion of which can be found in [61]. Several models have been derived from both constitutive and global approaches to examining cell mechanics.

At their most basic uncoupled state, purified polymer networks have provided a great deal of insight into the mechanics of subcellular cytoskeletal components [138]. Models based on entangled polymer networks, such as the sol-gel hypothesis involve the transformation of a solution (sol) of monomers into a biphasic gel or network of flexible polymers. These biphasic polymer networks are comparable to the cytoskeletal filaments contained within the cytoplasm of the cell. Treated as an elastic continuum, these networks deform under shear, but are incompressible to hydrostatic forces. Networks of short filaments and a low concentration of cross-linkers behave as a fluid when exposed to stress (the sol-state), whereas a high concentration of cross-linkers or lengthened filaments exhibit elasticity (the gel state). Traditional sol/gel states are only reliant upon thermal fluctuations; however, in the context of cells more complex ATP-driven mechanics are at play. Similarly, continuum models of active cross-linked gels have been proposed to describe the behaviours of reconstituted isotropic actomyosin networks [232-234]. By altering protein and cross-linker concentrations in vitro, self-assembly dynamics can be studied at different length, time and force scales. Under tension, models employing purified actinin and filamin, as passive cross-linkers, demonstrate power-law behaviours similar to cells. Similar to the contradictory findings in whole cells, both strain hardening and softening have been observed in reconstituted polymer networks [205, 235]. Protein unfolding/unbinding has been proposed to explain these behaviours, with unbinding dominating at low pulling rates, and unfolding of cross-linkers dominating at faster rates. Although gesolin (an actin binding protein) and filamin (cross-linker) have generated increasingly realistic cell behaviours [236], generally large discrepancies exist between rheological properties derived from purified systems of entangled cytoskeletal filaments and those of intact cells [235, 237].

Discreet models have also been used to describe whole-cell behaviour. First proposed by Ingber, the tensegrity model equates the cytoskeleton to pre-stressed structural components that act in unison to provide structural integrity to the cell [238]. In particular, the acto-myosin network is thought to generate pre-stress within the cytoskeleton, while extracellular tension is generated through cadherins or focal adhesions. Actin and intermediate filaments have been shown to generate and sustain tension, whereas microtubules and focal adhesions bear internal compressions of the cell. Moreover, pre-stress in cytoskeletal components has been shown to be

linearly related to overall cell stiffness. While useful for describing macroscopic deformations, tensegrity does not describe cellular phenomena related to frequency dependence, thermal and non-thermal fluctuations, or localized mechanical properties. Although cell stiffening has been shown in response to externally applied forces in vitro, it is not clear whether or not strain hardening, rather than tensegrity, might better describe such occurrences.

A model proposed by Sollich [231], SGR, has also been used to describe various cellular mechanical phenomena [230]. Using this model, a phase transition (aging) is brought about by a structural rearrangement within cells that likely relies on ATP or mechanical stress (Fig. 1.5 D). Promotion/inhibition of actin polymerization and myosin contractility both result in conflicting results in the literature. In contrast to the strain-hardening behaviour predicted by the tensegrity model, SGR predicts strain-softening will occur when cells undergo application of large forces. Although the application of SGR is widespread for describing the physical phenomena observed in many cellular dynamics experiments [91, 202, 203], it is best used to describe only the contractile actomyosin network.

Recently, poroelasticity has been used to describe the dynamic behaviour of whole-cells undergoing deformation [166, 181]. The premise of poroelasticity is based on deformations of soft gels [239]. As the material undergoes deformations the fluid phase flows through a solid mesh, thus a material's "poroelasticity" or deformability is limited by the pore size of the solid mesh (Fig. 1.5 C). Within the framework of a cell, the cytosol is characterized by the fluid component and the dense network of filaments and proteins comprises the solid mesh network. Moeendarbary et al. have recently shown that cell relaxation following mechanical perturbation (with a spherical indenter) can be described using this model [181]. Immediately following cessation of the external perturbation, the cell recovers quickly – and is attributed to the flow of cytosol through the filamentous cytoskeleton. By exposing cells to hypo-osmotic and hyperosmotic conditions, the authors demonstrate that the rate of flow of cytosol through the mesh is directly related to the pore size of the mesh. Considering that the cytoplasm is the largest cellular component by volume, its rheology in the context of cellular mechanics is likely dominant. While useful, poroelasticity does not describe long-duration recovery processes which are likely dominated by cytoskeletal remodelling.

Mechanical manipulation of cells has led to significant insight into their mechanics; however no consensus view of a general mechanical model has been reached. Much of the observed cellular phenomena are difficult to quantify, a complexity magnified by interactions between cellular components. It is probable that reported power law exponents and master curves represent an averaging of the behaviour of multiple structures, where one structure may dominate. Alternative models to the classical ones incorporate non-linear effects [240]. Models such as these have been proposed in order to describe phenomena such as cell fluidization; however they too are incomplete. Moreover, although protein unfolding/unbinding processes have been implicated in the mechanotransduction process, individual highly sensitive mechanosensors remain largely unknown. It is possible that molecules on the brink of a conformational change act as these sensors within a network of cross-linked biopolymers. Considering the number of cross-linking proteins within a given cell, it is likely that the sensing occurs by multiple proteins simultaneously, such as in focal

adhesions. Studies involving whole-cell mechanics as well as single polymer studies both have their drawbacks. A cell cannot be described by the sum of its components, as they comprise a complex hierarchy undergoing constant protein and structural turnover. Finding a unifying theory for cell rheology may rely intrinsically on a coarse-grained picture of the cell. However, measurements of bulk elastic and viscoelastic properties of the cell may only be useful in limiting cases. In an illuminating review on active biological materials, Fletcher and Geissler discuss how current theories involving linear and scaling-law rheological models only fit a small fraction of detail in the big picture of cell mechanics [138]. Difficulties include simultaneous deformation of a variety of cellular proteins and structures, meanwhile interactions with the probe are often ignored. As well, chemicals used for antagonizing or inhibiting the activity of certain cytoskeletal components are not specific, and can result in a myriad of other cellular changes. With these cautionary statements in mind, we note that only through careful examination of cellular mechanics will we be able to develop a clear understanding of the inner workings of cell mechanotransduction.

1.7 Conclusions

The cellular response to mechanical force is consequent upon both its structure and mechanical properties. Understanding and characterizing the cellular response to force is critical given that cell mechanics and extracellular forces themselves direct many important cellular processes, including differentiation, morphogenesis, and gene expression. Exactly how these forces are sensed and transferred into biochemical cues is still an area of intense investigation. It has been proposed that mechanotransduction occurs through a force-balancing act [241], wherein extra- and intra-cellular generated forces contribute to mechanosensory feedback mechanisms, largely controlled by actomyosin contractility [46, 93, 164]. Conformational changes in key proteins likely accounts for one avenue of direct conversion of mechanical signals into biochemical responses [242, 243].

Over recent decades, AFM has become a frequently employed tool used to examine the deformation response and rheological properties of cells. Apparent stiffness measurements generated from force-indentation curves have become useful for characterization and identification of normal and diseased cells. Moreover, force-feedback techniques are valuable for characterization of their viscoelastic properties. While useful, models used to interpret the observed cellular responses vary widely in the literature. A clear description of how cells respond to a variety of forces will provide insight into the mechanisms involved in many cellular functions. However, the complex interactions between many active components make it extremely difficult to obtain an all-encompassing picture of the cell. While the cytoskeleton, particularly the actin network and cortex, are particularly important in defining the elasticity of the cell, we now know that actin assembly and dynamics are largely influenced by extracellular mechanical cues, particularly those from the substrate of adherent cells. Linear and scaling-law rheological models only fit a small fraction of detail in the big picture of cell mechanics, as they do not consider non-equilibrium states [138]. Although theories of this nature will be required to describe cell behaviour, they will certainly be highly complex. And so, describing specific observed phenomena, such as actin growth at the leading edge or contractility consequent of molecular motors, with simpler models that relate to the length and time scales of experiments is beneficial.

Chapter 2| *Manuscript*

Resiliency of the plasma membrane and actin cortex to large-scale deformation

Kristina Haase[1] and Andrew E. Pelling[1,2,3]

[1]*Department of Physics, MacDonald Hall, 150 Louis Pasteur*
[2]*Department of Biology, Gendron Hall, 30 Marie Curie*
[3]*Institute for Science, Society and Policy, Desmarais Building, 55 Laurier Ave. East*
University of Ottawa, Ottawa, ON, K1N 6N5, Canada

Submitted October 22nd 2012 to *Cytoskeleton*
Accepted July 29th 2013, V.70. p. 494-514

- I, Kristina Haase, contributed towards the majority of the work including: cell culture, atomic force microscopy methods, image acquisition using confocal microscopy techniques, data and statistical analysis, preparation of the first draft and subsequent revisions.
- The arrangement of the manuscript has been modified for thesis formatting purposes.

Motivation |

Many studies have demonstrated the viscoelastic nature of cells in response to externally applied forces. The cytoskeleton, particularly the actin network, has been shown to play an important role in structurally supporting the cell. However, less is known about the nucleus and surrounding cytoplasmic regions. Moreover, although general relations between cellular components and deformation mechanics have been identified, the state of the membrane and underlying cortex has not been well-characterized with respect to cell shape recovery, particularly following prolonged deformations.

Hypothesis & Objectives |

The main objective of this manuscript is to characterize large-scale cellular deformations, and to identify key cellular components involved in the response. We used direct visualization methods to quantify the time-dependent deformations of the cell under localized loads at an extremum (large load magnitude and relatively long duration) while examining cell-shape recovery processes. We postulated that the actin cytoskeleton and nucleus also play a role in cell strain and recovery behaviour.

2 | Resiliency of the plasma membrane and actin cortex to large-scale deformation

2.1 Abstract

The tight coupling between the plasma membrane and actin cortex allows cells to rapidly change shape in response to mechanical cues and during physiological processes. Mechanical properties of the membrane are critical for organizing the actin cortex, which ultimately governs the conversion of mechanical information into signalling. The cortex has been shown to rapidly remodel on timescales of seconds to minutes, facilitating localized deformations and bundling dynamics that arise during the exertion of mechanical forces and cellular deformations. Here, we directly visualized and quantified the time-dependent deformation and recovery of the membrane and actin cortex of HeLa cells in response to externally applied loads both on- and off-nucleus using simultaneous confocal and atomic force microscopy. The local creep-like deformation of the membrane and actin cortex depends on both load magnitude and duration and does not appear to depend on cell confluency. The membrane and actin cortex rapidly recover their initial shape after prolonged loading (up to 10 minutes) with large forces (up to 20nN) and high aspect ratio deformations. Cytoplasmic regions surrounding the nucleus are shown to be more resistant to long-term creep than nuclear regions. These dynamics are highly regulated by actomyosin contractility and an intact actin cytoskeleton. Results suggest that in response to local deformations, the nucleus does not appear to provide significant resistance or play a major role in cell shape recovery. The membrane and actin cortex clearly possess remarkable mechanical stability, critical for the transduction of mechanical deformation into long term biochemical signals and cellular remodelling.

2.2 Introduction

It is becoming well recognized that mechanical stimuli in vivo influences a multitude of cellular and physiological processes [5, 244-246]. How cells sense and transduce these mechanical forces into biochemical signals (mechanosensation and mechanotransduction) is still an area under intense investigation [15, 244, 246]. Research has narrowed down many of the molecular components involved in mechanotransduction; however there remain many open questions with regard to the response of cells to mechanical stimulation. This response to mechanical force has been shown to be dependent on both the magnitude and timescale of force application [247]. Moreover, both local and global mechanical stimuli can give rise to rapid changes in cell signalling, deformation of the cytoarchitecture and changes in gene regulation [15, 248-251]. Cell-cell interactions have also been hypothesized as an influence in the response to loading, as densely packed cells are thought to act collectively during stimulation [252]. Cellular characteristics such as geometry and elasticity are important, and clearly influence the response to extracellular forces [253]. However these characteristics are derived from the behaviour of distinct subcellular features, in particular the plasma membrane, cytoskeleton, and surrounding extracellular matrix (ECM) [254].

The mechanical response of cells is largely influenced by the cytoskeleton, which provides structural support to the soft and flexible plasma membrane, and the cell as a whole [247]. The mechanical properties of the cell's microenvironment, contact with other cells, and chemical factors all influence the rigidity of the cytoskeleton [5, 245]. It has been hypothesized that cell surface receptors couple the cytoskeleton to the ECM and to neighbouring cells in order to transmit extra, intra, and inter-cellular forces [5, 156, 244-246]. Indeed, the physical properties of the underlying cell matrix also play a key role in governing many complex physiological processes [244, 246, 255, 256]. Cells generate traction forces as part of a mechanism to sense the mechanical properties of the surrounding microenvironment. Traction forces are mediated by actomyosin contractility and physical links to the microenvironment through membrane bound focal adhesion and integrin sites [244, 246]. Conversely, cells can also respond dramatically to physical forces arising in the microenvironment [15, 248-251, 257]. Some evidence suggests that the response of actin, following mechanical stimulation, is bimodal, i.e. rapid reinforcement, followed by a gradual reorientation of actin stress fibres [84]. Stress fibre formation is also influenced by mechanical cues [17, 258]. For example, zyxin (a known mechano-sensitive protein) has been shown to translocate from focal adhesion sites to actin filaments due to uniaxial cyclic stretch, thus increasing the thickness of stress fibres [259]. Physical forces arising from cyclic stretching and from cell-cell interactions have also been shown to result in rapid cytoskeletal remodelling [260, 261]. From these examples it is clear that the connection between the actin cytoskeleton and ECM are quite important in maintaining cell shape, rigidity, and the cell's ability to respond to external forces.

The actin cytoskeleton is often prized for its structural stability; however the plasma membrane must also withstand rapid and dynamic shape changes, and is obviously vital in cell physiology. Often, the plasma membrane is thought of as a soft and flexible structure, that can be ruptured quite easily in vivo [257], and so its rapid repair is critical for cell viability. Physical forces applied to the plasma membrane are transmitted throughout the cell [262], and laterally along the membrane causing changes in transmembrane protein conformation, leading to their activation [263]. As well, high local curvatures can cause a chemical rearrangement within the cell [245], implying that mechanical stimulation of the plasma membrane can lead to intracellular signalling, and potentially a change in function. In addition, there is an important and complex regulatory interplay between the mechanical properties of the plasma membrane and actomyosin cortex [100, 101]. The so-called cell cortex forms an interface between the external and internal cellular microenvironments and governs the mechanical properties of the cell. These properties are critical in the ability of a cell to rapidly change shape and respond to mechanical stresses during a multitude of physiological processes [262]. Importantly, the individual properties of the plasma membrane and actomyosin cortex have a significant influence on one another. The mechanical properties of the plasma membrane play a critical role in the local organization and bundling of actin at leading edge protrusions and filopodia [264, 265]. As well, cortical tension plays a key role during mitosis, controlling spindle positioning and morphogenesis, cell shape stabilization and cytokinesis [98, 100]. Although there are still many questions regarding the molecular and mechanical properties of the actin cortex [184], it has been shown to rapidly remodel (timescale of seconds to minutes) to allow for deformations that arise during motility [100], shape change [266] and during the exertion of mechanical forces [267]. Clearly,

the cell cortex must be resilient during deformation but remain dynamic to allow for rapid remodelling. In this study, our objective was to examine the time-dependent deformation and recovery of the membrane and underlying actin cytoskeleton in response to an externally applied mechanical load, while attempting to characterize the roles of the membrane, cortex, nucleus, and surrounding cytoplasmic regions during the response.

In order to probe the deformation and subsequent recovery of the cell membrane and actin cortex, HeLa cells were created transiently expressing the pleckstrin homology (PH) domain of phospholipase C conjugated to EGFP and LifeAct-Ruby to label the membrane and actin cytoskeleton, respectively. We applied nano-scale forces (5, 10, and 20nN) using the atomic force microscope (AFM) as a nano-indentor to the apical surface of HeLa cells for up to 10 minutes. Use of the AFM allowed us to apply precisely controlled forces to the cell membrane, either on- or off-nucleus. By combining AFM with simultaneous laser scanning confocal microscopy (AFM-LSCM) [15] we were able to systematically characterize the structural response of HeLa cells to external perturbations through direct visualization. We demonstrate that the response of the plasma membrane is dependent on both load magnitude and temporal factors, with perturbed cells exhibiting creeping deformation. By employing actin and actomyosin contractility inhibitors we demonstrate actin's crucial role in maintaining cellular resistance to deformation. Importantly, we observed a rapid recovery and maintenance of membrane integrity, following large local loads (20nN) for sustained periods of time (10min). Post-perturbation recovery of the cell membrane and cortex was observed to occur in < 2min without significant changes in F-actin stress fibre morphology, or deviation from the initial cell shape. Despite previous notions of the fragile nature of the cell membrane [257, 268], we show that the membrane, even without an intact cytoskeleton, proves to be surprisingly resilient to penetration. Our findings directly demonstrate that while cytoskeletal integrity is important for maintaining structural rigidity, the membrane and cytoskeleton can withstand and recover from large loads and deformations. Characterization of on- versus off-nucleus loading demonstrates that cytoplasmic regions surrounding the nucleus act in a more viscous manner in comparison to nuclear regions. This demonstrates the important finding that the soft nucleus does not resist deformation, and is not responsible for cell shape recovery in HeLa cells.

2.3 Results

2.3.1 Membrane indentation measurements in monolayers

Atomic force microscopy (AFM) and laser scanning confocal microscopy (LSCM) were employed to apply nanonewton forces to the plasma membrane of HeLa cells, while simultaneously imaging cellular deformation (Fig. 2.1 A). This was performed on cultured monolayers of HeLa cells transiently expressing the pleckstrin homology (PH) domain of phospholipase C (PLC-δ) conjugated to EGFP (PH-PLCδ-EGFP) and counter stained with the live-cell nuclear dye Hoechst 33342 (Fig. 2.1 B, C). This approach allowed us to directly visualize of the indentation of the AFM tip into the cell. The deformation of the cell membrane over time was investigated by applying a constant 5, 10, and 20nN force, applied to the cell nucleus, which closely approximates the centroid of the cell as we

have previously shown [15]. Force was applied for a period of 10 minutes followed by removal of the tip and continued imaging. LSCM volumes were acquired prior-to and during application of the force, from which YZ and XZ orthogonal views were examined (Fig. 2.1 B). Direct measurements of the indentation depth were made every minute over the ten-minute application time. We calculated the ratio of deformation to initial cell height in order to normalize cell-to-cell variations in height.

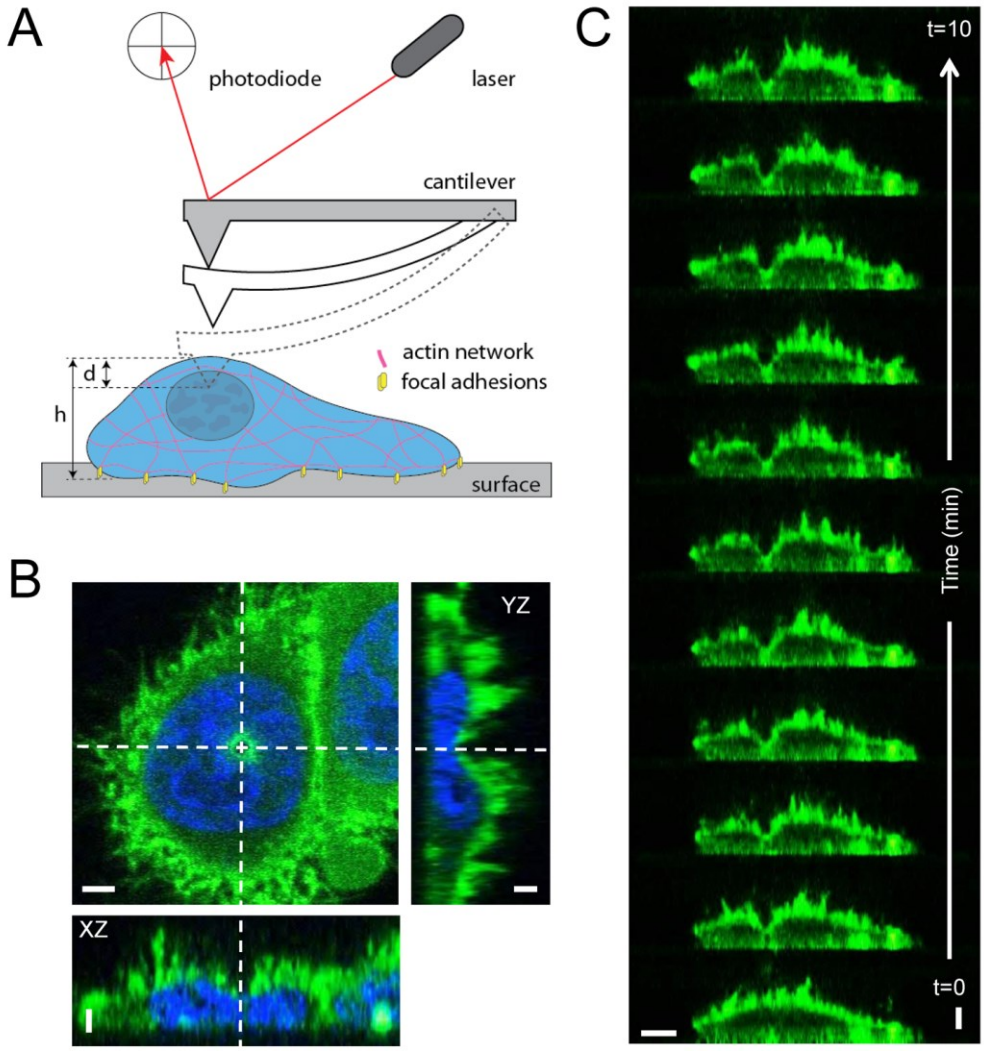

Figure 2.1 AFM setup and LSCM volume acquisition.
A) Schematic diagram of the AFM set-up used as a nano-indentor. The AFM is employed to impose an indentation of a given depth (d) into a cell of a given height (h). B) A living HeLa cell deformed by a 10nN force applied by an AFM tip above the cell's nucleus. Orthogonal views show that both the membrane and underlying nucleus were deformed. C) Deformation over a 10 minute duration – the depth of deformation increases as demonstrated from t=0 to t=10. Green: PH-PLCδ-EGFP, Blue: Hoechst 33342, Scale bars= 5µm.

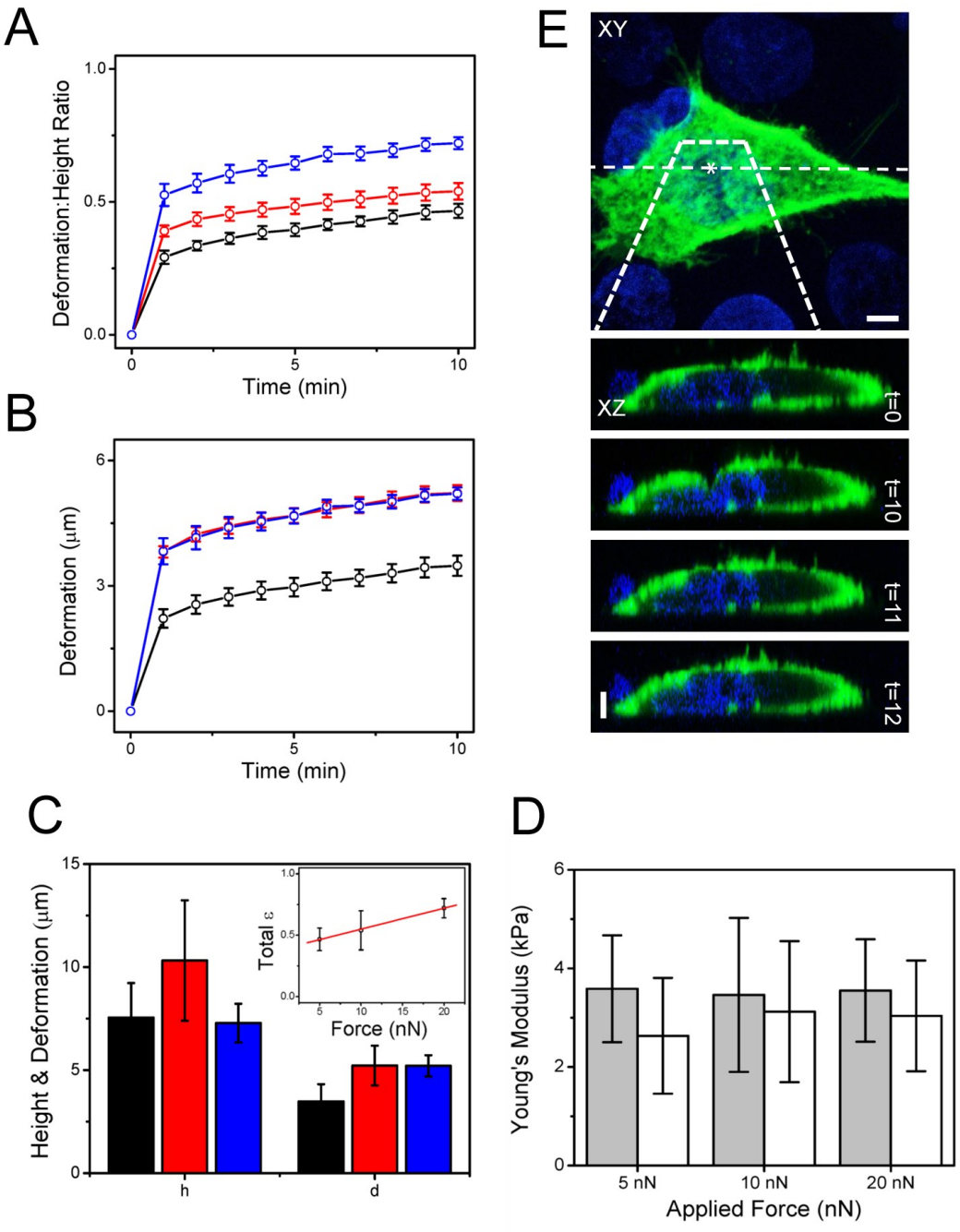

Figure 2.2 Force magnitude affects deformation but not elastic modulus.

A) The effect of force magnitude on normalized membrane deformation. The normalized depth of deformation (d/h) of the cell membrane is proportional to the magnitude of the applied force. There was a significant ($P < 0.05$) difference between the total deformation observed, after 10 min of constant force application, between 10 and 20nN forces applied to HeLa cell membranes. (5nN – black, n=12, 10nN – red, n=26, and 20nN – blue, n=12) B) Total deformation over time. Deformations involving 10 and 20nN result in similar depths (d) reached in cells, as they are both relatively large-scale forces in comparison to 5nN. C) Corresponding averages of total deformation (d) and initial cell heights (h). Inset shows that normalized deformation (strain) is linearly proportional to the applied force, within this range of magnitudes. Total strain is significantly higher for 20nN and is independent of variances in cell height. D) Young's modulus calculated

before (grey) and after (white) 10 min of force application. Shown are the differences in average Young's moduli – which are independent of force magnitude. E) Z-projection of a cell deformed by a 10nN load above the nucleus for 10 min. Orthogonal views demonstrate that no deformation is visible within 2 min following tip removal (t=11 min), as the membrane has recovered its initial pre-deformed shape (t=0). The (*) indicates the apex of the AFM tip. Green: PH-PLCδ-EGFP, Blue: Hoechst 33342, Scale bars=5µm. All time is in minutes and error bars shown are standard error.

As expected, the observed indentation was force dependent (Fig. 2.2 A-C). As well, the deformation was observed to creep over time under a constant applied force due to the viscoelastic behaviour of the cell (Fig. 2.2 A). As cells were randomly selected across samples there were significant height variations (Fig. 2.2 C). Regardless of this, the relative deformation depends linearly on force magnitudes within the range tested (Fig. 2.2 C *inset*), with 20nN resulting in a significant increase in total normalized deformation after 10 minutes of applied force (ε in the *inset* Fig. 2.2 C). In addition, Young's moduli, measured by fitting AFM force-distance curves to the Hertz model, were determined before and after the applied load, on the same cell. No significant change ($P > 0.5$ in all cases) in the elastic modulus was observed, even after a ten-minute period of perturbation (Fig. 2.2 D).

LSCM volumes were also acquired following removal of the tip in order to examine the post-deformation recovery of the cell. Interestingly, 1 minute after removal of the applied load showed that the membrane had already begun to recover from its initial deformation (Fig. 2.2 E). Within 2 minutes following 10 minutes of a 10nN load, the recovery of the membrane was complete or well underway in ~80% of the cells examined in this study. In this study, we defined a cell as recovered (or recovering) if after 2 minutes the induced membrane deformation has decreased at least 50%, however in most cases there was a 100% complete recovery by this time. Even after a 20nN load was applied for 10 minutes, cell membranes were observed to completely recover their initial morphology. Large deformations were also observed within the nucleus during the loading period; however the nucleus also returned to its initial morphology in the 2 minutes following tip removal.

In order to determine whether or not the nucleus is the driving force behind membrane recovery, we performed the same experiment off-nucleus (see Fig. 2.3 A). For untreated cells, the cell membrane again was observed to recover within 2 minutes after tip removal ~90% of the time. AFM measurements of whole cell force maps (n=3) showed that Young's moduli above the cells' nuclei are 2-3 fold softer than those in regions surrounding the nuclei (Fig. 2.3 B). Variances in stiffness, however, are apparent across the cytoplasmic surface due to inherent heterogeneity [183, 269]. These soft nuclear regions correspond with an observed increase in deformation over time, when compared to the stiffer off-nucleus regions (see Fig. 2.3 C and D). These results indicate that membrane recovery may be independent of the nucleus. Sustained deformation of the nucleus, however, may influence the rate of recovery of the membrane in the vicinity of the applied force as the nuclear envelope is highly interconnected to the cytoskeleton and the membrane cortex.

In order to assess the integrity of the membrane before, during, and after deformation we incubated the cells in propidium iodide (PI) [49]. PI is a potent nuclear stain that will fluoresce red when intercalated in the DNA. Importantly, it is membrane impermeable and cannot localize in the nucleus unless the plasma membrane has been disrupted. We exposed cells to a 20nN constant

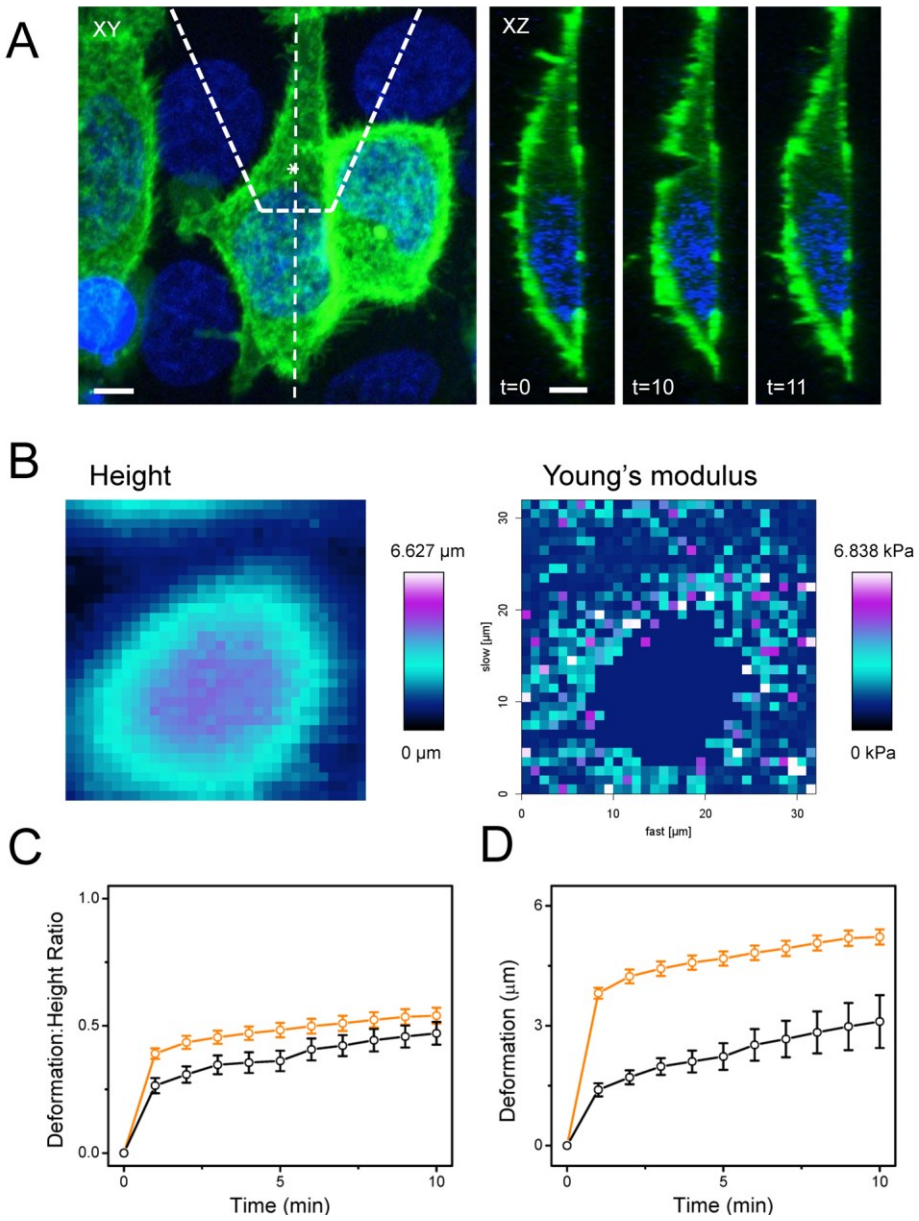

Figure 2.3 On versus off-nucleus deformations.
A) Off-nucleus loading with 10nN for 10 min was shown to result in membrane recovery in 90% of cells (n=10) within 2 min following tip removal, consistent with on-nucleus loading, demonstrating that the nucleus is not responsible for membrane recovery. The (*) indicates the apex of the AFM tip. B) Force-map of a HeLa cell showing the height measured, and the corresponding Young's modulus measurements (fit to the Hertz model). Results demonstrate that the nucleus is taller and the elastic modulus is 2-3 fold softer (~500Pa) than in surrounding cytoplasmic regions (~1.5kPa) for this particular cell, as measured by JPKSPM software here. C) Normalized deformation over time comparing on-nucleus (orange) and off-nucleus (black) loading. D) Corresponding average deformation over time for on-nucleus and off-nucleus loading. Deformation on-nucleus is significantly greater than off-nucleus. Green: PH-PLCδ-EGFP, Blue: Hoechst 33342, Scale bars=5µm. Error bars shown are standard error.

force for 10 min, followed by removal of the AFM tip while simultaneously imaging PH-PLCδ–EGFP, Hoechst 33342 and PI. No red fluorescence was observed from the perturbed cell nuclei before,

during, or after the application of a 20nN force (Fig. 2.4 A-C). After removing the tip and confirming membrane integrity, we conducted a positive control by adding a minimal amount of Triton X-100 (TX) (0.05% v/v final concentration) to the culture medium. TX rapidly permeabilized the plasma membrane and PI fluorescence was immediately observed (Fig. 2.4 D).

As a positive control paraformaldehyde was added to a sample dish prior to performing the same constant force experiment. The observed effect of PFA (a known fixative) was a near 5 fold increase in stiffness ($P < 0.05$), as measured by AFM Young's modulus measurements, and an increased resistance to deformation. Less than 20% of cells treated with PFA displayed any visible deformation upon application of a 10nN constant force for 10 min. In cells displaying a visible deformation, no recovery of the initial cell shape was observed following removal of the tip. Conversely, we also conducted an experiment in which PFA was added to live cells during the exposure to a constant force for 10min, but before the removal of the AFM tip. After allowing the PFA to fix the cells, the AFM tip was removed. Although PFA treatment did result in some image degradation, the induced deformation was still clearly observed 20 min later (Fig. 2.4 E).

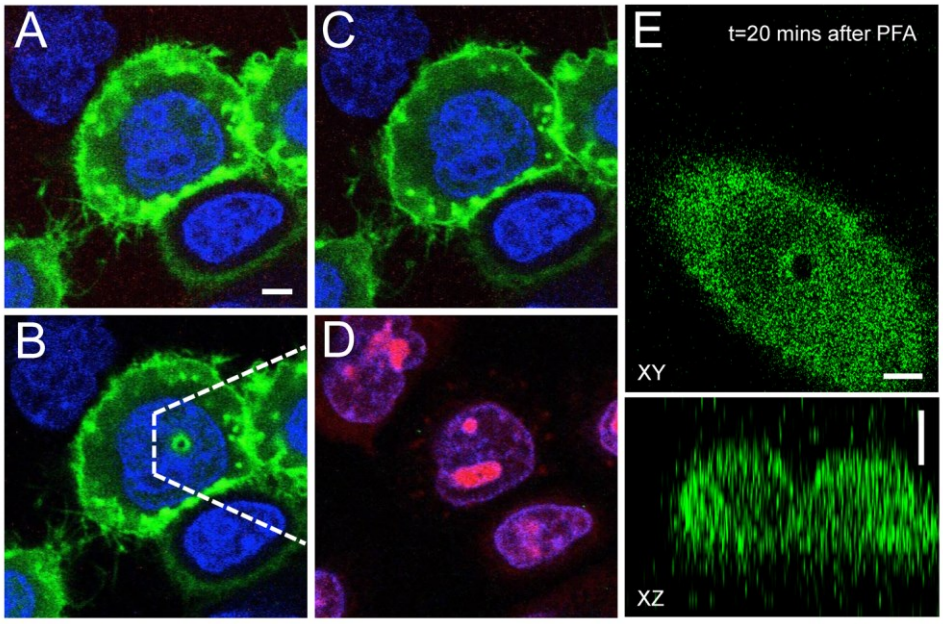

Figure 2.4 Control experiments: PI test and PFA.
A-D) PI test demonstrates that the membrane is not penetrated during or following tip removal. A) Cell prior to applied load. B) Cell deformed by a 20nN force. C) Load is removed. The membrane is not penetrated by the tip, as is seen by the lack of red fluorescence. D) Addition of TX-100 to the media, as a positive control, demonstrates that the membrane is permeated resulting in red fluorescence of the PI stain (PI and Hoechst channels are overlaid). E) PFA added to cells during deformation results in permanent deformation even 10 min after tip removal. Image shows deformation in the XY and XZ orthogonal view. Although there was a decrease in fluorescence intensity following addition of PFA, an image captured 10 min following tip removal shows the deformation remains. Young's modulus of PFA treated cells (n=6) (14.7±7.4kPa) was almost 5-fold higher in magnitude than untreated cells (3.4 ± 1.4kPa). Green: PH-PLCδ-EGFP, Blue: Hoechst 33342, Red: PI, Scale bars=5µm.

To further test the role of the membrane in the deformation response, we incubated the cells with membrane-bound fluorescent markers in an attempt to stiffen the membrane: Wheat germ agglutinin (WGA) [270, 271], a lectin which binds to N-acetyl-D-glucosamine and sialic acid, and DID, a lipophilic tracer. Both fluorescent markers were fluorescent in the 600-700nm emission spectra, which allowed us to simultaneously image the membrane transiently expressing EGFP-PLC-δ (Fig. 2.S1). The same experiment as described earlier was performed on-nucleus for these cells. AFM force-curves confirmed that Young's modulus of cells incubated with WGA (4.6 ± 2.0kPa, n=23) significantly increased ($P < 0.05$) by 35% in comparison to untreated cells (3.4 ± 1.3kPa). Deformation over time was measured (n=10), and plots show that normalized deformation is greater than untreated cells (Fig. 2.S2). Total normalized deformation at the maximum duration of loading was significantly higher ($P < 0.05$) for WGA (0.7 ± 0.3) in comparison to untreated cells (0.5 ± 0.2). Incubation with DiD also led to a slight increase in Young's modulus, (4.0 ± 1.2kPa, n=15). The deformation-height ratio versus time data followed a similar trend to that of WGA, and resulted in an increase (0.6 ± 0.1) (n=5). Despite the overall increased stiffness the effect on membrane deformation was surprising. Considering that the load applied is highly localized and results in high aspect ratio deformations, it is possible that a stiffer membrane experiences shearing effects rather than bending, as would be expected for softer materials [272].

Taken together, the results reveal that the cells are able to recover rapidly after a large-scale indentation for prolonged periods of time, even in cytoplasmic regions surrounding the nucleus. Moreover, the membrane does not rupture in response to relatively high aspect ratio indentations. Resiliency of the membrane herein refers to its ability to withstand these extreme forces without penetration. This was confirmed using a PI test and is directly visible - the cell membrane clearly deforms around the shape of the AFM tip as observed in the LSCM orthogonal views (see Fig. 2.1 C).

2.3.2 Membrane indentation measurements in single cells

HeLa cells in culture preferentially form highly interconnected monolayers. In order to investigate the influence of the monolayer microenvironment on the membrane deformation and recovery dynamics, we performed the same experiment again on cells cultured at low-confluence. In this situation it was possible to examine the mechanical dynamics of the cortex of single cells (Fig. 2.5). Here, we exposed single cells to a 10nN force for 10 minutes and recorded LSCM volumes as in the same manner as above. We observed no significant differences between the deformation dynamics of single cells in comparison to those in a monolayer (Fig. 2.5 B and C). This suggests that the response of a cell's membrane to a localized deformation induced by an AFM tip is independent of its neighbours.

2.3.3 Actin deformation

In order to examine the response of the underlying actin cortex and cytoskeleton we produced HeLa cells transiently expressing PH-PLCδ-EGFP and LifeAct-Ruby and performed experiments as above. Red fluorescence observed within the orthogonal views demonstrated the presence of actin underlying the membrane, with an increased intensity just underlying the green fluorescent membrane (the cortex) (Fig. 2.6 A). Simultaneous membrane and cortex deformations were

measured within the same cell (n=9), and demonstrated that the cortex deforms and creeps at the same rate as the membrane (Fig. 2.6 B). LSCM volumes captured before, during and after tip removal demonstrated that, not only the membrane, but also the actin cortex recovered following removal of the load (Fig. 2.6 A). This recovery was again observed in a relatively short time period of 2 minutes. We performed a commonly employed intensity correlation analysis (ICA) on orthogonal projections of LSCM volume images (see [273]) in order to quantify the similarity in the initial membrane morphology with the membrane morphology during and after deformation (full details are described in the Supplementary Information, Ch. 2.7.2). ICA compares a pair of images and provides an intensity correlation quotient (ICQ) that varies between -0.5 and +0.5. An ICQ value of -0.5 or +0.5 indicates that the images being compared are negatively or positively correlated, respectively. An ICQ of 0 indicates that a pair of images is completely decorrelated. As expected, comparing images of the membrane before and after full recovery leads to a positive ICQ of 0.19 ± 0.06. However, comparing images of the membrane before and during deformation results in a significantly smaller ICQ of 0.06 ± 0.03 ($P < 0.05$). These results demonstrate that cells recover their pre-deformed morphology, as determined by the larger ICQ values for before and after versus before and during deformation images (Fig. 2.6 C).

We also investigated the morphology of the actin stress fibres before, during and after deformation. It has been observed that cells exposed to planar uniaxial stretch undergo rapid and dramatic remodelling of the actin cytoskeleton [17, 84, 258]. In this study, although the mechanical stress is obviously very different, we were curious to observe if a similar phenomenon would take place. In HeLa cells, we observed stress fibres primarily appearing at the basal membrane near the substrate but also above and around the nucleus (Fig. 2.6 D). We acquired LSCM volumes before and after a 10 minute deformation caused by a constant 10nN force applied with the AFM tip. Although there appears to be some displacement of the actin stress fibres, consistent with our previous work [15], they were not observed to disassemble during the deformation. ICA performed on ROIs containing visible actin stress fibres demonstrates that there is only minor movement of F-actin within the basal plane, as shown in Fig. 2.6 D. Values of ICQs were similar for deformed (0.134) and recovered (0.139) cells, indicating very little movement of the fibres. In some cases, a minority of actin stress fibres were observed to remodel, however overall, the actin cytoskeleton was observed to remain intact and relatively stable. We also examined cortical regions of the cell membrane and similar ICA results were obtained. Ratios of fluorescence intensity in the regions were also examined before and after mechanical perturbation but no definitive results were obtained (data not shown). However, this analysis certainly does not rule out the possibility of cortical actin remodelling dynamics in response to mechanical perturbation due to the fact that such fine actin structure in the cortex is not easily resolvable with standard LSCM.

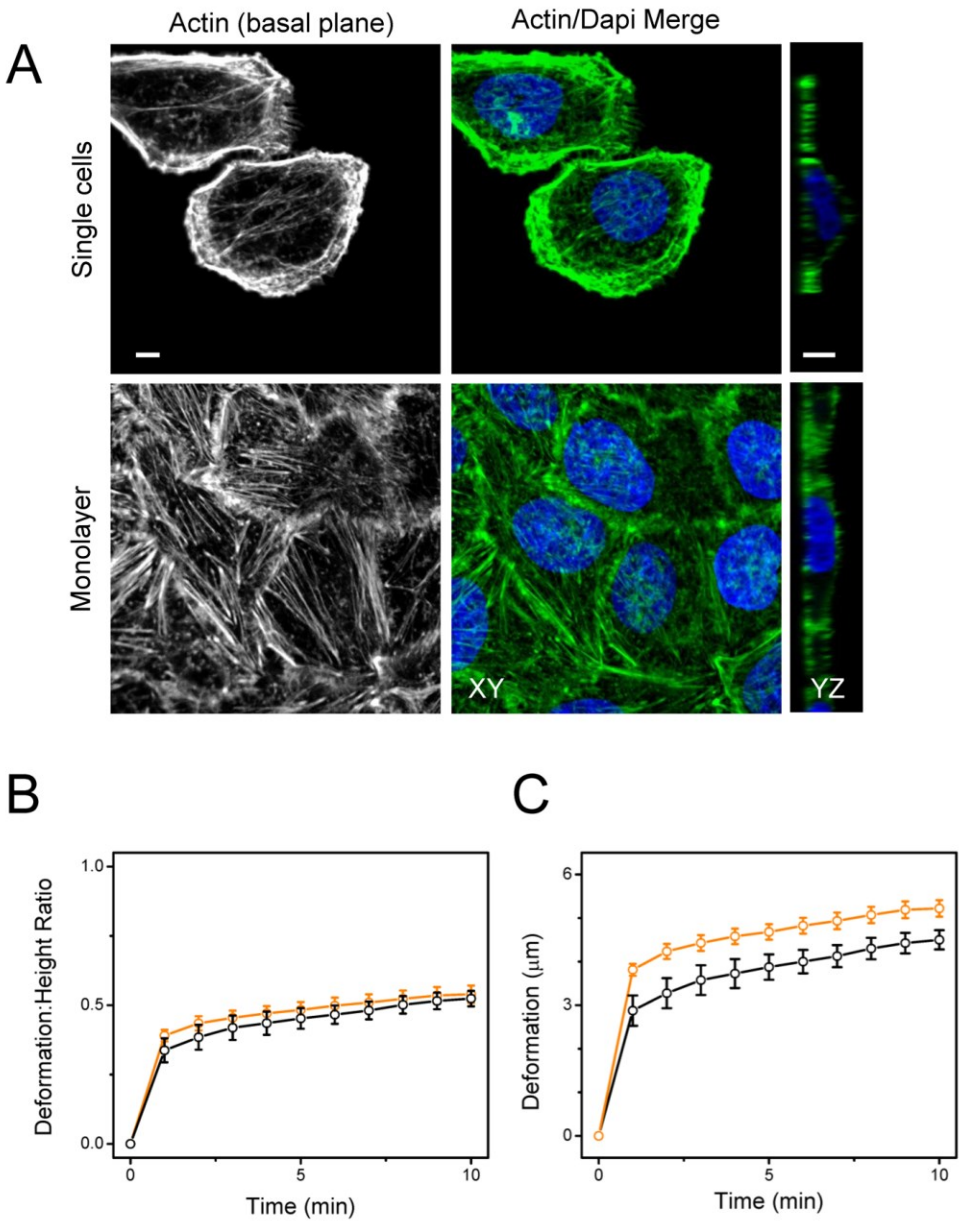

Figure 2.5 Comparison of single cell and monolayer deformation behaviour.
A) A comparison of single cell morphology and microenvironment to that of cells within a confluent monolayer. The shape of single cells is not influenced by its neighbours, in comparison to those in a dense monolayer, as is seen in these immunofluorescent images. Z-projections demonstrate the strong presence of actin fibres in the basal plane of the cell's membrane. Merged actin/DAPI images show z-projections of cortical actin throughout the cell. B) Comparison of normalized deformation over time of single cells (black, n=10) and HeLa cell monolayers (orange, n=26) for a 10nN applied force. The Young's modulus of cells in a dense monolayer (E=3.4 ± 1.4kPa) is not significantly (P > 0.9) different than that of single cells (E=3.4 ± 1.6kPa). Cell density does not appear to influence local cell elasticity. C) Corresponding total deformation over time for monolayer and single HeLa cells. Green-Phalloidin 488 (actin), Blue-DAPI (nuclei) Scale bars = 5μm.

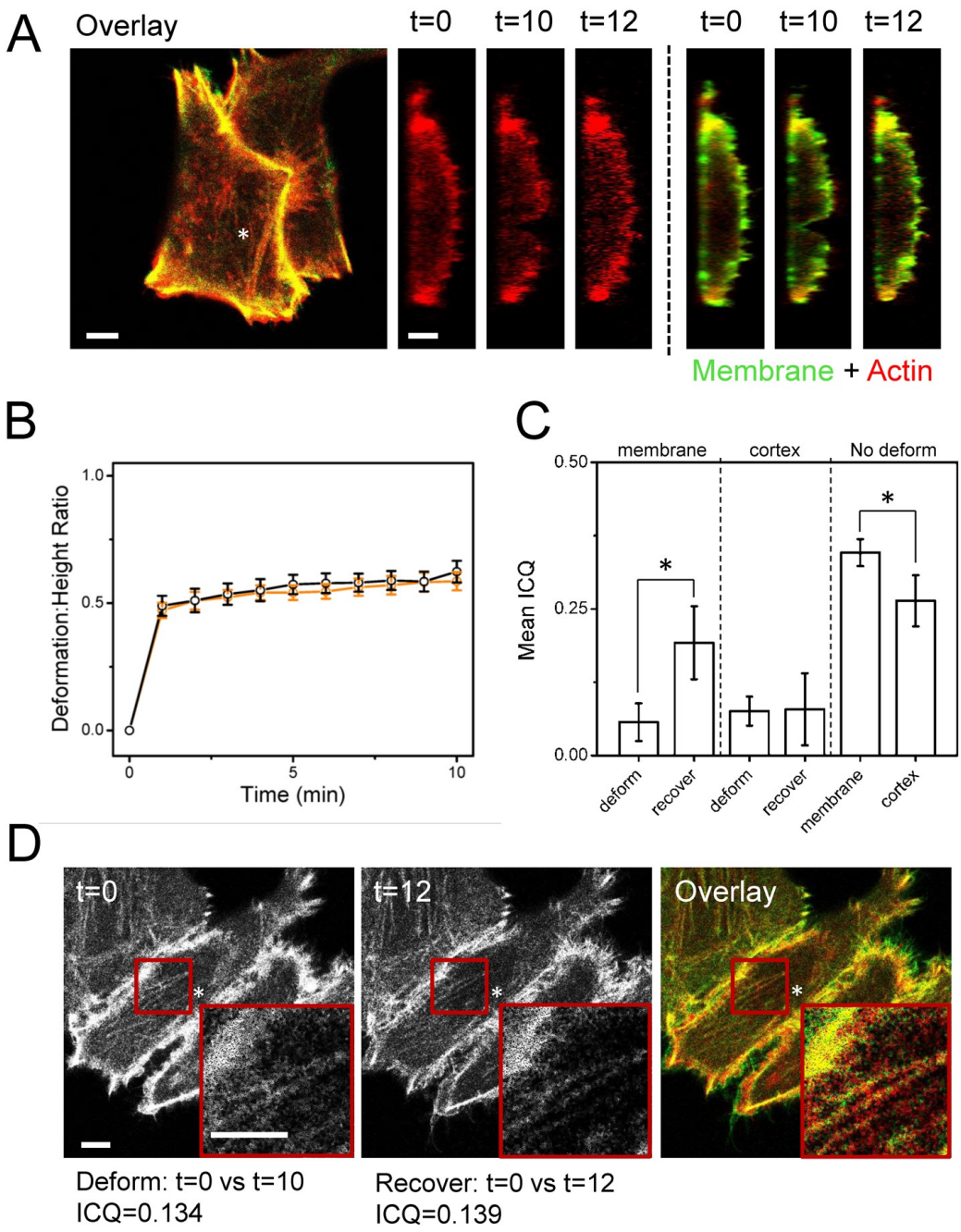

Figure 2.6 Cytoskeletal recovery following mechanical perturbation.
A) Overlay of actin fibres in the basal membrane of an untreated HeLa cell before (red) and after (green) 10 min of 10nN applied load. Both the membrane and underlying cortical actin network recover following mechanical loading (after 2 min of unloading, t=12), as seen in the orthogonal views. (*) indicates AFM tip position. B) Normalized deformation of actin (black) versus membrane (orange) over time demonstrates that the linked cellular components deform simultaneously. Error bars are standard error. C) Plot of mean intensity correlation quotients (ICQs). Intensity correlation analysis (ICA) was performed on orthogonal views of regions of interest (ROI) around the deformation comparing before (t=0 min), during (t=10), and after deformation (t=12) for both the membrane (PLC-δ-EGFP) and the cortex (LifeAct Ruby). Deform corresponds to ICA of t=0 vs t=10, and recovery corresponds to t=0 vs t=12.There was a significant ($P < 0.05$) increase in ICQ for ROIs in

recovery in comparison to deformation, as expected. However, there was an insignificant difference for the same comparison of the cortex intensities, due to high levels of noise, and negative effects of photobleaching. Comparison of control (non-deformed) cells over the course of t=0 and t=10 min again shows higher values for ICQ of the membrane in comparison to the cortex, demonstrating that ICA is more accurate at predicting correlation using the membrane tag PLC-δ-EGFP. Overall, ICA shows that the membrane shape recovers in comparison to the cell's deformed state. n=5 for each ICA (membrane, cortex, control). Error bars are standard deviation. D) Actin fibres (LifeAct Ruby) demonstrate little movement in the basal membrane. Zoomed images of actin fibres shown before deformation (t=0) and two minutes following deformation (t=12) show that no remodelling has taken place. Overlay shows non-deformed (red) and recovered (green) cell actin fibres in the basal membrane. Below, intensity correlation quotients are indicated, showing that ICA presents only limited fluctuations over the ten minutes of loading. See supplement (Ch. 2.7.2) for details of ICA. (*) indicates AFM tip position. Scale bar = 5μm.

2.3.4 Cytoskeletal disruption

Given the results of the experiments reported above, we hypothesize that the integrity and rapid recovery of the membrane is governed by the stability and contractility of the underlying actin cytoskeleton. To test this, we pre-treated cells for 15 and 30 minutes, respectively, prior to experiments with the well-known actomyosin contractility inhibitors, ML7 (inhibitor of myosin light chain kinase, MLCK) or Y-27632 (inhibitor of rho kinase, ROCK). Finally, we also performed experiments on cells pre-treated for 15 minutes prior to experiments with the actin destabilizing drug, Cytochalasin-D (CytD). The myosin-II inhibitor, blebbistattin, was not employed in this study, as it is sensitive to 488nm light and would decompose during the measurement [274, 275].

Although there was no noticeable morphological change shown in HeLa cells treated with ML7, there were vast differences in the appearances of cells treated with Y-27632 and CytD, in comparison to untreated HeLa cells (Fig. 2.7). Prominent stress fibres were visible along the basal membrane with some adjacent and apical to the nucleus in untreated HeLa cells. However, those treated with Y-27632 lacked stress fibres. Cells treated with CytD appeared to have completely destabilized actin networks, and cell height was slightly reduced. Cell height above the nucleus and surrounding cell periphery were alike, whereas untreated, ML7, and Y-27632-treated cells revealed a significant decrease in cell height when comparing on-nucleus to off-nucleus regions (Fig. 2.S3). It was also noted during experimentation (live cells) that a large number of membrane blebs formed following CytD treatment, as might be expected due to weakened interactions between the membrane and underlying cytoarchitecture [101, 271, 276, 277]. We have previously demonstrated that mechanically induced membrane blebs occur frequently in response to AFM indentation in mouse embryonic stem cells that have low phospho-ezrin-radixin-moesin expression levels [278]. Elasticity measurements also revealed that cells treated with ML7 demonstrated a non-significant ($P > 0.1$) change in cell cortical elasticity (4.0 ± 2.2kPa) in comparison to untreated cells (3.4 ± 1.3kPa), while those cells treated with either Y-27632 or CytD resulted in a significant decrease ($P < 0.05$) in elasticity (2.8 ± 1.3kPa and 2.5 ± 1.0kPa, respectively). The decrease in elasticity is in agreement with previous studies and occurs as a result of actomyosin inhibition and cytoskeleton destabilization [15, 50, 167, 196, 260, 278, 279].

Employing the cytoskeletal inhibitors, we repeated the experiments using a constant 10nN force applied above the cell's nucleus. In Fig. 2.8, normalized (A) and non-normalized deformation

(B) over a 10 min period of constant applied force is shown comparing untreated and pre-treated HeLa cells. Corresponding with the lack of change in morphology or Young's modulus, cells treated with ML7 differed only marginally from control cells. Comparing the total deformation at ten minutes of loading demonstrated that the difference was insignificant for ML7 ($P > 0.35$). On the other hand, cells treated with Y-27632, and CytD, both experienced a significant increase in the total deformation experienced by the cell's membrane ($P < 0.05$). The difference in deformation was noticed visually between untreated HeLa (Fig. 2.8 C) and treated cells (Fig. 2.8 D), as the treated cells exhibited a pronounced outward expansion and deeper deformation, almost reaching the basal membrane. This observation coincides with the effect of a lowered elastic modulus seen for these treated cells. Overall, we observed that regardless of the inhibitor employed, all cells respond to mechanical deformation in a similar manner to control cells. Initially, there is a rapid increase in deformation within the first minute followed by a creep-like response over time. However, inhibition of ROCK or destabilization of the actin CSK results in a ~22% and ~44% increase in deformation over control cells, respectively (Fig. 2.S3).

We again performed the experiment while applying the load off-nucleus (Fig. 2.3 A, and 2.S3) while simultaneously employing cytoskeletal inhibitors. We observed similar percentages of deformation recovery as shown with above nucleus-pushing experiments. In the case of ML7 treated cells, the membrane recovered from deformation in a similar manner to untreated cells (90%). Slower recovery was observed when cells were treated with Y-27632 and CytD. For example, only 60% of cells treated with Y-27632 and only 40% of cells treated with CytD experienced any significant recovery within the 2 min following tip removal. Time-dependent deformation-height ratios were significantly altered upon treatment with cytoskeletal inhibitors (Fig. 2.S3). Increases in deformation-height ratios were significant in comparison to untreated cells when Y-27632 and CytD were employed, however only on-nucleus. This result suggests that an intact actomyosin network is largely responsible for deformation resistance above the nucleus.

Repeating the experiment above the cell's nucleus, in these cases of cytoskeletal debilitation, demonstrated that the membrane still recovered its original, pre-deformed state. Within 2 min, almost all cells treated with ML7 recovered, consistent with the behaviour of untreated cells (80%). However, there was again a noticeable difference in the recovery of cells treated with Y-27632 and CytD. In these cases only 50% and 20% of the cells were able to recover a substantial portion of their undeformed height after 2 min, respectively. In some cases, even after several minutes of imaging, a small amount of membrane indentation was still visible (Fig. 2.8 E). PI tests reveal that although the membrane did not recover from indentation it indeed remained intact.

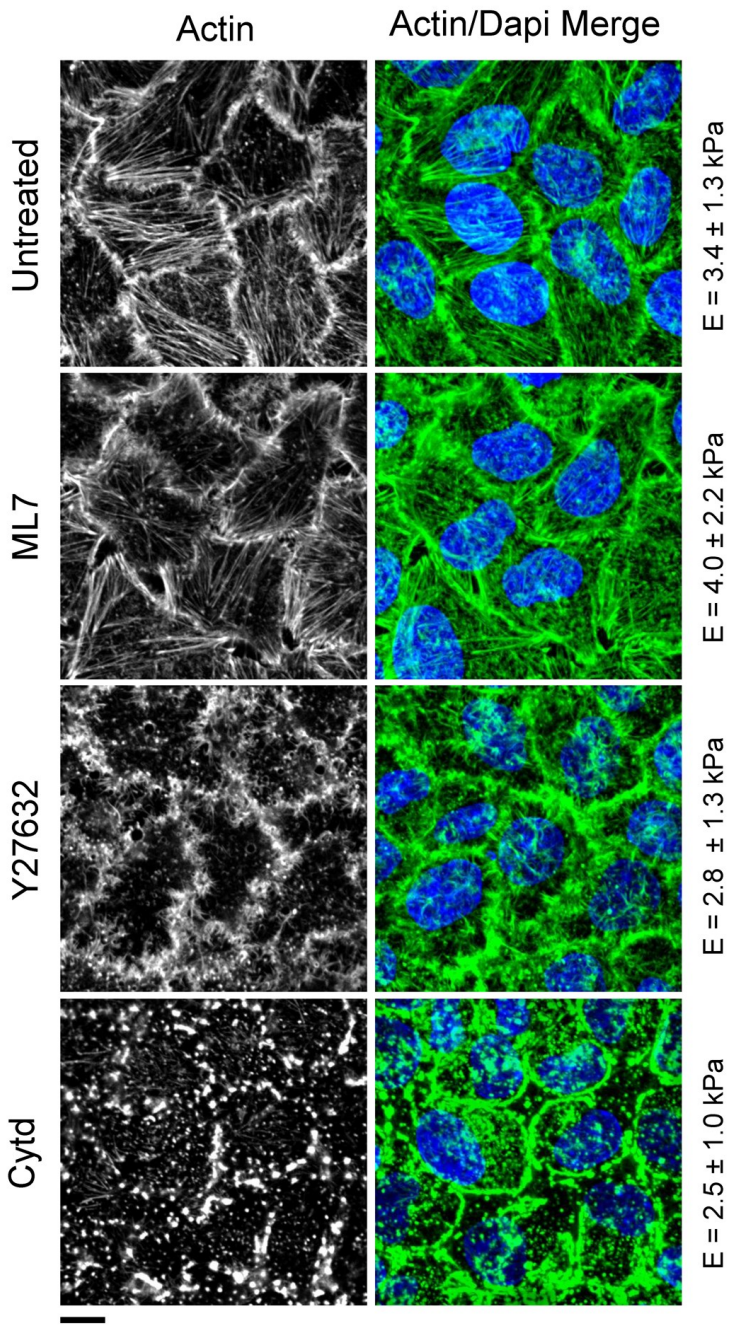

Figure 2.7 Immunofluorescent images of untreated and treated HeLa cells.
Immunofluorescent images of fixed HeLa cells – a comparison of untreated and drug-treated cells. Left column images are z-projections of the basal confocal planes containing actin stress fibres and images in the right column are whole-cell z-projections with corresponding YZ orthogonal views indicating the observed actin cortex. Cells treated with ML7 show no noticeable difference in the appearance of their actin cytoskeleton. However, those cells treated with Y-27632 and CytD show noticeable differences in their actin networks. Actin is completely de-polymerized in the case of CytD treated cells. Young's moduli are indicated with standard deviation. Green: Phalloidin 488 (actin), Blue: DAPI (nuclei), Scale bar = 10µm.

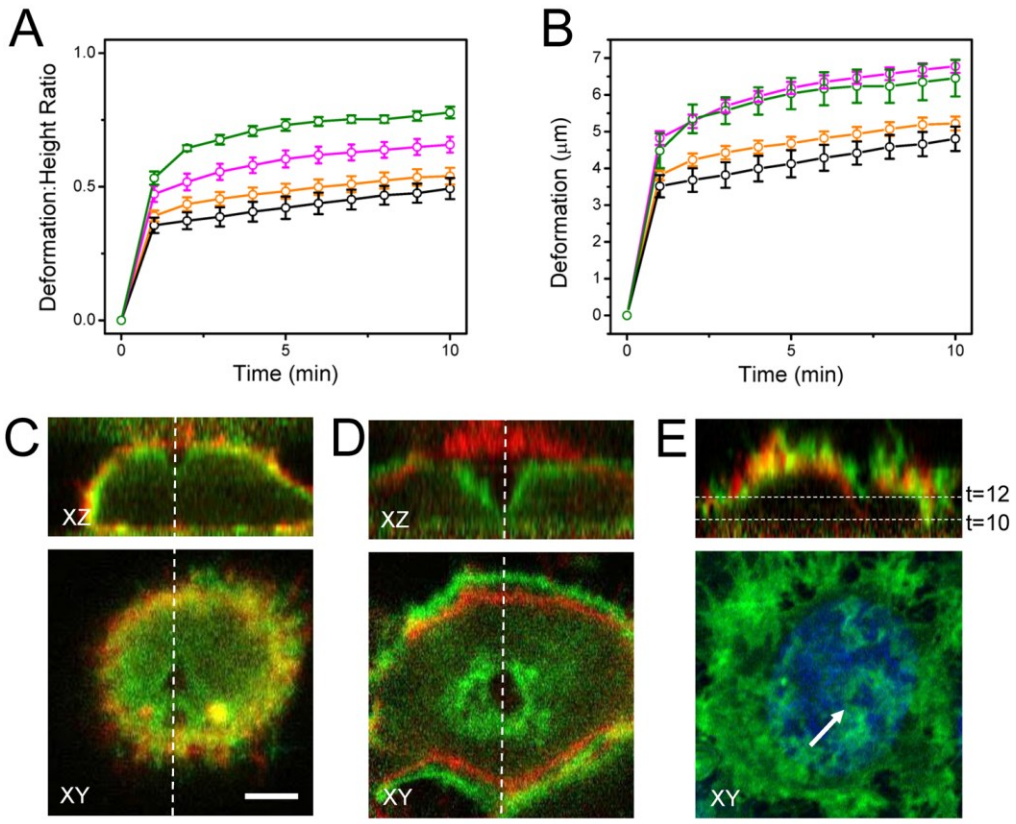

Figure 2.8 The effect of cytoskeletal drugs on the response to mechanical perturbation.
A) Plot of the average ratio of normalized deformation: initial cell height over time during a constant applied force of 10nN. Cells treated with Y-27632 (pink, n=19) and CytD (green, n=8) experienced significantly increased membrane deformations in comparison to untreated cells (orange, n=26), and those treated with ML7 (black, n=13) ($P < 0.05$). B) Corresponding deformation over time for untreated and treated HeLa. C) Red/green overlays comparing membrane deformation in untreated HeLa and D) CytD-treated HeLa, following 10 min of 10nN applied force. The deformation following treatment with both CytD and Y-27632 was much more severe than what was observed for untreated HeLa. Destabilizing the actin cytoskeleton severely increased deformation, and impaired the ability of the cell to recover following the perturbation. E) An example of a cell treated with Y-27632 that did not fully recover following 2 min post-force removal. The indentation is still visible in the XY plane as indicated by the arrow. Typically with an intact cytoskeleton we observed a quick return of the membrane to its inital state, however without an intact actin network, recovery appears to be slower. Green - plasma membrane at t=10 min of 10nN deformation, Red – initial cell morphology (PH-PLCδ-EGFP), Scale bars = 10μm.

2.3.5 Mechanical characterization of cell deformation

Time-dependent normalized deformation (assumed here as compressive strain) was fit to a Kelvin-Voigt model in an attempt to measure the viscous time constant of the membrane (see Supplementary methods for details, Ch. 2.7.1). The model fit the data extremely well ($R^2 > 0.95$), and results in time constants on the order of ~1 minute for both untreated and treated HeLa cells (see Supplementary methods Table 2.S1). Although these rates are within reason for the observed membrane creep, apparent viscosity values are an order of magnitude higher than expected, ~3-6 kPa·min. Previous studies have reported membrane viscosities within the range of 100-1000s of Pa·s [168, 196, 280, 281]. These values are intuitively high considering that honey, for example, is in the range of

~0.1-10s of Pa·s [282]. This discrepancy is caused by using a simple model to describe a highly complex biological system. As well, the assumption of isotropic compressive strain is a gross over-simplification of the loading conditions of the locally applied force via a conical AFM tip. Many other researchers have attempted to fit deformation and creep data to a variety of viscoelastic models, and relevant parameters also vary widely [44, 283-285]. Despite these limitations, it is worthwhile to note the significant difference between the creeping rates (Table 2.S1) and relative apparent viscosities of on- and off-nucleus data (Fig. 2.9). The creeping rate off-nucleus was observed to be ~55% longer than the on-nucleus data (from 1.16s to 1.80s) and the relative viscosity also increased by ~41%. These results correlate well with force-maps showing that off-nucleus stiffness is increased in comparison to on-nucleus regions (Fig. 2.3 B). This suggests that the dense mesh of the cytoskeleton in regions off-nucleus act in a more viscous-manner resisting long-term deformation, more so than the nuclear region (Fig. 2.3 C). In response to various drug treatments, only CytD resulted in a significant decrease in on-nucleus apparent viscosity. Under these conditions, the cell completely lacks an actin cortex in any form. By comparing on and off-nucleus deformation, we were able to approximate a relationship between total on- and off-nucleus strains, with and without an intact cortex. Without an intact cortex (CytD-treatment) strain off-nucleus is reduced in comparison to on-nucleus ($\varepsilon_{off}/\varepsilon_{on} = 0.70$), compared to a nearly equivalent strain ratio when the cortex is unperturbed ($\varepsilon_{off}/\varepsilon_{on} = 0.95$). Taken together, these results support the unsurprising notion that an intact actin cytoskeleton has a major influence on the deformation and the recovery of the cell to large deformations both on- and off- the nuclear region. More importantly however, the data suggests that the nucleus does not appear to play a major role in cell shape recovery following deformation in the nuclear region.

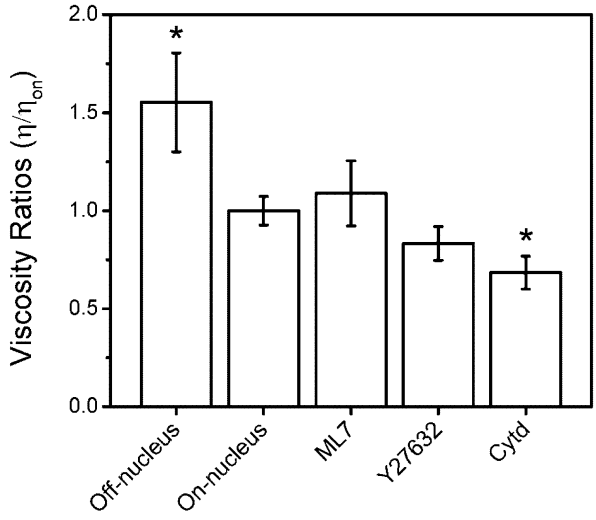

Figure 2.9 Relative viscosities of treated cells and cytoplasmic regions.
Comparison of relative viscosities of untreated (on-nucleus) membrane (η_o) with treated cells, and off-nucleus cytoplasmic regions. Relative viscosity off-nucleus is significantly higher than on-nucleus, which corresponds with increased stiffness observed in force maps, suggesting the density of cytoskeletal filaments is higher in those regions. The relative viscosity of CytD is also significantly lower than untreated HeLa, indicating a clear disruption in the actin cortex. Error bars are standard error of the mean. Significance (*) compared with on-nucleus untreated HeLa, determined with independent student's t-test ($P < 0.05$).

2.4 Discussion

Eukaryotic cells have developed mechanisms in order to respond to changes in their microenvironments – including mechanical stresses imposed on them by other cells, or their substrates, for example. Recently, researchers have begun to shed light on the response of cells to mechanical loading, which has been proposed as a regulator of cell function [15, 84, 91, 258, 260, 262, 263, 278]. Often, large-scale forces occur in vivo [286-288]. As well, large volumetric changes have been shown to occur in cases of cellular blebbing [289], and motility [290], thus it is important to quantify the response of cells to forces at an extremum. In this study, we have employed simultaneous AFM-LSCM to quantitatively measure deformation and recovery of the plasma membrane and underlying actin cytoskeleton in response to force at an extremum of magnitude and aspect ratio. We specifically examined the roles of the membrane, cortex, and nucleus in relation to the response to locally applied nanonewton forces. Specifically, cells expressing PLC-δ-EGFP allowed us to visualize and directly measure the deformation of the membrane, during a constant applied force of 10 minutes. We demonstrated that the depth of deformation of the plasma membrane was linearly dependent on the magnitude of the load applied within this range of forces (Fig. 2.2 A), and that despite prolonged stress and high aspect ratio deformations, the cell membrane was impermeable (Fig. 2.4). We showed that, for the majority of cells (~80%), the plasma membrane and cortex can recover quickly from high magnitude and high aspect ratio deformations, in fewer than 2 minutes. An intact actin network is necessary for cell shape recovery, and that the nucleus, despite encompassing a large portion of the cell, does not appear to contribute to this recovery process.

In an effort to extract a viscous time constant from the observed creeping behaviour, time-dependent strain data was fit to a Kelvin-Voigt model for the various conditions tested (on- and off-nucleus, cytoskeletal inhibitors, cortex versus membrane) (see Supplement, Ch. 2.7.1). Due to the lack of a realistic model and simplifying assumptions about the load applied and the cell material properties as well, absolute values obtained from the model must be taken with caution, however some important insights can still be gained (Table 2.S1). Likewise, variances in mechanical parameters have also been reported throughout relevant literature [44, 283-285]. Notably here, the relative apparent viscosity of the nucleus was significantly lower than that of the surrounding cytoplasm (Fig. 2.9), suggesting that creep occurs at an increased rate for the softer nucleus under a constant stress – which is observed in Fig. 2.3 C. As well, the relative viscosity of cells treated with CytD was significantly lower than that of untreated cells, corresponding with increased strain (Fig. 2.8 A and 2.S3 C). In addition, comparing the ratio of off- and on-nucleus total strains ($\varepsilon_{off}/\varepsilon_{on}$) for untreated and CytD treated cells reveals the importance of an intact actin cytoskeleton. In untreated cells this ratio approaches ~1 whereas the loss of intact actin results in a decrease to 0.7. This data demonstrates that the deformation of the membrane on and off the nucleus is very similar suggesting that the nucleus does not play a major role in resisting deformation. Cells treated with CytD clearly demonstrate that an intact actin cytoskeleton is required for resisting deformation.

More recently, poroelastic models have been used to describe relaxation of cells following mechanical perturbation [181]. The cytoplasm, which accounts for the majority of the cell volume, has been shown to act as a biphasic material – with an elastic component comprised of the dense mesh

of cytoskeletal filaments and proteins, interspersed with liquid cytosol. Moeendarbary et al. have directly shown that the rate of cellular deformation, and recovery, is dependent on the displacement of liquid through this mesh – which occurs on relatively short timescales [181]. It was directly demonstrated that by exposing HeLa cells to hypoosmotic and hyperosmotic media, they increased and decreased cellular volume, respectively, which corresponded to a corresponding increase and decrease in diffusion constants. Thus, increased cellular volume correlated with a more rapid stress relaxation. This phenomenon is consistent with our results that demonstrate greater strain on-nucleus, wherein the volume is much greater than the surrounding off-nuclear regions, which react in a more viscous-like manner in comparison.

Following 10min of a 10nN constant applied force, we have shown that untreated cells are compressed by approximately 50% (see Fig. 2.S3 C), which is consistent with a previous study that examined the deformation of cells with a spherical AFM indenter (~40-50% for forces around 50nN) [291]. Remarkably, even with relatively large loads (20nN), applied constantly for 10min, the cell membrane remains undamaged and rapidly recovers following removal of the AFM tip for the majority of cells (80% of cells within 2min) (Fig. 2.2 E). Using cytoskeletal inhibitors (ML7, Y-27632, CytD), we showed that total strains increased (Fig. 2.S3) and that cell recovery was highly dependent on an intact actin cytoskeleton. Y-27632 and CytD treatments resulted in greater overall deformation of the membrane during the 10min experiments (Fig. 2.8 A and B), as the cantilever itself was shown to deform the cells (Fig. 2.8 D). This is appreciable considering that elasticity measurements revealed a decrease in Young's modulus values by > 20% due to actin destabilization (Fig. 2.7). Elasticity measurements in the range of several kPa have been previously reported for epithelial cells measured using a similar approach [53, 292], and decreases in cell stiffness have also been noted previously when employing Y-27632 [228] and CytD [167] to destabilize the actin network. Others have reported Young's modulus values within the range of 1-several kPa for epithelial cells [53, 54, 292], and variances are expected due to various measurement and analysis techniques [55, 56]. Upon removal of the tip, recovery was not observed to occur as readily after 2min, compared to control cells (50% and 20% for Y-27632 and CytD-treated cells, respectively). In some cases, particularly for cells treated with CytD, the recovery was significantly impeded. These results demonstrate that although an intact actin cytoskeleton is required for rapid membrane shape recovery, its absence does not preclude a slow relaxation back to an initial state. This clearly indicates the importance of cell shape – which has been shown previously to influence function and pathology [93, 262, 264, 293].

Inhibition of rho-kinase mediated contractility with Y-27632 has been shown to drastically reduce the presence of actin fibres in HeLa cells (see Fig. 2.6 and [294]), as well as reduce the elastic modulus in a variety of cells [228, 295]. Charras et al. have also shown that metaphase HeLa cells treated with Y-27632 do not bleb when exposed to latrunculin, which induces blebbing in untreated cells, due to the loss of acto-myosin contractility [271]. Therefore, it is not surprising that the use of Y-27632 affects the ability of the cell to recover from large deformations. In a paper by Brzeska et al. [296] HeLa cells transfected with RacQ61 were used to determine if active Rac results in increased activity of kinases (PAK, ROCK, MLCK) and subsequently increased myosin light chain (MLC) phosphorylation (p-MLC). Transfected cells were subjected to inhibitors of the aforementioned kinases (Tat-PAK, Y-

27632, and ML7, respectively). The researchers found that RacQ61 did increase p-MLC which was co-localized with actin in fibres and peripheral bundles. Concentrations of 5µM and 10µM of ML7 had no effect on p-MLC of non-transfected HeLa and only a small decrease in RacQ61 transfected cells; however, cells treated with 10µM of Y-27632 resulted in a significant reduction of p-MLC for both non-transfected cells and those transfected with RacQ61 [296]. Furthermore, MLCK, as opposed to ROCK, has been shown to have an insignificant effect on the velocity of cleavage furrow contraction during cytokinesis of HeLa cells, as determined by inhibition with ML7 and Y-27632, respectively [294]. These results indicate that ROCK is the main kinase responsible for p-MLC in HeLa cells, which explains why there was no observed effect of ML7 in our study, for either Young's modulus measurements or deformation response of these cells, in comparison to untreated HeLa.

From our observations, and others [50, 100, 252, 277], it is evident that the cytoskeleton provides much of the necessary structural support required to maintain a cell's preferred morphology. Membrane tension, however, may be partially responsible for this observed recovery. Membrane tension has been shown to play a role in cell motility [297] and morphological changes [298, 299], and is also directly related to acto-myosin contractility [300, 301], however how tension affects whole-cell mechanics remains largely unknown (reviewed in [302]). In order to study the membrane's role in the time-dependent deformation response, the membrane-bound fluorescent labels WGA and DiD were employed (Fig. 2.S1). By labelling the membrane with the lipophilic tracer DiD, membrane stiffness was only nominally increased. Although lipophilic tracers insert themselves into the plasma membrane through partitioning, it has been shown that their inclusion has little effect on mechanical properties of the membrane [303]. Measurements are difficult to reproduce, owing to sensitivity of dye and cell concentration [304], as well as the occurrence of micro-environmental contamination [305]. In agreement with earlier studies [270, 271], incubation of cells with WGA significantly increased the apparent membrane elasticity, as determined by AFM force-indentation curves. Despite this increase in stiffness, WGA labelling led to a surprising increase in time-dependent deformation (see Fig. 2.S2). The load applied here is highly localized, resulting in high aspect ratio high magnitude deformations, and so it is possible that a stiffer membrane experiences shearing effects rather than bending. Plasma membranes of erythrocytes have been shown to have a low shear modulus [186] and a relatively high elastic modulus [185]. Compression resistance for soft membranes is supplied by the elastic modulus due to undulations as well as intermolecular separation [272]. Recently, caveolae have been shown to provide relief of the sudden onset of increased tension – by increasing the surface area of the membrane [187, 188]. It is probable that WGA lectin binding to the outer surface of the membrane reduces intermolecular separation and supresses these undulations and the ability to relieve tension by increases in surface area. Sterol-lipid interactions and their ordering also plays a role in membrane stiffness and bending rigidities [306], and so it is not surprising that binding to the outer membrane surface will also change its mechanical properties.

The plasma membrane offers little resistance to changes in shape [307], as observed here by prominent deformations that conform to the AFM probe (Fig. 2.8 B). Importantly, applied forces do not result in membrane damage as confirmed by PI tests (Fig. 2.4 A-D) and as seen by the EGFP

outlining the AFM tip during indentation (Fig. 2.1 C) [49]. Although not measured directly here, cells conserve their volume during these high aspect ratio deformations, as indicated by a return to initial cell height in most cases (80%) of untreated cell recovery without changes in basal membrane area, which is in agreement with volume conservation observed by others during mechanical deformation [228, 291, 308]. Prior research reports a range of force magnitudes which lead to puncturing of lipid bilayers in vitro [177, 219, 309], Break-through force was shown to be linearly proportional to the logarithm of the approach speed using model bi-layers on solid substrates [310]. Microinjection has been demonstrated in vitro with the use of carbon nanotube tips [311], but with less success using pyramidal tips [177]. A jump in the force-distance measurements made during tip indentation has been proposed to be correlated to a penetration of the lipid bilayer, and have been shown on solid-supported lipid bilayers as well as with eukaryotic cells [310]. Despite the success of membrane penetration with high aspect ratio tips, others have noted that standard conical tips, in opposition to sharp tips (such as carbon nanotubes), result in a gradual force increase upon tip-sample contact [308, 312]. This suggests that the membrane is deformed through bending and stretching around the tip when the applied force is distributed over a larger contact area. In our deformation experiments the force magnitude is quite large; however the surface area over which it is transmitted is also relatively large. Theoretical models propose that isotropic membrane tension distributes the highly localized load of the AFM tip radially [194]. These large deformations (without puncturing) of the plasma membrane support the idea of lipid recruitment – and possibly lipid trafficking, in order to maintain membrane integrity [313]. Long and short-range trafficking of lipids has been shown to occur along microtubules and actin filaments, respectively [314], thus if these filamentous networks are disrupted, membrane recovery may be delayed, which may explain the slow recovery observed with Y-27632 and CytD treatments.

The ability of the membrane to recover within a relatively short period of time (2min) could be influenced by a number of factors including surrounding intracellular components such as other cytoskeletal networks, or the nucleus, as well as mechanical regulators such as osmotic pressure. Filamentous networks such as microtubules, which are known to influence cell polarity and nuclear positioning [103, 315], may be partially responsible for the recovery response of the membrane. Intracellular organization has also been partially implicated to be the result of dynamic remodelling of intermediate filaments [316, 317], and so they too may influence the response to a local perturbation. Connectivity with microtubule and actin networks, via molecular motors such as kinesin and cytoplasmic dynein, links intermediate filaments with the response to any local deformation of either of these networks. Although we did not specifically address the role of microtubules or intermediate filaments here, it is clear that they must provide partial resistance to deformation, as they are tethered to both the actin network and membrane. As well, non-equilibrium hydrostatic pressure, caused by mechanical perturbation, has been shown in vitro to induce membrane blebbing in embryonic stem cells [101]. Considering that there were no observed adhesive interactions between the cell and membrane, as observed by measured AFM force-curves here, it is unlikely that adhesion to the retracting tip is the driving force behind the observed recovery. Osmotic driven pressure seems to be a likely candidate in the initiation of the recovery process.

Besides the role of filamentous networks and cellular pressure, the nucleus has been shown to play an important role in mechanotransduction [126, 318]. Extracellular forces are transmitted to the nucleus via the cytoskeleton, through the Linker of Nucleoskeleton and Cytoskeleton (LINC) complex, which involves proteins that connect the inner and outer nuclear membrane to the surrounding cytoskeleton [125]. Disruption of this complex is known to result in diseased pathologies and has been shown to result in loss of cellular stiffness [319]. Considering that the nucleus has been previously shown to be the stiffest cellular component [320], its presence in relation to a local mechanical load should be quite significant. Here, mechanical loads were locally applied above the cell's nucleus, and we hypothesized that the membrane recovery, following deformation, was largely attributed to that of the underlying nucleus. Although the nucleus was also deformed during the 10 minutes of sustained deformation, it was also observed to recover along with the membrane, as shown by a reduction in its deformation after 2 minutes following removal of the AFM tip (Fig. 2.2 C). By repeating the experiment off-nucleus (Fig. 2.3 A), we showed that the surrounding cytoplasm resulted in less creeping behaviour over time (Fig. 2.3 C and D). AFM force-maps showed that the nuclear regions are 2-3 times softer than the surrounding cytoplasmic regions (Fig. 2.3 B), in agreement with Yokokawa et al. [199]. Although a softer nucleus seems contrary to predominant reports of stiff nuclei [320-322], others have also noted stiffer cytoplasmic regions [269, 323, 324]. A stiff surrounding cytoplasm is likely due to higher density of cytoskeletal filaments [183, 269, 325], which corresponds with a decrease in normalized deformation (compressive strain) (Fig. 2.3 C) and increased relative viscosity (see Fig. 2.9, and 2.S3). Again, we observed rapid membrane deformation recovery within 2 minutes following removal of the tip in ~90% of cells, indicating that the cell can recover independently of the nucleus.

Local control of cell morphology has been proposed as a fundamental mechanism for regulation of tissue development [156], and so one would expect that neighbouring cells will influence one another. By performing the experiment (10nN for 10min) on single cells we unexpectedly demonstrated that there was no significant difference in overall deformation, in comparison to cells within a monolayer (Fig. 2.5 B). Although there appears to be no clear mechanical influence arising from cell density, there are several examples where a local deformation has been shown to induce biochemical effects in cells adjacent to the perturbation [50, 93, 262, 264, 293]. For example, mechanical stimulation has been shown to induce calcium signalling between cells [50]. Despite the lack of an observed influence of cell-cell contact on the total deformation by the AFM tip, we note that within a monolayer of cells there was often a clear transmission of force to neighbouring cells. Cell-cell contact may not provide enough structural influence to effect localized deformations, however it is clear from the results of others that these loads can lead to the onset of downstream intra-cellular biochemical signalling. Moreover, deformations taking place over much larger length scales (whole-cell) may be more significantly influenced by the presence of an intact cell monolayer.

Complete actin remodelling has been shown to occur within ~1 minute in vitro [326], therefore it is also reasonable to postulate this process as a driving force behind the observed cell shape recovery. However, a small percentage of cells treated with Y-27632 (50%) and CytD (20%), wherein actin polymerization is clearly inhibited (Fig. 2.7), still recover following prolonged deformation,

making it unlikely that the recovery process is related to remodelling of the actin cortex. By imaging in the plane of the basal membrane, during application of the applied load, we were also able to visualize any changes in the orientation and morphology of actin stress fibres (Fig. 2.6 D). In some cases we observed some minor actin stress fibre reorientation and remodelling over the 10min perturbation, but no clear differences were observed in contrast to our previous work on single fibroblast cells [15]. In previous studies, the actin cytoskeleton has been observed to fluidize in response to planar uniaxial stretch [90-92]. This type of response was not observed here, at least within the time frame of loading in our experiment. However, obviously the mechanical stimulus in this study is clearly very different than planar stretching. In some cases, we did observe a slight cellular contraction following removal of the load, which corresponds with previous works demonstrating that actin contractility occurs in response to an external mechanical load [93]. When examining the actin cortex, we also did not observe any quantifiable changes in fluorescence intensity and distribution. However, this certainly does not rule out the possibility of force-induced actin remodelling as imaging these structures is beyond the capabilities of a standard LSCM.

Although the membrane itself plays a role in the organization of actin filaments in vitro, it has become evident that the interplay between the actin cytoskeleton and plasma membrane governs their respective organization [98, 265, 327]. In particular, the plasma membrane has been shown to influence the local organization of actin at the cell periphery [264, 265]. Conversely, the cortex, acting as the primary junction between the inner and outer microenvironments, has been shown to enable rapid changes in cell shape, in response to mechanical stresses exerted on, or by, the cell [100, 266, 267]. The link between the membrane and actin cortex has been shown to influence both cellular function and form [100, 101, 184], and is important for cell shape recovery. For example, in skeletal muscle the basal lamina is directly linked to the cell membrane through transmembrane proteins. Han et al. have shown that dystroglycan, one of these proteins that link the basal lamina to the sarcolemma (underlying sarcomere structure) is a key player in maintaining membrane integrity during stretching motions [268]. By irradiating a region of damage into intact muscle fibres in situ, they demonstrated that although the membrane was able to repair itself in roughly 2min, the integrity of the membrane was disrupted with a lack of dystroglycan connecting the basal lamina. Other proteins such as the Ezrin-Radixin-Moesin family have also proved critical in maintaining cell shape and function [98]. Sub-cellular structures such as microvilli, which are prevalent in HeLa, and whose constituents include the plasma membrane and links to the cytoskeleton may also play a role in resisting deformations [328], albeit smaller deformations in comparison to those applied here. Research has shown that disrupting this link alters the mechanics of these elastic-like filamentous structures, and viscosity of the microvilli are reduced [329].

In this study, by deforming HeLa cells with high aspect ratio, high magnitude forces, we were able to demonstrate that the membrane strongly resists penetration, and that the cytoplasm, consisting of an intact actin network, is primarily responsible for the recovery of cells post-perturbation. Importantly, we demonstrated that the nucleus, which contributes to a large portion of the volume of the cell, is comparatively soft in regard to off-nucleus regions, non-resistant to deformation, and does not aid in cell shape recovery. Indeed, here we have directly shown

through direct visual measurements that the cortex allows the cell to recover from large-scale external perturbations. Without an intact cytoskeleton cells attempt to recover pre-deformed morphology – albeit more slowly. It is becoming increasingly evident that the link between these two major cellular components is quite important in any mechanotransduction process. Future studies disrupting this link, while characterizing cellular responses to deformation will shed more light into these crucial recovery processes.

2.5 Materials and methods

2.5.1 Cell culture

HeLa cells were cultured at 37°C and 5% CO_2 in DMEM with 10% heat inactivated fetal bovine serum and 1% penicillin (100 IU/mL), streptomycin (100 1g/mL) (Hyclone). Cells were cultured on 100mm dishes (Corning) and seeded onto 35mm glass bottom dishes (Mat Tek) in 2.5ml of culture media.

2.5.2 Plasmids and transfections

HeLa cells were cultured on 35mm glass bottom dishes (Mat Tek) to ~60% confluency before transfections. Plasmids for the PH domain of PLC-δ conjugated to EGFP and LifeAct-Ruby have been described previously [196, 278]. Transfections were performed using a 1:1 ratio of Lipofectamine 2000 (Invitrogen) and ~0.6µg of plasmid DNA diluted in OptiMEM (Invitrogen). The transfection complex was completely removed and replaced with culture medium 45min later. Experiments were performed the following day. Immediately prior to the experiment, Hoechst 33342 (Invitrogen) was used to stain the HeLa DNA, according to manufacturer specifications.

2.5.3 Drug treatments

Cells were pre-treated for 30min prior to an experiment with either the rho-kinase inhibitor Y-27632 (10µM, Sigma) or for 15min with the myosin light chain kinase inhibitor ML7 (30µM, Sigma). In other experiments cells were pre-treated for 15min with the actin destabilizing drug Cytochalasin-D (10µM, Sigma). All cells were pre-treated in a cell culture incubator at 37°C and 5% CO_2 immediately before experiments.

2.5.4 Membrane integrity test

Propidium Iodide (PI) nucleic acid dye (Invitrogen) was used to determine membrane integrity after deformation with the AFM tip. PI was mixed in DMEM (1:500) and added to the cells. 0.5% Triton X-100 (1:10) was added to the dish following imaging to deliberately destabilize the membrane as a positive control.

2.5.5 Membrane labelling

Membrane-bound dyes wheat germ agglutinin (WGA) (Invitrogen), and a long-chain dialkyl carbocyanine dye (DiD 700nm) (Invitrogen) were separately added to untreated HeLa in an attempt to stiffen the plasma membrane. WGA is a lectin that binds to N-acetyl-D-glucosamine and sialic acid, it is conjugated to Texas Red-X (595nm) and so produces a bright red fluorescent signal of the membrane when incubated with untreated HeLa cells. A ratio of 1:300 of 1 mg/ml WGA was added to DMEM before performing the experiment. Approximately 0.2% DiD total volume was added to

HBSS containing 5% 0.5M Ca_2^+ and 10% 0.5M $MgCl_2$ and incubated with untreated HeLa for 15min, followed by a change of HBSS prior to the experiment.

2.5.6 Immunofluorescence Staining

Cells were fixed using 3.5% paraformaldehyde and permeabilized using Triton X-100 at 37°C. Cells were stained for actin using Phalloidin Alexa Fluor 488 (Invitrogen), and DNA using DAPI (Invitrogen). Confocal microscopy images were acquired for untreated and drug-treated cells.

2.5.7 Combined Atomic Force and Confocal Microscopy

Images of living cells were acquired with the Nikon TiE A1-R high-speed resonant laser scanning confocal microscope (LSCM) using a 60x/NA1.2 water immersion objective lens. A NanoWizard II (JPK Instruments) AFM was integrated with the LSCM to perform simultaneous AFM-LSCM experiments. All membrane deformation experiments were performed in resonant mode. Experiments imaging of actin stress fibres deformation were performed in galvano mode. The thermal fluctuation method [330] was used to determine cantilever spring constants which had an average value of 0.07 ± 0.03N/m. MSCT-AUHW Gold coated silicon nitride cantilevers were used in all experiments (Veeco). Cell elasticity was determined by recording force-curves centered above the nucleus. The Hertz model for a conical tip (200nm indentations) was fit to the force-distance curves [331], in order to derive the local Young's modulus of the cell membrane (PUNIAS Software) [332]. Force-maps over entire cells (untreated HeLa only) were performed and analyzed using JPKSPM Data Processing software. A scan area of 32x32µm (1µm:1pixel) was probed with an approach rate of 2Hz and speed of 10µm/s for a relative set-point of 1nN. For AFM indentation experiments, we performed 4D imaging by acquiring confocal volumes every minute (each volume consisted of ~30 confocal planes, each 0.5µm thick). Appropriate laser lines and filter sets were employed for each fluorophore. Immediately following the first confocal volume at t=0 (before indentation), the AFM tip was brought into contact with the cell membrane, centred above the nucleus, and a constant force was applied (5nN, 10nN, or 20nN) for an additional 10min. Following the 10min of applied force, the tip was retracted and the cell membrane was allowed to recover and a final confocal volume was captured. Local elasticity measurements were made before and after indentation experiments.

2.5.8 Image analysis

ImageJ (open-source image processing software, http://rsbweb.nih.gov/ij/) was used for all analysis. The deformation of the plasma membrane was calculated by calculating the AFM tip indentation observed in the orthogonal views of each confocal volume, at each time point. Brightness and contrast settings were adjusted in order to optimize images of live and fixed cells. No other image manipulations were performed. In order to quantify the recovery of the plasma membrane and underlying actin cortex we used an ImageJ plugin - Intensity correlation analysis (ICA) [273]. Detailed methods for ICA can be found in the Supplement (Ch. 2.7.2).

2.5.9 Statistical analysis

Statistics were calculated using two sample t-tests, and a one way ANOVA with post-tests including Levene's test for equal variance, and a means comparison test using the Tukey method. All significance indicates $P < 0.05$.

2.6 Acknowledgements

A.E.P. gratefully acknowledges generous support from the Canada Research Chairs (CRC) program and a Province of Ontario Early Researcher Award. This work was supported by a Natural Sciences and Engineering Research Council (NSERC) Discovery Grant, an NSERC Discovery Accelerator Supplement, a CRC Operating Grant and the Canadian Foundation for Innovation Leaders Opportunity Fund.

2.7 Supplementary Methods

2.7.1 Analysis of time-dependent strain using Kelvin-Voigt model

By deforming the cell with a constant force of 10nN for 10min, we observed the creeping deformation of the cell membrane over time. In an attempt to obtain the creeping rate of membrane deformation, for untreated, treated, and off-nucleus loading, plots of time-dependent strain, as shown in Fig. 2.2A, 2.3B(i), 2.5B, 2.8A, 2.9A, were fit to the Kelvin-Voigt model for a constant applied stress:

$$\varepsilon(t) = \frac{\sigma_o}{E}\left(1 - e^{-t/\tau}\right) \quad [2.1]$$

where $\varepsilon(t)$ is the strain as a function of time (t), and is defined as the ratio of the deformation (d) versus initial height (h_o). The constant applied stress (σ_o) is defined as: $\sigma_o = F/A$, where F is the 10 nN applied force, and A is the contact area between the pyramidal tip and the cell's membrane. The creeping rate (τ) of the membrane is defined as a function of viscosity (η), and Young's modulus (E), as: $\tau = \eta/E$.

In order to fit the $\varepsilon(t)$ function to each dataset, the corresponding elastic modulus was used from fits of force-indentation curves to the Hertz model as described previously [196]. The contact area (A) was calculated for each dataset by substitution of the measured values for strain at the limit where t approaches infinity (assumed to be at t=10 minutes here), and using the approximation:

$$A = \frac{F}{\varepsilon(t=10min)*E} \quad [2.2]$$

This resulted in values in the range of ~6μm^2, which is consistent with approximations of tip volume based on manufacturer-based nominal geometry (see Methods for cantilever details). By applying a constant stress to a Kelvin-Voigt material the deformation tends toward that of a pure elastic material, i.e. $\lim_{t\to\infty} \varepsilon = \sigma_o/E$. An example of the fit of one plot for an untreated cell is found below:

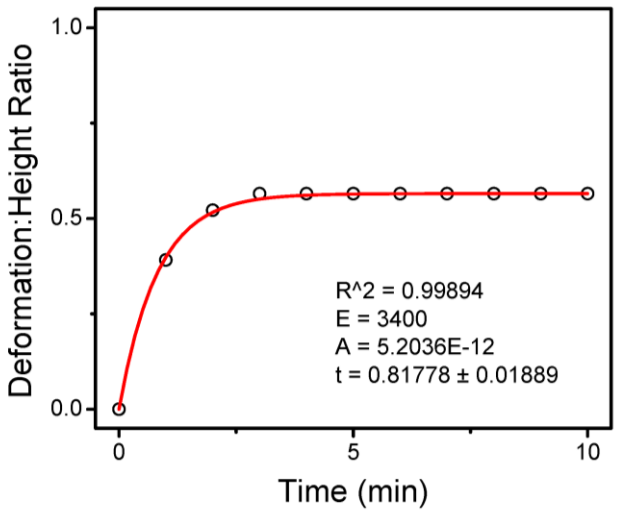

2.7.2 Co-localization analysis of membrane and cortex intensities

In order to quantify the recovery of the plasma membrane and underlying actin cortex we used an ImageJ plugin – Intensity Correlation Analysis (ICA) developed by Li et al. [273]. In this particular ICA, the mean intensity for a particular image A is subtracted from each pixel A_i and multiplied by the corresponding difference in pixel intensities from a second image B. This is called the product of the difference of the means (PDM):

$$\sum_N (A_i - A)(B_i - B) > 0 \qquad [2.3]$$

If the sum of this product is greater than 0, then the correlation is positive. A ratio of the number of positively correlated pixels to the total number of pixels was used to define the maximum intensity correlation quotient (ICQ):

$$ICQ = \frac{\sum_N (A_i - A)(B_i - B) > 0}{N} - 0.5 \qquad [2.4]$$

The maximum ICQ is +0.5, for a perfect correlation between image pixel intensities, in comparison with random pixel correlation having ICQ=~0, and completely isolated pixels with ICQ= -0.5.

In order to compare recovery images (t=12min – 2min following tip retraction) to initial cell morphology (t=0), orthogonal projections of both the YZ and XZ axes were generated. For comparison we also performed ICA on orthogonal projections from deformation images (t=10 min of 10nN) to initial cell morphology (t=0). It is expected that ICA on the latter will result in a lower ICQ than that resulting from the recovery images. We performed ICA after thresh-holding the images using the ImageJ plugin *BG subtract*. ICA was performed on whole cell orthogonal projections initially, however results showed no increase in ICQ for recovery images. This is due to the dynamic nature of the whole-cell membrane. For this reason a region of interest (ROI) was chosen to encompass the deformation and ICA was again performed. An example of ICA output is shown below:

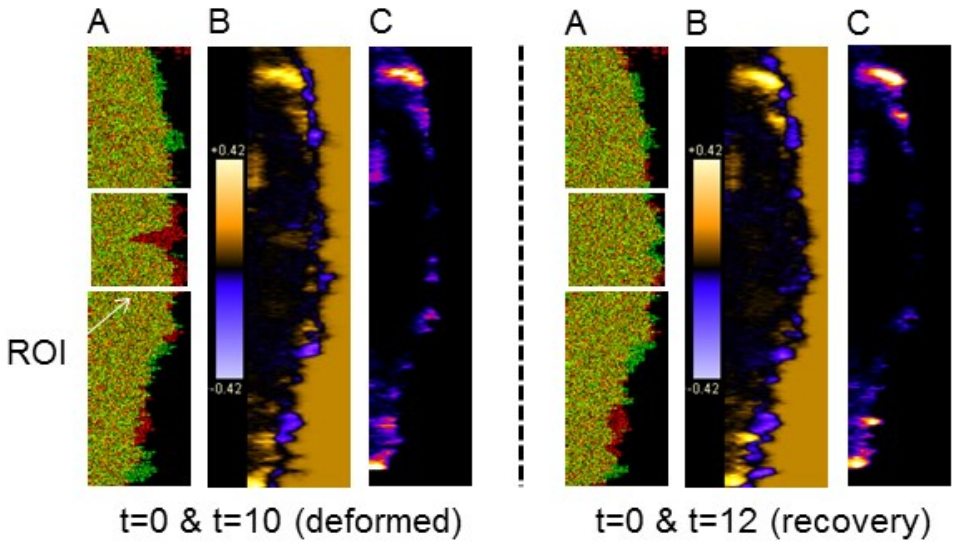

Overlays of before (red) and after (green) are shown in (A), and corresponding ICQ are plotted in (B) for both deformed and recovery images (ICA performed with initial t=0 images) Scale is from ICQ of -0.42 to + 0.42 (perfect correlation would be 0.5). Heat maps of positively correlated pixels are shown in (C), where dark → light is representative of more highly correlated regions.

2.8 Supplementary Tables

Table 2.S1. Mechanical parameters from fitting of Kelvin-Voigt model.

	$E\ (kPa)$	$\tau\ (min)$	$\eta\ (kPa \cdot min)$
Untreated (off-nucleus)	3.40 ± 1.31	1.80 ± 0.93	6.13 ± 3.15*
Untreated (on-nucleus)	3.40 ± 1.31	1.16 ± 0.43	3.94 ± 1.46
ML7 (on-nucleus)	3.99 ± 2.24	1.07 ± 0.54	4.29 ± 2.18
Y-27632 (on-nucleus)	2.80 ± 1.29	1.17 ± 0.53	3.29 ± 1.49
CytD (on-nucleus)	2.53 ± 1.02	1.08 ± 0.37	2.70 ± 0.94*

Below are the various parameters obtained from AFM force-indentation curve fitting - Young's modulus(E), and from fits of time-dependent strain data to the Kelvin-Voigt model: the time constant (τ) (or creeping rate), and viscosity (η). Measured E values from untreated HeLa were used to quantify τ and η for both off-nucleus and the cortex, since on and off-nucleus AFM force-curve measurements were insignificantly different. Magnitudes reported here are not realistic and should not be strictly considered, however relative values of viscosity provide more insight into mechanical characteristics of these varied cell populations. It has been shown that increased stiffness is a result of high frequency of loading [55]. Herein, over-estimation of Young's moduli is likely, and resultant from the rate at which force-curve measurements were made (10µm/s). This over-estimation would directly impact the fits to the model and subsequent obtained viscosities. Others have fit the time-dependent Hertz model to the stress-relaxation phase of AFM indentation curves, thus deriving mechanical parameters from the standard linear model [168]. Parameters from these models often report values that are much higher in magnitude (viscosities range from 100-1000s of Pa·s) [168, 196, 280, 281] than they intuitively should be; honey, for example is in the range of ~0.1-10s of Pa·s [282]. The (*) indicates significance in comparison to untreated (on-nucleus) HeLa determined by independent students' t-tests (P < 0.05).

2.9 Supplementary Figures

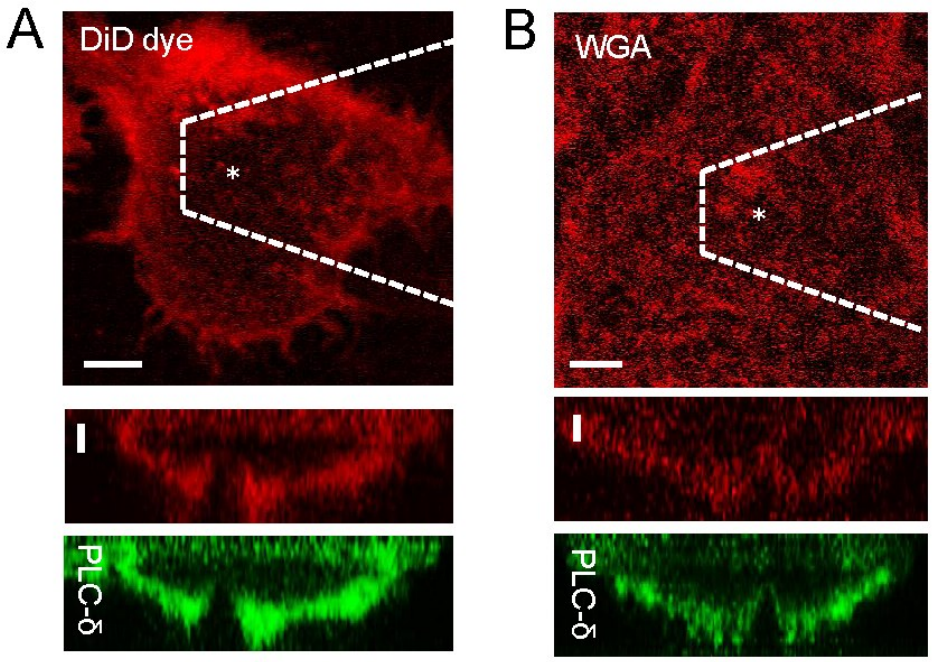

Figure 2.S1 Membrane-bound dyes used to increase tension.
A) DiD, a lipophilic tracer incubated with HeLa cells transiently expressing EGFP-PLC-δ is shown at t=10min of 10nN constant force. B) HeLa membranes labeled with wheat germ agglutinin (WGA), a lectin that binds to sialic acid and N-acetyl-D-glucosamine is shown. Scale bars are 10µm for both images in XY axes, and 5µm in orthogonal projections.

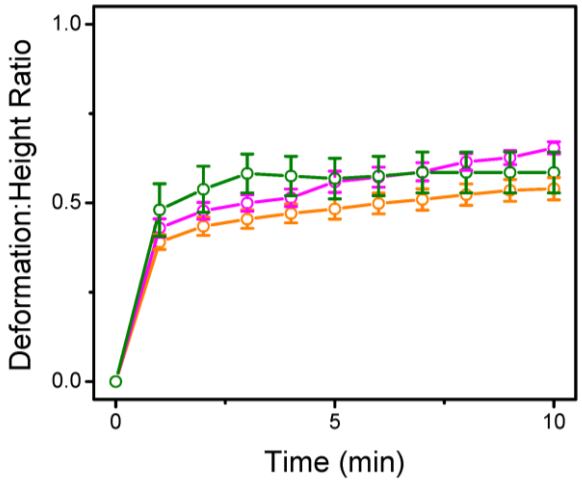

Figure 2.S2. Effect of membrane dyes on axial strain.
Time-dependent strain in untreated HeLa (orange) are compared to cells labelled with fluorescent membrane markers: Did (green), and WGA (magenta). Total time-dependent deformation-height ratios of WGA labelled membranes were significantly increased in comparison to untreated HeLa.

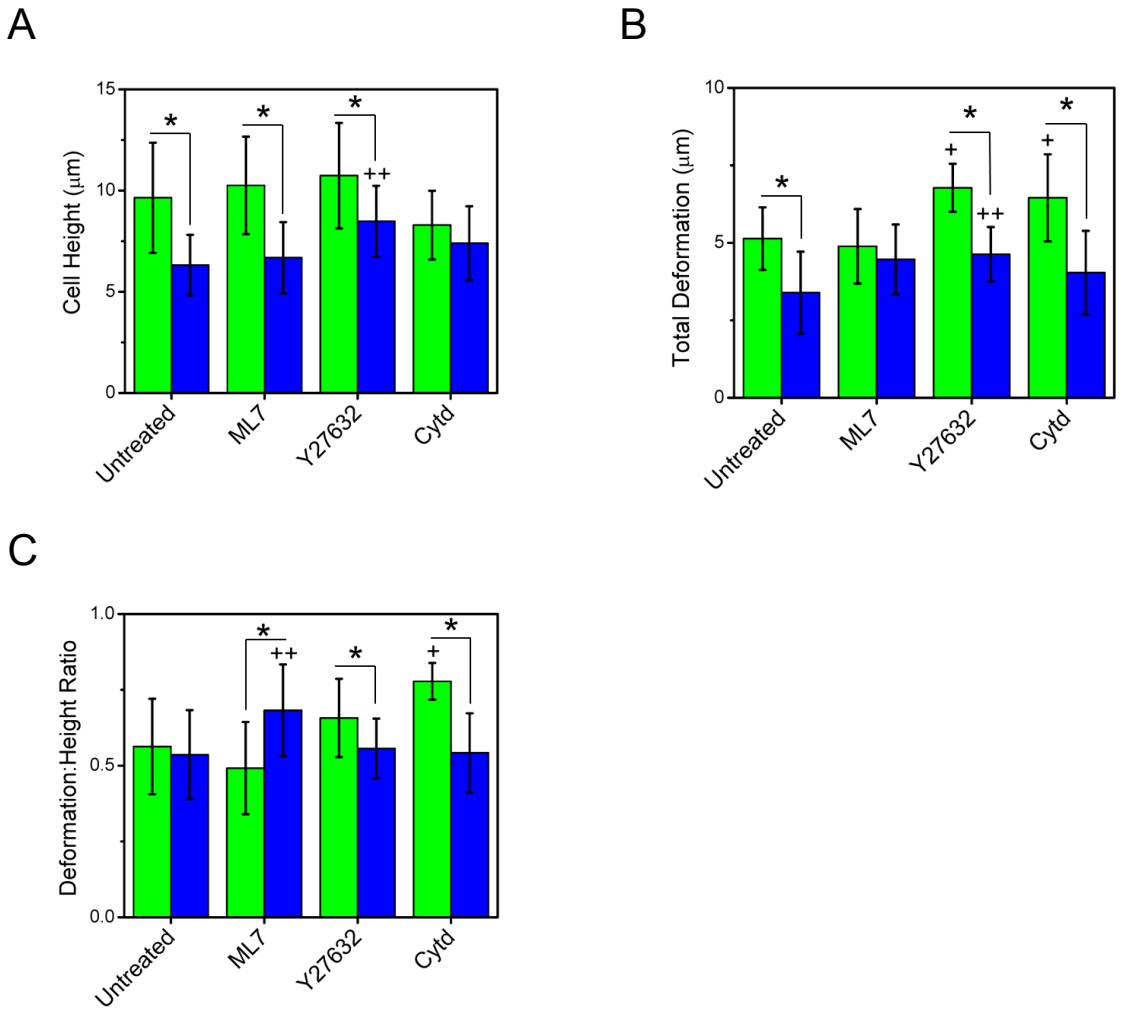

Figure 2.S3. Comparison of nuclear and cytoplasmic regions.
A) Plot of on-nucleus (green) and off-nucleus (blue) measurements of mean cell height. There were no significant differences between heights measured on-nucleus for untreated (n=38) and treated cells: ML7 (n=11), Y-27632 (n=19), CytD (n=8). No significant difference was apparent for off-nucleus loading of untreated (n=21) with ML7 (n=10) and CytD (n=10), however there was a difference with Y-27632 (n=11), indicated by (++). Significant differences (*) exist between on- and off-nucleus loading between groups, as shown. B) Plot of total deformation at t=10 minutes of 10nN applied load. Significant difference between on- and off-nucleus loading is indicated by (*). The total deformation for cells treated with Y-27632 and CytD were significantly increased in comparison to untreated cells, as indicated (+), and off-nucleus Y-27632-treated cells (++) compared to untreated. C) Plot of total deformation:height ratios (aprroximate strain at t=10 min) shows that on- and off-nucleus strains are significantly different when cells are treated with cytoskeletal inhibitors (*). On-nucleus strains are significant from untreated HeLa are indicated by (+), and off-nucleus ML7 strains are also signficant from off-nucleus untreated strains (++). Error bars shown are standard deviation. Significance (*) determined by student's t-test; (+) and (++) determined by ANOVA followed by Levene's equal variance, and means comparison using Tukey test.

Chapter 3 | *Short communication*

The role of the actin cortex in maintaining cell shape

Kristina Haase[1] and Andrew E. Pelling[1,2,3]*

[1]*Department of Physics; MacDonald Hall; University of Ottawa; Ottawa, ON Canada;*
[2]*Department of Biology; Gendron Hall; University of Ottawa; Ottawa, ON Canada;*
[3]*Institute for Science, Society and Policy; Simard Hall;*
University of Ottawa; Ottawa, ON Canada

Submitted Sept. 19th 2013 to *Communicative & Integrative Biology*
Accepted Oct. 4th 2013, V.6, p. e26714

- I, Kristina Haase, contributed towards the majority of the work including: cell culture, atomic force microscopy methods, image acquisition using confocal microscopy techniques, data and statistical analysis. I prepared the first draft and completed subsequent revisions.
- The format of the manuscript has been modified for formatting purposes.

Motivation |

We demonstrated in the previous study that the actin cortex, not the cell's nucleus, is largely responsible for resistance-to and recovery-from large scale deformations. Microtubules have also been proposed to resist compression, however it is unknown whether they can withstand large localized forces or aid in the cell shape recovery process following unloading.

Hypothesis & Objectives |

This manuscript provides an overview and commentary on our previous manuscript, and introduces new results involving the characterization of microtubules in cellular deformation and recovery responses. We hypothesized that inhibition of microtubule polymerization would lead to significantly increased cellular deformations and a potential decrease in cell shape recovery.

3 | The role of the actin cortex in maintaining cell shape

3.1 Abstract

Considering that the plasma membrane is host to a variety of mechanical cues in vivo, and the actin cortex is known to support cell shape, it comes as no surprise that the paired membrane-cortex plays a major role in cellular responses to deformation. In a recent study, we applied highly localized forces to HeLa cells in order to examine the deformation response of the membrane and cortex. Direct visualization of the deformation in the loading plane allowed for the characterization of the observed time-dependent strain. Despite large magnitude and long duration loading regimes, the majority of cells recovered their initial pre-deformed morphology within ~2min. Unexpectedly, perturbed regions above large-volume nuclei were shown to be quite soft and had negligible influence on morphological recovery. The resistance to deformation and ability to recover was found to be largely influenced by the actin network, and dependent upon rho-kinase mediated contractility.

3.2 Short communication

Mechanical cues are well-known to influence a variety of cellular functions and processes.[5, 7, 157] Key players such as the extracellular matrix, cytoskeleton and membrane play a concerted response to mechanical perturbations and numerous studies aim to characterize their roles in mechanotransduction and mechanosensitivity.[32] The cytoskeleton is well known as the structural edifice of the cell. Actin, in particular, responds dynamically to mechanical deformation by remodelling within a short period of time.[333] This structurally supportive network must act together with the flexible plasma membrane to resist deformations and also transmit extracellular forces throughout the cell.[15] Deformation of the membrane leads to chemical rearrangements, protein activation, and intracellular signalling events.[245, 264, 265, 267, 277, 334] Moreover, the membrane is linked to the actin cortex, and this membrane-cortex structure plays a major role in governing the mechanical properties of the cell.[100, 101] The cortex also plays a key role in controlling cell shape during processes such as mitosis and migration.[98, 100] The mechanical properties of these two linked cellular constituents clearly influence one another and influence how cells respond to external forces.

In this light, we recently published a study that examined time-dependent deformation of the membrane and cortex of HeLa cells, which we review here (Fig. 3.1).[335] By applying precise nanonewton forces using an atomic force microscope (AFM) while employing laser scanning confocal microscopy (LSCM), we simultaneously probed and directly visualized the deformation of these cells. The AFM tip was positioned over the center of the nucleus (Fig. 3.1 A), and forces of 5-20nN were applied to the cells for 10 minutes (Fig. 3.1 B). We observed a viscoelastic cellular response with creeping deformation that demonstrated a linear dependence on force magnitude for the range applied (Fig. 3.1 B *inset*). Notably, the majority of cells (80%) recovered at least 50% of their total deformation within 2 minutes following loading, most recovered fully (Figs. 3.1 A, 3.2 C).

In addition, deformation of the actin cortex was shown to follow that of the membrane, with the majority of the response occurring immediately, and creeping deformation observable during the remainder of loading (Fig. 3.1 B). Although no significant remodelling of F-actin stress fibres was observed in the basal membrane, we cannot rule out possible remodelling of the cortex during or following the deformation.[333]

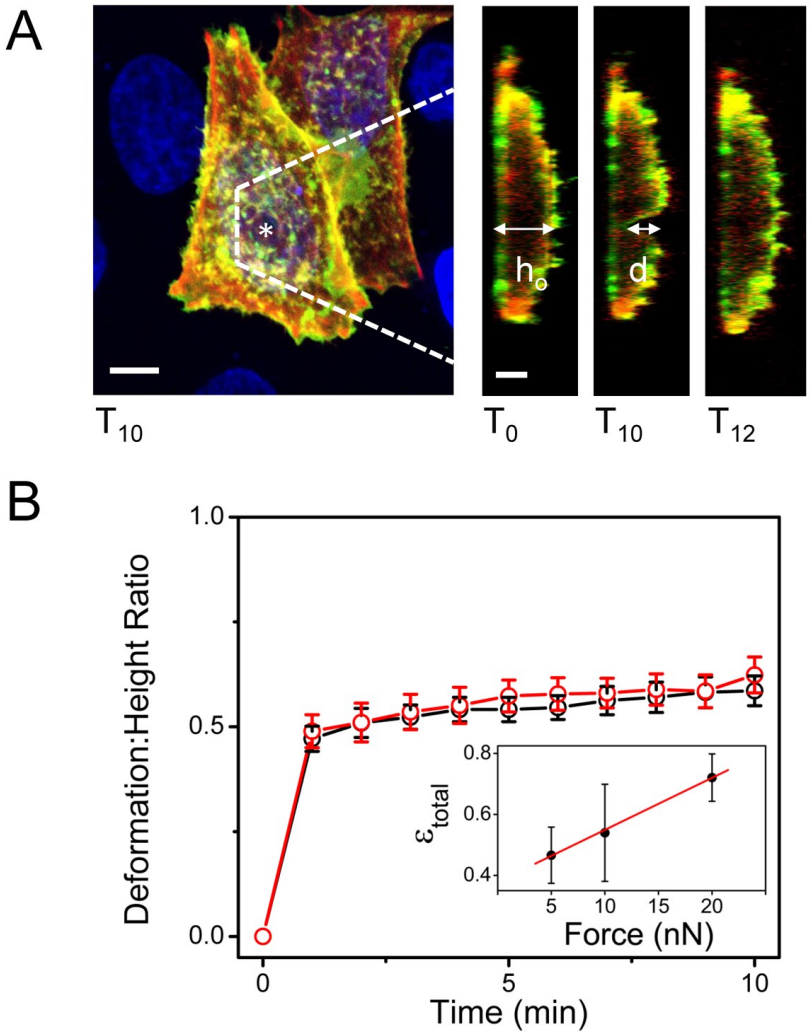

Figure 3.1 Membrane and cytoskeletal recovery following mechanical perturbation.
A) Both the plasma membrane and underlying cortical actin network recover following mechanical perturbation. Orthogonal YZ images show the undeformed cell height (h_o) prior to deformation (t=0), the deformation (d) after 10min of 10nN applied force (t=10min), and the recovered morphology following the removal of the tip (t=12 – 2 min following loading). This is an example of one particular cell that shows in-excess of 50% of cell deformation, but does not reflect the average value of normalized deformation seen in (B). (*) indicates AFM tip position. Green: PH-PLC-δ-EGFP (membrane), Red: LifeAct Ruby (actin cortex), Blue: Hoescht-33342 (nucleus). Scale bars shown are 10µm. B) Deformation: height ratio (d/h_o) demonstrates creeping behaviour of cell deformation over time. Normalized deformation of the membrane (black) versus actin cortex (red) here shows that the linked cellular components deform simultaneously. Error bars shown are standard error. Inset shows the linear dependence of time-dependent deformation, ε(t) or strain here, on force magnitude for the range tested (5, 10, and 20nN). Error bars for inset are standard deviation. Figure adapted from reference [335].

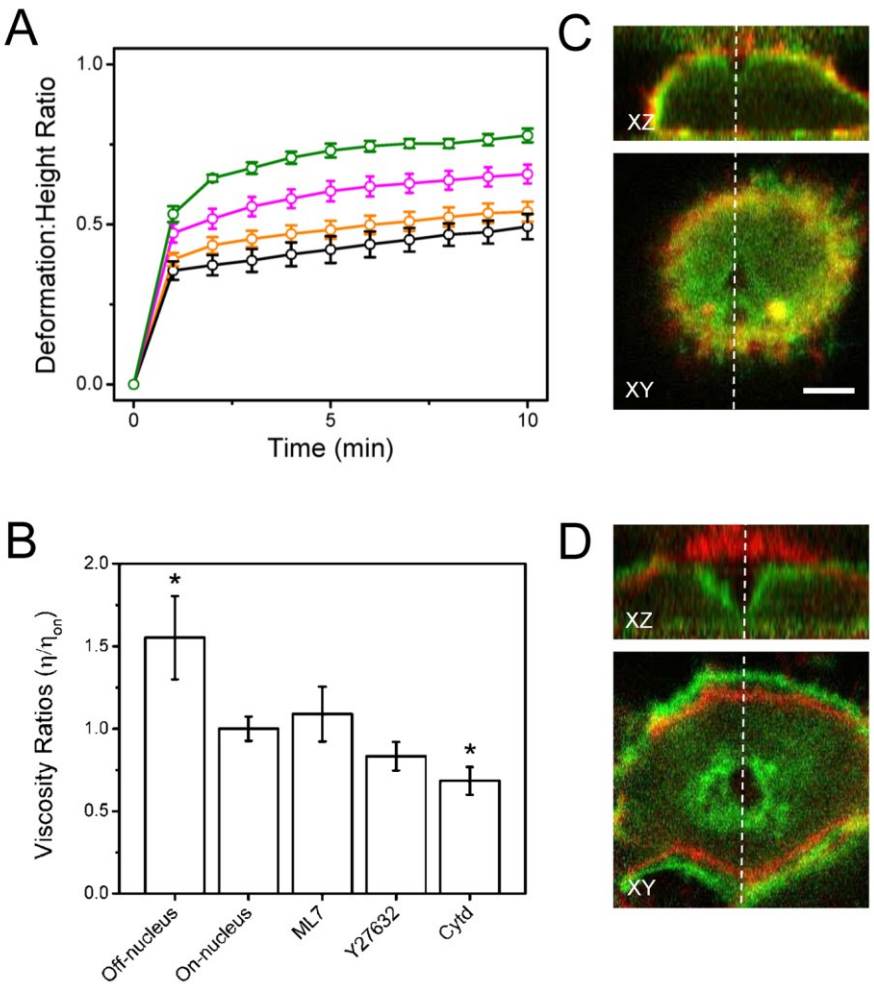

Figure 3.2 Resistance to deformation is dependent on the cytoskeleton.
A) Deformation: height ratios over time comparing untreated HeLa (orange) to cells treated with ML7 (black), Y-27632 (magenta), and CytD (green). Cells treated with Y-27632 and CytD deformed significantly more than untreated cells. B) Viscosity ratios derived from Kelvin-Voigt fits of time-dependent strain. Shown are the viscosities of treated cells relative to untreated cells (above the nucleus), as well as the cytoplasmic regions relative to the nuclear region (both untreated). The cytoplasmic regions are more viscous than the nuclear regions, suggesting that they are densely packed with cytoskeletal filaments. As well, cells treated with CytD are significantly less viscous than untreated cells, indicating that the actin cytoskeleton is mainly responsible for resistance to deformation. Error bars are standard error. (*) indicates $P < 0.05$ significance compared to on-nucleus results as determined by a t-test. C) Image overlay of untreated HeLa cells during (after 10mins of 10nN) (green) and prior-to deformation (red). D) Image overlay of CytD-treated HeLa cell during (green) and prior-to deformation (red). The deformation is much more pronounced in comparison to untreated cells. Figure adapted from reference [335].

A test for membrane permeation clearly demonstrated that cells were deformed rather than penetrated from pointed loads.[335] We speculated that the large-volume nucleus may play a role in the observed recovery. To test this hypothesis, the same experiment was performed in regions surrounding the nucleus. Surprisingly, cells perturbed in cytoplasmic regions also recovered (80%). AFM force-maps presented in our previous publication demonstrate that regions above nuclei are

softer than peripheral regions, corresponding to their minimal resistance to deformation.[335] In those experiments, force curves were analysed over a 200nm indentation in order to isolate the mechanical properties of the cortex and closely underlying nucleus while minimizing substrate effects. Although nuclei are often reported as the stiffest cellular organelle,[320-322] others demonstrate stiffer cytoplasmic regions, consistent with our observations, that likely arise due to an abundance of cytoskeletal filaments in these regions.[269, 323, 324] However, our observation is limited to the mechanical properties in a shallow region under the membrane. Young's modulus measurements performed with deeper indentation will sample different mechanical properties.[336]

Subsequently, a variety of cytoskeletal inhibitors were employed to examine the role of the cytoskeleton in the deformation/recovery response. Cells were pre-treated with ML7, an inhibitor of myosin light chain kinase (MLCK), Y-27632 an inhibitor of rho-kinase (ROCK), and the known actin depolymerizer Cytochalasin D (CytD). ML7 treatment resulted in no noticeable morphological changes; however, the actin network was partially or completely disrupted by the presence of Y-27632 and CytD, respectively. AFM force-curves (fit to the Hertz model)[331] demonstrated a significant decrease (~20%) in stiffness for cells treated with Y-27632 and CytD, in comparison to untreated cells. Reduced stiffness of Y-27632- and CytD-treated cells corresponds with the loss of an intact actin network, and resulted in increased deformation (Fig. 3.2 A). Moreover, cells treated with ML7 displayed a recovery consistent with untreated cells (90%), whereas those treated with Y-27632 and CytD resulted in only 50% and 20% of cells recovering, respectively. The experimental observed time-dependent membrane deformation data was fit with a simple Kelvin-Voigt model using experimentally determined values for Young's modulus in order to implicitly calculate the viscosity of these cells (Fig. 3.2 B) (see ref. [335] for experimental details). Although there are limitations to this simple model, by comparing viscosity values it was possible to determine that nuclear regions appeared less viscous than surrounding regions, again suggesting the cytoplasm consists of densely packed cytoskeletal filaments resistant to deformation. Moreover, CytD-treated cells were significantly less-viscous than untreated cells, and resulted in permanent damage (Fig. 3.2 D), unlike untreated cells (Fig. 3.2 C).

Following up on the results in our previous study,[335] here we report on the role of microtubules (MTs) in governing cortex deformation in HeLa cells by employing Nocodazole (Noco), a known MT inhibitor. As before, a 10nN force was applied above the cell's nucleus for 10 minutes (Fig. 3.3A). Although MTs were disrupted (Fig. 3.3B), there was neither a significant change in stiffness or deformation, in comparison to untreated cells. We observed 80% recovery of Noco-treated cells, with the majority recovering within 2 minutes. Both, our recent study,[335] and the complimentary results shown here demonstrate that actin plays a dominant role in providing mechanical resistance to deformation, for HeLa cells.

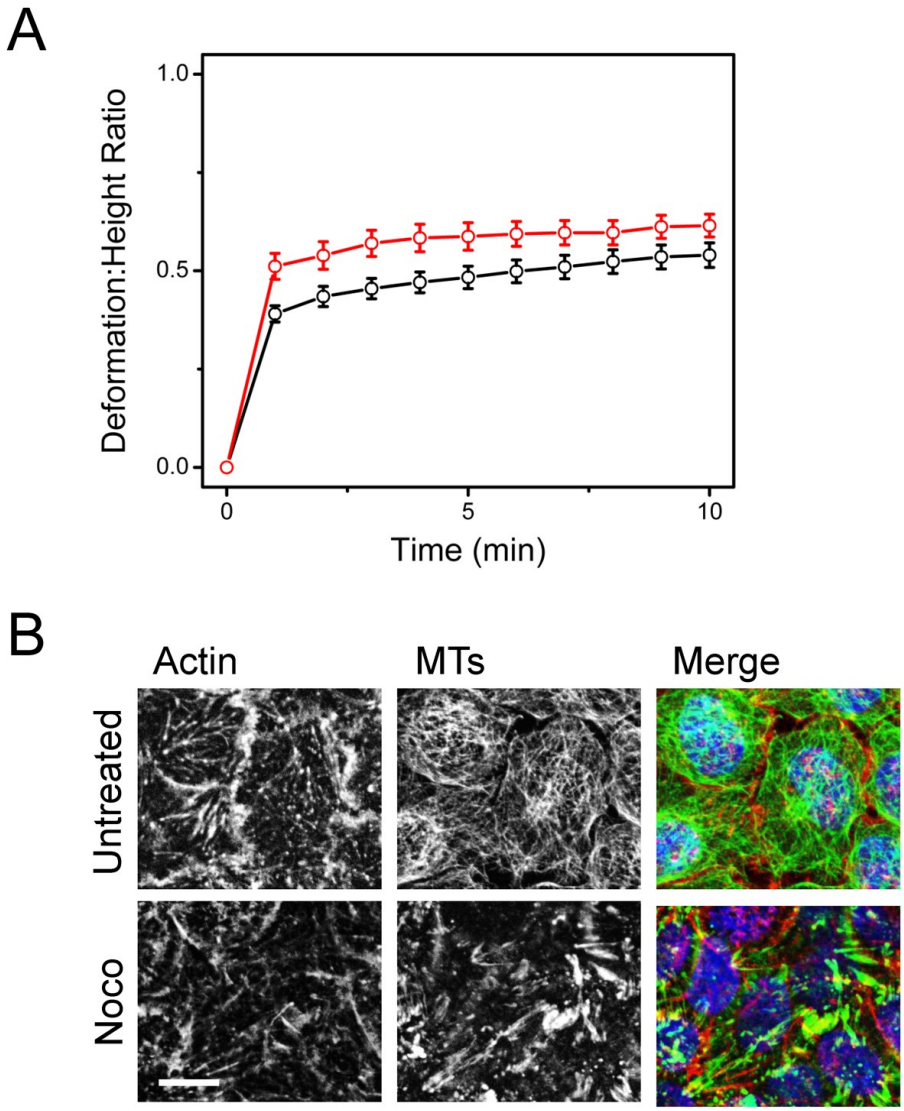

Figure 3.3 Microtubules are not essential for resisting deformation.
A) Deformation: height ratios over time comparing untreated HeLa (black) to cells treated with Nocodazole (red). Cells were treated with 10mM Noco for 15 min prior to experimentation. Although the average creeping deformation increased from d/h_o=0.54 for untreated HeLas (n=26) to d/h_o=0.61 for Noco-treated cells (n=10) at t=10min of deformation, the increase was insignificant (P > 0.17). This result suggests that the actin network, particularly the cortex, is the key influential cytoskeletal network responsible for the resistance to deformation. Error bars shown are standard error. B) Immunofluorescent images comparing untreated HeLa to those treated with Noco. Treatment with Noco disrupts the MTs, while leaving the actin network intact. Red: Alexa fluor 564 (actin), Green: Phalloidin (MTs), Blue: DAPI (DNA). Scale bars are 10µm.

Altogether, our results demonstrated that the membrane and cortex deform in a unified time-dependent manner, exhibiting near full-recovery within minutes following load-cessation.[335] Surprisingly, large-volume nuclear regions were observed to be highly deformable and do not appear to play a role in cell-shape recovery. This is possibly due to HeLas being a cancerous cell type. AFM force-curves have previously demonstrated that cancer cells and cancer cell nuclei tend

to be more deformable than benign cells.[171, 337-339] Moreover, considering that a small number (~20%) of CytD-treated cells recovered, actin cannot be the sole initiator of cell shape recovery. It is possible that movement of the cytosol, sub-cellular structure and the dense filamentous networks may also contribute to the observed recovery, in correlation with recently proposed poroelastic models.[181] Future studies that characterize the time-dependent mechanical deformations of a variety of sub-cellular structures in multiple cell types will provide further insight into these mechanical responses.

3.3 Acknowledgments

A.E.P. gratefully acknowledges generous support from the Canada Research Chairs (CRC) program and a Province of Ontario Early Researcher Award. This work was supported by an NSERC Discovery Grant, an NSERC Discovery Accelerator Supplement and a CRC Operating Grant.

Chapter 4 | *Manuscript*

Rapid dynamics of the membrane and actin cortex in response to local deformations

Kristina Haase[1], Tyler N. Shendruk[1], Gary W. Slater[1], and Andrew E. Pelling[1,2,3]

[1]*Department of Physics, MacDonald Hall, 150 Louis Pasteur,*
[2]*Department of Biology, Gendron Hall, 30 Marie Curie,*
[3]*Institute for Science, Society and Policy, Simard Hall, 60 University,*
University of Ottawa, Ottawa, ON, K1N 6N5, Canada

In preparation for *Nature Materials* Aug. 2014

- This scientific manuscript is in preparation for submission (prepared format for *Nature Materials*).
- I, Kristina Haase, contributed towards the majority of the work including: cell culture, atomic force microscopy methods, image acquisition using confocal microscopy techniques, data and statistical analysis. I prepared the first draft and completed subsequent revisions to date.
- Dr. Tyler Shendruk developed, programmed, and implemented the theoretical model.

Motivation |

We have shown in previous chapters that HeLa cells are able to recover their pre-deformed shape following large local deformations within minutes. While others have also shown that cells can recover shape, there is little information pertaining to their recovery processes. Recently, the flow of liquid cytosol has been proposed to contribute to force relaxation.

Hypothesis & Objectives |

The main objective of this manuscript is to identify cellular components involved in observed cell-shape recovery processes. We postulated that the actin cytoskeleton, not microtubules, as well as osmotic pressure likely play key roles in the recovery process. Direct visualization methods are employed to systematically characterize deformations of the plasma membrane and the underlying cortex.

4 | Rapid dynamics of the membrane and actin cortex in response to local deformations

4.1 Abstract

It is vital that cells respond rapidly to mechanical cues within their microenvironment. This time-dependent adaptation is reliant upon the mechanical properties of a cell's highly interconnected cytoskeletal network. The actomyosin cortex in particular plays a dominant role in resistance to, and recovery from deformations. As well, redistribution of liquid cytosol within the cell has been shown to relieve intracellular pressure during compression. Herein, we induce large local cellular deformations using an AFM tip in order to observe the immediate recovery response of cells following both short and long durations of loading. By imaging within the plane of the deformed membrane and cortex, we were able to both observe and characterize their immediate response to unloading. Cells exposed to cytoskeletal destabilizers as well as osmotic shock conditions, demonstrated the major contributions of actin and fluid flow in the dynamic recovery of cells following large localized cellular shape changes.

4.2 Introduction

The morphological state of a cell is in a continual state of flux, a consequence of normal cellular functions and physiological processes. These cellular shape changes are at times drastic, and typically result from actomyosin generated forces, or those arising from the extracellular microenvironment [61, 340]. Cells respond to these forces by adapting in a time-dependent manner [41], the response of which depends on the rate and duration of applied force [61, 138], as well as the mechanical properties of the cell. Both elastic [56] and viscous [179, 341, 342] cellular behaviours have been observed using direct deformation techniques, such as atomic force microscopy (AFM) [15, 174, 222, 343, 344]. Cantilever deflections during constant-height or constant-force experiments result in measureable stress-relaxation and creep compliance curves, respectively [182, 279, 280, 345]. Simple mechanical models, including the Kelvin-Voigt and the standard linear model [279], as well as more complex models including power-law and soft-glassy rheology [180, 346] are often employed to extract these mechanical properties. Often, broad assumptions, such as cellular incompressibility [347], are considered in order for these models to fit the data. Given their complex behaviour, it is unclear if an all-encompassing cell mechanics model can be defined. Investigations involving systematic characterization of cellular shape change, alongside mechanical properties, are vital to assess the mechanisms involved in key regulatory cell behaviours.

Actin is primarily responsible for resistance to and recovery from large-scale deformations [348]. However, cells have been shown to slowly adapt without an intact actin network, following large-scale force application [348]. This slower recovery is hypothesized to be a result of interstitial fluid flow [181, 348]. It is this cooperative behaviour of cytoplasmic and cytoskeletal constituents and their individual mechanical properties which dictate the extent of immediate and long-term changes in

cell morphology. However, there remains an incomplete picture of how mechanical forces affect cellular dynamics during deformation and recovery.

Recently, we showed that an intact actin network is critical for resisting large local deformations, demonstrating the importance of cortical prestress in cellular shape change [348]. Moreover, the actin cortex, in conjunction with the membrane, surprisingly recovers cell-shape within minutes following large-magnitude local loads [348]. The contractile actomyosin cortex is well-known to modulate cellular shape changes, as it undergoes remodelling at a relatively fast turnover rate [97] (on the order of seconds). However, experimental evidence has demonstrated that actin resists tension, yet buckles under compression at the molecular level [349, 350]. This leads to questions surrounding how the cell resists external compression, and more importantly how cells recover following loading at the macroscale? Previous observations of a slow recovery, independent of the cytoskeleton, suggest involvement of other cellular constituents such as the liquid phase of cytoplasm. Recently, researchers employed hyperosmotic stress to increase the solid volume fraction of cells, which resulted in an exponential increase in shear stiffness as the cell was compressed [346]. Decreased water content increases the viscosity of cells, leaving mainly the cytoskeleton and macromolecules to resist compression. More recently, force-relaxation curves have shown that redistribution of liquid cytosol is responsible for the initial pressure redistribution upon external loading of a cell [181]. The cytoplasm was demonstrated to behave as a biphasic material during the initial stages (~0.5s) of compression, wherein the liquid cytosol was confined to flow through a solid mesh (made up of cytoskeletal filaments and macromolecules) [181]. These studies suggest that while cytoskeletal prestress is required for resistance to deformation, changes in osmotic pressure dominate shear stiffness of the cell.

This cooperative behaviour, between the cytoskeleton and osmotic pressure, is responsible for the response and adaptation of cells to force. While the majority of research has focused on characterizing the initial cellular response to force [195, 202], the adaptive recovery of cells following drastic shape changes has not been well examined [180, 181, 351]. To address this gap in knowledge, we systematically characterized the response of the membrane and cortex immediately and following both short (seconds) and long (minutes) durations of mechanical loading. AFM and laser scanning confocal microscopy (LSCM) were simultaneously used to directly visualize and quantify deformation and characteristic recovery times of HeLa cells. Employing cytoskeletal inhibitors and osmotic shock conditions allowed us to investigate contributions of the actomyosin network and osmotic pressure in the duration and ability of cells to recover from external forces, respectively.

4.3 Results

4.3.1 Measuring the recovery dynamics of the membrane and cortex

Herein, we developed a framework for direct measurement of deformation and recovery dynamics of the cell membrane and underlying cortex through direct visualization. High-speed LSCM was used to capture these events during local deformations delivered by an AFM tip (Fig. 4.1 A,B). Loads of 10 or 20nN were applied above the nucleus of cells for both short (15s) and long durations (1 and 10 min). Although the nucleus does not significantly contribute to long-term shape recovery of HeLa

cells [348], the central region above the nucleus was chosen for consistency. Experiments were performed on cultured monolayers of HeLa cells transiently expressing PH-PLC-δ-EGFP and LifeAct Ruby [348], in order to measure the dynamics of both the plasma membrane and cortex, respectively (Fig. 4.1 B). During initial approach or retraction of the tip, high speed (7.69 fps) imaging was performed in a single plane ~2μm below the apical membrane. Imaging in this plane allowed for measurements of fluorescence intensity over time where the deformation was clearly visible (Fig. 4.1 C). A specified region of interest (ROI) located in the central region of the observed deformation was used to measure mean intensity over time.

First, the cell membrane and underlying actin cortex were shown to deform simultaneously with little resistance to force, in response to rapid indentation (10μm/s) (Supplementary Methods (Ch. 4.7.10-11 and Fig. 4.S1 A). Using the same approach, both short and long durations of constant force were applied apically to HeLa cells in order to examine their ability to recover from large local loads. Normalized intensity profiles (recovery curves), measured from time-lapse images of untreated cells were fit to a modified box-Lucas equation:

$$I(t) = A(e^{-\kappa_2 t} - e^{-\kappa_1 t}) \quad [4.1]$$

Mean fluorescence intensity, I, is a function of time described by a double exponential with two decay constants: κ_1(s^{-1}), corresponding to the initial recovery as the membrane/cortex approaches the imaging plane, and κ_2(s^{-1}), corresponding to movement of the membrane/cortex as they surpass the imaging plane. The unit-less factor $A = \kappa_1/(\kappa_1 - \kappa_2)$ is a ratio of the characteristic decay constants. Intensity profiles fit to eqn. [4.1] demonstrated that κ_1 is dominant in dictating the shape of the recovery curve, with paired t-tests indicating $\kappa_1 > \kappa_2$, in all cases ($P < 0.05$). The majority (90%) of intensity profiles for untreated cells behaved similarly to the exemplary curve in Fig. 4.2 A; however a small number recovered as shown in Fig. 4.2 B. Following 1min of a 10nN load, mean characteristic recovery decay constants measured from fits to eqn. [4.1] for the membrane were 2.35 ± 1.04 s^{-1} and 0.07 ± 0.06 s^{-1} for κ_1 and κ_2, respectively. Typically, intensity profiles of the cortex were similar to those of the membrane (Fig. S1b). Thus, mean characteristic decay rates of the cortex: κ_1 of 2.41 ± 1.00 s^{-1} and κ_2 of 0.07 ± 0.04 s^{-1}, were not significantly different from those of the membrane ($P > 0.05$, with paired t-test). Differences between fits of the recovery profiles for the membrane and cortex can be attributed to increased noise in RFP images (Supplementary Methods, Ch. 4.7).

Doubling the load magnitude from 10 to 20nN did not influence the recovery decay constants of either the membrane or cortex (Table 4.S1), despite significant increases in strain with increasing load (Supplementary Methods (Ch. 4.7.1.12, and 4.7.3.1) and Fig. 4.S2). Notably, load duration did not influence characteristic recovery decay rates (Table 4.S1). Initial characteristic recovery decay constants (κ_1) of the membrane and cortex were > $1s^{-1}$ following 15s, 1min, and 10min long durations of 10nN, indicating fast recovery (< 1s). Secondary decay constants (κ_2) were < $0.3s^{-1}$ for the membrane and < $0.1s^{-1}$ for the cortex (much slower). Box plots demonstrate the variance in fitting parameters for time constants of the membrane (Fig. 4.2 C,D). Mean κ_1 across all durations for the membrane was 2.65 ± $0.27s^{-1}$ (Fig. 4.2 C). On average, slower recovery occurred as the

membrane and cortex moved past the imaging plane, with a mean κ_2 for the membrane of 0.12 ± 0.09 s^{-1} (Fig. 4.2 D).

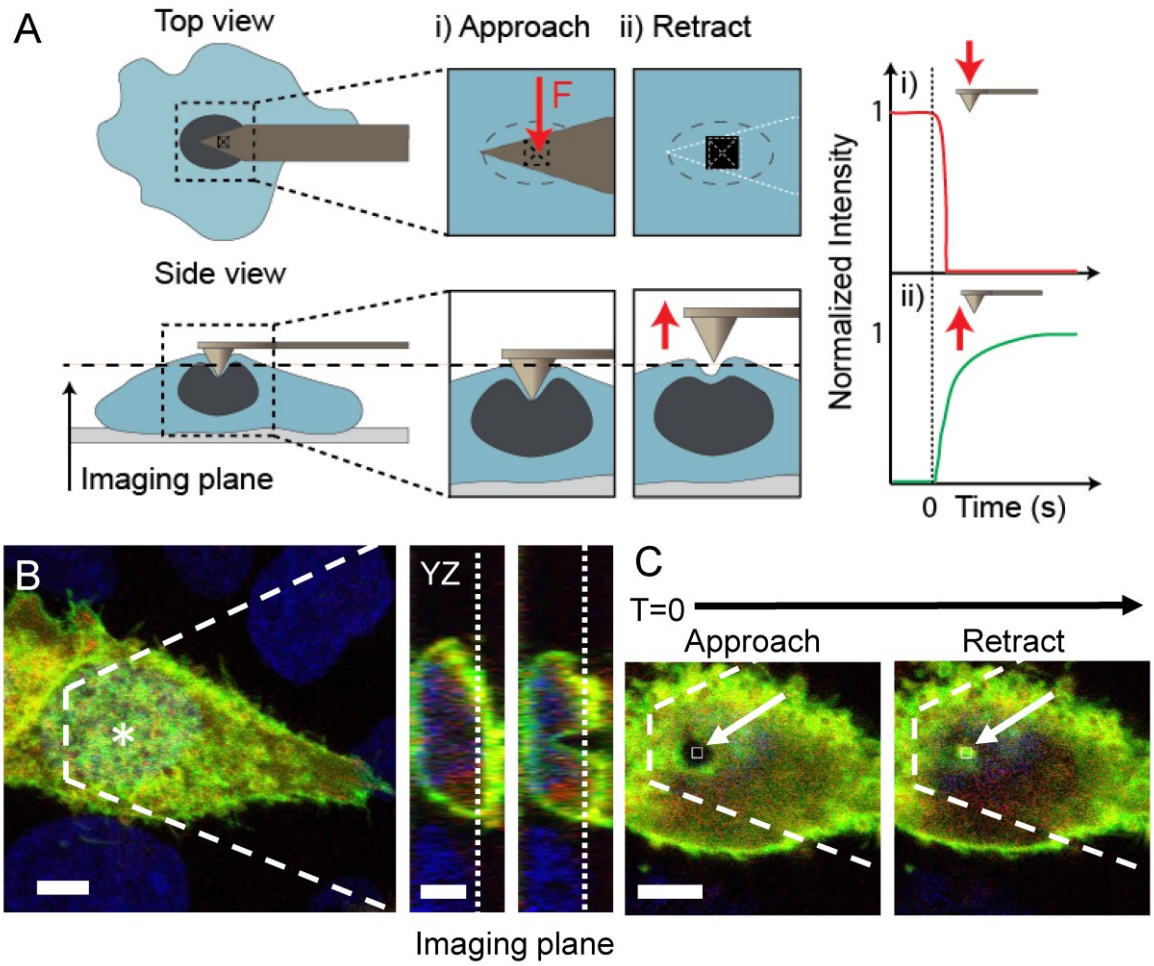

Figure 4.1 Measuring the dynamics of deformation and recovery.
A) Schematic of experimental setup and procedure. After acquiring volume-images of the undeformed cell, the imaging plane is set to ~2µm below the upper surface of the membrane and continuous time-lapse imaging occurs. (i) The AFM tip deforms the membrane above the central region of the nucleus with a set force magnitude. As the tip approaches and deforms the cell, time-lapse images result in a decrease of fluorescence within the imaging plane (where the deformation is visible). (ii) For dynamic recovery experiments, the tip is retracted from the cell following a specified duration of constant force. Corresponding depictions of intensity over time measured from an ROI within the visible deformation are shown. In the case of initial deformation dynamics, the initial fluorescence intensity observed from the EGFP-tagged membrane (normalized to a magnitude of 1 here) diminishes as it is deformed below the imaging plane. On the other hand, for recovery experiments, the membrane is initially deformed when the continuous imaging begins, and so at the outset there is a diminished fluorescence signal within the ROI, subsequently followed by an increase in intensity following tip retraction from the membrane surface. B) Z-projection and orthogonal views of an untreated HeLa cell prior to and undergoing 10nN of force. The imaging plane for subsequent continuous imaging following load removal is shown. C) XY-images from the time-lapse following load removal are shown, corresponding to the same cell in (B). Shown is the cell just prior to tip removal and after the tip is retracted. Arrows indicate the small ROI, where mean intensity is measured over time. Scale bars are 10µm.

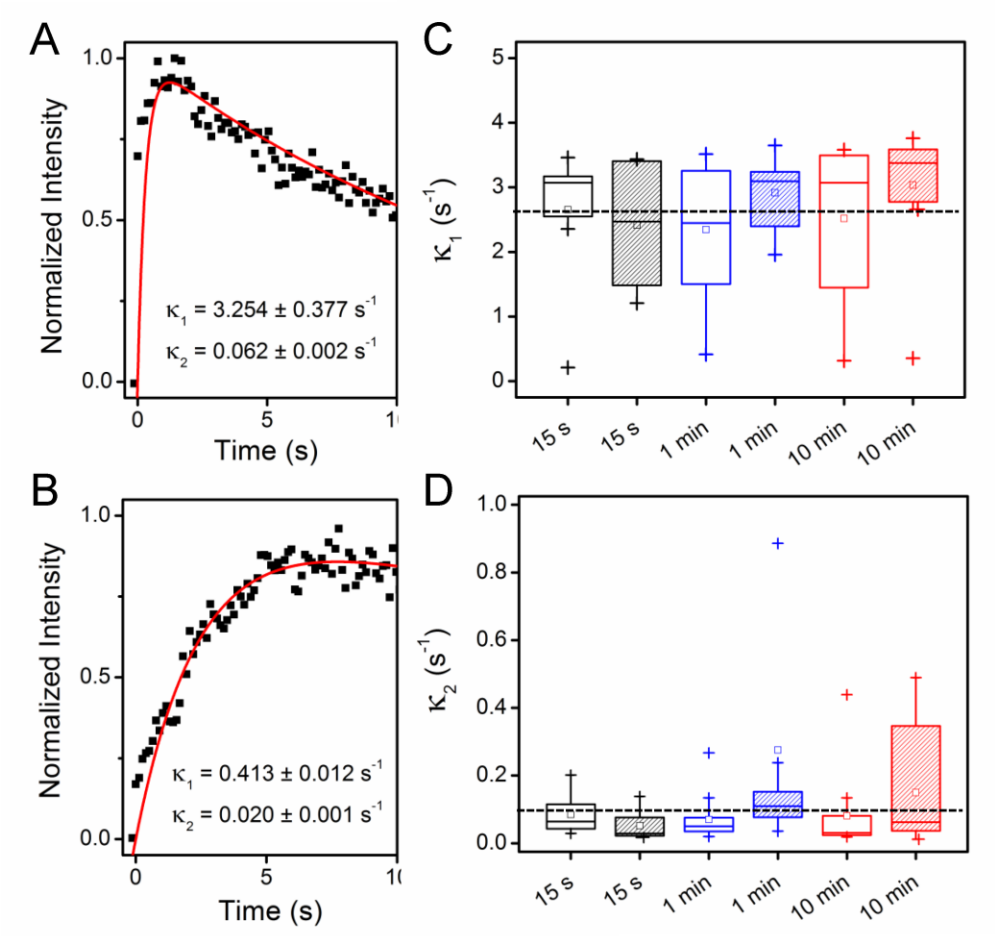

Figure 4.2 Recovery of HeLa cells is near-instantaneous.
A-B), Intensity recovery profiles are shown following retraction of the AFM tip (t=0). In (A), a typical profile for HeLa cells is shown where the peak intensity occurs in < 1s. In a small (10%) number of untreated cells a much slower recovery time was observed, as in (B). Only the first 10s of recovery are shown, however usually >20s was recorded. Corresponding decay constants, κ + s.e.m. are shown. C-D), Box plots of characteristic recovery time constants from fits of recovery curves as shown in (A) and (B) to [1] are shown. Box plots shown are 25th, 75th percentiles. Squares indicate mean values, and outlier data (1.5-fold) is indicated by plus signs (+). Decay constants shown are for recovery curves following 1s (black), 1min (blue) and 10min (red) durations of a 10nN (open boxes) and 20nN (shaded boxes) load. No significant differences appeared between characteristic decay rates or fits for different load magnitudes or durations (P > 0.05, using paired t-tests). Mean values across all experiments is indicated by a dashed line for both κ_1 and κ_2.

In order to characterize overall differences in cellular recovery, we defined a cell as "recovered" when the membrane/cortex passed the imaging plane within the ROI –the peak in intensity profiles (Fig. 4.2 A,B). We also defined a 'fast recovery' when cells exhibited a near-instantaneous recovery time (< 1s). Time-lapse images were visually inspected so that only cells that recovered fully following the deformation were included in the analysis (Fig. 4.S2) [348]. The majority (90%) of untreated HeLa cells (n=20) displayed a fast recovery, following 1min of a 10nN load. We also performed experiments (10nN applied for 1min) while imaging in the most apical region of the cell wherein the deformation was still visible in order to confirm that the position of the imaging plane

did not influence observed dynamics (Fig. 4.S3). In general, the fast recovery dynamics in untreated HeLa cells were observed to occur in a manner independent of force magnitude and duration. Therefore, we focussed on determining which cellular components were driving the recovery process.

4.3.2 The cytoskeleton largely influences shape regulation following unloading

The cytoskeleton is well-known to influence cellular elasticity and morphology [97, 133, 164, 352]. Moreover, we have shown that an intact actin network is necessary to provide stiffness while structurally supporting HeLa cells in order to recover cellular shape following long durations of localized loads [348]. Microtubules, on the other hand, were shown to be unnecessary for the observed recovery response in the minutes following unloading [344]. These cytoskeletal networks are highly interconnected, and so here we examined the role of both actin and microtubules immediately following large perturbations. As before, we performed single-plane imaging experiments in order to measure recovery of cells following 1min of a 10nN load. Cells were treated with Y-27632, a specific inhibitor of Rho-kinase, Cytochalasin D (CytD) a depolymerizer of actin, and Nocodazole (Noco), a known microtubule depolymerizer (Supplementary Fig. 4.S4).

Fits of intensity profiles to eqn. [4.1] revealed that actin is the main contributor to the immediate recovery of cells following highly localized loading (Fig. 4.3 A). Box plots of characteristic recovery decay constants demonstrate the variability in fitting parameters for the various treatments (Fig. 4.3 A,B). In comparison to untreated cells (2.35 ± 1.04 s^{-1}), κ_1 of the membrane was significantly increased for cells treated with Y-27632 (1.02 ± 1.09 s^{-1}) and CytD (1.05 ± 1.06 s^{-1}), however not for those treated with Noco (1.52 ± 1.56 s^{-1}). This increase in characteristic recovery decay constants was similarly observed for the cortex, following treatments with Y-27632 (0.71 ± 0.79 s^{-1}) and CytD (0.82 ± 1.01 s^{-1}), and again were not significantly altered for cells treated with Noco (1.50 ± 1.48 s^{-1}) in comparison to untreated cells (2.41 ± 1.00 s^{-1}). Large variances in fits of the secondary recovery decay constant κ_2 (movement past the imaging plane) made any significant distinctions between untreated and treated cells indiscernible (Fig. 4.3 B). Direct observation of time-lapse images of the membrane demonstrated that the number of cells recovering in < 1s decreased dramatically for actin-destabilized cells (30% of cells treated with CytD, n=17, and 10% of cells treated with Y-27632, n=20). A large number of Noco-treated cells (60%) recovered quickly. The increased strains observed for actin-destabilized cells (Supplementary Results, Ch. 4.7.3.2) may contribute to their prolonged initial recovery times. Despite the reduced recovery time constants following actin destabilization, a high percentage (50-65%) of cells still recovered their initial cell shape within minutes following unloading, and so we postulated that this was largely due to intracellular fluid flow.

4.3.3 Intracellular pressure is partly responsible for shape recovery

Osmotic pressure and interstitial fluid flow may be partially responsible for shape recovery following large deformations. Cytosolic flow within the cell's dense filamentous network has been shown to contribute to initial force relaxation measurements [181]. In order to examine what role cellular

pressure, and cell volume, have on shape recovery we subjected HeLa cells to hyper- and hypo-osmotic shock conditions, with 300mM of sucrose, and 30% dH_2O supplemented normal cell media,

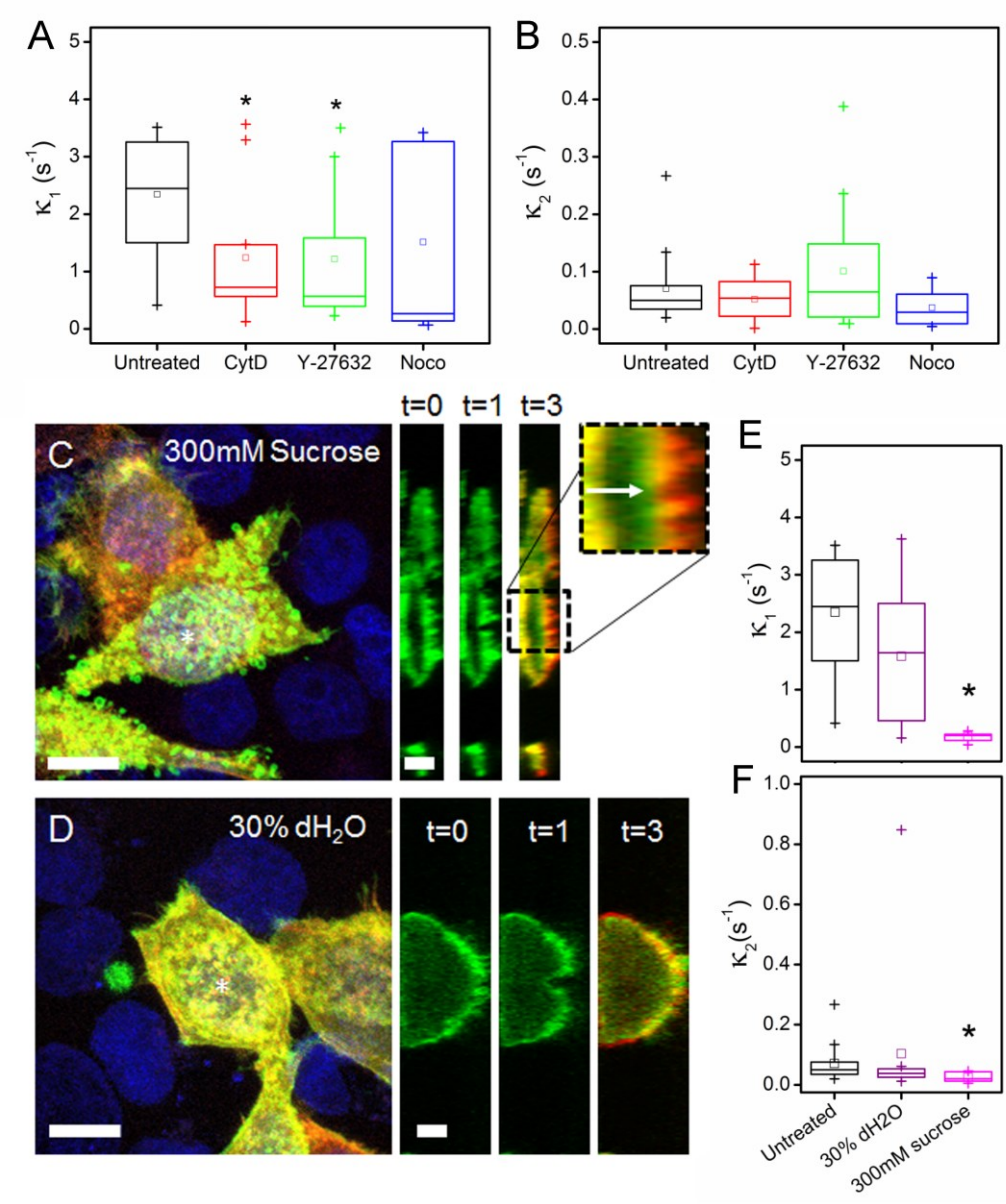

Figure 4.3 Actin and osmotic pressure are major contributors to the recovery response.
A-B) Box plots of characteristic decay constants are shown for fits of membrane recovery of untreated HeLa (black), and cells treated with CytD (red), Y-27632 (green), and Noco (blue). Decay constants shown are for recovery curves following 1 min of a 10 nN load. In (B), there is no significance ($P > 0.05$), even with removal of outliers. C-D) LSCM Z-projection images are shown with corresponding orthogonal projections prior to (t=0), during (t=1min) and a red (undeformed) / green (deformed) overlay following load removal (t=3). C) Hyper-osmotic treatment with 300mM sucrose results in reduced cell volume and reduced ability to recover cell shape. *Outset,* arrow indicates remaining deformed membrane. D) Hypo-osmotic treatment with 30% dH_2O resulted in increased volume of HeLa cells, and did not inhibit cell shape recovery (t=3). E-F) Box plots of characteristic recovery decay constants from membrane fits of osmotic-treated cell experiments are shown. Decay constants shown are for recovery curves following 1min of a 10nN load. All box plots shown are 25th,

75th percentiles. Squares indicate mean values, and outlier data (1.5-fold) is indicated by plus signs (+). * Indicates significant differences with untreated cells ($P < 0.05$, using paired t-tests).

respectively. Cells exposed to these conditions were incubated for 10min prior to performing the experiment to ensure that any transient increase in Ca^{2+} [353], as well as any transient volume compensation effects had subsided to baseline levels [354]. A 10nN constant force was applied to shocked cells for a 1min duration followed by subsequent unloading, which was again captured by imaging in a single plane where the deformation was visible.

Cells exposed to hyper-osmotic shock (sucrose) demonstrated a decrease in volume in comparison to cells in a neutrally osmotic environment, as indicated by a ~58% decrease in cell height (Supplementary Table 4.S3). Small blebs were observed on the membrane of these cells in vitro (Fig. 4.3 C). Single-plane imaging of these treated cells was performed as earlier, however the deformations observed were less distinguishable due to the degradation of fluorescence caused by the addition of the solute, and the significant reduction in overall deformation and cell height (Table 4.S1), which corresponded with a significant increase in stiffness (3.8 ± 1.8kPa, n=7, $P < 0.05$) in comparison to (2.8 ± 0.7kPa, n=9) untreated cells. Fits of the intensity profiles demonstrated drastically reduced characteristic recovery decay constants (Fig. 4.3 E) for the membrane (κ_1 = 0.18 ± 0.08 s^{-1}) and cortex (κ_2 = 0.16 ± 0.06s^{-1}) of hyper-osmotic cells ($P < 0.001$). Secondary decay constants were also significantly reduced, indicating a slow movement of the membrane/cortex past the imaging plane (Fig. 4.3 F). Post-processing of the recovery images was extremely difficult for treated cells; however deformations that were visible remained following unloading of the cell (Fig. 4.3 C, *3x zoom*).

Cells exposed to hypo-osmotic shock (30% dH_2O) conditions resulted in a drastic increase in volume (a 32% increase in cell height) (Fig. 4.3 D). However, absolute deformation remained unchanged (Table 4.S1). The initial recovery response of the membrane of cells under hypo-osmotic conditions (κ_1 =1.58 ± 1.19s^{-1}) was reduced ($P < 0.1$) in comparison to untreated cells (κ_1 = 2.35 ± 1.04s^{-1}), implying slower recovery (Fig. 4.3 E). This decrease was also observed between the initial decay constants of the cortex from hypo-osmotic treated cells (κ_1 =1.66 ± 1.22s^{-1}) versus untreated cells (κ_1 = 2.41 ± 1.00s^{-1}) ($P < 0.1$, and $P < 0.04$ with outliers removed). There was no statistical difference between hypo- and neutrally osmotic conditions for secondary decay constants κ_2 ($P > 0.05$ for both membrane and cortex). Approximately 59% of hypo-osmotic treated cells recovered in < 1s following unloading, however the mean recovery time constant was less than half that of untreated cells ($P < 0.1$). Young's modulus measurements demonstrated an increase ($P = 0.051$) in stiffness for hypo-osmotically stressed cells (3.4 ± 0.7 kPa, n=8). Increased membrane stiffness also resulted when methyl-β-cyclodextrin (MβCD) was used to deplete membrane cholesterol levels (see Supplementary Methods (Ch. 4.7.1.3) and Fig. 4.S6).

4.3.4 Mechanical characterization of viscoelastic shape recovery process

Having revealed the contributions of the cytoskeleton and osmotic pressure in the recovery process, we attempted to characterize the viscoelastic recovery response observed across both untreated

and treated cells. With this aim, we modelled the recovery curves of the membrane using an over-damped wave equation, containing both elastic (k) and viscous (μ) terms.

$$\frac{1}{r}\frac{\delta}{\delta r}\left(r\frac{\delta u}{\delta r}\right) - \mu\frac{\delta u}{\delta t} - ku = 0 \qquad [4.2]$$

Using this form of the wave eqn. [4.2], the displacement, u, of the linked membrane-cortex surface is modelled as a function of the radial distance, r, from the AFM tip (Fig. 4.4 A). The underlying theory of this model is that the surface is treated as a continuum. When the surface (here the membrane/cortex) is displaced, the viscoelastic inner material attempts to bring the surface to its equilibrium state (prior to deformation). Essentially, the surface is treated as a series of viscoelastic elements (Fig. 4.4 A) and corresponds to a Kelvin-Voigt model in which viscous damping and elastic storage act in parallel. Considering that this model assumes over-damped relaxation behaviour, we were able to ignore higher order inertia terms (see Supplementary Methods, Ch. 4.7.1.13-14).

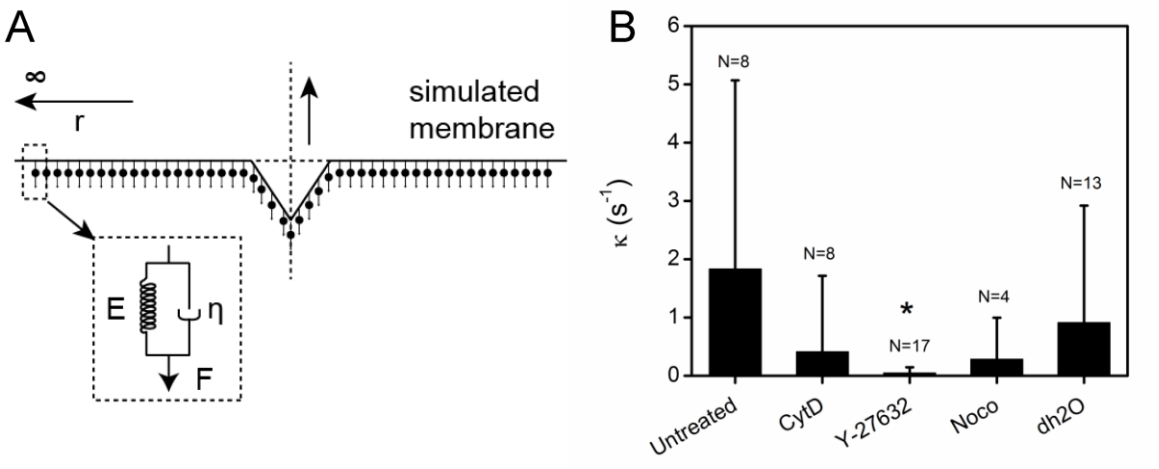

Figure 4.4 Mechanical characterization of recovery.
A) Schematic of the proposed mechanical model. Shown are multi-component viscoelastic elements, representative of the continuum surface treated as a modified wave-equation. B) Plot of decay constants ($\kappa = k/\eta\ s^{-1}$) derived from viscoelastic properties simulated using [4.2]. Only acceptable simulations were used, as indicated by N values shown. * Indicates significant difference with untreated cells ($P < 0.05$, using paired t-tests). Error bars are SD.

First, the intensity profiles from experiments performed on untreated HeLa cells were fit to eqn. [4.2] above. We would expect that cells experiencing a 'fast' recovery would have a large spring coefficient (high k), and a smaller damping coefficient (low η), whereas the reverse would be true for slower recovering cells. Alternatively, the damping coefficient alone could differ between fast and slow recovering cells. Preliminary analysis revealed that for fast-recovering cells fit to the model (n=6 of 8 total) the average spring coefficient (156 ± 34μm^{-2}) was greater than the damping coefficient (25 ± 22μm^{-2}), whereas for slowly recovering cells the reverse was true, the damping coefficient (198 ± 59s·μm^{-2}) was higher than the spring coefficient (33 ± 22μm^{-2}), for recovery following a 10nN load. Repeating the numerical calculation for recovery data following a 20nN load resulted in no change in mean parameters (Table 4.S4).

Cells treated with cytoskeletal inhibitors as well as those exposed to hypo-osmotic conditions were modelled using [4.2] (Table 4.S4). Although absolute values of individual parameters varied greatly between recovery curves within a given population, χ^2 values demonstrated linear minima between possible values of the parameters k and η. Hence, we proposed that a ratio of k/η, (a decay constant, $\kappa(s^{-1})$) would be sufficient for comparing differences between cells exposed to various treatment conditions (Fig. 4.4 B). Using this method, recovery time constants of cells treated with Y-27632 ($0.06 \pm 0.03 s^{-1}$) and CytD ($2.77 \pm 7.60 s^{-1}$) were significantly ($P < 0.05$) reduced compared to untreated HeLa cells ($7.17 \pm 6.64 s^{-1}$), following removal of the same magnitude (10nN), same duration (1min) load. Numerical modelling of recovery curves, using this method, has shown that cell recovery is dominated by a recovery time constant, which is dependent on the actin cytoskeleton, and not microtubules, consistent with our non-linear regression analysis performed earlier. These results must be interpreted with caution however, as only fits that corresponded with the observed response time in the time-lapse images were used.

4.3.5 Shape recovery is observed in other epithelial cells

HeLa cells appear to be quite resilient following large scale local loads, recovering their initial morphologies within seconds (~2.5s on average). We also performed the same deformation/recovery experiment (1min of 10nN) to other established epithelial cell lines; MDCK, HEK, and CHO cells. Experiments using MDCK, HEK and HeLa were performed on the same day and CHO cells were performed in a subsequent experiment, with the same AFM cantilever and calibration techniques. This insured against differences in measured values of deformations/strains arising from the calibration of the cantilever.

Force indentation measurements of these cell types revealed similar Young's moduli ($E \approx 3kPa$, for all cells, $P > 0.05$), cultured on glass substrates. Despite all being cultured to ~90% confluent monolayers, measured heights varied significantly between some cells (Fig. 4.5 A, *inset*). Deformations following 1min of a 10nN load, demonstrated that HeLa cells experienced significantly greater deformations in comparison to all other cell types examined (Fig. 4.5 A). Normalized deformations (treated here as axial strains) measured along the axis of loading were significantly greater for HeLa cells (72.23 ± 3.11%) in comparison to HEK (50.82 ± 15.45%) and MDCK (46.95 ± 9.77%). CHO cells also experienced significantly larger strains (59.82 ± 9.81%) than MDCK ($P < 0.05$, one-way ANOVA, and means comparison with Tukey test). All of the epithelial cells examined here recovered their initial shape within minutes following removal of the load.

As before, time-lapse imaging within the plane of deformation allowed for measurement of intensity profiles. Fits of these curves to [4.1] revealed that, MDCK, CHO, and HEK cells all recover in a similar manner to HeLa cells, with the initial characteristic recovery decay constant dominating the response ($\kappa_1 > \kappa_2$). Interestingly, unlike HeLa, all other cell types tested demonstrated a significantly decreased initial decay constant of the cortex in comparison to the corresponding membrane data ($P < 0.05$, paired t-test), a finding that will require further examination. Moreover, there was significant variability amongst the cells examined. Recovery characteristic decay constants for CHO cells were higher than those of the other cell types for both initial, κ_1, and secondary, κ_2, decay constants ($P < 0.05$, one-way ANOVA). Time-lapse images revealed that 100%

of CHO cells recovered in less than 1s (similar to HeLa, 90%). In stark contrast, only a small percentage (32%) of HEK cells recovered quickly, and none of the MDCK examined (0%) recovered in less than 1s.

It is clear from these results that cell shape recovery, following highly localized large magnitude perturbations, is a response present amongst different epithelial cell types, at least for those examined here. While all of these cells recovered their pre-deformed shape over the long term (within minutes), the immediate recovery decay constants of this phenomenon were cell-type dependent. All cells recovered in less than 3 seconds, on average. It is also interesting to note that the characteristic recovery decay constants of the cortex were slower than that of the membrane for these cells, with HeLa as the exception. This observed difference may be partially due to increased noise in RFP images (see Supplementary Methods, Ch. 4.7.1.6). However, since there was no observable difference between membrane and cortex decay constants for HeLa cells, future investigations should examine this interesting observation.

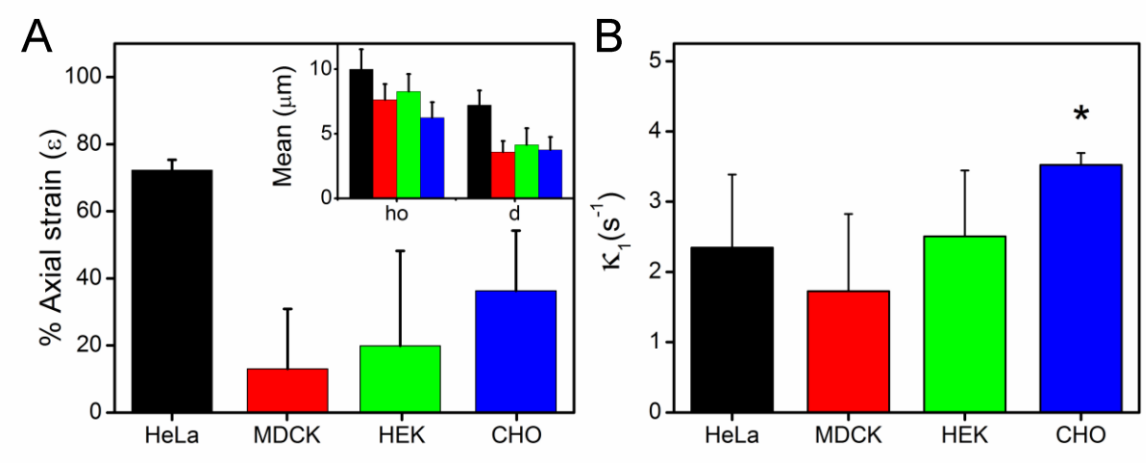

Figure 4.5 Epithelial cells recover shape following loading.
A) Plots of axial strain are shown for HeLa (black), MDCK (red), HEK (green), and CHO (blue) cells. *Inset*, Initial height (h_o) and deformation (d) following 1min of 10nN load. B) Plot of mean initial characteristic recovery decay constants, κ_1. * Indicates significant difference between CHO and all other cell types ($P < 0.05$, paired t-test). Error bars are SD.

4.4 Discussion

Significant shape changes are pervasive during the life cycle of a cell, and are consequent of both internal and external forces that arise during events such as cell-cell communication, motility, and tissue-level strain [340]. In response to these mechanical signals, cells have been shown to quickly alter their morphology, while maintaining their structural integrity [138, 348, 355]. That being said, the mechanisms behind this extraordinary ability that cells possess - to actively respond to mechanical cues, are largely unknown. Herein, this work involves examination of cellular behaviours following large local deformations and complete force removal. A combination of AFM and LSCM was used to characterize the response of the membrane and cortex immediately, during, and following both short (seconds) and long (minutes) durations of mechanical loading. Surprisingly, the majority (90%)

of HeLa cells were shown to withstand and recover from large local forces near-instantaneously (< 1s). Unsurprisingly, the dynamics of recovery were shown to occur simultaneously for the coupled membrane and cortex (Supplementary Fig. 4.S1). With the use of cytoskeletal inhibitors and osmotic-shock conditions, we demonstrated that the deformation and recovery response of HeLa cells are predominantly affected by the presence of its contractile actomyosin network and intracellular pressure.

Our results provide strong evidence that actin is a key regulator in cell shape recovery processes. As we also demonstrated that actin [348], not microtubules [344], are also crucial for resistance to deformation (Table 4.S3), in agreement with others [168, 182]. Herein, inhibition with CytD and Y-27632 led to a drastic reduction in initial cell shape recovery time constants (Fig. 4.3 A). The ROCK pathway in particular, appears to play a considerable role in the recovery process, since 90% were observably impaired by its inhibition. Considering that ROCK inhibition effects myosin light chain downstream, it is not surprising that contractility of the cortex would be reduced, resulting in larger deformations, and slower recovery dynamics. While both the elastic and viscous components of the cell have been previously shown to heavily rely upon actin organization, they do not significantly depend on microtubules [168]. Moreover, recent observations have shown that neither microtubules nor keratin intermediate filaments affect cellular rheology [181].

Microtubules, however, have been shown to transmit forces from the apical cell membrane, causing stress fibre deformation in the basal plane of fibroblasts [182]. Moreover, recovery of chondrocytes following compression has been shown to be drastically reduced following inhibition of microtubule polymerization, using cholchicine [355]. While our results did demonstrate reduced recovery in the absence of intact microtubules (Table 4.S2), Noco treatment did not present a significant change from the recovery dynamics observed in untreated cells, and results were highly variable (Fig. 4.3 A,B). We postulated that any effect caused by the depolymerisation of microtubules might be obscured by secondary effects of treatment, in particular increased actomyosin contraction. Noco treatment has been shown to effectively redistribute tubulin to surrounding stress fibre adhesion sites in HeLa cells [356]. This results in increased stress fibre formation; a result of GEF-H1 release brought about by activation of RhoA. Immunofluorescent images confirmed that tubulin co-localized with actin following treatment (Fig. 4.S4).

To limit any increase in contractility that might occur from Noco treatment, we first inhibited ROCK (the up-regulation of which is associated with stress-fibre formation) with Y-27632, followed by subsequent treatment with Noco for a group of cells (Supplementary Methods, Ch. 4.7.1.3). Although cells treated with Y-27632+Noco still appeared to possess a large number of actin stress fibres in the basal plane, microtubules were completely disrupted and no longer co-localized with fibres (Fig. 4.S6). Interestingly, the ability of Y-27632+Noco treated cells to recover quickly was drastically reduced (20%). Significantly decreased strain measured in these cells indicated increased contractility (Supplementary Results, Ch. 4.7.3.3), counter to the desired effect. This could be caused by a short initial incubation time with Y-27632, the effects of which could be counteracted by Noco treatment. Recently, we demonstrated that Noco treatment results in increased focal adhesion size and contractility, alongside a reduction in cell height in fibroblasts [357]. However, this

effect was shown to be transient and was significantly reduced following prolonged incubation. One explanation for the observed behaviour here could be attributed to cofilin regulation. In particular, actin depolymerizing factor (ADF)/cofilin has been shown to inhibit myosin II binding to F-actin, thereby regulating actomyosin assembly and contractile force generation [358]. In particular, increased actomyosin II assembly and activity has been observed following depletion of cofilin in HeLa cells [358]. Considering that the inhibition of ROCK with Y-27632 has been shown to increase cofilin phosphorylation in esophageal squamous cancer cells [359], it is probable that pre-treatment here results in an accumulation of cortical F-actin. Increased phosphorylation of cofilin (by LIM-kinase 1)[360], which results in an accumulation of actin filaments will result in an overly contractile cortex. This effect could account for the observed increased resistance to deformation and slowed recovery, although future studies will be necessary to determine the exact cause.

By exposing cells to both hyper- and hypo-osmotic conditions we demonstrated that the flow of cytosol is crucial for cell-shape recovery following mechanical perturbations, in direct agreement with current poroelastic models of cell mechanics [181]. Treating HeLa cells by hyper-osmotic shock conditions (300mM sucrose) led to a drastic decrease in deformation and slower recovery. This was to be expected considering that the liquid volume fraction of the cell was diminished, as demonstrated by a significant decrease in cell height (Table 4.S3). Previous reports using fluorescence correlation spectroscopy have shown that cells treated to equivalent concentrations of sucrose have resulted in significant increases in the shear moduli of HeLa cells, with its elastic contributions considerably reduced in comparison to viscous components [361]. Interestingly, storage and loss moduli of untreated HeLas were reduced in the nucleoplasm region, in comparison to the cytoplasm, an effect that was reversed following osmotic stress. Treatment with hypo-osmotic conditions demonstrated increased cell volume, but did not significantly alter the recovery dynamics of untreated HeLa (Fig. 4.3 E,F). In fact, the percentage of cells that recovered quickly was reduced to 56% from 90% for hypo-osmotic stressed cells in comparison to osmotically neutral cells, respectively. To confirm that osmotic pressure and cytosolic flow positively contribute to the recovery dynamics of HeLa cells, we exposed Y-27632+Noco treated cells to hypo-osmotic shock (Supplementary Results, Ch. 4.7.3.3). The increased contractility, demonstrated by resistance to deformation and reduced recovery (20%), of Y-27632+Noco treated cells was abolished following osmotic treatment (80% recovered in < 1s). Together, these results suggest that while intracellular fluid flow may contribute to stress relaxation [181], there may be an upper threshold osmotic pressure that limits the speed of cell shape recovery. While transmembrane proteins such as integrins, and tyrosine kinase receptors have also been proposed as volume sensors, actin has been shown to play a role in cell volume regulation [362]. It is possible that the reduction in ‘fast’ recovering hypo-osmotically treated cells is due to active contractility of the cortex in response to volume changes, which must be further examined in future work. However, the results here demonstrate that actin, in concert with osmotic pressure, appears to be majorly responsible for cell shape recovery following local deformations.

Cellular pressure is controlled and maintained by regulation across the plasma membrane. Whether or not the membrane composition itself critically affects the recovery process remains an

open question. Various membrane-bound dyes have been shown to stiffen the membrane but not affect the deformability of HeLa cells, or long-term recovery of cell shape [348]. Here, rather than inserting a membrane marker, we employed a cyclic oligosaccharide, methyl-β-cyclodextrin (MβCD) to effectively deplete cholesterol levels of the plasma membrane (Supplementary Methods, Ch. 4.7.1.3). While increased stiffness associated with MβCD treatment has been observed in endothelial cells [363], AFM force-indentation curves herein revealed that stiffening of MβCD-treated cells was a result of increased cellular pressure (Supplementary Results (Ch. 4.7.3.4) and Fig. 4.S7). This increased stiffness resulted in a significant decrease in strain of cholesterol depleted cells, but did not alter the ability of cells to recover (100% fast recovery for n=10 cells). Considering that the membrane and cortex are directly linked by proteins, such as ERM [98], it is unsurprising that cholesterol depletion alone would not cause a considerable change in deformation or recovery dynamics. An interplay of membrane and cortex dynamics affect both cell shape and function [99, 101], and so they must be decoupled in future studies in order to examine their respective contributions to the recovery process.

Recently, compression has been shown to result in an increased migratory response of cancer cells [364], demonstrating the need for characterization of deformation and recovery processes, particularly in diseased states. Here, HeLa cells, a cancerous cell line, have been shown to withstand large magnitude forces, and generally recover near-instantaneously, a response largely dependent upon the actin network and osmotic pressure. Interestingly, other non-cancerous cell types (CHO, HEK, MDCK) were also shown to recover within minutes following deformations, although with drastically varied decay constants (Fig. 4.5). Others have demonstrated recovery of chondrocytes following whole-cell compression [355], however these cells were shown to possess a critical strain threshold ~30% [365], considerably lower than recovered strains in HeLa cells (upwards of 60%). This difference is quite surprising, considering that chondrocytes undergo continuous compression cycles *in vivo*. Clearly, investigation into the differences between recovery behaviour of a variety of cells is needed. Differences between cell types are undoubtedly influenced by variations in cytoskeletal organization.

Only a limited number of studies have examined the mechanisms involved in shape recovery processes. For example, Ofek et al. employed a secondary CCD camera to visualize cells in the orthogonal planes under whole-cell compression [355]. While useful for measurement of whole-cell volumetric changes, their rate of image acquisition (0.25 fps) would not be able to capture the fast dynamics or difference in recovery times observed herein. Others have also inferred recovery from cantilever deflection data, as in stress-relaxation experiments. Here, we developed a direct visual method using a traditional LSCM set-up involving high speed time-lapse imaging to interpret the recovery times of HeLa cells following mechanical stimulation. This method allowed us to examine and characterize the contributions from the actin and microtubule cytoskeleton, as well as effects of intracellular pressure. Furthermore, time-dependent intensity profiles obtained from these experiments were used in subsequent modelling (Fig. 4.4). Treating the cell membrane/cortex as a series of interconnected viscoelastic elements revealed that recovery is dominated by a single decay constant. While many others have employed viscoelastic models to characterize cell behaviour, to

the best of our knowledge, we are the first to employ this continuous model to observed cell-shape recovery behaviour. Numerical modelling using this over-damped form of the wave equation (Supplementary Methods, Ch. 4.7.13-14) confirmed that a large damping coefficient was associated with actin destabilized cells (particularly those treated with Y-27632).

Characterization of mechanisms underlying cell-shape recovery processes are important, as it might unveil potential changes brought about by diseased states. We have shown that both cancerous and non-cancerous epithelial cells recover shape following large magnitude compressive loads, although differences in characteristic recovery decay constants suggest that the mechanisms may differ between cell types. Importantly, for HeLa cells, we demonstrated that load duration does not have an effect on how fast these cells recover, despite the fact that actin remodelling certainly takes place within the time frame of our experiment [89]. Organization and contractility of the cortex appears to be critical in the recovery process following large local deformations, as indicated by the severe reduction in fast-recovering cells following cytoskeletal disruption of actin, contractility and hyper-osmotic conditions.

4.5 Methods

Details on cell culture and drug treatments can be found in the Supplement (Ch. 4.7.1-3). Briefly, AFM was used to apply a constant force to cells, while high-speed LSCM was used to capture time-lapse images within a plane of visible cell deformation. Fluorescence intensities were then used to determine the recovery decay constants of the membrane and cortex (Ch. 4.7.1.7-8). An over-damped wave equation was also used to model the recovery behaviour of the membrane/cortex as an infinite surface comprised of a series of viscoelastic elements, as described in full detail in the Supplementary Methods (Ch. 4.7.13-14).

4.6 Acknowledgements

K.H. would like to thank Dr. Nickolay V. Bukoreshtliev for his enthusiasm and insightful suggestions, and Dr. Martin Bertrand for valuable discussions. A.E.P. gratefully acknowledges generous support from the Canada Research Chairs (CRC) program and a Province of Ontario Early Researcher Award. This work was supported by a Natural Sciences and Engineering Research Council (NSERC) Discovery Grant, an NSERC Discovery Accelerator Supplement, a CRC Operating Grant and the Canadian Foundation for Innovation Leaders Opportunity Fund.

4.7 Supplementary Information

4.7.1 Supplementary Methods

4.7.1.1 Cell culture

HeLa cells were cultured at 37°C and 5% CO_2 in DMEM with 10% heat inactivated fetal bovine serum and 1% penicillin (100 IU/mL), streptomycin (100 1g/mL) (Hyclone). Cells were cultured on 100mm dishes (Corning) and seeded onto 35mm glass bottom dishes (laser-cut 35mm plastic culture dishes

(TPP) affixed with 1.5 glass 25mm round coverslips (Harvard apparatus Canada) using PDMS (Dow Corning)), in 2.5ml of culture media.

4.7.1.2 Plasmids and transfections.

HeLa cells were cultured on 35mm glass bottom dishes to ~60% confluency before transfections. Plasmids (~0.6µg) for the PH domain of PLC-δ conjugated to EGFP (kind gift of Guillaume Charras) and LifeAct-Ruby (kind gift of Buzz Baum) were diluted in OptiMEM (Invitrogen) as described previously [348]. The transfection complex was completely removed and replaced with culture medium 45min later. Experiments were performed the following day. Immediately prior to the experiment, Hoechst 33342 (Invitrogen) was used to stain for DNA, according to manufacturer specifications.

4.7.1.3 Drug treatments

Cells were pre-treated in a cell culture incubator at 37°C and 5% CO_2 immediately before experiments. Cells were pre-treated for 30min with either the rho-kinase inhibitor Y-27632 (10µM in DMSO, Sigma) or the microtubule depolymerizer Nocodazole (Noco) (10µM in DMSO, Sigma), or pre-treated for 15min with the actin destabilizing drug Cytochalasin-D (CytD) (10µM in DMSO, Sigma). In some cases, cells were pre-treated with Y-27632 for 15min followed by subsequent treatment with Noco for 15min.

In order to deplete cholesterol levels, methyl-β-cyclodextrin (MβCD), a cyclic oligosaccharide, was used (10mM diluted in dH_2O, Sigma). Cells were incubated with MβCD for 30min at 37°C and 5% CO_2 in serum-free media followed by washing twice with PBS and complete media change. Considering that MβCD was dissolved in a large volume of dH_2O, we used a control population where cells from the same passage number were incubated with serum-free medium and the equivalent ratio of dH_2O (~500µL MβCD solution added to 2mL media) for 30min.

4.7.1.4 Immunofluorescent staining of cytoskeletal filaments

Cells were fixed using 3.5% paraformaldehyde and permeabilized using Triton X-100 at 37°C. Cells were then stained for actin using Alexa Fluor 546 Phalloidin (Invitrogen), and DNA using DAPI (Invitrogen). Microtubules were stained with a mouse monoclonal anti-α-tubulin (Abcam) primary antibody followed by an Alexa Fluor 488 rabbit anti-mouse immunoglobin (Invitrogen) secondary antibody. Full details on the staining protocol have been described previously [196].

4.7.1.5 Image acquisition using confocal microscopy

All images, for live and fixed cells, were acquired with a Nikon TiE A1-R high-speed resonant laser scanning confocal microscope (LSCM), using a 60x (NA=1.2) water immersion objective lens. Appropriate laser lines and filter sets were employed; GFP was excited using a 488 nm laser and measured at 525nm, and RFP was excited using a 561nm laser with fluorescence measured at 595nm. Fixed samples were imaged using LSCM volumes in galvano scanning mode. Imaging of live cell experiments were performed in resonant scanning mode. In this mode, LSCM volume images were captured prior-to and during deformation experiments, and consisted of ~30 confocal planes, each 0.5µm thick. Time-lapse images were performed in a single XY-plane in order to capture the

intensity decrease/increase due to deformation/recovery of the cell, at a scan rate of 7.69 fps. To reduce noise, line averaging (2x) was used.

4.7.1.6 Measuring confocal resolution

To determine the confocal resolution of GFPs and RFPs used herein, we employed green and red fluorescent (200nm) carboxylate-modified microspheres (Invitrogen) diluted in dH_2O to a final concentration of 10^6, as outlined in the protocol in [366]. A 20µl drop of the diluted stock solution was pipetted onto a clean 1.5 glass coverslip and allowed to dry overnight. LSCM imaging of microspheres was performed the following day with the same excitation wavelength ($\lambda_{exc} = 488$nm for a 525nm emission, and $\lambda_{exc} =$ 561nm for 595nm emission) and sampling rate (0.069 x 0.069 x 0.18µm) used during experiments. Here, we based our theoretical confocal resolution on the Rayleigh criterion [366, 367]:

$$\text{Lateral resolution } = \frac{0.51\,\lambda_{exc}}{NA} \quad [4.S1]$$

$$\text{Axial resolution } = \frac{0.88\,\lambda_{exc}}{\left(n-\sqrt{n^2-NA^2}\right)} \quad [4.S2]$$

Based on eqn. (S.1, S.2), (using n=1.33 for water) the theoretical resolution for GFP was calculated to be 207nm in x and y, and 567nm in z. Theoretical resolution for RFP was calculated as 238nm in x and y, and 652nm in z. Using an ImageJ plugin, MetroloJ (the plugin and manual can be found: //imagejdocu.tudor.lu/doku.php?id=plugin:analysis:metroloj), we were able to generate a report of the miscrosphere PSF data. Fits of microsphere intensity to a Gaussian equation were used to determine the FWHM. This produced a mean resolution of: 0.248µm in x, 0.281µm in y, and 0.701µm in z for GFP microscpheres (n=10). Mean confocal resolution was lower for RFP microspheres (n=10): 0.305µm in x, 0.351µm in y, and 1.043µm in z.

4.7.1.7 Atomic force microscopy methods

A NanoWizard II (JPK Instruments) AFM was mounted on the LSCM to perform integrated AFM-LSCM experiments. All experiments were performed at 37°C, using a temperature-controlled AFM stage (JPK).The thermal fluctuation method of Hutter and Bechhoefer was used to calibrate AFM tips [330]. The sensitivity and stiffness was measured prior to experiments. All AFM cantilevers had an experimentally determined stiffness, k = 0.08 ± 0.01N/m (PNP-TR triangular, Nanoworld). Young's modulus (E) was determined by recording force-curves measured over the center of cell nuclei. A shallow region (200nm) of indentation was fit to the Hertz model for a conical tip [331] to measure local E of the cell (PUNIAS Software) [332].

4.7.1.8 Deformation and recovery experiments

First, LSCM volume images were recorded prior to and following deformation experiments to ensure cells recovered their initial shape (Fig. 4.S2). Next, tracking of membrane-cortex deformation and recovery involved capturing images in a single XY-plane set approximately 2µm below the apical region of the membrane (as determined by LSCM volume images) (Fig. 4.1, main text). To capture the initial deformation, images were recorded prior to (~5s) and during 20s of constant force application. The AFM cantilever was set to approach the sample rapidly (10µm/s), with forces of

either 10 or 20nN applied above the approximate center of cell nuclei (visualized by the nuclear dye Hoescht).

A similar method was used to examine the dynamics of cell shape recovery. A series of constant force (10nN) experiments were performed for varied durations: 15s, 1min, or 10min. Again, time-lapse imaging was performed in a single XY-plane during the retraction phase of the tip (following the specified load duration). For long durations (1 and 10min), LSCM volume images were acquired once every minute. For instance, a 10nN force was applied at the approximate center of the cell for 10min, during which 11 LSCM volume images were taken corresponding to t=0 (before indentation), t=1 (indentation after 1min) and so on, up to t=10 minutes of applied force. Following the constant applied force, the focal plane is set to a plane where indentation by the AFM tip is seen (~2μm below the fluorescent apical membrane). As the AFM tip is retracted, continuous XY-plane time-lapse images are acquired to capture the recovery of the membrane/cortex (~30s). Following this, a final LSCM volume image was captured (t≈12 min).

4.7.1.9 Statistics.

Statistics were calculated using two sample t-tests. Where indicated, one-way ANOVA analyses with post-tests including Levene's test for equal variance, and a means comparison test using the Bonferroni and Tukey methods were employed. Unless otherwise noted, all significance indicates $P < 0.05$.

4.7.1.10 Image analysis of deformation/recovery profiles.

ImageJ (open-source image processing software, http://rsbweb.nih.gov/ij/) was used for all analysis. A square region of interest (ROI) ($0.69\mu m^2$) was chosen; one containing the deformed cell membrane and cortex, as demonstrated by changes in GFP and RFP intensity over time. Brightness and contrast settings were adjusted in order to optimize images of live and fixed cells. No other image manipulations were performed. In order to examine the deformation dynamics of the membrane and cortex, time-lapse images were analyzed by capturing mean intensity over time within the ROI (Fig. 4.1 C, main text). These intensity profiles were normalized for initial deformation experiments (Fig. 4.1 B) by averaging initial intensity values observed within the ROI 2 seconds prior to unloading. A value of 1 represents the maximum intensity immediately prior to deformation (t=0), and 0 representing the minimum intensity after the AFM tip is extended (intensity was not 0 in actuality due to noise in resonant images scans). For recovery profiles, 0 is again representative of the minimum intensity, which occurs during the deformation while the AFM tip is approached (now, t=0). Following tip retraction, the intensity within the ROI increases as the membrane/cortex recover shape (with maximum intensity normalized to 1).

4.7.1.11 Non-linear regression of intensity profiles during deformation

We chose to fit the deformation intensity profiles to a first-order decay, based on Akaike's (AIC), and Bayesian (BIC) information criteria (Origin v.9.1.) [368]. Non-linear regression of intensity-time profiles allowed us to compare time constants (τ (s)) of the membrane and cortex using equation [4.S3].

$$I(t) = I_o + Ae^{-t/\tau} \quad [4.S3]$$

Using normalized intensity data, the offset, I_o, was set to zero, and the amplitude, A, was set to 1. The only free fit parameter was τ, a characteristic time constant.

4.7.1.12 Measuring cellular strain

Approximate axial strain measurements were made on cells during long (1 and 10min) deformation experiments, as we previously reported [348]. Axial strain was measured in the plane of loading, as:

$$\varepsilon = d/h_o \quad [4.S4]$$

where d is the deformation and h_o is initial cell height. An average of two measurements were used as strain was measured in both orthogonal XZ and YZ projections of LSCM volumes, using ImageJ.

4.7.1.13 Derivation of viscoelastic model of relaxation/recovery

Here, we demonstrate a simple derivation of the wave equation, as used to model the relaxation (recovery) behaviour of the membrane/cortex. First, consider a series of masses (m) connected by springs (k) separated by a horizontal distance l (Fig. 4.4 A, main text). In the deformed state (when the tip is approached), these masses are displaced from equilibrium, where at a time t, the i^{th} mass is displaced by a height u_i^t. This mass is acted upon by the spring force (F_s) of its neighbours, and so is accelerating with inertial force:

$$F_t = m\ddot{u}_i^t$$

Where the net spring force due to the i^{th} mass' neighbours is:

$$F_s = F_{S,i+1} - F_{S,i-1} = k\left[u_{i+1}^t - u_i^t\right] - k\left[u_i^t - u_{i-1}^t\right]$$

Setting the total inertial force (F_t) to the Hookian spring force (F_s):

$$m\ddot{u}_i^t = k\left[u_{i+1}^t - u_i^t\right] - k\left[u_i^t - u_{i-1}^t\right]$$
$$\frac{\partial^2 u_i^t}{\partial t^2} = \frac{k}{m}\left[u_{i+1}^t - 2u_i^t + u_{i-1}^t\right]$$

Treating this surface as a continuum, and in the limit of a large number of spring elements (i.e. $K = k/N\,, L = Nl, M = Nm, as\ N \to \infty, and\ l \to 0$) we then have:

$$\frac{\partial^2 u_i^t}{\partial t^2} - c^2 \frac{\partial^2 u_i^t}{\partial x^2} = 0 \quad [4.S5]$$

Where the speed of wave propagation is defined as:

$$c^2 \equiv KL^2/M$$

And employing the d'Alembert operator:

$$\square^2 = \frac{\partial^2}{\partial t^2} - c^2 \bigtriangledown^2$$
$$\square^2 u = 0 \quad [4.S6]$$

This represents a continuum model of an elastic membrane. Any additional forces can be superimposed onto each element causing the simple wave equation [4.S6] to generalize into a form of the Telegrapher's equation. Here, we employed forces from a single elastic (E) and damping (γ) element in parallel acting on each element. Since the elastic and viscous contributions act in parallel, this amounts to a Kelvin-Voigt viscoelastic model and the net force on each element of the surface is then $F_{KV} = F_E + F_V$. The resulting Telegrapher's equation is

$$\begin{aligned}
F_T &= F_S + F_{KV} \\
F_T &= F_S + F_E + F_V \\
m\frac{\partial^2 u_i^t}{\partial t^2} &= k\left[u_{i+1}^t - 2u_i^t + u_{i-1}^t\right] - Eu_i^t - \gamma\frac{\partial u_i^t}{\partial t} \\
0 &= \frac{\partial^2 u_i^t}{\partial t^2} - \frac{kh^2}{m}\bigtriangledown^2 u_i^t + \frac{E}{m}u_i^t + \frac{\gamma}{m}\frac{\partial u_i^t}{\partial t} \\
0 &= \square^2 u_i^t + \frac{E}{m}u_i^t + \frac{\gamma}{m}\frac{\partial u_i^t}{\partial t} \\
0 &= \left(\frac{\partial^2 u_i^t}{\partial t^2} - c^2\bigtriangledown^2 u_i^t\right) + \frac{E}{m}u_i^t + \frac{\gamma}{m}\frac{\partial u_i^t}{\partial t} \\
0 &\approx -c^2\bigtriangledown^2 u_i^t + \tfrac{E}{m}u_i^t + \tfrac{\gamma}{m}\tfrac{\partial u_i^t}{\partial t}
\end{aligned} \qquad [4.S7]$$

In this form, the above equation can be described as a surface connected to equilibrium by elements of the Kelvin-Voigt model. Comparing to equation [4.S2] in the main text, we see that $k = E/mc^2$ and $\mu = \gamma/mc^2$. In the final form of equation [4.S7] we neglect the inertial term by assuming that we are in the over-damped regime and will not observe wave-like dynamics on the membrane surface. We expect a monotonic return to equilibrium, which is reasonable considering that the cell is surrounded by fluid and is largely composed of cytoplasm.

4.7.1.14 Numerical implementation of the viscoelastic model calculation

Equation 7 does not have an analytic solution and so is solved numerically. The AFM tip is modelled as a cylindrically symmetric cone defined by a solid angle $\Omega = 35°$ and a maximum indentation depth h. An implicit Euler method was found to be stable and employed to determine the displacement u_i^t at all radial points and times. As is common numerical practice, non-dimensionalized variables were used in this process. The characteristic length scale was identified to be the maximum displacement h, the characteristic time is μh^2. In the following, all variables are properly non-dimensionalized by these scales. In the implicit Euler method the spatial derivatives are approximated to be:

$$\frac{\partial u_i}{\partial r} \approx \frac{u_{i+1} - u_{i-1}}{2\Delta r}$$

$$\frac{\partial^2 u_i}{\partial r^2} \approx \frac{u_{i+1} - 2u_i + u_{i-1}}{(\Delta r)^2}$$

and are all performed at the future time $t + 1$. Therefore, [7] is discretized into

$$u_i^t = \left[\frac{a}{r_i} - b\right]u_{i-1}^{t+1} + [1 + c + 2b]u_i^{t+1} - \left[\frac{a}{r_i} + b\right]u_{i+1}^{t+1} \qquad [4.S8]$$

where $a = \Delta t/(2\Delta r)$, b= $\Delta t/(\Delta r)^2$ and $c = k\Delta t$. Equation [4.S8] holds for all discretization nodes except at the boundaries. The assumed cylindrical symmetry demands that $u_{i-1}^{t+1} = u_i^{t+1}$ at $i = 0$ (i.e. a von Neumann boundary condition) and we assume a Dirichlet boundary condition of $u_i^{t+1} = u_i^t$ at the last node $i = N$. All of this can be written concisely in the form $\vec{u}^t = \boldsymbol{A}\vec{u}^{t+1}$, where $\vec{u}$ is the list of displacements at each node and $\boldsymbol{A}$ is the invertable tridiagonal matrix defined by inspection of [4.S8]. Because $\boldsymbol{A}$ can be numerically inverted using standard algorithms, the Euler method can calculate all the future displacements from the current displacements via $\vec{u}^{t+1} = \boldsymbol{A}^{-1}\vec{u}^t$.

Measurements of intensity profiles do not directly measure displacement height; rather they infer changes in height from the measured intensity at the focal plane, which lies at a depth $f \approx 2$µm below the equilibrium surface $u = 0$ in the ROI. In order to estimate the intensity, we assume that fluorescence occurs homogeneously and constantly on the apical membrane. Since the emitted photons must transverse the dispersive intracellular medium (along with the movement of the membrane/cortex) to arrive at the focal plane, we approximated the intensity at each point by a Gaussian dispersion about the focal plane. In this way, the total intensity is the integral of the intensity at each point on the focal plane in the ROI, where the intensity at each point is the integral of the Gaussian dispersion with a variance σ^2 from each point on the membrane as given by the displacement eqn. [4.S8]. This is done numerically, with cylindrical symmetry and with a numerical cut-off of $r_{cut} = 100h$, used in integrating the intensity at each point in the ROI. In this way, the experimental intensity as a function of time can be predicted.

Experimental parameters, such as the maximum tip depth h, the focal plane f, and the dispersion σ^2 (an optical property that may vary substantially between fluorescent protein expression levels), all vary between experiments. Therefore, these parameters must be prescribed using best estimates, or as fitting parameters along with the viscoelastic properties of interest, k and μ. In our fitting procedure, the average value $h = 5$µm (~maximum deformation range, see Table 4.S3), $\sigma = 0.2$µm (approximate theoretical x-y resolution of GFP) and an ROI radius of 0.469µm are used in each fit. The number of radial nodes is set to $N = 500$, the radial step size is $\Delta r = 0.06$ µm and the time step used is $\Delta t = 100$µs. The position of the focal plane f, the elastic constant k and viscous coefficient μ are fit using an iterative least-squares method. In each iteration, the focal plane is first updated by comparing the χ^2 value between the theoretical curve and the experimental data. If increasing or decreasing the value is a better fit, then f is updated, otherwise the step size is halved. This procedure is repeated for k and then for μ. This routine is then repeated until the step sizes for f, k and μ are all less than the prescribed tolerance (tolerance $\varepsilon = 10^{-5}$ is sufficient).

The numerical actualization of the iterative least-squares fitting procedure and the implicit Euler method for solving [4.S7] was programmed using C. Calculations were performed on Scinet, through Compute/Calcul Canada. Analysis was launched using simple shell scripts and individual jobs generally ran for < 1 hour. The viscoelastic model employed here showed the most success fitting slow recovery, but was less successful when dealing with extremely fast recovery instances. This may indicate that additional mechanisms must be taken into account in fast recovery situations

but not in slow or that different combination of viscous and elastic elements are needed to adequately model cell-shape recovery.

4.7.2 Supplementary Tables

Table 4.S1 Load magnitude and duration do not affect fast recovery of HeLa cells.

			Membrane		Cortex	
Load	Duration	N	$\kappa_1(s^{-1})$	$\kappa_2(s^{-1})$	$\kappa_1(s^{-1})$	$\kappa_2(s^{-1})$
10nN	15s	8	2.66 ± 1.04	0.08 ± 0.06	2.84 ± 0.60	0.05 ± 0.01
	1min	14	2.35 ± 1.04	0.07 ± 0.06	2.41 ± 1.00	0.07 ± 0.04
	10min	11	2.52 ± 1.22	0.08 ± 0.12	2.21 ± 1.13	0.05 ± 0.04
20nN	15s	6	2.41 ± 0.94	0.05 ± 0.05	1.53 ± 0.73	0.03 ± 0.01
	1min	13	2.91 ± 0.54	0.28 ± 0.43	2.83 ± 0.64	0.09 ± 0.05
	10min	11	3.04 ± 0.96	0.15 ± 0.17	2.36 ± 1.09	0.07 ± 0.07

Mean characteristic recovery decay constants following different durations and magnitudes of loading. Decay constants remain unchanged following short (15s) and long (1 and 10min) durations and different magnitudes of loading (10 and 20nN), as determined by one-way ANOVA analysis with both Tukey and Bonferroni post-tests. Levene's test determined that the variance, however, was significantly different between populations ($P < 0.05$). Values shown are means ± SD.

Table 4.S2 Cytoskeleton and osmotic conditions effect recovery.

		Membrane		Cortex	
	N	$\kappa_1(s^{-1})$	$\kappa_2(s^{-1})$	$\kappa_1(s^{-1})$	$\kappa_2(s^{-1})$
Untreated	14	2.35 ± 1.04	0.07 ± 0.06	2.41 ± 1.00	0.07 ± 0.04
Untreated (top)	9	1.86 ± 1.01	0.05 ± 0.03	0.64 ± 0.36*	0.06 ± 0.03
CytD	12	1.24 ± 1.10*	0.05 ± 0.04	0.98 ± 1.08*	0.05 ± 0.02
Y-27632	13	1.22 ± 1.10*	0.10 ± 0.11	0.85 ± 0.82*	0.07 ± 0.06
Noco	11	1.52 ± 1.52	0.04 ± 0.03	1.50 ± 1.48	0.04 ± 0.01
300 mM Sucrose	7	0.18 ± 0.08*	0.02 ± 0.02**	0.16 ± 0.06*	0.08 ± 0.10
30% dH_2O	12	1.58 ± 1.19*	0.10 ± 0.23	1.66 ± 1.22*	0.07 ± 0.11

Characteristic recovery decay constants of the membrane and cortex are shown following a 1min 10nN load. Top refers to measurements made at the most apical region of the cell wherein the deformation was still visible. Values shown are means ± SD. * indicates $P < 0.05$, and ** indicates $P < 0.08$.

Table 4.S3 Cytoskeleton and osmotic conditions effect cellular strain.

	N	h_o, height (μm)	d, deformation (μm)	ε, axial strain (%)
Untreated (10nN)	20	7.62 ± 1.24	3.73 ± 1.35	50 ± 19
Untreated (20nN)	20	8.07 ± 2.35	5.04 ± 1.23*	66 ± 19*
CytD	18	9.38 ± 1.41*	6.45 ± 1.18*	69 ± 13*
Y-27632	20	9.70 ± 1.85*	6.36 ± 1.21*	66 ± 09*
Noco	11	7.09 ± 1.42	4.13 ± 1.24	58 ± 12
300 mM Sucrose	9	4.41 ± 2.26*	1.46 ± 0.89*	32 ± 12*
30% dH_2O	17	10.08 ± 1.62*	3.61 ± 1.26	37 ± 13*

Direct measurement of initial height (h_o), deformation (d), and axial strain of cells following 1min of 10nN force (except where indicated). Values shown are means ± SD. * Indicates significance ($P < 0.05$).

Table 4.S4 Mechanical characterization of the cell.

	N	k (μm^{-2})	η ($s \cdot \mu m^{-2}$)	κ = k/η (^{-}s)
Untreated (10nN)	8	125.01 ± 64.34	68.08 ± 84.94	7.17 ± 6.64
Untreated (20nN)	12	120.49 ± 74.55	62.33 ± 66.09	5.32 ± 6.56
CytD	8	58.98 ± 135.08	141.80 ± 118.51	*2.77 ± 7.60
Y-27632	17	3.89 ± 3.94	71.82 ± 49.27	*0.06 ± 0.03
Noco	4	203.19 ± 341.74	703.79 ± 547.43	8.03 ± 15.98
30% dH_2O	13	132.22 ± 64.34	143.98 ± 171.71	5.61 ± 9.48

Intensity (recovery) profiles were modelled by eqn. [4.2]. Deformation of the cell is modelled as an infinite surface bound to a viscoelastic material that recovers an equilibrium state via spring and viscous components. Here, the parameters listed correspond to both untreated and treated HeLa cells. Although χ^2 values were reduced, large variations in absolute parameter values resulted, a ratio of k to η, a decay constant $\kappa(^{-}s)$, was used to compare cells. * Indicates significant difference with untreated HeLa (10nN) ($P < 0.05$, using t-test). Values shown are means ± SD.

Table 4.S5 Recovery decay constants of various epithelial cells.

		Membrane		Cortex	
	N	$\kappa_1(s^{-1})$	$\kappa_2(s^{-1})$	$\kappa_1(s^{-1})$	$\kappa_2(s^{-1})$
MDCK	21	1.73 ± 1.10	0.11 ± 0.09	1.11 ± 0.82	0.13 ± 0.09
HEK	16	2.51 ± 0.94	0.09 ± 0.06	1.17 ± 1.08	0.09 ± 0.03
CHO	4	3.52 ± 0.17	0.21 ± 0.13	1.72 ± 0.59	0.07 ± 0.03

Intensity profiles of the membrane and cortex following a 1min 10nN load were fit to a box-Lucas exponential function [4.1] in order to derive characteristic recovery decay constants (κ).Values shown are means ± SD.

4.7.3 Supplementary Results

4.7.3.1 Deformation dynamics

Normalized plots of intensity over time are shown for the first 20s of deformation (Fig. 4.S1). These intensity plots revealed a sharp decrease in fluorescence intensity, corresponding with initial contact and increasing force applied by the AFM tip to the cell. Fitting multiple curves to eqn. [4.S1] resulted in no difference in means between membrane and cortex deformation time constants. However, since the variances were significantly different for these populations ($P = 0.04$), we also compared concatenated fits (Fig. 4.S1 *inset*). An F-test again demonstrated no significant difference ($P > 0.05$, and F=0.70) between the membrane (τ = 1.78 ± 0.04 s) and cortex (τ = 1.04 ± 0.03 s) characteristic time constants (here, reported for 10nN loads). Both linked components deformed rapidly in response to load. Since the cantilever approach speed was rapid (10μm/s), varying the load magnitude (from 10 to 20nN) did not significantly alter the observed response of the membrane, or the cortex ($P > 0.05$). We previously observed that the majority of deformation occurs immediately following 10min of a locally applied load, and that HeLa cells (~90%) recovered their initial shape in minutes thereafter [348]. Together, these results demonstrate that the cell

membrane and cortex provide little resistance to large magnitude, rapidly applied local forces, initiating the examination of the recovery dynamics following load cessation.

4.7.3.2 Cellular strain depends on the cytoskeleton and osmotic conditions

As with untreated HeLa, we measured approximate strains of treated cells exposed to 1min durations of a 10nN load (as in Fig. 4.S2). Despite variations in initial cell height (h_o), the deformation (d) of cells exposed to Y-27632 and CytD were significantly increased in comparison to untreated cells (Table 4.S3). Cells lacking an intact actin cytoskeleton (Y-27632 and CytD) experienced significantly larger strains (66 ± 9.4% and 69 ± 12%, respectively) than untreated cells (50 ± 19%), whereas cells treated with Noco (58 ± 12%) were not significantly altered. The measured strains confirm our earlier findings [369], that the actin cytoskeleton, not microtubules, is necessary for resisting external perturbations. Moreover, the mean strain of cells treated by hyperosmotic stress (sucrose) was significantly reduced (32 ± 12%) in comparison to untreated cells (50 ± 19%). Hypo-osmotic stress also resulted in a reduced strain (37 ± 13%), due to the increased initial cell height (deformation depth d was not altered, see Table 4.S3).

4.7.3.3 Limiting contractility and osmolarity

In order to inhibit increased contractility brought about by Noco treatment, we employed Y-27632 to selectively inhibit ROCK, as was shown in ref [356]. Cells were pre-treated with Y-27632 for 15min followed by subsequent treatment with Noco for 15min in an incubator at 37°C and 5% CO_2. Immediately following incubation, we performed AFM-LSCM deformation experiments. Recovery, following 1min of a 10nN load, was drastically reduced for Y-27632+Noco treated cells, with only 20% fast-recovery observed from time-lapse images (n=5). Recovery was difficult to quantify for these treated cells since the deformation was drastically reduced and significant variability was observed in the apical regions of the membrane. Decay constants (κ_1 = 0.31 ± 0.39 s^{-1}, and κ_2 = 6.18 ± 13.59 s^{-1}, n=5) demonstrated slow recovery of Y-27632+Noco treated cells. Although less than 2% strain remained (on average) following 1min after load removal, the mean strain (measured as in Fig. 4.S2) was significantly reduced for Y-27632+Noco treated cells (15 ± 10%), in comparison to untreated HeLa (50 ± 19%). Immunofluorescent images revealed that actin fibres were present, although microtubules were no longer co-localized and were completely depolymerized (Fig. 4.S6).

In an attempt to regain the fast recovery dynamics observed with untreated and noco-treated cells, we treated the same cells (Y-27632+Noco treated) by incubating with 30% dH_2O for 10min prior to further experiments. The addition of 30% dH_2O did not affect the appearance of actin fibres or microtubules (Fig. 4.S6). The cell volume was significantly (P = 0.022) increased, denoted by increased height (13.08 ± 1.70µm) in comparison to osmotically neutral Y-27632+Noco treated cells 9.68 ± 2.09µm. Approximate axial strain was also significantly (P = 0.028) increased for hypo-osmotic cells (29 ± 5%). Importantly, 80% of cells recovered in < 1s following hypo-osmotic shock, which was reflected in recovery decay constants (κ_1= 1.87 ± 1.38s^{-1}, and κ_2= 0.29 ± 0.46s^{-1}, n=5).

4.7.3.4 Effect of cholesterol depletion on cell shape recovery.

We have shown that two membrane bound fluorescent markers: wheat germ agglutinin and a lipophilic tracer, DiD, led to an increase in membrane-cortical stiffness and a decrease in the

membrane's ability to resist deformation [344]. Here, rather than inserting a membrane marker, we employed MβCD to effectively deplete cholesterol levels of the plasma membrane. Treatment with MβCD has previously been shown to decrease cholesterol levels significantly (upwards of 50% [363]). Our aim was to examine cholesterol depletion on the deformability and the recovery response of HeLa cells. First, AFM force-indentation curves were measured on cells treated with (10mM) MβCD, as well as untreated HeLa cells. Force curves demonstrated significant cellular stiffening of MβCD treated cells (E = 4.4 ± 0.8kPa) in comparison to untreated HeLa (E = 3.4 ± 1.3kPa). Cholesterol depletion using MβCD has been previously shown to stiffen cell membranes of aortic endothelial cells [363]. Since the solubility of MβCD is low, we performed stiffness measurements on two controls: cells treated with MβCD in serum-free media, as well as cells treated with the addition of the same concentration of dH_2O to normal DMEM. Both controls resulted in a stiffness increase in comparison to untreated cells (Fig. 4.S7), and so increased osmotic pressure likely contributes to the increased stiffness. Measurement of recovery dynamics following 10min of a 10nN load demonstrated that recovery times for MβCD-treated cells occurred near instantaneously (< 1s) in all cases (n=10 cells). Fits of intensity profiles revealed no significant difference ($P > 0.05$) between characteristic recovery decay constants of cells treated with MβCD (κ_1= 2.42 ± 0.58s^{-1}, and κ_2= 0.03 ± 0.01s^{-1}, n=4) and untreated HeLa (κ_1= 2.52 ± 1.22s^{-1}, and κ_2= 0.08 ± 0.12s^{-1}, n=11). Note that only a number of datasets were successfully fit (as reflected in the n values quoted above), since fast recovery resulted in a discontinuity in the intensity profiles. Time-lapse images of the recovery revealed a contraction as cells recovered the deformation, followed by a gradual expansion. We postulated that this expansion was due to intracellular flow of cytosol, as previously shown [181]. However, there was no significant change in cell height (8.8 ± 1.8μm) following treatment with MβCD ($P < 0.01$), in comparison to untreated cells (10.3 ± 2.9μm). By directly measuring the deformation depth of the cells following 10nN of load, a significant decrease ($P < 0.01$, using t-test) in time-dependent strain was observed for MβCD-treated cells (ε = 40 ± 11%, n=10), in comparison to untreated HeLa (ε = 50 ± 18%, n=20), corresponding with their increased stiffness.

4.7.4 Supplementary Figures

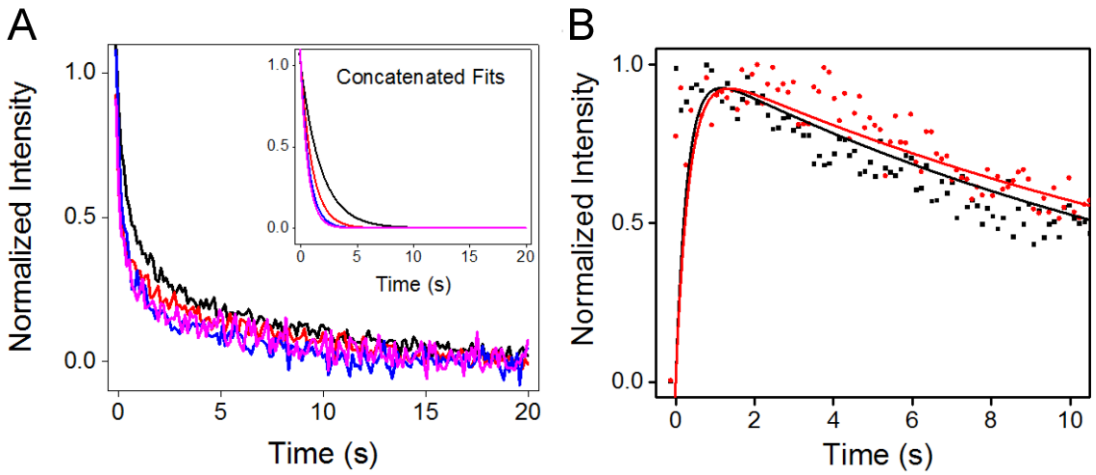

Figure 4.S1 Cell membrane and cortex deform and recover simultaneously.
A) Normalized intensity versus time profiles are shown for the initial 20s of membrane (n=13, black – 10nN, blue – 20nN) and cortex (n=7, red – 10nN, magenta – 20nN) deformations following approach of the AFM tip (t=0). *Inset* shows concatenated fits of data fit to an exponential decay. B) Fits of normalized intensity profiles are shown overlaying raw data for an untreated HeLa cell recovering following a 10nN load applied for 1min. No significant differences appeared between characteristic time constants or decay rates or fits between membrane and cortex or load magnitudes ($P > 0.05$, using paired t-tests and F-test for fits comparison).

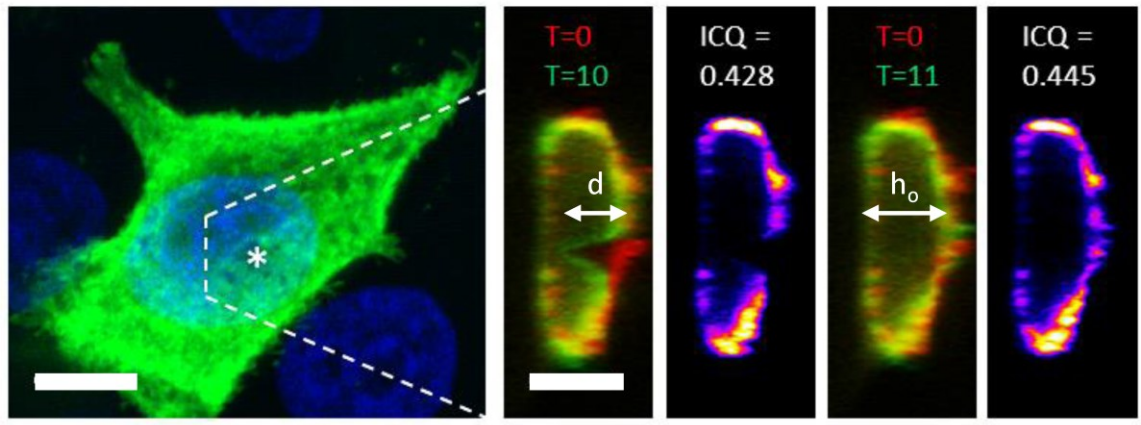

Figure 4.S2 HeLa cells recover from large deformations within minutes.
Shown is an LSCM volume projection image of a typical HeLa cell deformed by a 10nN constant force applied for 10min. Red (t=0) / green (t=10min) overlays of orthogonal projections demonstrate the deformation (d) in comparison to the initial cell height (h_o). The cell shown recovered initial morphology within 1min, as shown by the red (t=0) /green (t=11min) overlay after load cessation. Adjacent plots of intensity correlation analysis demonstrate positively correlated intensities (lighter colours) and increased intensity correlation quotient (ICQ) values following tip retraction. See reference [273] for details on ICA. Scale bars are10µm.

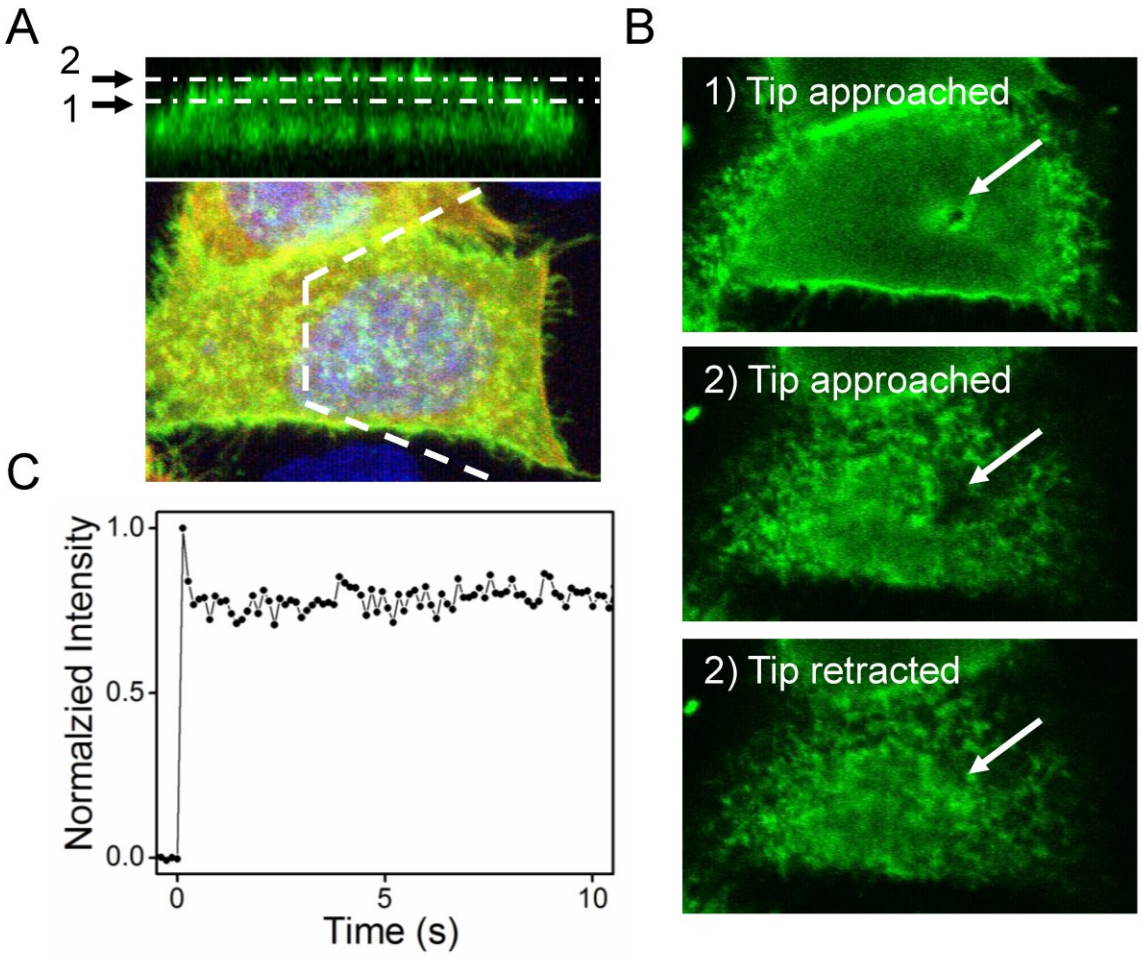

Figure 4.S3 Imaging plane does not affect recovery profiles.
A) LSCM image of a HeLa cell with XZ orthogonal projection demonstrating a typical imaging plane (1), and imaging in the most apical region (2). B) XY-images during tip approach demonstrating differences in visible deformations corresponding to (A). Arrow indicates deformed regions. Scale bars are 10μm. C) Intensity profile from imaging plane (2) following recovery of cell in (A) after 10nN load removal. Sharp intensity peak demonstrates near-instantaneous recovery.

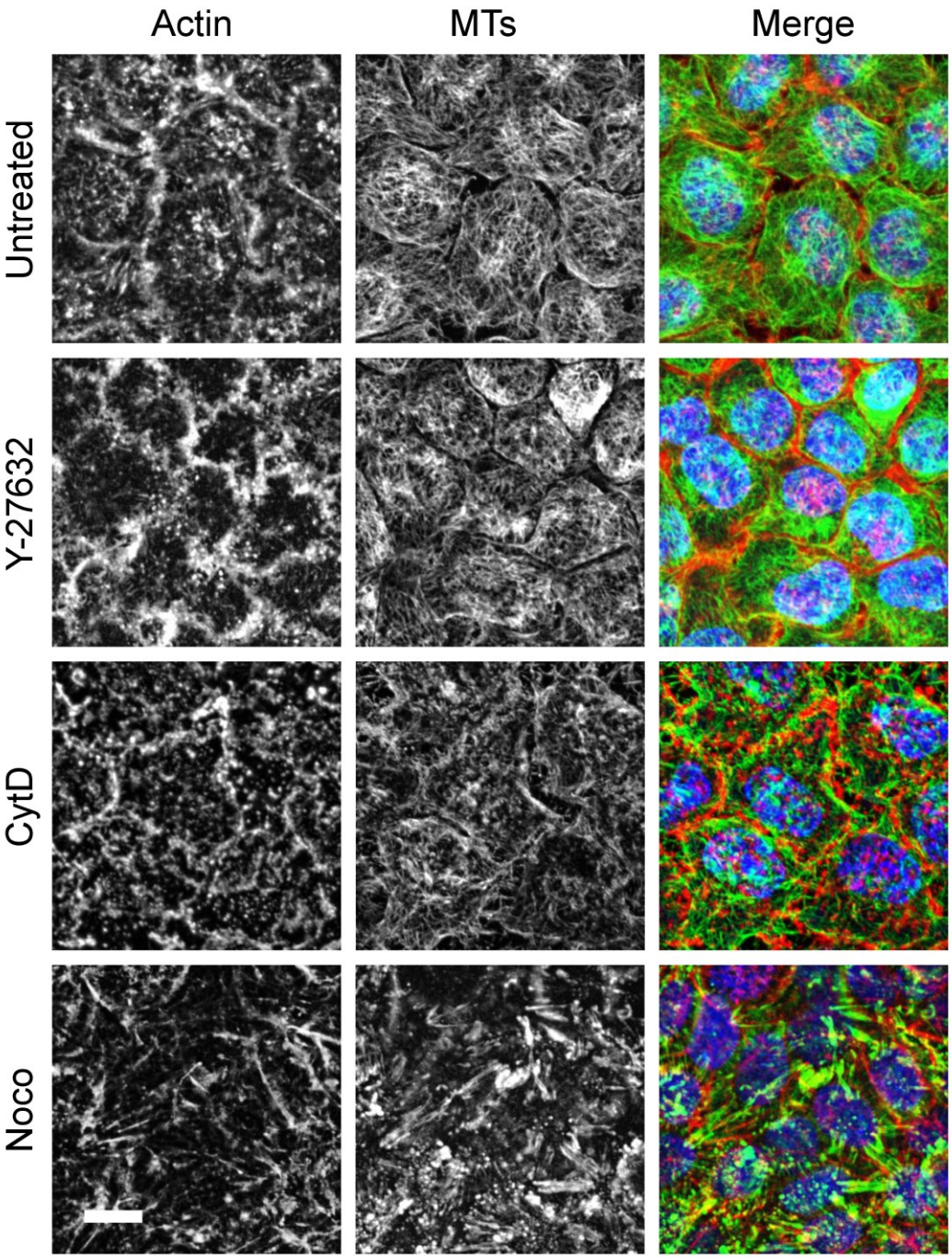

Figure 4.S4 Cytoskeletal disruption by inhibitors.
Immunofluorescent images of fixed cells demonstrate differences in cytoskeletal morphologies following treatment with the indicated cytoskeleton inhibitors. Scale bar is 10µm.

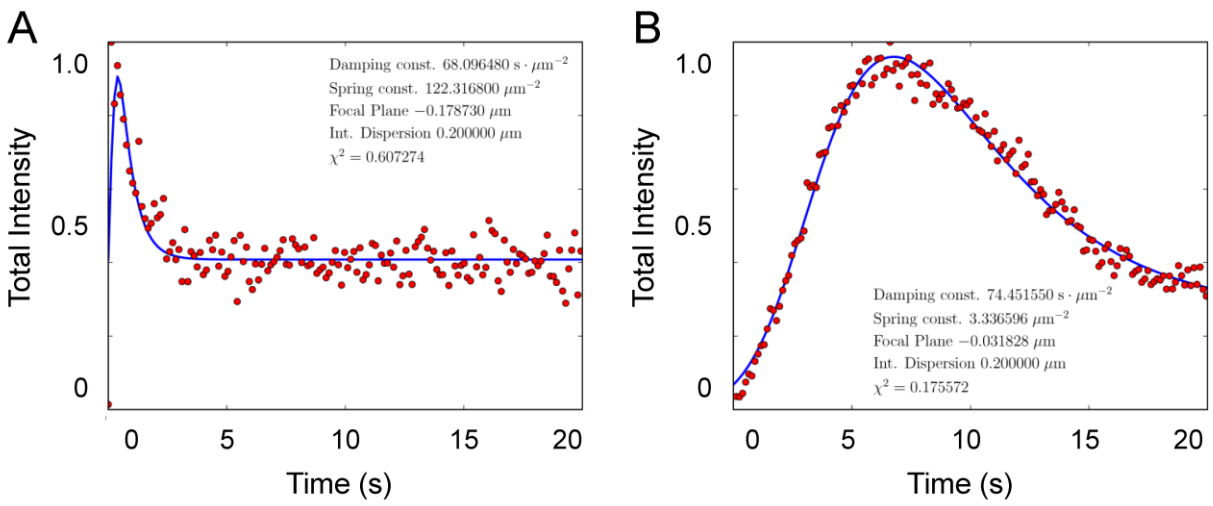

Figure 4.S5 Simulation of recovery using viscoelastic model.
Shown are example outputs from the simulation of a HeLa cell undergoing A), a fast recovery, and B), a slow recovery following 1min of 10nN. Fits are shown in blue overlay the normalized intensity data (red).

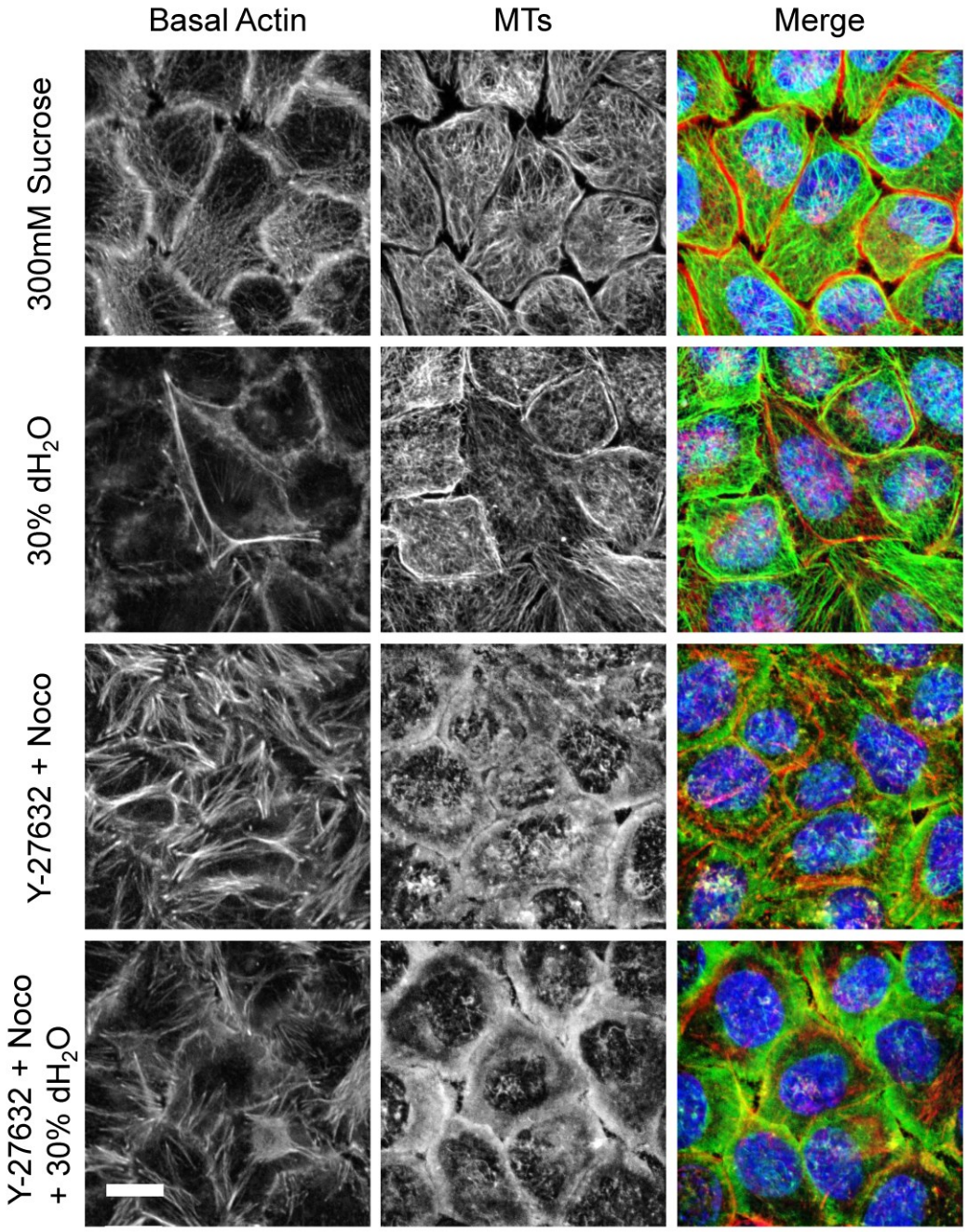

Figure 4.S6 Effect of osmolarity and Y-27632+Noco treatment on the cytoskeleton.
Immunofluorescent images of fixed cells demonstrate differences in cytoskeletal morphologies following indicated treatments. Scale bar is 10µm.

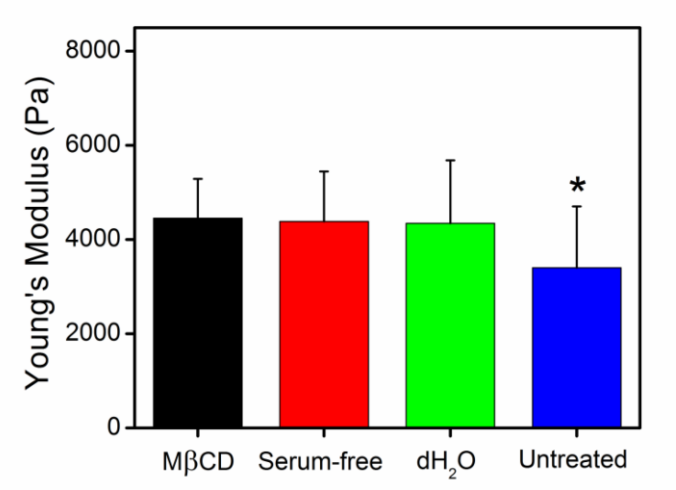

Figure 4.S7 Effect of cholesterol depletion on HeLa cells.
A) Plots of Young's modulus measurements from AFM force-curves. Shown are mean ± SD. *Indicates significance of untreated cells in comparison to all other conditions ($P < 0.05$, with paired t-tests).

Chapter 5| *Manuscript*

Extracellular forces cause the nucleus to deform in a highly controlled and anisotropic manner

Kristina Haase[a], Joan K. L. Macadangdang[a], Charles M. Cuerrier[a], Sebastian Hadjiantoniou[a,b], James L. Harden[a,c], Ilona S. Skerjanc[d], and Andrew E. Pelling[a,b,e]

[a]*Centre for Interdisciplinary NanoPhysics, Department of Physics, MacDonald Hall, 150 Louis Pasteur*
[b]*Department of Biology, Gendron Hall, 30 Marie Curie*
[c]*Ottawa Institute of Systems Biology, Roger Guindon Hall, 451 Smyth Road*
[d]*Department of Biochemistry, Microbiology & Immunology, Roger Guindon Hall, 451 Smyth Road*
[e]*Institute for Science Society and Policy, Simard Hall, 60 University*
University of Ottawa, Ottawa, ON, K1N 6N5, Canada.

Submitted Aug. 1st 2014 to *PNAS*

- I, Kristina Haase, contributed towards the majority of the work including: cell culture, atomic force microscopy, confocal microscopy, data and statistical analysis. I re-wrote the manuscript following a change in the direction and scope of the project and completed subsequent revisions.
- Joan Karla Macadangdang, as a Master's student in the Pelling lab, performed the preliminary experiments and wrote the first draft of the original manuscript.
- Dr. Charles M. Cuerrier, a post-Doc in the Pelling lab, cultured primary cells used in the experiments.
- Sebastian Hidjiantoniou, a Ph.D. candidate, cultured embryonic stem cells for experiments.
- Dr. Ilona S. Skerjanc provided the stem cells and culture training.
- Dr. James L. Harden provided advice on data analysis and assisted in editing of the manuscript.
- The format of the manuscript has been modified for formatting purposes.

Motivation |

Physical forces arising from the extracellular environment are transmitted to the nucleus via the cytoskeleton. It has been proposed that these forces directly affect gene regulation; however this process is poorly understood, stemming from an incomplete picture of force transmission to the nucleus. Recently, anisotropic deformations of the nucleus have been observed in response to mechanical force, in contrast to the often employed assumption of nuclear isotropy. Considering the importance of nuclear deformations in potential gene regulation processes it is imperative to characterize nuclear strains.

Hypothesis & objectives |

Here, we consider whether anisotropic deformations of cell nuclei result from a direct local compressive force. We characterize the response of nuclei from a variety of cells and demonstrate that anisotropic deformations are prevalent, with nuclei predominantly deforming along a preferred minor axis. We hypothesize that this anisotropy is regulated by the cytoskeleton as well as nuclear structural components, which we examine herein.

5 | Extracellular forces cause the nucleus to deform in a highly controlled and anisotropic manner

5.1 Abstract

Mechanical forces in the biological microenvironment impact many critical cellular processes. These forces may impact gene regulation and signalling due to the direct deformation of the nucleus and genome. Therefore, the physical properties of the nucleus inside living cells, and its response to extra-cellular forces, must be characterized. Previous studies have typically described nuclei as isotropic materials; however recent evidence suggests that this may not be the case. Here, we demonstrate that extra-cellular forces delivered with an atomic force microscope cause cell nuclei to rapidly deform (within seconds) in a controlled and anisotropic fashion. Notably, elliptical nuclei of fibroblast cells deformed significantly more along the short axis, rather than along the long axis. The cytoskeleton regulates the deformation magnitude and the degree of anisotropy. However, studies on isolated nuclei suggest the presence of intrinsic anisotropic material properties. Disruption of chromatin organization severely impaired nuclear deformation in a majority of cells. In cases where deformation was visible, it occurred in a more isotropic fashion but with a significant degree of variability. Conversely, changes in lamin-A expression had a clear influence on the mechanical properties of the cell but had no clear role in regulating anisotropy. Anisotropic deformation was also highly conserved amongst an array of differentiated and undifferentiated cell types. Although the functional purpose of this conserved anisotropy remains elusive, cells exhibit tight control over how the nucleus deforms. This may provide a mechanism through which mechanical cues in the microenvironment are rapidly transmitted to the genome.

5.2 Introduction

Mechanical forces transmitted through the cell directly affect nuclear shape and function, thereby affecting gene expression and numerous processes at the cellular level [126, 370, 371]. Such forces result in internal remodelling of the nuclear cytoarchitecture and chromatin [126, 372-374], leading to alterations in transcriptional activity [22, 375]. How nuclei respond to physical cues depends on their inherent mechanical properties, which alone direct diverse biological functions. Mechanosensitive proteins, such as lamins, are known to control and regulate these properties by physically coupling the inner nucleus with the cell's cytoskeleton, focal adhesions and integrins [126, 372, 376]. Mutations in these proteins result in a number of diseased states, and manifest in misshapen nuclei and increased nuclear fragility, particularly under applied strain [189, 377-380]. The importance of nuclear mechanics is evidenced during differentiation and development wherein mechanical forces are necessary [381-383] to direct deformable undifferentiated stem cells into committed cell types [384, 385]. Matrix stiffness also influences lamin-A levels [386] thereby governing nuclear resistance to force [246, 387, 388]. Clearly, characterizing how the nucleus deforms and remodels in response to force is of critical importance.

A large body of research involves examination of isolated nuclei [189, 321, 385, 389]. However, the nuclear response to force, in the context of its integration within the cyto-architecture has not been well-characterized to date. Importantly, nuclei are often denoted as isotropic materials [189, 190], however, during physical perturbation [384, 390] they display anisotropic material properties. Laser ablation studies have shown that the disruption of heterochromatin nodes causes elliptical nuclei to undergo anisotropic shrinkage in which they collapse significantly more along their minor axis as opposed to their major axis [384]. Planar stretching of cell monolayers also reveals an inherent mechanical anisotropy [390]. In both cases, cytoskeletal disruption resulted in a significant loss of anisotropy. These studies show that intrinsic nuclear prestress governs nuclear shape, while cytoskeletal organization governs nuclear deformation in response to mechanical stress [372, 380, 384]. Whether or not the observed mechanical anisotropy is a widespread phenomenon amongst cells remains an open question. Moreover, if an intrinsic nuclear anisotropy exists, how is it regulated? Which cytoskeletal or nuclear components influence this behaviour? It seems likely that the cytoskeleton plays a role in directing anisotropy of nuclear deformations since it acts as a direct link to external force. However, nuclear components such as lamins or chromatin organization may also influence this behaviour.

Here, we characterize the anisotropic deformation of nuclei within living cells in response to controlled extra-cellular forces. By measuring nuclear strains and defining a quantitative measure of anisotropy, we demonstrate that nuclear anisotropy is prominent in NIH 3T3 fibroblasts, and highly conserved in a variety of cell types. Using 3T3s as a model, we investigate the role of cytoskeletal components in nuclear deformation. We also discuss the implications of chromatin organization and lamin-A expression in nuclear anisotropy. Nuclear anisotropy may provide a direct mechanism through which extra-cellular forces are controllably transmitted to the genome, thus the nucleus itself may act as a mechanosensor in the cell, as recently proposed [371].

5.3 Results

5.3.1 Nuclear deformations reveal anisotropy

Nuclear deformations were examined by applying a constant force above the nuclei of 3T3 fibroblasts using an atomic force microscope (AFM) tip, while simultaneously acquiring laser scanning confocal microscopy (LSCM) time-lapse images (Fig. 5.1 A and B) in a manner described previously [335, 374]. Employing the nuclear dye Hoechst 33342 enabled us to visualize nuclear area during the deformation (Fig. 5.1 A). The confocal acquisition plane was set in the middle of the nucleus (region of greatest fluorescence intensity), and images were collected at a rate of 4 fps. In order to avoid any artefacts due to focal drift, we acquired data for only 5s. Longer durations were also examined (~20s); however no significant difference was observed in the total deformation. Image quantification allowed us to characterize strain (ε) along the major and minor axes of the nucleus as a function of time (Fig. 5.1 D and E) as we described previously [390].

Within 1s following force application, nuclear area rapidly expanded (Fig. 5.1 C). There is a clear dependence of nuclear expansion on force magnitude ($P < 0.003$), and no change in the absence of an applied force ($P > 0.09$). Nuclear area increased by 7.8 ± 0.8% and 11.4 ± 1.4% following 5s of a

10nN and 20nN constant force, respectively. Interestingly, nuclear deformation was anisotropic, with absolute deformation along the major axis significantly less than the minor axis ($P < 0.05$). This anisotropy is demonstrated by plots of the force dependent strain, ε_{major} and ε_{minor}, as a function of time (Fig. 5.1 D and E). Following loading, 3T3 nuclei experienced strains of ε_{major} = 2.4 ± 0.3% and ε_{minor} = 5.2 ± 0.6% in response to 10nN, and larger strains of ε_{major} = 3.2 ± 0.5% and ε_{minor} = 7.9 ± 1.3% when exposed to 20nN of force. The nucleus was confirmed not to move in the confocal volume due to mechanical loading, as demonstrated by stationary nucleoli during nuclear expansion (Fig. 5.S1 and Vid. 5.S1).

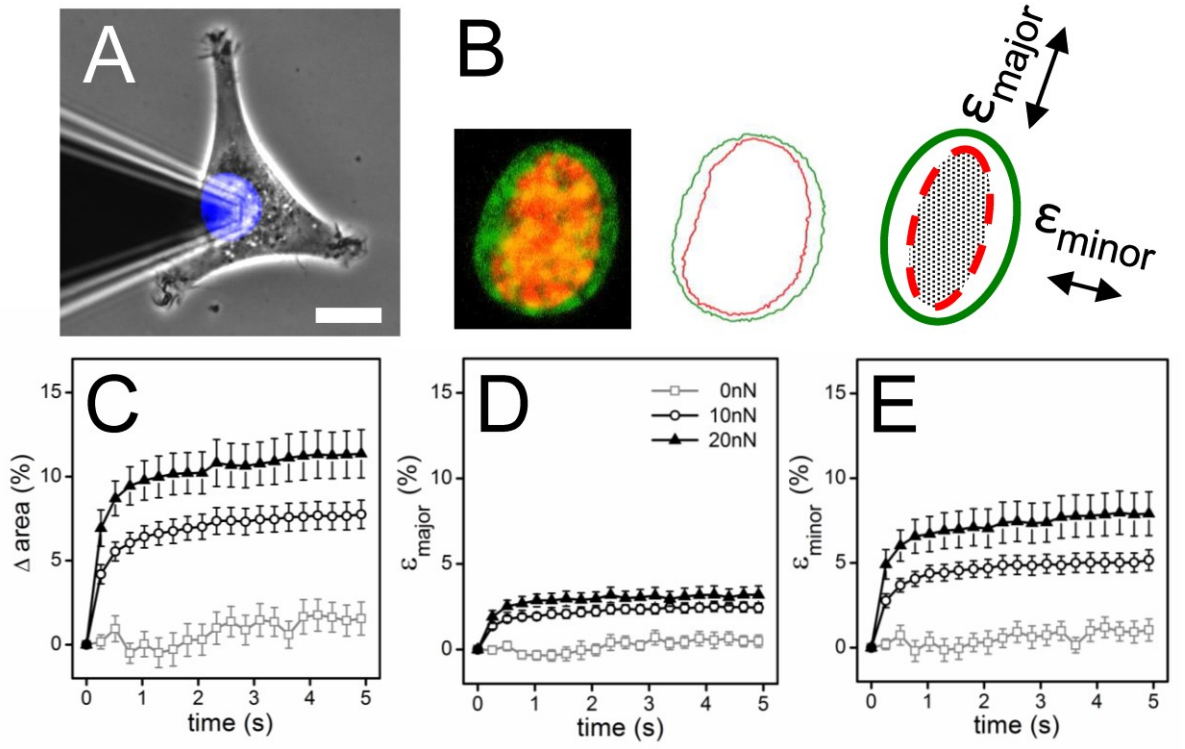

Figure 5.1 Extracellular forces applied to cell nuclei reveal anisotropic deformations.
A) Force application over the central nuclear region was carried out using AFM while simultaneously tracking nuclear deformation using LSCM. Scale bar is 10μm B) Process of strain measurement. Staining the nuclei with Hoechst 33342 allowed for the capture of nuclear outlines. Shown is a 3T3 fibroblast nucleus prior to loading (red), and following force application (green), image is 12μm wide. Nuclear outlines were extracted: before (red) and during (green) the deformation. Outlines were fit to an ellipse in order to extract the change in area and strain along the major (ε_{major}) and minor (ε_{minor}) axes over time. C) Area expansion following 5s of 0nN (grey squares) n=14, 10nN (white circles) n=21, and 20nN (black triangles) n=14. D) Percent strain over time in the major axis and E) minor nuclear axis. Axial strains reveal a clear mechanical anisotropy. Error bars are SEM.

To quantify the observed anisotropic strain dynamics, we fit the time dependent strain data to an expression that predicts deformation of a viscoelastic Kelvin-Voigt material [391] (*SI Materials and Methods*). From the fits, we extracted plateau strains $\varepsilon_{p\ major}$ and $\varepsilon_{p\ minor}$, and characteristic deformation time constants τ_{major} and τ_{minor}. We then defined a dimensionless anisotropic strain ratio ($\alpha = \varepsilon_{p\ major}/\varepsilon_{p\ minor}$). Small values of α imply a large deformation anisotropy ($\varepsilon_{p\ minor} > \varepsilon_{p\ major}$) and α =

1 represents isotropic deformation ($\varepsilon_{p\ minor} = \varepsilon_{p\ major}$). Accordingly, $\alpha > 1$ also implies anisotropy, but was rarely observed. Strain ratios were independent of load magnitude ($P > 0.50$) with mean $\alpha = 0.53 \pm 0.06$ for 10nN and $\alpha = 0.62 \pm 0.15$ for 20nN. Taken together, these results demonstrate that change in area and strain are force dependent, but not anisotropy. We also confirmed that α displayed no clear dependence on the orientation of the nucleus with respect to the AFM cantilever (Fig. 5.S2). Moreover, anisotropic nuclear behaviour persists, as shown by performing the experiment over long durations (15min). Strain measurements revealed that the nucleus reached 90-95% of its ultimate strain within 1min of loading and resulted in significant strain anisotropy (Fig. 5.S3).

To examine whether nuclear anisotropy is a pervasive phenomenon, we performed the short deformation experiment (10nN for 5s) on a variety of other cells (immortalized and primary fibroblast, epithelial, myoblast and embryonic stem cells) derived from several species (human, mouse, canine, hamster). Although strain magnitudes varied widely in response to force (Table 5.S1), in all cases α was observed to be < 1 (Fig. 5.2). Importantly, primary fibroblasts isolated from BALB/c mice displayed the same level of anisotropy (0.51 ± 0.10) as the 3T3 cells (0.53 ± 0.06). Nuclear shape, as characterized by circularity (*SI method*s), varied greatly between cells but did not appear to be correlated with α. This data demonstrates that deformation anisotropy appears to persist among the diverse cell and species types surveyed here. Obviously, numerous complexities exist when assaying such a diversity of cell types. Therefore, to systematically examine the origins of this phenomenon, we focus our attention on 3T3 fibroblasts as a model system in all subsequent experiments.

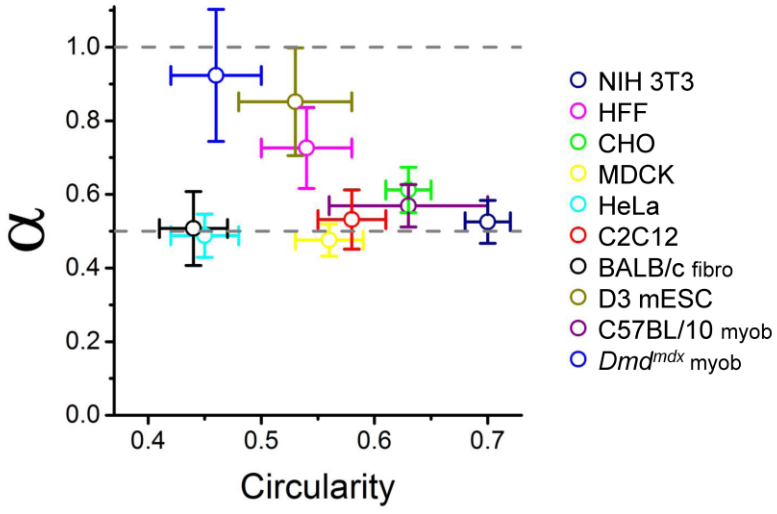

Figure 5.2 Nuclear anisotropy is variable amongst cell types.
Plot of anisotropic strain ratio (α) versus circularity for various established cell lines: 3T3s (n=21), HFF (n=19), CHO (n=14), MDCK (n=19), HeLa (n=16), C2C12 (n=13), D3 mESC (n=10), and primary cells including fibroblasts from BALB/c mice (n=12), and myoblasts from C57BL/10 (n=7) and *Dmd*^{mdx} (n=8) mice. Established cell types demonstrated a clear nuclear anisotropy, as demonstrated by α consistently < 1. Deformations associated with mESC and *Dmd* cell types were more isotropic than other cells, possibly due to a lack of lamins A/C and altered chromatin organization. Error bars are SEM.

5.3.2 The role of cytoskeletal structure in anisotropy

In order to determine the effect of the cytoskeleton on nuclear deformation, we made use of two very well-known anti-cytoskeletal drugs to selectively inhibit specific components [167, 196, 384, 392-394]. CytD and Noco inhibit polymerization of actin filaments and microtubules (MTs), respectively [167, 196, 392]. Immunofluorescent images of fixed cells stained for actin, tubulin, and DNA demonstrate clear differences between untreated and treated cells (Fig. 5.3 A-D). A combination of Noco and CytD (NocoCytD) was also used in some cases, which led to depolymerisation of both actin and MTs (Fig. 5.3 D). Treated cells responded to 10nN of force similarly to untreated cells, with the majority of the deformation occurring within seconds following loading (Fig. 5.3 E-G). Area expansion was greatest for cells treated with NocoCytD (24.8 ± 3.2%) and CytD (24.9 ± 2.8%), both of which deformed significantly more than untreated cells (7.4 ± 0.6%). Cells treated with Noco only resulted in a marginal increase in nuclear expansion (9.5 ± 0.9%). However, initial area magnitude of 3T3 nuclei remained unchanged following treatment with the cytoskeletal inhibitors ($P > 0.05$).

In general, there is a statistically significant drug-dependent response in $\varepsilon_{p\ major}$ and $\varepsilon_{p\ minor}$ for cells treated with CytD and NocoCytD (Table 5.S2 and Fig. 5.3 F and G). Cells treated with NocoCytD exhibited the largest values of $\varepsilon_{p\ minor}$, followed by cells treated exclusively with CytD. CytD treatment also resulted in the largest $\varepsilon_{p\ major}$. Surprisingly, in comparison to untreated cells, Noco resulted in a significant increase in $\varepsilon_{p\ major}$. Calculations of α (Fig. 5.4 A and Table 5.S2) revealed anisotropy of nuclear strain ($\alpha < 1$) that remains apparent irrespective of an intact cytoskeleton. Cells treated with CytD (alone or in combination with Noco) led to $\alpha = 0.71 \pm 0.10$ and $\alpha = 0.68 \pm 0.14$, respectively. These values were not statistically significant from untreated cells (0.53 ± 0.06). However, the loss of MTs alone (Noco) resulted in a significant increase in α (0.88 ± 0.14, $P < 0.02$), which indicates less anisotropic behaviour.

Nuclear circularity was also measured prior-to and in response to extracellular force (*SI method*s and Fig. 5.S4). Results indicate that anisotropic strain induces an increase in circularity (the nucleus becomes less elliptical) due to the fact that $\varepsilon_{minor} > 2x\ \varepsilon_{major}$ (Fig. 5.1 D and E). Moreover, circularity drastically decreased with CytD and NocoCytD treatments, but was less pronounced for cells treated solely with Noco. In other words, upon loss of actin (alone or in combination with MTs), the nucleus became more elliptical. Force application also increased the circularity of all cells on average, as expected (Fig. 5.S4). Although nuclear shape depends on the cytoskeleton, there is no clear correlation between nuclear shape and the observed level of anisotropy following loading (Fig. 5.4 B).

Inside intact cells, the cytoskeleton plays a major role in governing nuclear shape (in concert with the nucleoskeleton) [321, 372, 384]. Therefore, we isolated nuclei in order to probe its mechanical anisotropy in the absence of any confining structures (Fig. 5.3 C). Our results demonstrate that isolated nuclei become less circular after removal from the cell, suggestive of an intrinsic prestress. Strain was observed to be highly anisotropic in isolated nuclei, with mean strain in the minor axis ~5-fold larger than strain in the major axis. Anisotropy (α) was more pronounced in isolated nuclei (0.22 ± 0.03) compared to nuclei within intact cells (0.53 ± 0.06). This result suggests that anisotropic mechanical properties are inherent to these nuclei, and likely depend on nuclear

structure, possibly dictated by chromatin organization and/or key structural nuclear proteins (lamins).

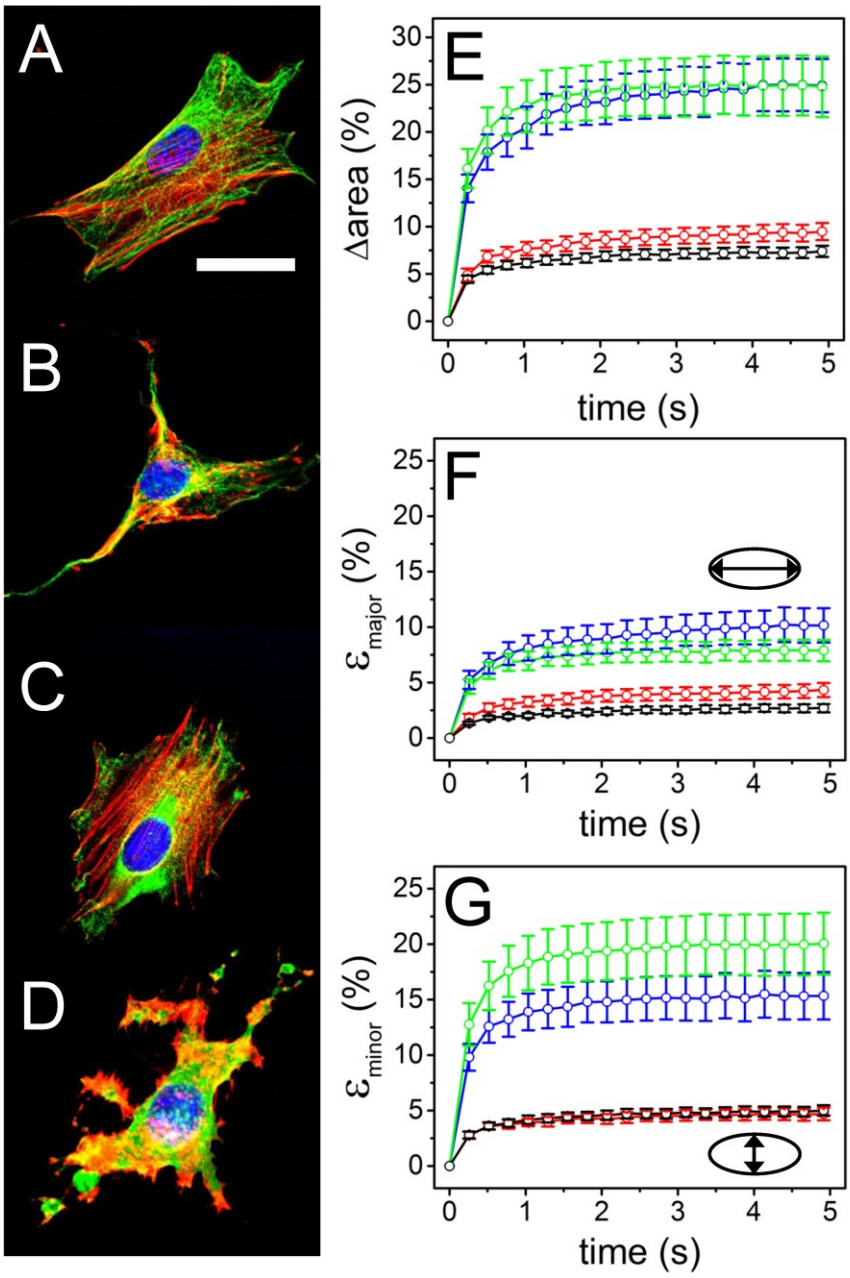

Figure 5.3 Role of the cytoskeleton in nuclear deformation and structure.
A-D) Immunofluorescent images of fixed 3T3 cells showing DNA (blue), actin (red), and MTs (green). A) Untreated 3T3 cells, B) CytD, C) Noco, and D) NocoCytD treated cells. Scale bar is 20µm. E) Change in projected nuclear area as a function of time for untreated (black), Noco (red), CytD (blue), and NocoCytD (green) treated 3T3s. Corresponding strains shown for F) the major axis (ε_{major}) and G) the minor axis (ε_{minor}) over 5s of a 10nN load. Error bars are SEM.

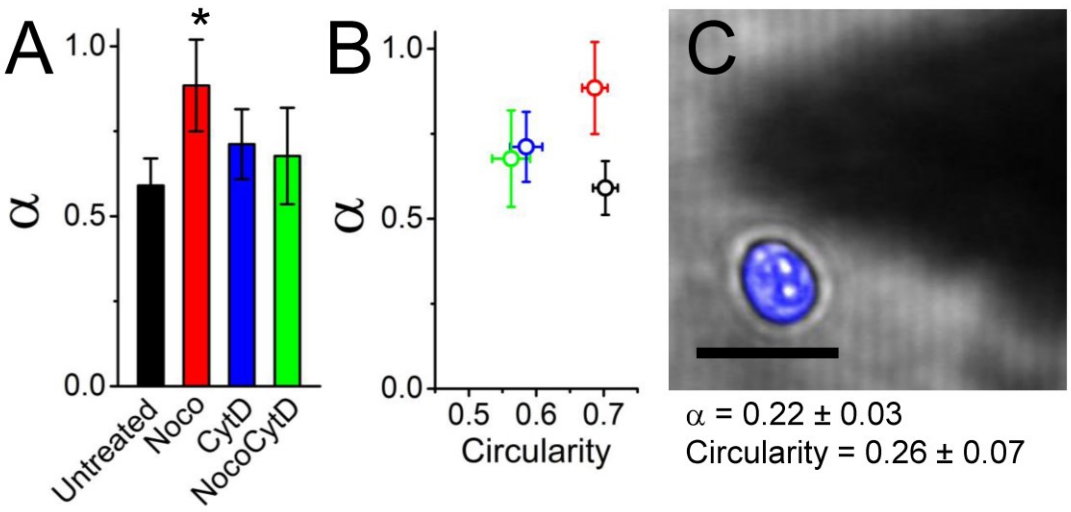

Figure 5.4 Nuclear anisotropy appears to be intrinsic.
A) Anisotropic strain ratio (α) is shown for untreated and treated 3T3s. Anisotropy was demonstrated in all cases ($\alpha < 1$). Noco treatment demonstrated significantly less anisotropic behaviour ($P < 0.05$, using t-test). B) Plot of anisotropic strain ratio versus circularity. Nuclear shape (prior to deformation) does not account for the observed anisotropy. Untreated 3T3 (black), Noco (red), CytD (blue) and NocoCytD (green). Error bars shown are SEM. C) Typical isolated 3T3 nucleus (blue). Forces applied to elongated isolated nuclei (n=10) by an AFM tip (shadow) demonstrated increased α. Scale bar is 20μm.

5.3.3 The role of nuclear architecture

Chromatin organization plays an important role in regulating transcription processes [395] and governing the physical properties of the nucleus [384, 396]. Moreover, extra-cellular forces impact the structure and organization of the nucleus and chromatin remodelling [22, 375]. Here, to address the role of chromatin organization in anisotropy, we treated 3T3s with Trichostatin A (TSA), a specific inhibitor of histone deacetylase, which leads to chromatin decondensation. TSA has been used in several studies of nuclear mechanics [397-399]. Cells treated with TSA underwent large morphological changes; they appeared more well-spread and exhibited extremely long extensions in comparison to untreated cells (Fig. 5.5 A and B) consistent with previous studies [398, 400]. TSA treatment led to a significant amount of variability and several outlier values in the response of the nucleus to applied forces (Fig. 5.5 C). Only a small population of cells (~43%) produced data that could be analyzed using the methods presented in this study. The majority of nuclei did not deform at all or exhibited a very small creeping deformation with no plateau. Notably, when considering the nuclei that displayed a response to force, the variability in the data was significantly higher. This variability becomes evident when displayed as box charts with several outlier data points detected (outliers were identified as data lying outside the inner quartile range by 1.5-fold). Nuclear circularity decreased upon TSA treatment likely due to the elongation of the cells ($P < 0.02$) (Fig. 5.5 C). TSA-treated nuclei also displayed anisotropic strain behaviour, with an average $\alpha < 1$. However, α did not change significantly ($P > 0.1$) with TSA treatment (0.42 ± 0.07 and 0.60 ± 0.09 for wild type and TSA, respectively). Interestingly, removal of the outliers from the data sets did lead to a statistically significant increase in α ($P < 0.03$). However, we limit our conclusions to the complete data set. Despite the increased variability in the data the observations suggest two very important

phenomena. First, disrupting chromatin structure directly impacts mechanosensitivity as evidenced by the fact that a significant number of cells displayed no response to force. Second, when TSA-treated nuclei do deform, the results are highly variable and characterized by a more isotropic deformation or a slow creeping deformation. Taken together, chromatin organization plays a critical role in regulating the mechanosensitivity and deformation response of the nucleus to mechanical forces arising in the extracellular environment. However, the large variability in TSA-treated responses is likely masking the origin of the observed nuclear deformation anisotropy.

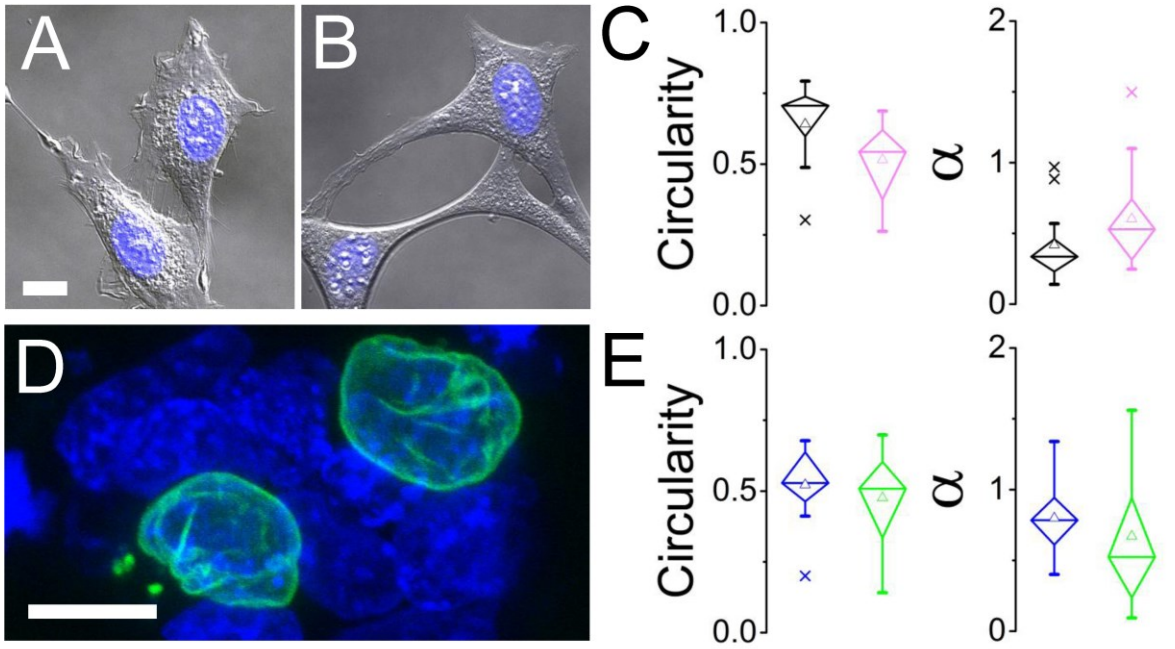

Figure 5.5 Role of nuclear architecture in anisotropy.
A) DIC images of live untreated 3T3 cells (n=13) and B) cells treated with TSA (n=15). Scale bar is 10µm. C) Box plots of circularity and α for control (black) and TSA-treated (pink) 3T3s. Box plots shown are 25th, 75th percentiles. Triangles indicate mean values. Outlier data is indicated by crosses (x). D) Over-expression of lamin-A in D3 mESC. Live-cell image of mESCs in which some cells are transiently expressing lamin-A-EGFP in the nuclear envelope. DNA in blue, lamin-A EGFP (green). Scale bar is 12.5µm. E) Box plots of circularity and anisotropic strain ratio (α) for untreated mESC (blue) (n=10) and lamin-A transfected cells (green) (n=13).

Alternatively, lamin proteins are known to influence nuclear mechanics and structure. Lamin deficient mice have been employed in previous studies of nuclear mechanics [378, 398, 401, 402]. Complications can arise in this approach due to numerous altered states and compensation mechanisms that occur in response to lamin deficiency [378, 401]. Here, we employed the alternative strategy of transiently over-expressing lamin-A EGFP in D3 mouse embryonic stem cells (mESCs) (Fig. 5.5 D) that do not express lamin-A when pluripotent [131, 403, 404]. This was confirmed with immunofluorescent staining (Fig. 5.S5). In contrast to the data collected on 3T3 cells, wild type and lamin-A EGFP mESCs displayed a large variability in nuclear shape, in agreement with previous studies [404-406]. This led to the observation that lamin-A EGFP cells (Fig. 5.5 E) exhibited no significant change in circularity compared to the wild type ($P > 0.4$, removal of outliers had no effect on

significance). AFM elasticity measurements, as described previously [335], were performed on visibly transfected cells (n=19) and neighbouring cells lacking GFP (n=11). Cells visibly transfected with lamin-A resulted in significantly stiffer Young's moduli (3.2 ± 0.3 kPa) than cells lacking lamin-A (2.4 ± 0.2 kPa) ($P < 0.04$) as expected [378, 399]. The deformation of mESCs was still anisotropic ($\alpha < 1$) but was extremely variable, consistent with TSA treatments. Our results revealed that mESCs possessed $\alpha = 0.67 \pm 0.13$ and 0.80 ± 0.09, for transfected and wild type cells, respectively (Fig. 5.5 E). Although lamin-A over-expression resulted in a decreasing trend in α, it was not significant ($P > 0.4$) and no outlier data points were identified. Therefore, although lamin-A plays a role in regulating nuclear/cell mechanics, it does not appear to regulate the anisotropic deformation of the nucleus in response to extracellular forces.

5.4 Discussion

Recent observations of nuclear anisotropy [384, 390] suggest that the mechanical properties of the nucleus may not be isotropic, as often described [189, 321, 385, 389, 399]. In previous work, laser ablation was used to destroy heterochromatin nodes in nuclei of fibroblasts and pluripotent mESCs, resulting in the anisotropic shrinkage of the nucleus, with the minor axis contracting more than the major axis [384]. Substrate stretch was also observed to transmit mechanical stress to nuclei of MDCK monolayers, resulting in their anisotropic deformation [390]. In contrast, here we sought to examine how nuclei deform inside living cells when directly exposed to controlled nanomechanical forces. This is of crucial importance, as extracellular forces may impact gene regulation and signalling through direct physical changes in nuclear and genomic structure [22, 375, 407]. Therefore, systematically characterizing the deformation of the nucleus in response to force, and its mechanical anisotropy, is a critical first step in understanding this complex process. Here, using 3T3 fibroblasts as a model, we demonstrated that nuclei deform anisotropically in response to externally applied forces from an AFM tip. The deformation occurs very rapidly (< 1 s), eventually reaching a plateau that persists for long periods (up to 15min, max length of study). Strain along the minor nuclear axis was ~50% larger than the strain along the major axis, as characterized by a strain ratio ($\alpha = \varepsilon_{p\ major}/\varepsilon_{p\ minor}$), with mean values < 1, consistent with recent studies [384, 390]. Our results are the first to demonstrate the controlled anisotropic deformation of the nucleus in direct response to extracellular forces.

To examine how widespread nuclear deformation anisotropy is in other cells, we performed the experiment on a variety of established cell and species types. Although nuclear shape and strain magnitudes following perturbation varied widely, α was always observed to be < 1. Importantly, primary fibroblasts possessed an α almost identical to the immortalized 3T3 cell line. This survey also shows that highly circular nuclei can display anisotropic deformation. Consistent with the 3T3 data, initial nuclear shape does not influence anisotropy. Interestingly, pluripotent mESCs and diseased primary cells (*Dmd*^{mdx} myoblasts) possessed $\alpha > 0.8$, indicating an almost isotropic response. *Dmd*^{mdx} myoblasts also exhibited significantly ($P < 0.05$) less anisotropic strain in comparison to myoblasts isolated from control mice (C57BL/10), possibly attributed to global histone modification, as witnessed by dispersed and open chromatin configurations in *Dmd*^{mdx} myoblasts [408, 409]. Taken together, these results indicate that anisotropy appears to be highly conserved, at least among the diverse cell types examined here.

Using 3T3s to characterize the origins of nuclear anisotropy, we also demonstrated that the cytoskeleton plays an important role in regulating nuclear shape and the magnitude, timescale and anisotropy of nuclear deformation. A loss of intact actin causes a significant increase in the magnitude of nuclear deformation along both axes and the rate of expansion of the minor axis (Fig. 5.S6). Actin is highly cross-linked to the nuclear architecture through nesprin-1 and -2 proteins [126, 372] and plays an important role in regulating nuclear deformation, consistent with previous studies [384, 390]. A loss of MTs resulted in increased strain along the major axis, leading to an increase in α. MTs have been shown to distribute radially near centrosomes [410], and are now well known to contribute to cell polarization during migration independently of actin [139]. It is plausible that perinuclear MTs create a dense filament mesh at the ends of the major axis, contributing to strain resistance and the observed anisotropy. These results correspond with our other recent findings suggesting an MT-dependent resistance in the major axis, and actin-dependent resistance in the minor nuclear axis, following strain via planar stretch [390]. Finally, isolated nuclei revealed that anisotropic deformation is intrinsic to the structure of the nucleus itself. In the complete absence of prestress or confinement arising from the cytoskeleton/cytoplasm, isolated nuclei display strain that primarily occurs along the minor axis resulting in a highly anisotropic deformation ($\alpha \sim 0.2$). Perhaps the main role of the cytoskeleton is to limit the degree of nuclear anisotropy. It has been proposed that anisotropy in global cellular deformation is dominated by the presence of actin fibres, which tend to align parallel to the long axis of the cell [411]. Our results strongly agree with these findings, as the major axis tended to align with the polarization of the actin cytoskeleton. While actin plays a key role in dictating nuclear shape and its resistance to deformation, nuclear anisotropy appears to stem from the existence of an intrinsically prestressed nucleus due to the nucleoskeleton, nuclear envelope and/or chromatin organization [126, 372].

We hypothesized that nuclear architecture, including lamins and/or chromatin structure, might regulate nuclear anisotropic behaviour, since they both play a role in nuclear mechanics [405]. While expression of lamins B1 and B2 have been shown in mESC [131, 403], only very low levels of lamins A and C have been detected [404], with their expression closely related to differentiation [132]. And so, we examined the role of lamin-A by its overexpression in mESCs. Lamin-A over-expression significantly increased the stiffness of mESCs, as lamin-A is known to provide structural stability to the nucleus [378, 386]. However, lamin-A had an insignificant effect on the observed α. Nevertheless, the importance of lamins should not be underestimated, since they influence overall nuclear stiffness and play an important role in chromatin regulation [412]. In a recent study, mESCs in a transitional state were shown to exhibit complex auxetic behaviours in response to compression [193]. Moreover, mESC in a naïve pluripotency state responded with auxetic behaviour only upon TSA treatment. Their findings suggest that mESC mechanical properties are highly complex and depend on transitional state and chromatin organization. Here, TSA was used to loosen chromatin organization in 3T3s [397-399], which resulted in large morphological changes, likely due to the inhibition of gelatinase A, a matrix metalloproteinase [400]. TSA treatment resulted in a highly variable response of cells to applied forces. TSA abolished any response to force in the majority of cells measured, indicating a key role of chromatin organization in mechanosensitivity. Of the cells that did respond, they did so more isotropically, however the large variability in the measurement impairs our ability

to draw further conclusions. Although speculative, nuclear mechanical anisotropy may indeed arise from chromatin organization and play a role in force-mediated transcription processes [395].

Although we have not established the functional role of nuclear anisotropy, it is intriguing to observe that 3T3 fibroblasts exhibit a high degree of regulation over nuclear deformation. Moreover, the observed anisotropy is also conserved among diverse cell types from several species. Therefore, future studies will focus on examining how key proteins (post-translational modifiers to histone tails [413]) involved in chromatin organization, chromatin territories and the nucleoskeleton regulate deformation anisotropy [372, 395, 414]. Moreover, several studies have shown that cyclic stretch can induce gene expression changes and it remains unclear how inhibiting anisotropy (TSA treatment or specific knock outs) may impact these findings [396, 415, 416]. Clearly, more work is required to confirm whether or not nuclear deformation anisotropy is simply a result of nuclear organization, or if it plays a functional role in cell biology. Regardless, we have shown that living 3T3 cells regulate nuclear deformation at the cytoskeletal and organizational levels of the nucleus itself, in such a way that the nucleus is significantly more sensitive to deformation along the minor axis. Notably, anisotropic deformation occurs whether the mechanical stress is emanating from below the cell (substrate stretch [390]) or from above (direct AFM compression). Though highly speculative, we suggest that nuclear structure and organization is optimized to enhance its sensitivity to extra-cellular forces in order to promote mechanically induced gene expression.

5.5 Materials and methods

Detailed descriptions of reagents, cell lines, animal models, plasmids, simultaneous AFM-LSCM, image analysis and statistical tests are contained in the *SI Methods* (Chapter 5.7.1). All values quoted are mean ± SEM.

5.6 Acknowledgements

The authors acknowledge support from individual Natural Sciences and Engineering Resource Council (NSERC) Discovery Grants (J.L.H. and A.E.P.) and an NSERC Discovery Accelerator Supplement (A.E.P.). C.M.C. was supported by a postdoctoral training award from the "Fonds de Recherche du Québec – Santé" (FRQS). A.E.P also acknowledges generous support from the Canada Research Chairs program and a Province of Ontario Early Researcher Award. The authors would like to thank Daniel Modulevsky and Claire Edrington for experimental assistance.

5.7 Supplementary Information

5.7.1 Materials and Methods

5.7.1.1 Cell Culture

Mouse (NIH3T3) and human (HFF) fibroblasts, hamster (CHO), canine (MDCK), and human (HeLa) epithelial cells, as well as mouse muscle (C2C12) cells, were cultured in Dulbecco's Modified Eagle's Medium (DMEM) supplemented with 10% FBS and 1% penicillin/streptomycin at 37°C and 5% CO_2. Cells used in experiments were grown on 35mm glass bottom tissue culture dishes (MatTek)

containing 2mL of culture media, and their nuclei were stained with Hoechst 33342 (Invitrogen) according to manufacturer protocols one hour prior to imaging. D3 mouse embryonic stem cells (mESC) (ATTC, #CRL-1934) were cultured in DMEM supplemented with 12.5% FBS, 0.1mM Non-essential amino acids, 30μg/ml Gentamicin (Gibco), 0.1mM 2-mercaptoenthanol (Sigma) and 1000 U/ml leukemia inhibitory Factor (LIF) (Millipore). Cells were passaged every 48 hours to prevent differentiation.

5.7.1.2 Isolation of 3T3 Nuclei

Cells were first pre-stained with the nuclear dye Hoechst 33342 (Invitrogen) at a concentration of 0.5 uL/mL. Cells were then trypsinized, pelleted, and re-suspended in ice cold AFM buffer: Protease inhibitor tablets (Roche), 1 mM EDTA (Fisher) in 50mL PBS (Fisher), and again spun down. Cells were re-suspended in ice cold extraction buffer (protease inhibitor tablets (Roche), 1 mM EDTA, and 25mM sucrose in 10mL PBS), and left on ice for 30min. A dounce homogenizer was used to slowly break up the sample (50 times on ice). Samples were spun down at 1000rpm for 10min at 4°C, and then re-suspended in ice cold AFM buffer. The supernatant was placed on Poly-L-Lysine (Sigma) coated petri dishes for 1 hour at 4°C, followed by aspiration and fresh supply of AFM buffer (at room temperature). All experiments were performed immediately following.

5.7.1.3 Murine Models

BALB/c mice, C57BL/10ScSnJ mice and Duchenne muscular dystrophic mouse model C57BL/10ScSn-*Dmd*^{mdx}/J were purchased from The Jackson Laboratory (Bar Harbor, ME, USA). All animals were kept at constant room temperature (23°C) and humidity (78%) under a controlled light/dark cycle. Mice were fed a normal chow diet and were euthanized by CO_2 inhalation followed by cervical dislocation. All experimental procedures involving laboratory animals were approved by the Animal Care and Use Committee of the University of Ottawa.

5.7.1.4 Isolation of Myoblasts from Muscle Tissue

The isolation of myoblast cells from the murine Duchenne muscular dystrophy model (*Dmd*^{mdx}) and its control murine model (C57BL/10) was based on the protocol of Li *et al.*, 2011 [417], and was performed as follows: Following euthanasia at 4 weeks of age, muscle tissues were resected from the lower mouse limbs in a sterile environment. The tissues were kept in PBS (Fischer), minced into a coarse slurry using sterile scissors, and centrifuged for 5 min at 2500 rpm at 4°C. After a second wash/centrifugation, the tissue slurry was digested by a succession of protease treatment starting with collagenase (0.2%, 60min at 37°C; Sigma), followed by dispase I (2.4 U/ml, 45min at 37°C; Sigma) and ending with trypsin (0.25%, 20min at 37°C; Wisent). The cells were then re-suspended in DMEM (High glucose, HyClone) containing 10% FBS (HyClone), 10% horse serum (HyClone), 1% newborn calf serum (HyClone), 1% amphotericin B (Wisent), 1% penicillin/streptomycin (pen/strep) (Wisent) and 1% L-glutamine (Wisent). The cells were dissociated by passing the cell suspension 3 times through a 21G needle and filtered through a 70μm cell strainer (Fisher) to remove any larger debris. After a last centrifugation, the cells were plated in a collagen-coated T-25 flask for 2 hours at 37°C in a 5% CO_2 incubator. This first flask mainly contained fibroblasts and myofibroblasts. The non-adherent cells were then transferred into a second T-25 flask for 24 hours at 37°C in a 5% CO_2

incubator. This dish mainly contained myoblasts (confirmed by desmin staining, data not shown) and was used for experiments in the following days.

5.7.1.5 Isolation of Fibroblasts from Skin Tissue

The isolation of skin fibroblasts from BALB/c mice was performed as follows: After euthanasia, the mouse dorsal skin was shaved and sterilized using 70% ethanol, and a $2cm^2$ dorsal skin section was resected. In a sterile environment, the skin was cut into small square sections ($2mm^2$) and stored in PBS. These samples were then placed into Petri dishes, where physical contact between the skin samples and Petri dish surface were formed by positioning sterile glass coverslips over each sample. The samples were then immersed in DMEM (High glucose, HyClone) containing 50% FBS (HyClone), 1% amphotericin B (Wisent), 2% pen/strep and 1% L-glutamine (Wisent). When fibroblast cells migrated out of the skin (after 6-8 days), skin samples were then removed and the medium changed to normal growth media (DMEM: 10% FBS, 1% amphotericin B, 1% pen/strep and 1% L-glutamine).

5.7.1.6 Plasmids and Transfection

D3 mESC were transfected with lamin A-GFP plasmids (a kind gift of Tom Rapoport, Harvard University) using Lipofectamine 2000 (Invitrogen) according to manufacturer protocols. Transfections were done 24 hours after cell passage, 24 hours prior to experiments.

5.7.1.7 Immunofluorescence

Staining for actin, microtubules (MTs) and DAPI was achieved following a previously reported protocol [196]. In brief, cells were first rinsed with warm PBS (Fischer) and fixed with a solution of 2% sucrose and 3.5% paraformaldehyde (Fischer). They were permeabilized with warm 0.5% Triton X-100 (Fischer). Samples were incubated with Phalloidin Alexa Fluor 546 (Invitrogen) to stain for actin. MTs were stained on ice by first incubating with monoclonal (mouse) anti-α-tubulin (Sigma), then with Alexa Fluor 488 conjugated rabbit anti-mouse immunoglobins (Invitrogen) for 15min with a 15min wash following each incubation. Lastly, nuclei were labelled by incubating with DAPI (Invitrogen). Staining for lamin-A in mESC was achieved using a mouse anti-lamin-A (Abcam) primary antibody.

5.7.1.8 Drug Treatments

In order to study the influence of the cytoskeleton on nuclear deformation, cells were treated with either Cytochalasin-D (CytD) (10μM in DMSO, Sigma) or nocodazole (Noco) (10μM in DMSO, Sigma) to specifically depolymerize actin or tubulin, respectively. Double-drug experiments, in which the cells were treated with both of these drugs (NocoCytD) simultaneously, were also performed. Appropriate amounts of each drug were added to the culture media 15min prior to the experiment or, in the case of staining, 15min prior to fixing. In order to examine the role of chromatin organization, cells were treated with trichostatin A (TSA, Sigma), a known histone deacetylase inhibitor [418, 419]. Cells were treated with 150ng/mL TSA solubilized in DMSO for 24 hours prior to experimentation/imaging.

5.7.1.9 Simultaneous Optical and Atomic Force Microscopy

AFM and high-speed LSCM were performed simultaneously by mounting the AFM (NanoWizard II, JPK Instruments AG, Berlin, Germany) onto a Nikon TiE inverted microscope with a resonant scanner A1-R confocal. A 60x, NA=1.2 water immersion objective was used for all experiments, and the culture dish was kept at 37°C with a temperature-controlled stage. All AFM cantilevers had an experimentally determined stiffness, k = 0.06 ± 0.01N/m (Veeco: MSCT-AUHW).

Tracking nuclear deformation entailed capturing images in a single plane (x-y) set in the middle of the nucleus at a rate of 4 fps. Images were recorded through 5s of constant force application, as well as 2.5s before extension of the AFM tip as control. During imaging, the AFM cantilever was brought into contact with the cell surface, above the centre of the nucleus, and a constant force was applied. Long-term nuclear deformation (15min) was recorded by performing simultaneous AFM and 4D LSCM. Image volumes of the nucleus were recorded 1min prior to force application and once every min for 15min thereafter. As before, the AFM cantilever was aligned over the centre of the cell nucleus and used to apply a constant force of 10nN or 20nN for 15min while the structural deformation of the nucleus was recorded.

Measurements of mESC Young's moduli were made by recording force-curves measured over the center of nuclei. The first 200nm of indentation was fit to the Hertz model for a conical tip [331] to measure local Young's modulus of the cell (PUNIAS Software) [332].

5.7.1.10 Image Analysis

Following AFM/LSCM experiments, raw image data was analysed using ImageJ [420] in order to quantify the deformation of the nucleus. A small macro was generated in order to automate the analysis. For long-term (15min) deformation analysis, maximum intensity projections of image volumes of nuclei were acquired at each time point. Each resulting image was converted into a corresponding binary mask, which allowed the border of the nucleus to be selected and the area automatically determined at each time point. Simultaneously, each selection was fitted to an ellipse, from which we obtained the lengths of the major and minor axes. The method for processing short-term (5s) deformation was very similar but did not require a maximum intensity projection at each time point. Typically, mESC transfected with lamin-A EGFP appeared as clusters of embryoid bodies, and so the green fluorescent channel was used to fit the nuclear ellipse instead of the blue fluorescent channel (Hoescht, DNA).

5.7.1.11 Statistical Tests and Fitting Data

All statistical analyses were performed using Origin 8.5. For all experiments, the response of cells was averaged for each condition (untreated, CytD, Noco and NocoCytD) and for each force (0nN, 10nN and 20nN). In total ~75% of cells displayed behaviour consistent with the data presented. In a minority of cases nuclei did not deform or move during the measurement and were excluded from the analysis. All data presented are mean ± SEM. Statistical significance is considered for *P*-values where $P < 0.05$, as determined by two-tailed student's t-tests, unless noted otherwise.

Plateau strains in both the major and minor nuclear axes were obtained by fitting the time-dependent strain data (see Fig. 5.1 A and B) to a viscoelastic Kelvin-Voigt model:

$$\varepsilon(t) = \varepsilon_p\left(1 - e^{-t/\tau}\right) \quad [5.S1]$$

where ε(t) is the time-dependent strain, ε_p represents the plateau strain observed in the long duration elastic regime, and τ is the characteristic deformation time constant which is inversely proportional to the deformation rate ($\kappa = \tau^{-1}$). From the fits, we extracted $\varepsilon_{p,\,major}$ and $\varepsilon_{p,\,minor}$ for the major and minor axis, respectively. Average R^2 values were > 0.90 on average, indicating a good fit.

5.7.1.12 Characterization of Nuclear Shape Change

Change in nuclear shape was examined by measuring circularity (*Circ*) using a built-in shape descriptor in ImageJ, measured as:

$$Circ = \frac{4\pi \times Area}{Perimeter^2} \quad [5.S2]$$

A value of 1.0 represents a perfect circle, whereas values approaching zero signify an elliptical shape.

5.7.2 Supplementary Tables

Table 5.S1 Nuclear strain is anisotropic in established and primary cells.

	N	$\varepsilon_{p\ major}$ (%)	$\varepsilon_{p\ minor}$ (%)	α ($\varepsilon_{p\ major}/\varepsilon_{p\ minor}$)	Circularity (0nN)
NIH 3T3	21	2.4 ± 0.3	4.9 ± 0.6	0.53 ± 0.06	0.70 ± 0.02
HFF	19	3.1 ± 0.5	4.3 ± 0.7	0.77 ± 0.11	0.54 ± 0.04
CHO	14	3.2 ± 0.4	5.4 ± 0.5	0.61 ± 0.06	0.63 ± 0.02
MDCK	19	2.1 ± 0.2	4.5 ± 0.4	0.48 ± 0.04	0.57 ± 0.02
HeLa	16	2.9 ± 0.3	6.9 ± 0.8	0.49 ± 0.06	0.45 ± 0.03
C2C12	13	2.2 ± 0.4	4.6 ± 0.7	0.53 ± 0.08	0.58 ± 0.03
BALB/c fibro	12	3.9 ± 0.6	9.8 ± 1.6	0.51 ± 0.10	0.44 ± 0.03
D3 mESC	10	5.6 ± 0.8	8.0 ± 1.7	0.80 ± 0.09	0.52 ± 0.05
C57BL/10 myob	7	3.5 ± 0.4	6.4 ± 0.6	0.57 ± 0.06	0.63 ± 0.07
Dmd^{mdx} myob	8	5.6 ± 1.0	6.5 ± 0.8	0.92 ± 0.18	0.46 ± 0.04

Mean plateau strains (ε_p) in the minor axis were significantly greater than the major axis for all cell types ($P < 0.05$, paired t-test), except for mESC ($P = 0.11$) and Dmd myoblasts ($P = 0.42$). Population means of anisotropic ratios (α) are significantly different, but variances are not (using one-way ANOVA with Tukey and Levene's test with $P < 0.05$). Values shown are mean ± SEM.

Table 5.S2 The cytoskeleton dictates nuclear strain but not anisotropy.

NIH 3T3	N	$\varepsilon_{p\ major}$ (%)	$\varepsilon_{p\ minor}$ (%)	α ($\varepsilon_{p\ major}/\varepsilon_{p\ minor}$)	τ_{major} (s^{-1})	τ_{minor} (s^{-1})
Untreated	21	2.40 ± 0.27	4.93 ± 0.55	0.53 ± 0.06	3.8 ± 2.8	3.3 ± 1.3
Noco	16	4.15 ± 0.57*	5.02 ± 0.53	0.88 ± 0.14*	2.7 ± 2.3	4.4 ± 2.6
Cytd	19	9.82 ± 1.45*	15.21 ± 2.02*	0.71 ± 0.10	4.3 ± 3.7	5.7 ± 4.4*
NocoCytd	21	8.59 ± 0.96*	20.29 ± 2.75*	0.68 ± 0.14	4.0 ± 3.1	5.3 ± 3.9*

Using equation [5.S1], we determined the plateau strain (ε_p) for the major and minor nuclear axes respectively. In all cases, $\varepsilon_{p,\ minor}$ was significantly greater than $\varepsilon_{p,\ major}$. There was a significant increase in $\varepsilon_{p,\ major}$ for cells treated with Noco, and both, $\varepsilon_{p,\ major}$ and $\varepsilon_{p,\ minor}$, for CytD and NocoCytD, in comparison to untreated cells (denoted by *). An anisotropy parameter ($\alpha = \varepsilon_{p,\ major}/\varepsilon_{p,\ minor}$) demonstrates $\alpha < 1$ on average, indicative of anisotropic nuclear expansion. Loss of MTs resulted in a significant decrease in anisotropy in comparison to untreated cells. Characteristic deformation rate constants (τ (s^{-1})) were significantly increased in the minor axis with the loss of an intact actin network. (* indicates $P < 0.05$ significance with t-test). Values shown are mean ± SEM.

5.7.3 Supplementary Figures

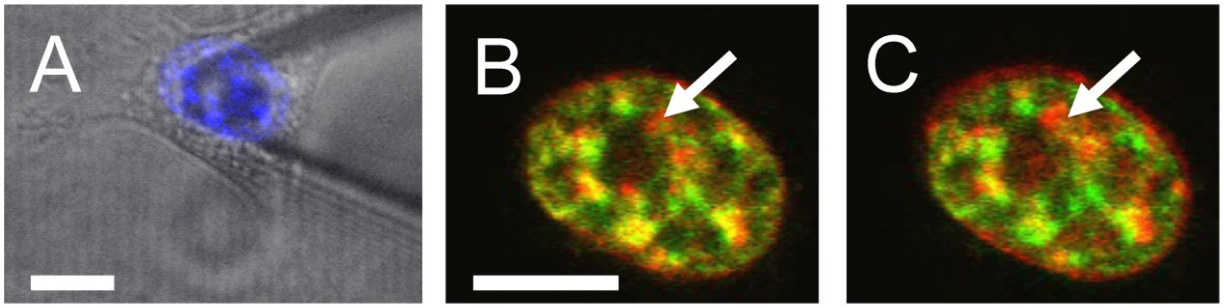

Figure 5.S1 Expansion is evident in the mid-plane of nuclei following loading.
A) Transmitted light image of 3T3 nuclei during a 10nN load, applied by AFM. Blue = DNA. The nucleus does not move out of the imaging plane due to mechanical loading, see Vid. 5.S1 and image overlays of 0nN (red) and 10nN (green) following B) 0.25s, and C) 5s of force. Movement of small sub-nuclear components occurs following nuclear expansion; however large nucleoli (arrows) remain stationary during the applied stress, indicating no substantial out-of-plane motion. Scale bar is 10µm.

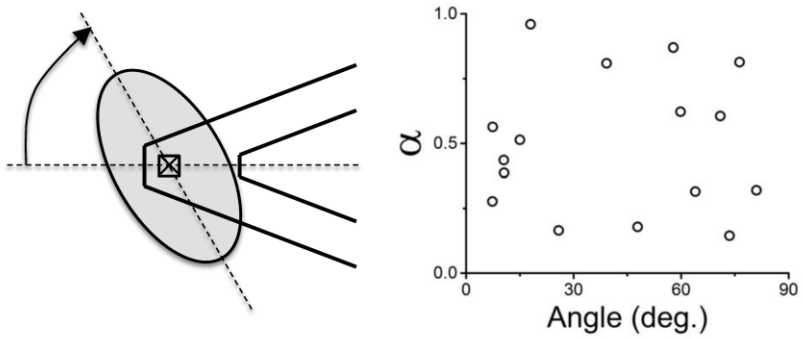

Figure 5.S2 The AFM tip is pyramidal with a square base.
To ensure that the orientation of the tip with respect to nuclear orientation had no influence on the observed α, we calculated the angle the long nuclear axis formed with the long axis of the AFM cantilever (n=16 cells). Nuclei were always randomly oriented between 0-90 degrees in all experiments, and no effort was made to choose cells oriented in a particular fashion. The orientation of the nucleus had no clear influence on the observed anisotropy as revealed in the plot of α versus orientation angle.

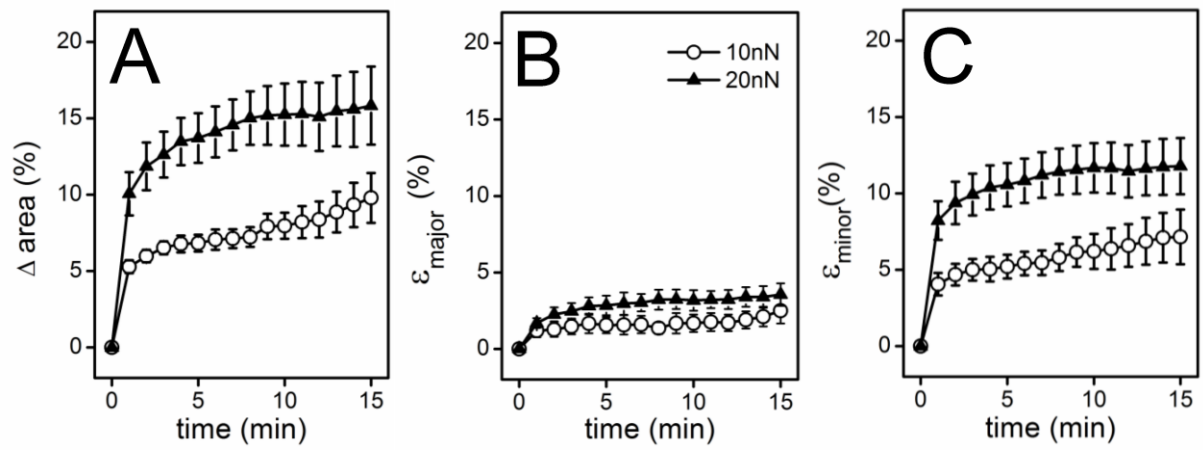

Figure 5.S3 Nuclear anisotropy is observed over long-term deformations.
A) Projected nuclear area following 15min of 10nN (white circle) and 20nN loads (black triangle). Nuclear expansion is clearly dependent on force magnitude ($P < 0.001$). Projected area increased by 7.2 ± 1.6% and 14.1 ± 2.1% following 15min of a 10nN (n=12) and 20nN (n=11) constant force, respectively. Plots of force-dependent strain: along the B) major axis and C) minor nuclear axis as a function of time. Cells experienced highly anisotropic nuclear strains of ε_{major} = 1.6 ± 0.7% versus ε_{minor} = 5.6 ± 1.5% when exposed to 10nN, and larger strains of ε_{major} = 2.6 ± 1.1% versus ε_{minor} = 11.3 ± 2.0% when exposed to 20nN. After 15min, anisotropic strain ratios were α = 0.48 ± 0.20 for 10nN and α = 0.3 ± 0. 04 for a 20nN applied force ($P > 0.350$, using t-test). Change in area and strain are dependent on the magnitude of the force applied, however, α is not. Error bars are SEM.

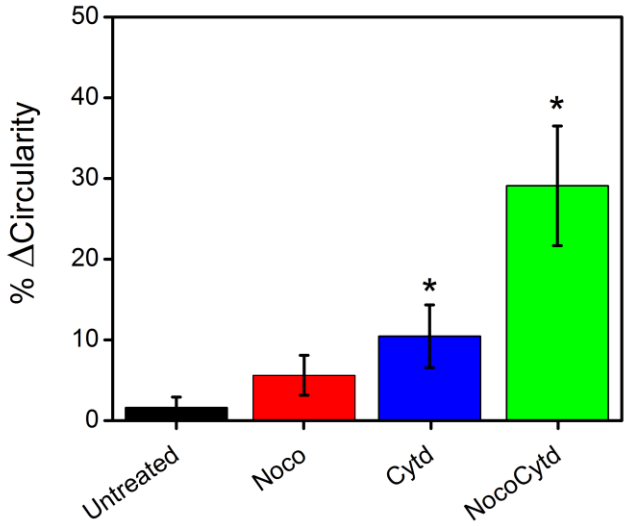

Figure 5.S4 Circularity increases following loading.
Percentage change in circularity following a 10nN load is shown. Treatment with CytD (blue) and NocoCytD (green) resulted in significantly increased change in circularity following loading, in comparison to untreated 3T3s (black), however Noco (red) was unchanged, as measured by [5.S2]. (*) Indicates significance ($P < 0.05$) with two sample t-test. Error bars are SEM.

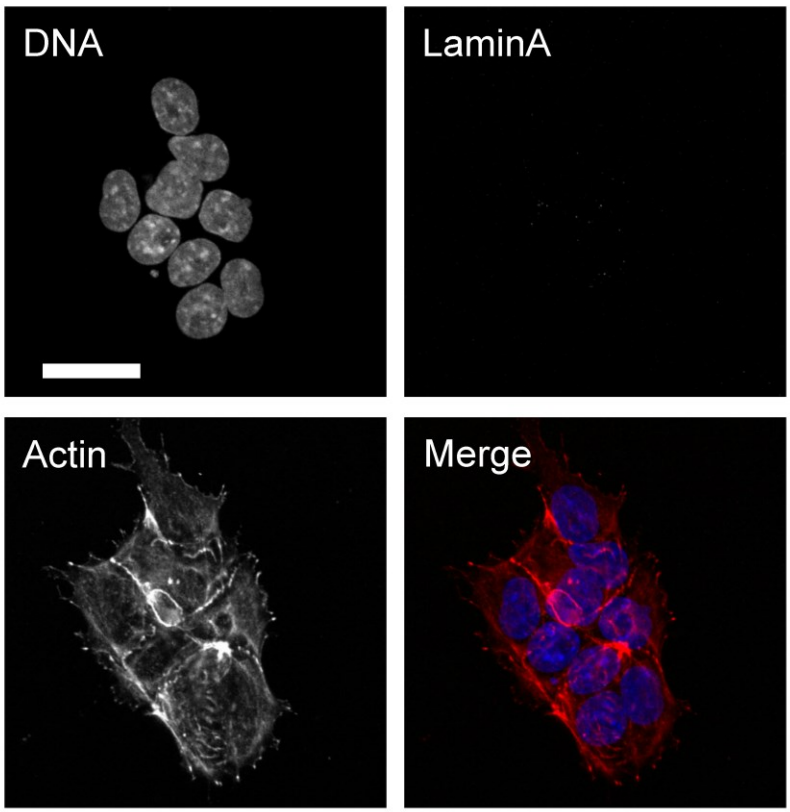

Figure 5.S5 Immunofluorescent images of D3 mESC demonstrate their lack of lamin-A.
D3 stem cells were stained for DNA (blue), lamin-A EGFP (green), and actin (red). Only a very faint fluorescent signal is observed for lamin-A in mESC. Scale bar is 25µm.

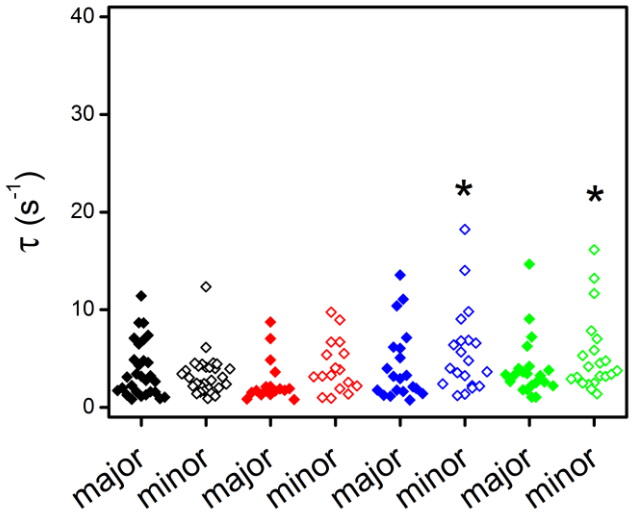

Figure 5.S6 Actin influences the characteristic deformation time constant.
Distribution of deformation time constants ($\tau(s^{-1})$) for untreated (black), and treated cells: Noco (red), CytD (blue) and NocoCytD (green), as determined by fits of the strain data to equation [5.S1]. Characteristic relaxation time constants (untreated: $\tau_{major} \approx \tau_{minor} \approx 4s^{-1}$) display a significant amount of variance: 0.7-18s^{-1}. No significant dependence was observed between major and minor axes ($P > 0.3$); however there was a dependence on drug treatment in the minor axis for cells treated with CytD or a combination of NocoCytD ($P < 0.05$). Loss of an intact actin network resulted in a decreased deformation rate in the minor axis, from $\kappa_{minor} \approx 0.3s$ (untreated) to $\kappa_{minor} \approx 0.2s$ for cells treated with CytD ($P < 0.02$) and NocoCytD ($P < 0.03$).

5.7.4 Supplementary Videos

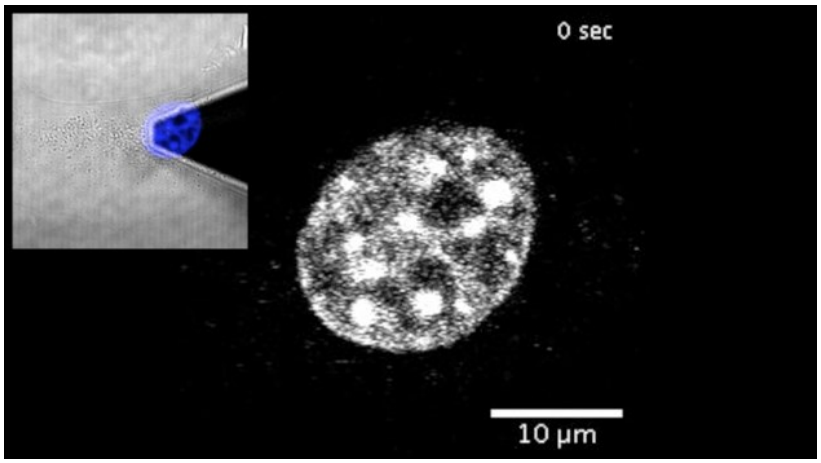

Video 5.S1 Nuclear expansion occurs anisotropically in its mid-plane.

6 | Future directions

The manuscripts presented in preceding chapters of this thesis have demonstrated a need for an appropriate model to describe the observed cellular behaviours in vitro. In particular, a rheological model that accounts for both the deformation and recovery behaviour of cells will greatly benefit our understanding of cellular mechanics. In our previous work [335, 421], similarly to others [44, 280, 283-285], we attempted to use simple mechanical models to describe the deformation behaviour of cells and their nuclei (Chapters 2-5). These simple models were deemed useful for demonstrating viscoelastic creeping behaviour of the membrane, cortex, and nucleus and for comparing relative mechanical parameters (elastic moduli and viscosity). However, more complex models will be necessary to fully describe cellular behaviours following external perturbations. Finite element (FE) modelling, in particular may be useful for the eventual development of complex continuum models of the cell.

FE modelling has become increasingly popular for the study of single cells [283, 422-428]. While early FE models treated the cell as highly over-simplified structures, more recent AFM and confocal-based models of single cells have emerged. The benefit of *in situ* modelling is that a variety of mechanical loads can be simulated to reveal intracellular stresses and strains, which will be necessary for a complete understanding of mechanosensing and mechanotransduction processes. For example, strains resulting from static and cyclic stretching [426], cell compression [283, 423, 424], micropipette aspiration [427], shear flow [422], cellular prestress[428], and hydrostatic pressure[421] have all been measured. However, the majority of FE models to date have employed over-simplified assumptions, such as the use of small strain theories, or incorporation of only a limited number of intracellular organelles to model the cell.

FE modelling presents its own set of challenges. Representing cell shape, for example, becomes extremely difficult with increasing complexity of the model. While it might be relatively simple to capture strains on the larger outer membrane (micron scale), it is challenging to couple these deformations to much smaller (nanometre scale) inner components, such as organelles, and cytoskeletal networks of filaments. Although recent models have incorporated large deformation theories and some main cellular components (i.e. the membrane, nucleus, cytoskeleton, and cytosol) [427], they remain highly simplified in nature and do not accurately represent the cell. Moreover, constitutive modelling of mechanical interactions between cellular components poses a serious challenge. Elements of the cell are typically represented as having simple elastic, and isotropic material properties – which we [422], and others have shown [44, 280, 283-285], are not a valid representation of the cell. Some have attempted to employ viscoelastic elements[423], but using simplified geometry as a trade-off in order to alleviate computational costs.

In light of these advances, and stemming from our work presented in this thesis, we recommend that future work should include a confocal-based finite element model of single cells. We propose that the FE model should employ a reverse-engineering approach to determine bulk rheological properties of the cell. These properties can be validated using rigorous analysis of AFM force-curves, as in reference [176]. Initial work towards this effort has commenced, with the studies presented in this thesis acting as a catalyst. Considering the complexity in modelling the small

volume (~2-3µm^3) pyramidal AFM tip, we have already employed a modified tip to perform compressive force experiments, as was done in Chapters 2-4. In particular, a spherical indenter (10µm) has been employed to provide a more even distribution of compressive stress over a larger surface area of the membrane, which is clearly visible and easier to model (Fig. 6.1 A). Preliminary Matlab models (programmed by Corinne Gullekson, a PhD candidate in the Pelling lab) and simulations based on confocal volumes of compressed cells are already underway, and have begun to demonstrate regions of high local stresses on the membrane (Fig. 6.1 B,C).

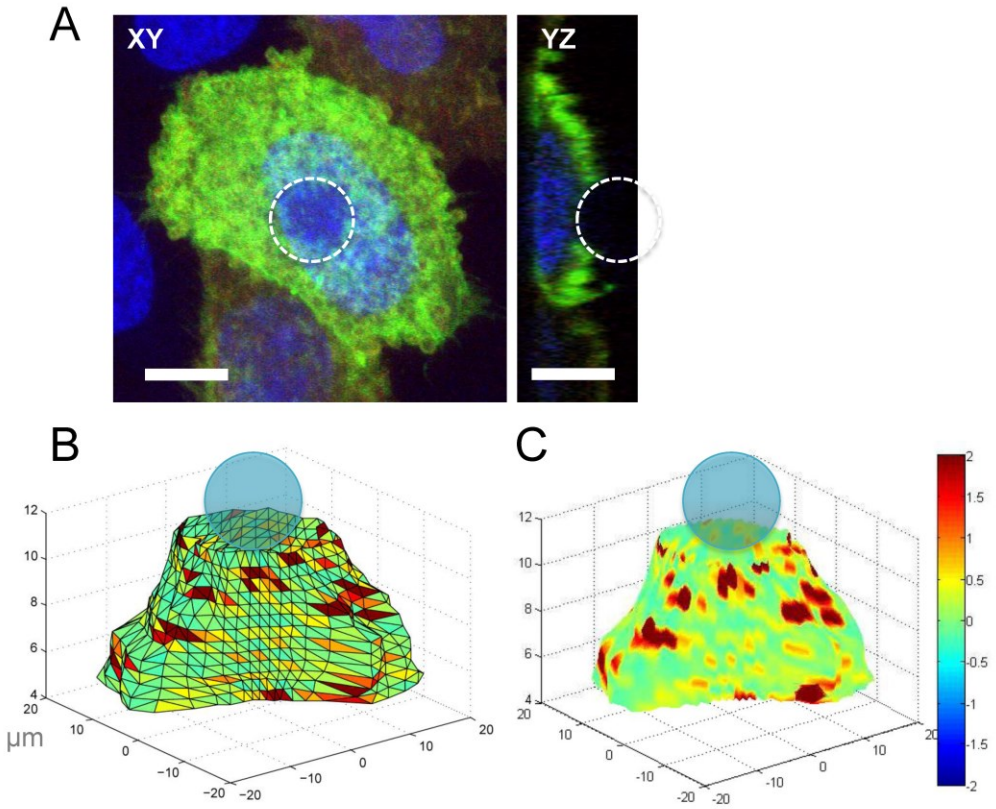

Figure 6.1 Proposed FE model to determine bulk cellular mechanical properties.
A) Confocal maximum z-projection of a HeLa cell deformed by a spherical indenter. Orthogonal image demonstrates the compressive strain in the membrane resulting from 10min of a 10nN force applied using a spherical indentor. Polystyrene beads (10µm, Fluka Sigma-Aldridge) were glued to an AFM cantilever (PNP-TR-50, Nanoworld) using a UV-curing optical adhesive (Norland) as in the JPK technical notes (found at http://www.jpk.com/afm.230.en.html). Green - membrane, red – actin, blue – DNA. Scale bars are 10µm. B) Matlab model generated from outline of fluorescent membrane of cell in (A) displaying the mean strain in constant strain triangle elements. C) Interpolated strain across elements in (B). Colour scale shows strain values (2 = 200%). A representation of the bead is shown (blue overlaid sphere) for demonstration purposes in (B) and (C).

This thesis has demonstrated two important, widespread, cellular response mechanisms: cellular shape recovery, and anisotropic deformations of the nucleus, that both occur in response to directed mechanical loads. In particular, cells were shown to possess an innate ability to recover their shape following mechanical loading, a response dominated by an interplay between

cytoskeletal and cytosolic components. This work stimulates future work surrounding how the actin cortex, membrane, and osmotic pressure coordinate to produce a concerted response during deformation and cell-shape recovery processes. While actomyosin contractility appears to be a key player in cell shape regulation, it is still unknown how it integrates with the flow of cytosol in the recovery process. Moreover, while we did not observe large volume changes during the deformation/recovery responses, it is possible that mechanical loading stimulates an increased exchange of fluid cytosol or ions across the membrane [354]. This exchange could stimulate a change in osmolarity or small changes in volume – that might be relieved by membrane tension [263] or cytoskeletal remodelling of the cortex [362]; avenues which should be actively explored in the future.

While the actin cortex was shown to be necessary for resistance-to and recovery-from deformations [335], microtubules appear to have a much smaller role in structurally supporting the cell [147], at least for HeLa cells. However, microtubules do appear to influence force transmission to the nucleus. Importantly, we characterized a clear nuclear anisotropy, apparent across many cell types. This led to questions surrounding its purpose - perhaps nuclear anisotropy directs gene regulation during embryonic development and morphogenesis? Considering their large role in mitosis, and the fact that undifferentiated nuclei produced less anisotropic deformations (see Chapter 5), perhaps microtubules contribute to the development of an intrinsic anisotropy – a characteristic that may increase during differentiation. Furthermore, a range of nuclear anisotropy was observed across cell types, suggesting that differences in nuclear organization should be examined.

This work importantly demonstrates that the cell and its components should not be represented by homogeneous, isotropic material properties, and that there is a clear need for an all-encompassing rheological model of the cell. Future FE models may be required to develop these complex models which should include dynamic interactions between cellular components. Moreover, this body of work has also demonstrated the need to examine differences in shape regulation between cell types. This work has evoked a number of questions for future research. Understanding these mechanical response mechanisms are important since, as mentioned throughout this thesis, mechanical cues have been shown to direct normal cellular processes [244, 246], including gene expression [126, 371]. Characterization of changes in cellular deformations, or bulk rheological properties of cells will undoubtedly play a crucial role in understanding the etiologic factors and pathogenesis of diseased states of the cell.

7 | Technical notes

7. 1 Cell culture & transfection protocols

7.1.1 Mammalian cell culture

1. Except where noted, all cells were cultured in 100ml dishes (Corning) at 37°C and 5% CO_2 in Dulbeco's Modified Eagle Medium (DMEM) with added 10% heat inactivated fetal bovine serum (FBS) and 1% penicillin (100 IU/mL) streptomycin (100 1g/mL) (Hyclone).
2. Once cells reached ~70% confluency, they were passaged and seeded onto 35mm glass bottom dishes (Mat Tek or laser-cut TPP plates affixed with 1.5 round glass coverslips) for two days, or until ~60% confluent.

7.1.2 Transient transfection of a plasma membrane and actin

Transfections were performed a day after seeding cells, and a day before combined AFM-LSCM experiments. Here, plasmids for the plekstrin homology (PH) domain of phospholipase C (PLC-δ) conjugated to an enhanced green fluorescent protein (EGFP) (PH-PLCδ-EGFP) and LifeAct-Ruby were used for transfections and have been described earlier by Pelling [196] and Hemsley [429]. The concentration and incubation period of the transfection reagents and plasmid solutions were adjusted for HeLa cells, and must be optimized if different cell types are to be employed.

1. Lipofectamine 2000 (LF2K) (Invitrogen) is first diluted in OptiMEM (Invitrogen); 2µl of LF2K in 48µL of OptiMEM, resulting in a 50µl solution.
2. Approximately 1µg of plasmid DNA each (both PH-PLC-δ-EGFP and LifeAct-Ruby) is diluted in a separate, but equivalent volume of OptiMEM.
3. Following 5 minutes, the LF2K solution is added to the plasmid DNA solution. Pipette up and down to mix gently, but thoroughly. This results in an OptiMEM solution containing a 1:1 ratio of LF2K-DNA.
4. Incubate the mixture in the hood at room temperature for 10 minutes. In the meantime, remove culture media from the glass bottom dishes and replace with 1ml of OptiMEM. Return the dishes to the incubator until the 10 minutes have passed.
5. Add the transfection mixture to the cells. Rock back and forth gently before returning to the incubator (37°C and 5% CO_2) for 20-30 minutes. Place culture media in the water bath at 37°C.
6. Remove transfection mixture completely by carefully suctioning it out with a glass pipette. Add 2ml of warmed culture media to the dishes.
7. Leave transfected cells overnight in the incubator.

7.2 AFM calibration

1. A silicon nitride cantilever (Pnp-tr-50, NanoWorld) is placed on the quartz head using a small amount of vacuum grease. The quartz head is then secured into place on the Nanowizard II (JPK Instruments) AFM head.

2. Using the JPK-SPM software's user interface, the AFM is retracted ~1000µm, in order to ensure it will not touch the sample surface (a glass slide for calibration). The AFM head is then positioned over the sample on an AFM stage (JPK Instruments), which sits on an inverted Nikon TiE A1-R high speed resonant laser scanning confocal microscope.
3. Using a separate camera connected to the microscope and the 10x objective, the triangular AFM cantilever is brought into focus. The dichroic mirror is used to view the AFM laser and position it at the end of the cantilever where the pyramidal tip is located.
4. After adjusting the laser mirrors (on the AFM head) and appropriate feedback gains using the JPK-SPM software, the cantilever is lowered towards the sample with a set-point of 1V.
5. Once the cantilever has approached and contacted the glass slide (Fig. 7.2 A), force-displacement curves are recorded with a low set-point voltage of 0.4V. Force curves are acquired continuously at 1Hz and a sampling rate of 512Hz.
6. Calibration of the cantilever's sensitivity is achieved by fitting the linear portion of the retract portion of the approach-retract curve (Fig. 7.2 B), thus resulting in a sensitivity of approximately 35-40mN/V.
7. Once the sensitivity has been selected, the cantilever is retracted away from the sample surface (~50µm) and the thermal fluctuation method is used to extract the cantilever stiffness [330].
8. The JPK-SPM software allows for an easy fit of the first resonant peak of the cantilever to a Lorentzian curve (Fig. 7.2 C), resulting in a spring constant of ~70mN/m, for these Pnp-tr-50 cantilevers (NanoWorld).
9. The cantilever is retracted far from the sample surface and the cantilever's sensitivity is now re-calibrated in distilled water (dH_2O) by first de-selecting the sensitivity previously acquired and completely removing the AFM head. Approximately 2ml of dH_2O was warmed in a separate glass bottom dish using a petri dish heater (JPK instruments).
10. A small drop of dimethyl sulfoxide (DMSO) was added to the tip of the cantilever before returning the AFM head above the sample. This step is performed in order to reduce the likelihood of bubbles attaching to the tip upon contact with the dH_2O. Be careful not to touch the cantilever. Absorb any excess DMSO with a Kimwipe.
11. Once the tip is in the liquid, the mirror inside the AFM head must be re-adjusted to account for the change in refractive index. The laser is re-aligned prior to approaching the bottom of the dish.
12. The cantilever is again set to approach the glass bottom surface of the dish and a new sensitivity is found for the cantilever in dH_2O, as in step 6. The sensitivity in distilled water is ~30-35mN/V.

Once the AFM tip has been calibrated in air and water, you are ready to perform an AFM experiment with cells in culture media. Do not to let the AFM cantilever dry before starting your experiment. It can be left in the distilled water at 37°C until the sample is ready.

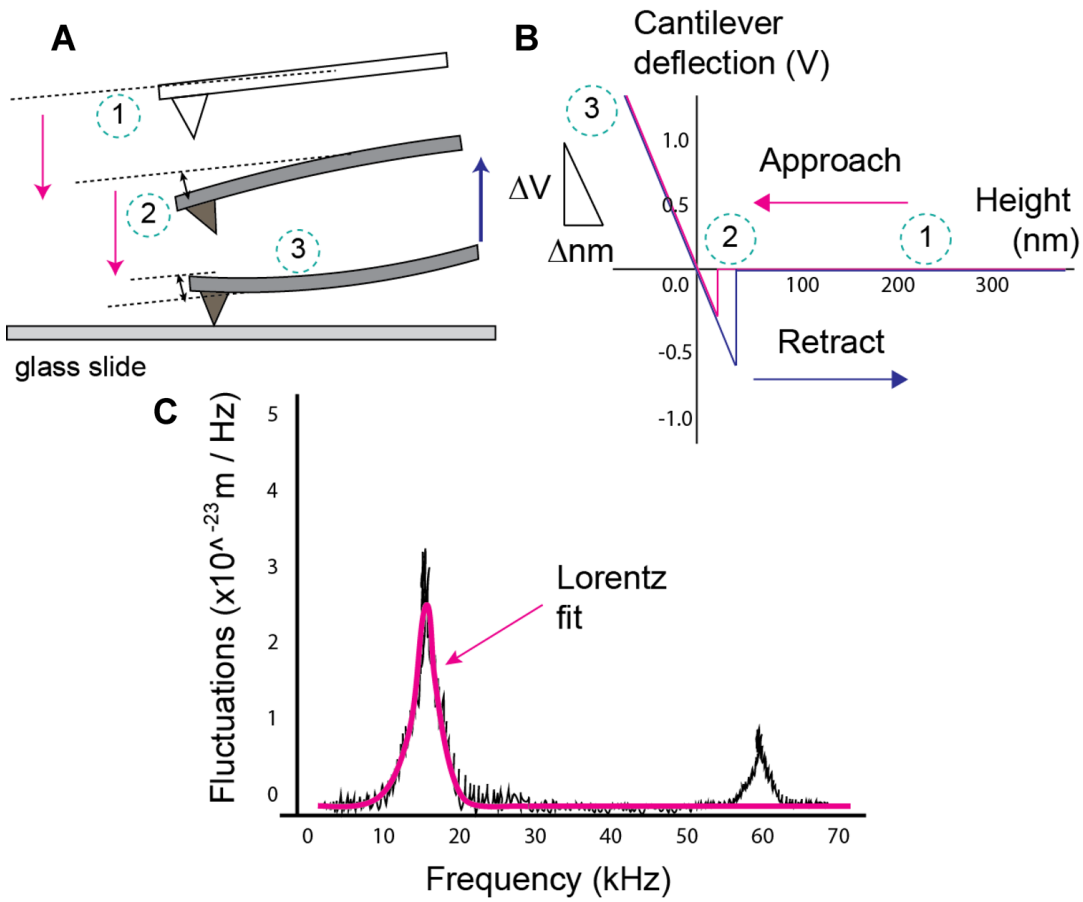

Figure 7.1 Calibration of the AFM cantilever on a hard glass substrate.
A) As the cantilever approaches the glass substrate (1) it nears the substrate and experiences a "jump to contact" (2), followed by a linear increase of cantilever deflection as the voltage increases until it reaches the voltage setpoint (3). B) An example of an approach/retract curve corresponding to the deflections seen in (A). The sensitivity is measured from the slope of the linear portion of contact between the cantilever tip and sample surface. C) Example of a thermal noise power spectrum, used with the thermal fluctuation method to determine the stiffness of the cantilever. This involves measurement of the frequency dependence of the thermal fluctuations of the cantilever. A Lorentz fit (of the first peak) is used to determine the energy associated with the resonance (areas under the curve). By the equipartition thereom, the energy of the free modes of this system (treated as a harmonic oscillator) are equal to $1/2\,k_bT$, where k_b is Boltzmann's constant. Therefore, assuming only one degree of freedom we have a relation between the energy and mean-squared vertical fluctuations of the cantilever: $1/2\,k_bT = 1/2\,k\langle x^2\rangle$, where x^2 (mean-squared vertical fluctuations) in the time domain can be represented by the power (P) in the frequency domain. This leads to the relation: $k = k_bT/P$, where P is measured as the area under the curve of the Lorentzian.

7.3 Combined AFM and LSCM

1. Immediately before performing the experiment, 1µg/ml of Hoescht 33342 (Invitrogen) (a known nuclear dye) is added to the transfected cells. Leave in the incubator at 37°C for 5-10 minutes. Following incubation, change the media before bringing the dish to the AFM-LSCM setup (Fig. 7.3 A).
2. Remove the AFM head and the dish with distilled water from the heater. Switch objectives from the 10x to the 60x/NA=1.2 water immersion objective lens.
3. Once the sample is placed into focus using the eyepiece, the AFM head is returned above the sample and the tip is set to approach the sample surface at a relatively low force of ~3-5nN.
4. Once the AFM cantilever is in contact with the surface, the tip is retracted by at least 50µm. This allows one to move the sample dish around without damaging the tip.
5. The LSCM is set to resonant mode and the appropriate filter blocks set. The 405nm laser is used excite the nuclear dye Hoescht 33342, while the 488nm and 546nm laser lines are used to excite the fluorescence of the PH-PLC-δ-EGFP (plasma membrane) and LifeAct-Ruby (actin cortex), respectively. The transmitted light detector is set to the "in" position in order to visualize the AFM tip in a pseudo-DIC image acquisition format.
6. A cell is chosen and the tip is moved either above or adjacent to the nucleus (Fig. 7.3 B). A digital zoom of 4 is used to clearly observe the fine adjustments of the AFM tip.
7. LSCM images can then be captured as a single plane time lapse or volume images (Fig. 7.3 C). First, the z-position of the scanner must be calibrated, and the thickness of each imaging plane is set to 0.5µm.

LSCM volume images can be adjusted to capture higher resolution orthogonal projections by decreasing the step-size. Scanning in resonant mode allows for rapid acquisition of images, up to 15 fps (four channels with 512 x 512 pixel resolution). Higher imaging rates (up >30 fps) can be obtained with smaller imaging regions.

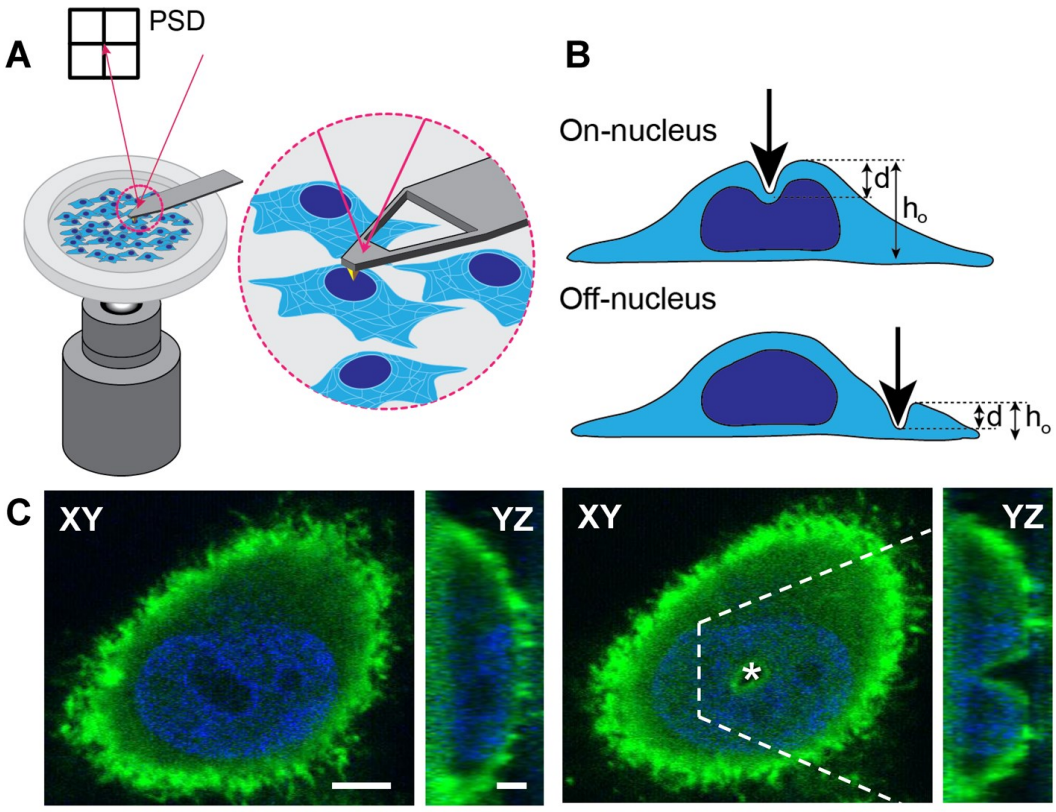

Figure 7.2 AFM/LSCM experimental setup.
A) Depiction of combined AFM/LSCM. A 60x water immersion objective is used to simulatneously image transiently transfected cells while applying precise nano-scale forces to cells using an AFM tip. Using built-in feedback mechanisms, reflection of a laser onto a photo-sensitive diode (PSD) indicates the amount of bending of the cantilever as it approaches the sample, thus allowing for precise control of force magnitude. B) Depiction of nano-scale forces applied above the nucleus and surrounding cytoplasm. The figure demonstrates how the deformation (d), and initial cell height (h_o) are measured from orthogonal planes as seen in (C), in order to approximate axial strain as $\varepsilon=d/h_o$ for both on-nucleus and off-nucleus loading. C) Confocal image of a HeLa cell prior to and following 10 minutes of deformation. Here, a 10nN force was applied to the cell above the nucleus, as visualized by the nuclear dye Hoescht 33342 (blue). By transiently transfecting cells with PH-PLC-δ-EGFP (green) the membrane, and its deformation, are readily observed. The deformation is directly observable by projecting the LSCM volume image in orthogonal planes (only YZ shown). Scale bars = 5µm.

7.4 Measuring cellular stiffness using AFM

7.4.1 AFM force-curves

Here, we describe the method for determining Youngs' modulus (E) of cells using AFM.

1. The AFM tip is positioned over the nucleus of the cell (observable by the nuclear dye Hoescht) (Fig. 7.3 A).
2. The cantilever is set to approach the cell with a low set-point force of 2nN.
3. After initial contact with the cell membrane, the tip repeatedly retracts and approaches the cell at a set frequency (10µm/s or less) with a relative set-point of 1nN at a sample rate of 512Hz.

4. The approach-retract curves are saved and used for analysis following repetitive measurements either on- or adjacent-to the cell's nucleus. An example curve can be found in Fig. 7.3 B).
5. Using Punias software [430], the first 200nm of indentation of the approach portion of the curve is fit to the Sneddon model [160], a modification of the Hertz model [431], by careful selection of the contact point between the tip and sample. The Poisson's ratio is set to 0.5 here, which is commonly used for biological samples (see the next section, 7.4.2).

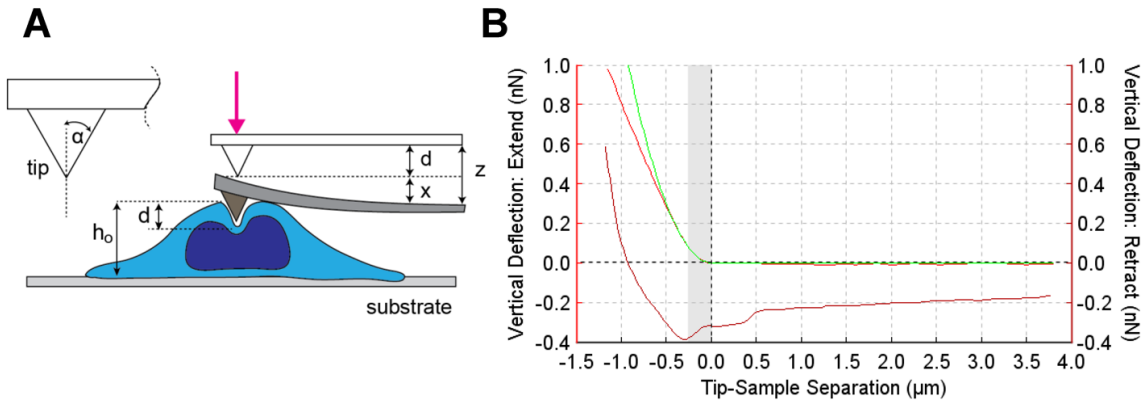

Figure 7.3 Measuring force-indentation curves.
A) Schematic of AFM tip deforming a cell (approach portion of the force-curve). The indentation of the sample, d, is related to the measured deflection of the cantilever (x) and cell height (z), by d=z-x. Where the deflection of the cantilever is related to the stiffness, k, of the cantilever, and force applied, by Hooke's law (F=kx). For fitting of the Hertz model, the opening angle of the tip must be known. Here α is shown for a conical tip (a simplification of a pyramidial tip) – α=35° for the tips used here. B) Example force-curve (JPK SPM software). Figure shows approach and retract portions of the force curve. Fit (light green line) of the first 200nm of indentation to the modified Hertz model (for a conical indentor) is highlighted in grey.

7.4.2 Fitting force-curves to the modified Hertz model

One of the most frequently investigated material properties of cells is its Young's (or elastic) modulus. The elastic modulus is important as it gives us an idea of the cell's stiffness, which is largely known to be influenced by the cytoskeletal network. This property is well known to be cell type dependent, and has been shown to range between 100's-1000's of Pa. Here, the AFM was employed to measure the elastic modulus of HeLa cells for all treated and untreated populations used in the experiments. Employing the nuclear dye Hoescht 33342 allowed us to position the AFM tip either above the center of the cell's nucleus, or in adjacent cytoplasmic regions. Force-indentation curves were obtained by first approaching the tip towards the cell with a low set-point of 2nN, followed by oscillations of the tip with a relative set-point of 1nN at a rate of 10µm/s. The first 200nm of the force-indentation curves were then fit to the modified Hertz contact model [331] using Punias software [430]. Herein, the Hertz model for a conical indenter was used as an approximation and has the general form:

$$F = \frac{E}{1-\upsilon^2} ad \qquad [7.1]$$

Where F is the applied force (1nN), E is the Young's modulus (determined by the fit), a Poisson's ratio of $\upsilon = 0.5$ is used, and d is the indentation of the tip within the sample. The indentation (d) is calculated by subtracting the cantilever deflection (x) from the measured cell height (z):

$$d = z - x$$

Where x is related to the applied force (F) via Hookes' law:

$$F = kx \qquad [7.2]$$

The spring constant, k, was determined by calibrating the AFM cantilever by the thermal fluctuation method (k = 0.07 ± 0.03N/m) [330].

The semi-opening angle of the cone is:

$$a = \frac{2tan\alpha}{\pi} d \qquad [7.3]$$

Where α is approximated by the cantilever manufacturer's (Veeco) reported opening angle of 35°.

7.5 Image and statistical analysis

Open source software, ImageJ (http://rsbweb.nih.gov/ij/), was used for all image analysis. Origin data analysis and graphing software (v.7, v.8.3, and v.9.1) were used (http://www.originlab.com/) for all graphing and statistics throughout this thesis.

8 | Conclusions

The influence of mechanical cues in directing central cellular processes is undeniable. However, many questions still surround the mechanics involved in the translation of physical cues to a cascade of biochemical responses (discussed in Chapter 1). In this light, this compendium of experimental work has demonstrated a systematic characterization of cellular mechanics, which is crucial for our understanding of mechanotranduction. We have focused our examination on the deformation behaviour of major cellular components, namely the plasma membrane, its underlying cortex, and the nucleus. By employing combined AFM-LSCM techniques in a variety of ways, we were able to examine the cellular response to directed forces. Visual imaging techniques were used to examine the dynamics involved, while various treatments aided in the identification of key cellular players, while attempting to explain the mechanics using models.

In an initial study (Chapter 2) we revealed that the membrane and cortex of a human cervical cancer cell line (HeLa cells) are highly resilient, and can withstand large magnitude local forces. Importantly, the majority of these cells were shown to deform and recover without permanent damage or membrane rupture. The cytoskeleton, particularly the cortical actin network, was found to be predominantly responsible for resistance to these external forces. Microtubules, on the other hand, were not important despite previous views of these filaments as compression-resistant (Chapter 3). Contrary to previous reports, we demonstrated that the large-volume nucleus of HeLa cells are in fact soft, and surprisingly do not significantly contribute to the recovery mechanics of these cells.

While many studies have focused on the deformation mechanics of a variety of cells, only a limited number have attempted to characterize cell shape recovery processes. To address this gap in knowledge, we characterized cell shape recovery through examination of recovery time constants of both the membrane and underlying cortex (Chapter 4). We demonstrated that the coupled membrane and cortex deform and recover simultaneously - a response determined to depend mainly on actomyosin contractility and osmotic pressure. By examining several other epithelial cell lines, we also demonstrated that the ability to recover cell-shape is likely a pervasive process. We noted, however, that the response time varied drastically between cells, a difference that must be fully addressed in future studies.

The final focus of this thesis revealed important nuclear mechanical properties (Chapter 5). As gene regulator and host, the nucleus and its mechanical properties are of high interest to the biophysical community. Previous notions of the nucleus as a simplified isotropic mechanical component have recently been challenged by observations of anisotropic behaviours in response to mechanical forces. We explore this mechanical anisotropy, and demonstrate that elliptical nuclei deform preferentially along their short axis in response to a compressive local force. Importantly, nuclear anisotropy was observed in a variety of cells from established and primary cultures. While the reason behind this behaviour remains unknown, we have demonstrated that while the cytoskeleton does influence anisotropy, it is an intrinsic nuclear characteristic. Chromatin organization was revealed as a potential regulator of this behaviour, while well-known structural

components, lamins, were not. This study suggests that future investigations should avoid treating the nucleus as a simple isotropic component, as nuclear anisotropy appears to be a widespread cellular phenomenon.

Overall, this work reveals two seemingly ubiquitous cellular reactions that occur in response to directed mechanical cues: anisotropic nuclear deformations, and the ability to recover cell shape. Although a simplification of the true nature of the cell, viscoelastic models were reasonably used to characterize these responses and identify key cellular players involved. This work stimulates many more questions for future exploration: How does the actomyosin network integrate with the flow of cytosol in the recovery process? Why do cells of the same type, but from various species, respond at varying rates? What is the purpose of nuclear anisotropy? Does it play a role in gene regulation during embryonic development and morphogenesis? Moreover, there is still a need for an all-encompassing rheological model of the cell. This study provides the foundation for future finite element based models, which will be necessary for characterization of complex mechanical properties (as discussed in Chapter 6). Highlighting the response to mechanical forces, as well as identifying cellular mechanical properties are critical and have already proven beneficial for the identification of healthy and diseased cells.

9 | References

1. Lucey BP, Nelson-Rees WA and Hutchins GM. Henrietta Lacks, HeLa Cells, and Cell Culture Contamination. *Arch Pathol Lab Med*. 2009; 133: 1463-7.
2. Skloot R and Turpin B. *The immortal life of Henrietta Lacks*. Crown Publishers New York, 2010.
3. Callaway E. *Deal done over HeLa cell line*. Nature. 2013 Aug 8;500(7461):132-3. doi: 10.1038/500132a.
4. Heckman C, Kanagasundaram S, Cayer M and Paige J. Preparation of cultured cells for scanning electron microscope. 2007.
5. Bao G and Suresh S. Cell and molecular mechanics of biological materials. *Nat Mater*. 2003; 2: 715-25.
6. Buxboim A, Ivanovska IL and Discher DE. Matrix elasticity, cytoskeletal forces and physics of the nucleus: how deeply do cells 'feel' outside and in? *J Cell Sci*. 2010; 123: 297-308.
7. Janmey PA and Miller RT. Mechanisms of mechanical signaling in development and disease. *J Cell Sci*. 2011; 124: 9-18.
8. White CR and Frangos JA. The shear stress of it all: the cell membrane and mechanochemical transduction. *Philos T R Soc B*. 2007; 362: 1459-67.
9. Huiskes R, Ruimerman R, van Lenthe GH and Janssen JD. Effects of mechanical forces on maintenance and adaptation of form in trabecular bone. *Nature*. 2000; 405: 704-6.
10. Sumpio BE, Banes AJ, Levin LG and Johnson G. Mechanical-Stress Stimulates Aortic Endothelial-Cells to Proliferate. *J Vasc Surg*. 1987; 6: 252-6.
11. Neidlinger-Wilke C, Grood ES, Wang JHC, Brand RA and Claes L. Cell alignment is induced by cyclic changes in cell length: studies of cells grown in cyclically stretched substrates. *J Orthopaed Res*. 2001; 19: 286-93.
12. Moretti M, Prina-Mello A, Reid AJ, Barron V and Prendergast PJ. Endothelial cell alignment on cyclically-stretched silicone surfaces. *J Mater Sci-Mater M*. 2004; 15: 1159-64.
13. Wang JHC, Goldschmidt-Clermont P, Wille J and Yin FCP. Specificity of endothelial cell reorientation in response to cyclic mechanical stretching. *Journal of Biomechanics*. 2001; 34: 1563-72.
14. Malek AM and Izumo S. Mechanism of endothelial cell shape change and cytoskeletal remodeling in response to fluid shear stress. *Journal of Cell Science*. 1996; 109: 713-26.
15. Guolla L, Bertrand M, Haase K and Pelling AE. Force transduction and strain dynamics in actin stress fibres in response to nanonewton forces. *J Cell Sci*. 2012; 125: 603-13.
16. Pravincumar P, Bader DL and Knight MM. Viscoelastic Cell Mechanics and Actin Remodelling Are Dependent on the Rate of Applied Pressure. *Plos One*. 2012; 7.
17. Lee CF, Haase C, Deguchi S and Kaunas R. Cyclic stretch-induced stress fiber dynamics - Dependence on strain rate, Rho-kinase and MLCK. *Biochem Bioph Res Co*. 2010; 401: 344-9.
18. Jungbauer S, Gao HJ, Spatz JP and Kemkemer R. Two characteristic regimes in frequency-dependent dynamic reorientation of fibroblasts on cyclically stretched substrates. *Biophys J*. 2008; 95: 3470-8.
19. Tondon A, Hsu HJ and Kaunas R. Dependence of cyclic stretch-induced stress fiber reorientation on stretch waveform. *Journal of Biomechanics*. 2012; 45: 728-35.
20. Wang N, Butler JP and Ingber DE. Mechanotransduction across the Cell-Surface and through the Cytoskeleton. *Science*. 1993; 260: 1124-7.
21. Dahl KN and Kalinowski A. Nucleoskeleton mechanics at a glance. *J Cell Sci*. 2011; 124: 675-8.
22. Booth-Gauthier EA, Alcoser TA, Yang G and Dahl KN. Force-Induced Changes in Subnuclear Movement and Rheology. *Biophys J*. 2012; 103: 2423-31.
23. Veigel C and Schmidt CF. Moving into the cell: single-molecule studies of molecular motors in complex environments. *Nature Reviews Molecular Cell Biology*. 2011; 12: 163-76.
24. Chaudhuri O and Fletcher DA. Protrusive Forces Generated by Dendritic Actin Networks During Cell Crawling. *Actin-based Motility*. Springer, 2010, p. 359-79.
25. Ji L, Lim J and Danuser G. Fluctuations of intracellular forces during cell protrusion. *Nat Cell Biol*. 2008; 10: 1393-400.
26. Ananthakrishnan R and Ehrlicher A. The forces behind cell movement. *Int J Biol Sci*. 2007; 3: 303-17.

27. Moore JK and Cooper JA. Coordinating mitosis with cell polarity: Molecular motors at the cell cortex. *Semin Cell Dev Biol*. 2010; 21: 283-9.
28. Reinhart-King CA, Dembo M and Hammer DA. Cell-Cell Mechanical Communication through Compliant Substrates. *Biophys J*. 2008; 95: 6044-51.
29. Sachs F. Stretch-Activated Ion Channels: What Are They? *Physiology*. 2010; 25: 50-6.
30. Shyy JY and Chien S. Role of integrins in endothelial mechanosensing of shear stress. *Circulation Research*. 2002; 91: 769-75.
31. Malone AMD, Anderson CT, Tummala P, et al. Primary cilia mediate mechanosensing in bone cells by a calcium-independent mechanism (vol 104, pg 13325, 2007). *P Natl Acad Sci USA*. 2008; 105: 825-.
32. Hoffman BD, Grashoff C and Schwartz MA. Dynamic molecular processes mediate cellular mechanotransduction. *Nature*. 2011; 475: 316-23.
33. Yamada S, Wirtz D and Kuo SC. Mechanics of living cells measured by laser tracking microrheology. *Biophys J*. 2000; 78: 1736-47.
34. Girard KD, Kuo SC and Robinson DN. Dictyostelium myosin II mechanochemistry promotes active behavior of the cortex on long time scales. *P Natl Acad Sci USA*. 2006; 103: 2103-8.
35. Jonas M, Huang HD, Kamm RD and So PTC. Fast fluorescence laser tracking microrheometry, II: Quantitative studies of cytoskeletal mechanotransduction. *Biophys J*. 2008; 95: 895-909.
36. Jonas M, Huang H, Kamm RD and So PTC. Fast fluorescence laser tracking microrheometry, I: Instrument development. *Biophys J*. 2008; 94: 1459-69.
37. Hoffman BD, Massiera G, Van Citters KM and Crocker JC. The consensus mechanics of cultured mammalian cells. *P Natl Acad Sci USA*. 2006; 103: 10259-64.
38. Crocker JC and Hoffman BD. Multiple-particle tracking and two-point microrheology in cells. *Method Cell Biol*. 2007; 83: 141-78.
39. Gardel ML, Valentine MT, Crocker JC, Bausch AR and Weitz DA. Microrheology of entangled F-actin solutions. *Phys Rev Lett*. 2003; 91.
40. Deng LH, Trepat X, Butler JP, et al. Fast and slow dynamics of the cytoskeleton. *Nat Mater*. 2006; 5: 636-40.
41. Stamenovic D, Rosenblatt N, Montoya-Zavala M, et al. Rheological Behavior of living cells is timescale-dependent. *Biophys J*. 2007; 93: L39-L41.
42. Massiera G, Van Citters KM, Biancaniello PL and Crocker JC. Mechanics of single cells: Rheology, time depndence, and fluctuations. *Biophys J*. 2007; 93: 3703-13.
43. Trepat X, Grabulosa M, Puig F, Maksym GN, Navajas D and Farre R. Viscoelasticity of human alveolar epithelial cells subjected to stretch. *American Journal of Physiology-Lung Cellular and Molecular Physiology*. 2004; 287: L1025-L34.
44. Desprat N, Richert A, Simeon J and Asnacios A. Creep function of a single living cell. *Biophys J*. 2005; 88: 2224-33.
45. Zhou EH, Quek ST and Lim CT. Power-law rheology analysis of cells undergoing micropipette aspiration. *Biomech Model Mechan*. 2010; 9: 563-72.
46. Balland M, Richert A and Gallet F. The dissipative contribution of myosin II in the cytoskeleton dynamics of myoblasts. *Eur Biophys J Biophy*. 2005; 34: 255-61.
47. Wei MT, Zaorski A, Yalcin HC, et al. A comparative study of living cell micromechanical properties by oscillatory optical tweezers. *Opt Express*. 2008; 16: 8594-603.
48. Yanai M, Butler JP, Suzuki T, Sasaki H and Higuchi H. Regional rheological differences in locomoting neutrophils. *Am J Physiol-Cell Ph*. 2004; 287: C603-C11.
49. Silberberg YR, Pelling AE, Yakubov GE, Crum WR, Hawkes DJ and Horton MA. Mitochondrial displacements in response to nanomechanical forces. *J Mol Recognit*. 2008; 21: 30-6.
50. Charras GT and Horton MA. Single cell mechanotransduction and its modulation analyzed by atomic force microscope indentation. *Biophys J*. 2002; 82: 2970-81.
51. Gardel ML, Shin JH, MacKintosh FC, Mahadevan L, Matsudaira P and Weitz DA. Elastic Behavior of cross-linked and bundled actin networks. *Science*. 2004; 304: 1301-5.
52. Suresh S. Biomechanics and biophysics of cancer cells. *Acta Mater*. 2007; 55: 3989-4014.

53. Charras GT, Mitchison TJ and Mahadevan L. Animal cell hydraulics. *Journal of cell science*. 2009; 122: 3233-41.
54. Poh YC, Shevtsov SP, Chowdhury F, et al. Dynamic force-induced direct dissociation of protein complexes in a nuclear body in living cells. *Nat Commun*. 2012; 3.
55. Mathur AB, Collinsworth AM, Reichert WM, Kraus WE and Truskey GA. Endothelial, cardiac muscle and skeletal muscle exhibit different viscous and elastic properties as determined by atomic force microscopy. *Journal of Biomechanics*. 2001; 34: 1545-53.
56. Kuznetsova TG, Starodubtseva MN, Yegorenkov NI, Chizhik SA and Zhdanov RI. Atomic force microscopy probing of cell elasticity. *Micron*. 2007; 38: 824-33.
57. Kamgoue A, Ohayon J and Tracqui P. Estimation of cell young's modulus of adherent cells probed by optical and magnetic tweezers: Influence of cell thickness and bead immersion. *J Biomech Eng-T Asme*. 2007; 129: 523-30.
58. Fabry B, Maksym GN, Butler JP, et al. Time scale and other invariants of integrative mechanical behavior in living cells. *Phys Rev E*. 2003; 68.
59. Orr AW, Helmke BP, Blackman BR and Schwartz MA. Mechanisms of mechanotransduction. *Dev Cell*. 2006; 10: 11-20.
60. Sawada Y, Tamada M, Dubin-Thaler BJ, et al. Force sensing by mechanical extension of the Src family kinase substrate p130Cas. *Cell*. 2006; 127: 1015-26.
61. Hoffman BD and Crocker JC. Cell Mechanics: Dissecting the Physical Responses of Cells to Force. *Annual Review of Biomedical Engineering*. 2009; 11: 259-88.
62. Yim EKF, Darling EM, Kulangara K, Guilak F and Leong KW. Nanotopography-induced changes in focal adhesions, cytoskeletal organization, and mechanical properties of human mesenchymal stem cells. *Biomaterials*. 2010; 31: 1299-306.
63. Provenzano PP and Keely PJ. Mechanical signaling through the cytoskeleton regulates cell proliferation by coordinated focal adhesion and Rho GTPase signaling. *Journal of Cell Science*. 2011; 124: 1195-205.
64. Reilly GC and Engler AJ. Intrinsic extracellular matrix properties regulate stem cell differentiation. *Journal of Biomechanics*. 2010; 43: 55-62.
65. Discher DE, Janmey P and Wang YL. Tissue cells feel and respond to the stiffness of their substrate. *Science*. 2005; 310: 1139-43.
66. Pelham RJ and Wang YL. Cell locomotion and focal adhesions are regulated by substrate flexibility. *P Natl Acad Sci USA*. 1997; 94: 13661-5.
67. Evans ND, Minelli C, Gentleman E, et al. Substrate Stiffness Affects Early Differentiation Events in Embryonic Stem Cells. *Eur Cells Mater*. 2009; 18: 1-14.
68. Spatz JP and Geiger B. Molecular engineering of cellular environments: Cell adhesion to nano-digital surfaces. *Method Cell Biol*. 2007; 83: 89-+.
69. Discher DE, Sweeney L, Sen S and Engler A. Matrix elasticity directs stem cell lineage specification. *Biophys J*. 2007: 32a-a.
70. Xia N, Thodeti CK, Hunt TP, et al. Directional control of cell motility through focal adhesion positioning and spatial control of Rac activation. *Faseb J*. 2008; 22: 1649-59.
71. Ladoux B, Anon E, Lambert M, et al. Strength Dependence of Cadherin-Mediated Adhesions. *Biophys J*. 2010; 98: 534-42.
72. Mertz AF, Che YL, Banerjee S, et al. Cadherin-based intercellular adhesions organize epithelial cell-matrix traction forces. *P Natl Acad Sci USA*. 2013; 110: 842-7.
73. Geiger B and Bershadsky A. Exploring the neighborhood: Adhesion-coupled cell mechanosensors. *Cell*. 2002; 110: 139-42.
74. Sokabe M, Naruse K, Sai S, et al. Mechanotransduction and intracellular signaling mechanisms of stretch-induced remodeling in endothelial cells. *Heart Vessels*. 1997: 191-3.
75. Lansman JB, Hallam TJ and Rink TJ. Single Stretch-Activated Ion Channels in Vascular Endothelial-Cells as Mechanotransducers. *Nature*. 1987; 325: 811-3.
76. Guharay F and Sachs F. Stretch-Activated Single Ion Channel Currents in Tissue-Cultured Embryonic Chick Skeletal-Muscle. *J Physiol-London*. 1984; 352: 685-701.

77. Harburger DS and Calderwood DA. Integrin signalling at a glance. *Journal of Cell Science*. 2009; 122: 159-63.
78. Riveline D, Zamir E, Balaban NQ, et al. Focal contacts as mechanosensors: Externally applied local mechanical force induces growth of focal contacts by an mDia1-dependent and ROCK-independent mechanism. *J Cell Biol*. 2001; 153: 1175-85.
79. Geiger B and Bershadsky A. Assembly and mechanosensory function of focal contacts. *Current Opinion in Cell Biology*. 2001; 13: 584-92.
80. ChrzanowskaWodnicka M and Burridge K. Rho-stimulated contractility drives the formation of stress fibers and focal adhesions. *J Cell Biol*. 1996; 133: 1403-15.
81. Helfman DM, Levy ET, Berthier C, et al. Caldesmon inhibits nonmuscle cell contractility and interferes with the formation of focal adhesions. *Molecular Biology of the Cell*. 1999; 10: 3097-112.
82. Knies Y, Bernd A, Kaufmann R, Bereiter-Hahn J and Kippenberger S. Mechanical stretch induces clustering of beta 1-integrins and facilitates adhesion. *Exp Dermatol*. 2006; 15: 347-55.
83. Shikata Y, Rios A, Kawkitinarong K, DePaola N, Garcia JGN and Birukov KG. Differential effects of shear stress and cyclic stretch on focal adhesion remodeling, site-specific FAK phosphorylation, and small GTPases in human lung endothelial cells. *Exp Cell Res*. 2005; 304: 40-9.
84. Yoshigi M, Hoffman LM, Jensen CC, Yost HJ and Beckerle MC. Mechanical force mobilizes zyxin from focal adhesions to actin filaments and regulates cytoskeletal reinforcement. *J Cell Biol*. 2005; 171: 209-15.
85. Young SRL, Gerard-O'Riley R, Kim JB and Pavalko FM. Focal Adhesion Kinase Is Important for Fluid Shear Stress-Induced Mechanotransduction in Osteoblasts. *J Bone Miner Res*. 2009; 24: 411-24.
86. Tzima E, del Pozo MA, Shattil SJ, Chien S and Schwartz MA. Activation of integrins in endothelial cells by fluid shear stress mediates Rho-dependent cytoskeletal alignment. *Embo J*. 2001; 20: 4639-47.
87. Wang N and Suo ZG. Long-distance propagation of forces in a cell. *Biochem Bioph Res Co*. 2005; 328: 1133-8.
88. Yap B and Kamm RD. Cytoskeletal remodeling and cellular activation during deformation of neutrophils into narrow channels. *Journal of Applied Physiology*. 2005; 99: 2323-30.
89. Bursac P, Lenormand G, Fabry B, et al. Cytoskeletal remodelling and slow dynamics in the living cell. *Nat Mater*. 2005; 4: 557-61.
90. Fabry B and Fredberg JJ. Remodeling of the airway smooth muscle cell: are we built of glass? *Resp Physiol Neurobi*. 2003; 137: 109-24.
91. Trepat X, Deng LH, An SS, et al. Universal physical responses to stretch in the living cell. *Nature*. 2007; 447: 592-+.
92. Krishnan R, Park CY, Lin YC, et al. Reinforcement versus Fluidization in Cytoskeletal Mechanoresponsiveness. *Plos One*. 2009; 4.
93. Levayer R and Lecuit T. Biomechanical regulation of contractility: spatial control and dynamics. *Trends in Cell Biology*. 2012; 22: 61-81.
94. Yogurtcu ON, Kim JS and Sun SX. A Mechanochemical Model of Actin Filaments. *Biophys J*. 2012; 103: 719-27.
95. Alenghat FJ and Ingber DE. Mechanotransduction: all signals point to cytoskeleton, matrix, and integrins. *Science Signaling*. 2002; 2002: pe6.
96. Ukropec JA, Hollinger MK and Woolkalis MJ. Regulation of VE-cadherin linkage to the cytoskeleton in endothelial cells exposed to fluid shear stress. *Exp Cell Res*. 2002; 273: 240-7.
97. Salbreux G, Charras G and Paluch E. Actin cortex mechanics and cellular morphogenesis. *Trends in Cell Biology*. 2012; 22: 536-45.
98. Kunda P, Pelling AE, Liu T and Baum B. Moesin controls cortical rigidity, cell rounding, and spindle morphogenesis during mitosis. *Curr Biol*. 2008; 18: 91-101.
99. Saarikangas J, Zhao HX and Lappalainen P. Regulation of the Actin Cytoskeleton-Plasma Membrane Interplay by Phosphoinositides. *Physiol Rev*. 2010; 90: 259-89.
100. Diz-Munoz A, Krieg M, Bergert M, et al. Control of Directed Cell Migration In Vivo by Membrane-to-Cortex Attachment. *Plos Biol*. 2010; 8.
101. Charras GT, Hu CK, Coughlin M and Mitchison TJ. Reassembly of contractile actin cortex in cell blebs. *J Cell Biol*. 2006; 175: 477-90.

102. Goldman RD, Grin B, Mendez MG and Kuczmarski ER. Intermediate filaments: versatile building blocks of cell structure. *Current Opinion in Cell Biology*. 2008; 20: 28-34.
103. Brangwynne CP, MacKintosh FC, Kumar S, et al. Microtubules can bear enhanced compressive loads in living cells because of lateral reinforcement. *J Cell Biol*. 2006; 173: 733-41.
104. Wang N, Tytell JD and Ingber DE. Mechanotransduction at a distance: mechanically coupling the extracellular matrix with the nucleus. *Nature Reviews Molecular Cell Biology*. 2009; 10: 75-82.
105. Weinbaum S, Tarbell JM and Damiano ER. The structure and function of the endothelial glycocalyx layer. *Annual Review of Biomedical Engineering*. 2007; 9: 121-67.
106. Tarbell JM and Pahakis MY. Mechanotransduction and the glycocalyx. *J Intern Med*. 2006; 259: 339-50.
107. Mulivor AW and Lipowsky HH. Role of glycocalyx in leukocyte-endothelial cell adhesion. *Am J Physiol-Heart C*. 2002; 283: H1282-H91.
108. Tarbell JM, Weinbaum S and Kamm RD. Cellular fluid mechanics and mechanotransduction. *Ann Biomed Eng*. 2005; 33: 1719-23.
109. Dimmeler S, Fleming I, Fisslthaler B, Hermann C, Busse R and Zeiher AM. Activation of nitric oxide synthase in endothelial cells by Akt-dependent phosphorylation. *Nature*. 1999; 399: 601-5.
110. Florian JA, Kosky JR, Ainslie K, Pang ZY, Dull RO and Tarbell JM. Heparan sulfate proteoglycan is a mechanosensor on endothelial cells. *Circulation Research*. 2003; 93: E136-E42.
111. Pahakis MY, Kosky JR, Dull RO and Tarbell JM. The role of endothelial glycocalyx components in mechanotransduction of fluid shear stress. *Biochem Bioph Res Co*. 2007; 355: 228-33.
112. Weinbaum S, Zhang XB, Han YF, Vink H and Cowin SC. Mechanotransduction and flow across the endothelial glycocalyx. *P Natl Acad Sci USA*. 2003; 100: 7988-95.
113. Squire JM, Chew M, Nneji G, Neal C, Barry J and Michel C. Quasi-periodic substructure in the microvessel endothelial glycocalyx: A possible explanation for molecular filtering? *J Struct Biol*. 2001; 136: 239-55.
114. Alonso MA and Millan J. The role of lipid rafts in signalling and membrane trafficking in T lymphocytes. *Journal of Cell Science*. 2001; 114: 3957-65.
115. Jacobson K, Mouritsen OG and Anderson RGW. Lipid rafts: at a crossroad between cell biology and physics. *Nat Cell Biol*. 2007; 9: 7-14.
116. Quest AFG, Leyton L and Parraga M. Caveolins, caveolae, and lipid rafts in cellular transport, signaling, and disease. *Biochem Cell Biol*. 2004; 82: 129-44.
117. Brazer SCW, Singh BB, Liu XB, Swaim W and Ambudkar IS. Caveolin-1 contributes to assembly of store-operated Ca2+ influx channels by regulating plasma membrane localization of TRPC1. *J Biol Chem*. 2003; 278: 27208-15.
118. Murata T, Lin MI, Stan RV, Bauer PM, Yu J and Sessa WC. Genetic evidence supporting caveolae microdomain regulation of calcium entry in endothelial cells. *J Biol Chem*. 2007; 282: 16631-43.
119. Pani B and Singh BB. Lipid rafts/caveolae as microdomains of calcium signaling. *Cell Calcium*. 2009; 45: 625-33.
120. Ferraro JT, Daneshmand M, Bizios R and Rizzo V. Depletion of plasma membrane cholesterol dampens hydrostatic pressure and shear stress-induced mechanotransduction pathways in osteoblast cultures. *Am J Physiol-Cell Ph*. 2004; 286: C831-C9.
121. Satir P, Pedersen LB and Christensen ST. The primary cilium at a glance. *Journal of Cell Science*. 2010; 123: 499-503.
122. Nguyen AM and Jacobs CR. Emerging role of primary cilia as mechanosensors in osteocytes. *Bone*. 2013; 54: 196-204.
123. Rydholm S, Zwartz G, Kowalewski JM, Kamali-Zare P, Frisk T and Brismar H. Mechanical properties of primary cilia regulate the response to fluid flow. *Am J Physiol-Renal*. 2010; 298: F1096-F102.
124. Dalby MJ. Topographically induced direct cell mechanotransduction. *Med Eng Phys*. 2005; 27: 730-42.
125. Crisp M, Liu Q, Roux K, et al. Coupling of the nucleus and cytoplasm: role of the LINC complex. *J Cell Biol*. 2006; 172: 41-53.
126. Dahl KN, Ribeiro AJS and Lammerding J. Nuclear shape, mechanics, and mechanotransduction. *Circulation research*. 2008; 102: 1307-18.
127. Misteli T. Beyond the sequence: Cellular organization of genome function. *Cell*. 2007; 128: 787-800.
128. Pederson T. Half a century of "the nuclear matrix". *Molecular Biology of the Cell*. 2000; 11: 799-805.

129. Lammerding J, Fong LG, Ji JY, et al. Lamins A and C but not lamin B1 regulate nuclear mechanics. *J Biol Chem*. 2006; 281: 25768-80.
130. Broers JLV, Bronnenberg NMHJ, Kuijpers HJH, Schutte B, Hutchison CJ and Ramaekers FCS. Partial cleavage of A-type lamins concurs with their total disintegration from the nuclear lamina during apoptosis. *Eur J Cell Biol*. 2002; 81: 677-91.
131. Constantinescu D, Gray HL, Sammak PJ, Schatten GP and Csoka AB. Lamin A/C expression is a marker of mouse and human embryonic stem cell differentiation (vol 24, pg 177, 2006). *Stem Cells*. 2006; 24: 474-.
132. Dechat T, Pfleghaar K, Sengupta K, et al. Nuclear lamins: major factors in the structural organization and function of the nucleus and chromatin. *Gene Dev*. 2008; 22: 832-53.
133. Wozniak MA and Chen CS. Mechanotransduction in development: a growing role for contractility. *Nature Reviews Molecular Cell Biology*. 2009; 10: 34-43.
134. Huxley AF and Simmons RM. Proposed Mechanism of Force Generation in Striated Muscle. *Nature*. 1971; 233: 533-&.
135. Mogilner A and Oster G. Cell motility driven by actin polymerization. *Biophys J*. 1996; 71: 3030-45.
136. Pronk S, Geissler PL and Fletcher DA. Limits of filopodium stability. *Phys Rev Lett*. 2008; 100.
137. Blanchoin L, Amann KJ, Higgs HN, Marchand JB, Kaiser DA and Pollard TD. Direct observation of dendritic actin filament networks nucleated by Arp2/3 complex and WASP/Scar proteins. *Nature*. 2000; 404: 1007-11.
138. Fletcher DA and Geissler PL. Active Biological Materials. *Annu Rev Phys Chem*. 2009; 60: 469-86.
139. Magdalena J, Millard TH and Machesky LM. Microtubule involvement in NIH 3T3 Golgi and MTOC polarity establishment. *Journal of Cell Science*. 2003; 116: 743-56.
140. Waterman-Storer CM, Worthylake RA, Liu BP, Burridge K and Salmon ED. Microtubule growth activates Rac1 to promote lamellipodial profusion in fibroblasts. *Nat Cell Biol*. 1999; 1: 45-50.
141. Sankaranarayanan S, Atluri PP and Ryan TA. Actin has a molecular scaffolding, not propulsive, role in presynaptic function. *Nat Neurosci*. 2003; 6: 127-35.
142. Theriot JA and Mitchison TJ. Actin Microfilament Dynamics in Locomoting Cells. *Nature*. 1991; 352: 126-31.
143. Svitkina TM and Borisy GG. Arp2/3 complex and actin depolymerizing factor cofilin in dendritic organization and treadmilling of actin filament array in lamellipodia. *J Cell Biol*. 1999; 145: 1009-26.
144. Pollard TD, Blanchoin L and Mullins RD. Molecular mechanisms controlling actin filament dynamics in nonmuscle cells. *Annu Rev Bioph Biom*. 2000; 29: 545-76.
145. Falzone TT, Oakes PW, Sees J, Kovar DR and Gardel ML. Actin Assembly Factors Regulate the Gelation Kinetics and Architecture of F-actin Networks. *Biophys J*. 2013; 104: 1709-19.
146. Lazarides E. Actin, Alpha-Actinin, and Tropomyosin Interaction in Structural Organization of Actin-Filaments in Nonmuscle Cells. *J Cell Biol*. 1976; 68: 202-19.
147. Heintzelman MB and Mooseker MS. Assembly of the Intestinal Brush-Border Cytoskeleton. *Curr Top Dev Biol*. 1992; 26: 93-122.
148. Rodriguez OC, Schaefer AW, Mandato CA, Forscher P, Bement WM and Waterman-Storer CM. Conserved microtubule-actin interactions in cell movement and morphogenesis. *Nat Cell Biol*. 2003; 5: 599-609.
149. Wittmann T and Waterman-Storer CM. Cell motility: can Rho GTPases and microtubules point the way? *Journal of Cell Science*. 2001; 114: 3795-803.
150. Ren XD, Kiosses WB and Schwartz MA. Regulation of the small GTP-binding protein Rho by cell adhesion and the cytoskeleton. *Embo J*. 1999; 18: 578-85.
151. Gundersen GG. Evolutionary conservation of microtubule-capture mechanisms. *Nature Reviews Molecular Cell Biology*. 2002; 3: 296-304.
152. Salmon WC, Adams MC and Waterman-Storer CM. Dual-wavelength fluorescent speckle microscopy reveals coupling of microtubule and actin movements in migrating cells. *J Cell Biol*. 2002; 158: 31-7.
153. Krylyshkina O, Anderson KI, Kaverina I, et al. Nanometer targeting of microtubules to focal adhesions. *J Cell Biol*. 2003; 161: 853-9.
154. DiPaolo BC, Lenormand G, Fredberg JJ and Margulies SS. Stretch magnitude and frequency-dependent actin cytoskeleton remodeling in alveolar epithelia. *Am J Physiol-Cell Ph*. 2010; 299: C345-C53.

155. Haase K and Pelling AE. Resiliency of the Plasma Membrane and Actin Cortex to Large-Scale Deformation. *Cytoskeleton*. 2013; 70: 494-514.
156. Chen CS, Mrksich M, Huang S, Whitesides GM and Ingber DE. Geometric control of cell life and death. *Science*. 1997; 276: 1425-8.
157. Fletcher DA and Mullins D. Cell mechanics and the cytoskeleton. *Nature*. 2010; 463: 485-92.
158. Jin H, Xing XB, Zhao HX, et al. Detection of erythrocytes influenced by aging and type 2 diabetes using atomic force microscope. *Biochem Bioph Res Co*. 2010; 391: 1698-702.
159. Hertz H. Uber den Kontakt elastischer Körper J. fuer die Reine Angew. Math, 1882.
160. Sneddon IN. The relation between load and penetration in the axisymmetric boussinesq problem for a punch of arbitrary profile. *International Journal of Engineering Science*. 1965; 3: 47-57.
161. Radmacher M. Measuring the elastic properties of biological samples with the AFM. *Ieee Eng Med Biol*. 1997; 16: 47-57.
162. Gavara N and Chadwick RS. Determination of the elastic moduli of thin samples and adherent cells using conical atomic force microscope tips. *Nat Nanotechnol*. 2012; 7: 733-6.
163. Guo QQ, Xia Y, Sandig M and Yang J. Characterization of cell elasticity correlated with cell morphology by atomic force microscope. *Journal of Biomechanics*. 2012; 45: 304-9.
164. Kumar S, Maxwell IZ, Heisterkamp A, et al. Viscoelastic retraction of single living stress fibers and its impact on cell shape, cytoskeletal organization, and extracellular matrix mechanics. *Biophys J*. 2006; 90: 3762-73.
165. Campbell JJ, Blain EJ, Chowdhury TT and Knight MM. Loading alters actin dynamics and up-regulates cofilin gene expression in chondrocytes. *Biochem Bioph Res Co*. 2007; 361: 329-34.
166. Stewart MP, Helenius J, Toyoda Y, Ramanathan SP, Muller DJ and Hyman AA. Hydrostatic pressure and the actomyosin cortex drive mitotic cell rounding. *Nature*. 2011; 469: 226-30.
167. Rotsch C and Radmacher M. Drug-induced changes of cytoskeletal structure and mechanics in fibroblasts: an atomic force microscopy study. *Biophys J*. 2000; 78: 520-35.
168. Ketene AN, Roberts PC, Shea AA, Schmelz EM and Agah M. Actin filaments play a primary role for structural integrity and viscoelastic response in cells. *Integr Biol-Uk*. 2012; 4: 540-9.
169. Tojkander S, Gateva G and Lappalainen P. Actin stress fibers - assembly, dynamics and biological roles. *Journal of Cell Science*. 2012; 125: 1855-64.
170. Lekka M, Gil D, Pogoda K, et al. Cancer cell detection in tissue sections using AFM. *Arch Biochem Biophys*. 2012; 518: 151-6.
171. Cross SE, Jin YS, Rao J and Gimzewski JK. Nanomechanical analysis of cells from cancer patients. *Nat Nanotechnol*. 2007; 2: 780-3.
172. Khairallah RJ, Shi GL, Sbrana F, et al. Microtubules Underlie Dysfunction in Duchenne Muscular Dystrophy. *Science Signaling*. 2012; 5.
173. Iyer S, Gaikwad RM, Subba-Rao V, Woodworth CD and Sokolov I. Atomic force microscopy detects differences in the surface brush of normal and cancerous cells. *Nat Nanotechnol*. 2009; 4: 389-93.
174. Li QS, Lee GYH, Ong CN and Lim CT. AFM indentation study of breast cancer cells. *Biochem Bioph Res Co*. 2008; 374: 609-13.
175. Ochalek T, Nordt FJ, Tullberg K and Burger MM. Correlation between Cell Deformability and Metastatic Potential in B16-F1 Melanoma Cell Variants. *Cancer Res*. 1988; 48: 5124-8.
176. Nawaz S, Sanchez P, Bodensiek K, Li S, Simons M and Schaap IAT. Cell Visco-Elasticity Measured with AFM and Optical Trapping at Sub-Micrometer Deformations. *Plos One*. 2012; 7.
177. Cuerrier CM, Lebel R and Grandbois M. Single cell transfection using plasmid decorated AFM probes. *Biochem Bioph Res Co*. 2007; 355: 632-6.
178. Clark AG, Dierkes K and Paluch EK. Monitoring Actin Cortex Thickness in Live Cells. *Biophys J*. 2013; 105: 570-80.
179. Mahaffy RE, Park S, Gerde E, Kas J and Shih CK. Quantitative analysis of the viscoelastic properties of thin regions of fibroblasts using atomic force microscopy. *Biophys J*. 2004; 86: 1777-93.
180. Kollmannsberger P and Fabry B. Linear and Nonlinear Rheology of Living Cells. *Annu Rev Mater Res*. 2011; 41: 75-97.

181. Moeendarbary E, Valon L, Fritzsche M, et al. The cytoplasm of living cells behaves as a poroelastic material. *Nat Mater*. 2013; 12: 253-61.
182. Darling EM, Topel M, Zauscher S, Vail TP and Guilak F. Viscoelastic properties of human mesenchymally-derived stem cells and primary osteoblasts, chondrocytes, and adipocytes. *J Biomech*. 2008; 41: 454-64.
183. Hofmann UG, Rotsch C, Parak WJ and Radmacher M. Investigating the cytoskeleton of chicken cardiocytes with the atomic force microscope. *J Struct Biol*. 1997; 119: 84-91.
184. Salbreux G, Charras GT and Paluch E. Actin cortex mechanics and cellular morphogenesis. *Trends in Cell Biology*. 2012; In press: 1-10.
185. Hochmuth RM and Waugh RE. Erythrocyte-Membrane Elasticity and Viscosity. *Annu Rev Physiol*. 1987; 49: 209-19.
186. Henon S, Lenormand G, Richert A and Gallet F. A new determination of the shear modulus of the human erythrocyte membrane using optical tweezers. *Biophys J*. 1999; 76: 1145-51.
187. Sinha B, Koster D, Ruez R, et al. Cells Respond to Mechanical Stress by Rapid Disassembly of Caveolae. *Cell*. 2011; 144: 402-13.
188. Gervasio OL, Phillips WD, Cole L and Allen DG. Caveolae respond to cell stretch and contribute to stretch-induced signaling. *Journal of cell science*. 2011; 124: 3581-90.
189. Dahl KN, Kahn SM, Wilson KL and Discher DE. The nuclear envelope lamina network has elasticity and a compressibility limit suggestive of a molecular shock absorber. *Journal of Cell Science*. 2004; 117: 4779.
190. Vaziri A, Lee H and Mofrad MRK. Deformation of the cell nucleus under indentation: Mechanics and mechanisms. *Journal of materials research*. 2006; 21: 2126-35.
191. Tremblay D, Andrzejewski L, Leclerc A and Pelling AE. Actin and Microtubules Play Distinct Roles in Governing the Anisotropic Deformation of Cell Nuclei in Response to Substrate Strain. *Cytoskeleton*. 2013; 70: 837-48.
192. Mazumder A and Shivashankar GV. Emergence of a prestressed eukaryotic nucleus during cellular differentiation and development. *Journal of the Royal Society Interface*. 2010; 7: S321-S30.
193. Pagliara S, Franze K, McClain CR, et al. Auxetic nuclei in embryonic stem cells exiting pluripotency. *Nat Mater*. 2014; 13: 638-44.
194. Sen S, Subramanian S and Discher DE. Indentation and adhesive probing of a cell membrane with AFM: Theoretical model and experiments. *Biophys J*. 2005; 89: 3203-13.
195. Lulevich V, Zink T, Chen HY, Liu FT and Liu GY. Cell mechanics using atomic force microscopy-based single-cell compression. *Langmuir*. 2006; 22: 8151-5.
196. Pelling AE, Veraitch FS, Chu CPK, Mason C and Horton MA. Mechanical Dynamics of Single Cells During Early Apoptosis. *Cell Motil Cytoskel*. 2009; 66: 409-22.
197. Scheuring S and Dufrene YF. Atomic force microscopy: probing the spatial organization, interactions and elasticity of microbial cell envelopes at molecular resolution. *Mol Microbiol*. 2010; 75: 1327-36.
198. Haydon PG, Lartius R, Parpura V and MarcheseRagona SP. Membrane deformation of living glial cells using atomic force microscopy. *Journal of Microscopy-Oxford*. 1996; 182: 114-20.
199. Yokokawa M, Takeyasu K and Yoshimura SH. Mechanical properties of plasma membrane and nuclear envelope measured by scanning probe microscope. *J Microsc-Oxford*. 2008; 232: 82-90.
200. Gonzalez-Cruz RD, Fonseca VC and Darling EM. Cellular mechanical properties reflect the differentiation potential of adipose-derived mesenchymal stem cells. *P Natl Acad Sci USA*. 2012; 109: E1523-E9.
201. Raman A, Trigueros S, Cartagena A, et al. Mapping nanomechanical properties of live cells using multi-harmonic atomic force microscopy. *Nat Nanotechnol*. 2011; 6: 809-14.
202. Alcaraz J, Buscemi L, Grabulosa M, et al. Microrheology of human lung epithelial cells measured by atomic force microscopy. *Biophys J*. 2003; 84: 2071-9.
203. Lenormand G, Millet E, Fabry B, Butler JP and Fredberg JJ. Linearity and time-scale invariance of the creep function in living cells. *Journal of the Royal Society Interface*. 2004; 1: 91-7.
204. Puig-de-Morales M, Millet E, Fabry B, et al. Cytoskeletal mechanics in adherent human airway smooth muscle cells: probe specificity and scaling of protein-protein dynamics. *Am J Physiol-Cell Ph*. 2004; 287: C643-C54.
205. Chaudhuri O, Parekh SH and Fletcher DA. Reversible stress softening of actin networks. *Nature*. 2007; 445: 295-8.

206. Nobes CD and Hall A. Rho, Rac, and Cdc42 Gtpases Regulate the Assembly of Multimolecular Focal Complexes Associated with Actin Stress Fibers, Lamellipodia, and Filopodia. *Cell*. 1995; 81: 53-62.
207. Bae YH, Mui KL, Hsu BY, et al. A FAK-Cas-Rac-Lamellipodin Signaling Module Transduces Extracellular Matrix Stiffness into Mechanosensitive Cell Cycling. *Science Signaling*. 2014; 7.
208. Al-Rekabi Z and Pelling AE. Cross talk between matrix elasticity and mechanical force regulates myoblast traction dynamics. *Phys Biol*. 2013; 10.
209. Parekh SH, Chaudhuri O, Theriot JA and Fletcher DA. Loading history determines the velocity of actin-network growth. *Nat Cell Biol*. 2005; 7: 1219-23.
210. Marcy Y, Prost J, Carlier MF and Sykes C. Forces generated during actin-based propulsion: A direct measurement by micromanipulation. *P Natl Acad Sci USA*. 2004; 101: 5992-7.
211. Chen C, Krishnan R, Zhou EH, et al. Fluidization and Resolidification of the Human Bladder Smooth Muscle Cell in Response to Transient Stretch. *Plos One*. 2010; 5.
212. Watanabe-Nakayama T, Machida S, Harada I, Sekiguchi H, Afrin R and Ikai A. Direct Detection of Cellular Adaptation to Local Cyclic Stretching at the Single Cell Level by Atomic Force Microscopy. *Biophys J*. 2011; 100: 564-72.
213. Simon A and Durrieu MC. Strategies and results of atomic force microscopy in the study of cellular adhesion. *Micron*. 2006; 37: 1-13.
214. Scheffer L, Bitler A, Ben-Jacob E and Korenstein R. Atomic force pulling: probing the local elasticity of the cell membrane. *Eur Biophys J Biophy*. 2001; 30: 83-90.
215. Panorchan P, Thompson MS, Davis KJ, Tseng Y, Konstantopoulos K and Wirtz D. Single-molecule analysis of cadherin-mediated cell-cell adhesion. *Journal of Cell Science*. 2006; 119: 66-74.
216. Puntheeranurak T, Neundlinger I, Kinne RKH and Hinterdorfer P. Single-molecule recognition force spectroscopy of transmembrane transporters on living cells. *Nat Protoc*. 2011; 6: 1443-52.
217. Lee CY, Lou JZ, Wen KK, et al. Actin depolymerization under force is governed by lysine 113:glutamic acid 195-mediated catch-slip bonds. *P Natl Acad Sci USA*. 2013; 110: 5022-7.
218. Almqvist N, Bhatia R, Primbs G, Desai N, Banerjee S and Lal R. Elasticity and adhesion force mapping reveals real-time clustering of growth factor receptors and associated changes in local cellular rheological properties. *Biophys J*. 2004; 86: 1753-62.
219. Obataya I, Nakamura C, Han S, Nakamura N and Miyake J. Nanoscale operation of a living cell using an atomic force microscope with a nanoneedle. *Nano Lett*. 2005; 5: 27-30.
220. Stewart MP, Toyoda Y, Hyman AA and Muller DJ. Tracking mechanics and volume of globular cells with atomic force microscopy using a constant-height clamp. *Nat Protoc*. 2012; 7: 143-54.
221. Stewart MP, Hodel AW, Spielhofer A, Cattin CJ, Muller DJ and Helenius J. Wedged AFM-cantilevers for parallel plate cell mechanics. *Methods*. 2013; 60: 186-94.
222. Chaudhuri O, Parekh SH, Lam WA and Fletcher DA. Combined atomic force microscopy and side-view optical imaging for mechanical studies of cells. *Nat Methods*. 2009; 6: 383-U92.
223. Jonas O and Duschl C. Force Propagation and Force Generation in Cells. *Cytoskeleton*. 2010; 67: 555-63.
224. Bippes CA and Muller DJ. High-resolution atomic force microscopy and spectroscopy of native membrane proteins. *Rep Prog Phys*. 2011; 74.
225. Muller DJ and Engel A. Atomic force microscopy and spectroscopy of native membrane proteins. *Nat Protoc*. 2007; 2: 2191-7.
226. Jung SH, Park D, Park JH, Kim YM and Ha KS. Molecular imaging of membrane proteins and microfilaments using atomic force microscopy. *Exp Mol Med*. 2010; 42: 597-605.
227. Tambe DT, Hardin CC, Angelini TE, et al. Collective cell guidance by cooperative intercellular forces. *Nat Mater*. 2011; 10: 469-75.
228. Harris AR, Peter L, Bellis J, Baum B, Kabla AJ and Charras GT. Characterizing the mechanics of cultured cell monolayers. *P Natl Acad Sci USA*. 2012; 109: 16449-54.
229. Tremblay D, Cuerrier CM, Andrzejewski L, O'Brien ER and Pelling AE. A novel stretching platform for applications in cell and tissue mechanobiology. *J Vis Exp*. 2014; 3: 51454.
230. Kollmannsberger P and Fabry B. Active soft glassy rheology of adherent cells. *Soft Matter*. 2009; 5: 1771-4.

231. Sollich P. Rheological constitutive equation for a model of soft glassy materials. *Phys Rev E*. 1998; 58: 738-59.
232. Banerjee S, Liverpool TB and Marchetti MC. Generic phases of cross-linked active gels: Relaxation, oscillation and contractility. *Epl-Europhys Lett*. 2011; 96.
233. Wang SS and Wolynes PG. Active contractility in actomyosin networks. *P Natl Acad Sci USA*. 2012; 109: 6446-51.
234. Thoresen T, Lenz M and Gardel ML. Reconstitution of Contractile Actomyosin Bundles. *Biophys J*. 2011; 100: 2698-705.
235. Xu JY, Tseng Y and Wirtz D. Strain hardening of actin filament networks - Regulation by the dynamic cross-linking protein alpha-actinin. *J Biol Chem*. 2000; 275: 35886-92.
236. Gardel ML, Nakamura F, Hartwig JH, Crocker JC, Stossel TP and Weitz DA. Prestressed F-actin networks cross-linked by hinged filamins replicate mechanical properties of cells. *P Natl Acad Sci USA*. 2006; 103: 1762-7.
237. Janmey PA, Hvidt S, Lamb J and Stossel TP. Resemblance of Actin-Binding Protein Actin Gels to Covalently Cross-Linked Networks. *Nature*. 1990; 345: 89-92.
238. Ingber DE. Tensegrity: The architectural basis of cellular mechanotransduction. *Annu Rev Physiol*. 1997; 59: 575-99.
239. Hu YH, Zhao XH, Vlassak JJ and Suo ZG. Using indentation to characterize the poroelasticity of gels. *Appl Phys Lett*. 2010; 96.
240. Wolff L, Fernandez P and Kroy K. Resolving the Stiffening-Softening Paradox in Cell Mechanics. *Plos One*. 2012; 7.
241. Chen CS. Mechanotransduction - a field pulling together? *J Cell Sci*. 2008; 121: 3285-92.
242. Smith ML, Gourdon D, Little WC, et al. Force-induced unfolding of fibronectin in the extracellular matrix of living cells. *Plos Biol*. 2007; 5: 2243-54.
243. Johnson CP, Tang HY, Carag C, Speicher DW and Discher DE. Forced unfolding of proteins within cells. *Science*. 2007; 317: 663-6.
244. Janmey PA and Miller RT. Mechanisms of mechanical signaling in development and disease. *Journal of cell science*. 2011; 124: 9-18.
245. Janmey PA and Weitz DA. Dealing with mechanics: mechanisms of force transduction in cells. *Trends in Biochemical Sciences*. 2004; 29: 364-70.
246. Buxboim A, Ivanovska IL and Discher DE. Matrix elasticity, cytoskeletal forces and physics of the nucleus: how deeply do cells 'feel' outside and in? *Journal of Cell Science*. 2010; 123: 297-308.
247. Fletcher DA and Mullins RD. Cell mechanics and the cytoskeleton. *Nature*. 2010; 463: 485-92.
248. Wang J, Chen H, Seth A and McCulloch CA. Mechanical force regulation of myofibroblast differentiation in cardiac fibroblasts. *Am J Physiol Heart Circ Physiol*. 2003; 285: H1871-81.
249. Krishnan R, Park CY, Lin YC, et al. Reinforcement versus fluidization in cytoskeletal mechanoresponsiveness. *Plos One*. 2009; 4: e5486.
250. Na S, Collin O, Chowdhury F, et al. Rapid signal transduction in living cells is a unique feature of mechanotransduction. *P Natl Acad Sci USA*. 2008; 105: 6626-31.
251. Chen C, Krishnan R, Zhou E, et al. Fluidization and resolidification of the human bladder smooth muscle cell in response to transient stretch. *Plos One*. 2010; 5: e12035.
252. Blanchard GB, Kabla AJ, Schultz NL, et al. Tissue tectonics: morphogenetic strain rates, cell shape change and intercalation. *Nature Methods*. 2009; 6: 458-U86.
253. Engler AJ, Sweeney HL and Discher DE. Substrate elasticity alters human mesenchymal stem cell differentiation. *Biophys J*. 2005; 88: 500a-a.
254. DuFort CC, Paszek MJ and Weaver VM. Balancing forces: architectural control of mechanotransduction. *Nature Reviews Molecular Cell Biology*. 2011; 12: 308-19.
255. Guvendiren M and Burdick JA. Stiffening hydrogels to probe short- and long-term cellular responses to dynamic mechanics. *Nat Commun*. 2012; 3: 792.
256. Engler AJ, Sen S, Sweeney HL and Discher DE. Matrix elasticity directs stem cell lineage specification. *Cell*. 2006; 126: 677-89.

257. McNeil PL and Steinhardt RA. Plasma membrane disruption: Repair, prevention, adaptation. *Annual Review of Cell and Developmental Biology*. 2003; 19: 697-731.
258. Hsu HJ, Lee CF, Locke A, Vanderzyl SQ and Kaunas R. Stretch-Induced Stress Fiber Remodeling and the Activations of JNK and ERK Depend on Mechanical Strain Rate, but Not FAK. *Plos One*. 2010; 5.
259. Bershadsky A, Kozlov M and Geiger B. Adhesion-mediated mechanosensitivity: a time to experiment, and a time to theorize. *Current Opinion in Cell Biology*. 2006; 18: 472-81.
260. Liu MY, Tanswell AK and Post M. Mechanical force-induced signal transduction in lung cells. *American Journal of Physiology-Lung Cellular and Molecular Physiology*. 1999; 277: L667-L83.
261. Waters CM, Sporn PHS, Liu MY and Fredberg JJ. Cellular biomechanics in the lung. *American Journal of Physiology-Lung Cellular and Molecular Physiology*. 2002; 283: L503-L9.
262. Lecuit T, Lenne PF and Munro E. Force Generation, Transmission, and Integration during Cell and Tissue Morphogenesis. *Annu Rev Cell Dev Bi*. 2011; 27: 157-84.
263. Dai J and Sheetz MP. Regulation of endocytosis, exocytosis, and shape by membrane tension. *Cold Spring Harb Sym*. 1995; 60: 567-71.
264. Grimm HP, Verkhovsky AB, Mogilner A and Meister JJ. Analysis of actin dynamics at the leading edge of crawling cells: implications for the shape of keratocyte lamellipodia. *Eur Biophys J Biophy*. 2003; 32: 563-77.
265. Yang CS, Hoelzle M, Disanza A, Scita G and Svitkina T. Coordination of Membrane and Actin Cytoskeleton Dynamics during Filopodia Protrusion. *Plos One*. 2009; 4.
266. Liu AP, Richmond DL, Maibaum L, Pronk S, Geissler PL and Fletcher DA. Membrane-induced bundling of actin filaments. *Nat Phys*. 2008; 4: 789-93.
267. Farsad K and De Camilli P. Mechanisms of membrane deformation. *Current Opinion in Cell Biology*. 2003; 15: 372-81.
268. Han R, Kanagawa M, Yoshida-Moriguchi T, et al. Basal lamina strengthens cell membrane integrity via the laminin G domain-binding motif of alpha-dystroglycan. *P Natl Acad Sci USA*. 2009; 106: 12573-9.
269. Yamane Y, Shiga H, Haga H, Kawabata K, Abe K and Ito E. Quantitative analyses of topography and elasticity of living and fixed astrocytes. *J Electron Microsc*. 2000; 49: 463-71.
270. Evans E and Leung A. Adhesivity and Rigidity of Erythrocyte-Membrane in Relation to Wheat-Germ-Agglutinin Binding. *J Cell Biol*. 1984; 98: 1201-8.
271. Charras GT, Coughlin M, Mitchison TJ and Mahadevan L. Life and times of a cellular bleb. *Biophys J*. 2008; 94: 1836-53.
272. Boal D. Mechanics of the Cell. In: Press CU, (ed.). 2 ed. New York2012, p. 243-82.
273. Li Q, Lau A, Morris TJ, Guo L, Fordyce CB and Stanley EF. A syntaxin 1, G alpha(o), and N-type calcium channel complex at a presynaptic nerve terminal: Analysis by quantitative immunocolocalization. *J Neurosci*. 2004; 24: 4070-81.
274. Mikulich A, Kavaliauskiene S and Juzenas P. Blebbistatin, a myosin inhibitor, is phototoxic to human cancer cells under exposure to blue light. *Bba-Gen Subjects*. 2012; 1820: 870-7.
275. Sakamoto T, Limouze J, Straight AF, Combs CA and Sellers JR. Blebbistatin, a myosin II inhibitor, is rapidly photoinactivated by blue light. *Biophys J*. 2005; 88: 633a-a.
276. Barros LF, Kanaseki T, Sabirov R, et al. Apoptotic and necrotic blebs in epithelial cells display similar neck diameters but different kinase dependency. *Cell Death Differ*. 2003; 10: 687-97.
277. Dai JW and Sheetz MP. Membrane tether formation from blebbing cells. *Biophys J*. 1999; 77: 3363-70.
278. Hemsley AL, Hernandez, D., Mason, C., Pelling, A. E. and Veraitch, F. S. Precisely delivered nanomechanical forces induce blebbing in undifferentiated mouse embryonic stem cells. *Cell Health & Cytoskeleton*. 2011; 3: 23-34.
279. Wu HW, Kuhn T and Moy VT. Mechanical properties of l929 cells measured by atomic force microscopy: Effects of anticytoskeletal drugs and membrane crosslinking. *Scanning*. 1998; 20: 389-97.
280. Darling EM, Zauscher S and Guilak F. Viscoelastic properties of zonal articular chondrocytes measured by atomic force microscopy. *Osteoarthr Cartilage*. 2006; 14: 571-9.
281. Darling EM, Zauscher S, Block JA and Guilak F. A thin-layer model for viscoelastic, stress-relaxation testing of cells using atomic force microscopy: Do cell properties reflect metastatic potential? *Biophys J*. 2007; 92: 1784-91.

282. Yanniotis S, Skaltsi S and Karaburnioti S. Effect of moisture content on the viscosity of honey at different temperatures. *J Food Eng*. 2006; 72: 372-7.
283. Karcher H, Lammerding J, Huang HD, Lee RT, Kamm RD and Kaazempur-Mofrad MR. A three-dimensional viscoelastic model for cell deformation with experimental verification. *Biophys J*. 2003; 85: 3336-49.
284. Smith BA, Tolloczko B, Martin JG and Grutter P. Probing the viscoelastic behavior of cultured airway smooth muscle cells with atomic force microscopy: Stiffening induced by contractile agonist. *Biophys J*. 2005; 88: 2994-3007.
285. Guilluy C, Swaminathan V, Garcia-Mata R, O'Brien ET, Superfine R and Burridge K. The Rho GEFs LARG and GEF-H1 regulate the mechanical response to force on integrins. *Nat Cell Biol*. 2011; 13: 722-U211.
286. Ali MH and Schumacker PT. Endothelial responses to mechanical stress: Where is the mechanosensor? *Crit Care Med*. 2002; 30: S198-S206.
287. Lehoux S and Tedgui A. Cellular mechanics and gene expression in blood vessels. *Journal of Biomechanics*. 2003; 36: 631-43.
288. Yin SH, Zhang XQ, Zhan C, Wu JT, Xu JC and Cheung J. Measuring single cardiac myocyte contractile force via moving a magnetic bead. *Biophys J*. 2005; 88: 1489-95.
289. Charras GT, Yarrow JC, Horton MA, Mahadevan L and Mitchison TJ. Non-equilibration of hydrostatic pressure in blebbing cells. *Nature*. 2005; 435: 365-9.
290. Keren K, Yam PT, Kinkhabwala A, Mogilner A and Theriot JA. Intracellular fluid flow in rapidly moving cells. *Nat Cell Biol*. 2009; 11: 1219-U137.
291. Zimmer CC, Shi LF, Shih YP, et al. F-Actin reassembly during focal adhesion impacts single cell mechanics and nanoscale membrane structure. *Sci China Chem*. 2012; 55: 1922-30.
292. Suresh S. Biomechanics and biophysics of cancer cells. *Acta Biomater*. 2007; 3: 413-38.
293. Ingber DE. Mechanical control of tissue morphogenesis during embryological development. *Int J Dev Biol*. 2006; 50: 255-66.
294. Yoshizaki H, Ohba Y, Parrini MC, et al. Cell type-specific regulation of RhoA activity during cytokinesis. *J Biol Chem*. 2004; 279: 44756-62.
295. Tinevez JY, Schulze U, Salbreux G, Roensch J, Joanny JF and Paluch E. Role of cortical tension in bleb growth. *P Natl Acad Sci USA*. 2009; 106: 18581-6.
296. Brzeska H, Szczepanowska J, Matsumura F and Korn ED. Rac-induced increase of phosphorylation of myosin regulatory light chain in HeLa cells. *Cell Motil Cytoskel*. 2004; 58: 186-99.
297. Houk AR, Jilkine A, Mejean CO, et al. Membrane Tension Maintains Cell Polarity by Confining Signals to the Leading Edge during Neutrophil Migration. *Cell*. 2012; 148: 175-88.
298. Boulant S, Kural C, Zeeh JC, Ubelmann F and Kirchhausen T. Actin dynamics counteract membrane tension during clathrin-mediated endocytosis. *Nat Cell Biol*. 2011; 13: 1124-U158.
299. Gauthier NC, Fardin MA, Roca-Cusachs P and Sheetz MP. Temporary increase in plasma membrane tension coordinates the activation of exocytosis and contraction during cell spreading. *P Natl Acad Sci USA*. 2011; 108: 14467-72.
300. Delanoe-Ayari H, Al Kurdi R, Vallade M, Gulino-Debrac D and Riveline D. Membrane and acto-myosin tension promote clustering of adhesion proteins. *P Natl Acad Sci USA*. 2004; 101: 2229-34.
301. Morris CE and Homann U. Cell surface area regulation and membrane tension. *J Membrane Biol*. 2001; 179: 79-102.
302. Diz-Munoz A, Fletcher DA and Weiner OD. Use the force: membrane tension as an organizer of cell shape and motility. *Trends in Cell Biology*. 2013; 23: 47-53.
303. Bouvrais H, Pott T, Bagatolli LA, Ipsen JH and Meleard P. Impact of membrane-anchored fluorescent probes on the mechanical properties of lipid bilayers. *Bba-Biomembranes*. 2010; 1798: 1333-7.
304. Jensen EC. Use of Fluorescent Probes: Their Effect on Cell Biology and Limitations. *Anat Rec*. 2012; 295: 2031-6.
305. Lassailly F, Griessinger E and Bonnet D. "Microenvironmental contaminations" induced by fluorescent lipophilic dyes used for noninvasive in vitro and in vivo cell tracking. *Blood*. 2010; 115: 5347-54.
306. Henriksen J, Rowat AC, Brief E, et al. Universal behavior of membranes with sterols. *Biophys J*. 2006; 90: 1639-49.

307. Vlahakis NE and Hubmayr RD. Plasma membrane stress failure in alveolar epithelial cells. *Journal of Applied Physiology*. 2000; 89.
308. Harris AR and Charras GT. Experimental validation of atomic force microscopy-based cell elasticity measurements. *Nanotechnology*. 2011; 22: 345102.
309. Hategan A, Law R, Kahn S and Discher DE. Adhesively-tensed cell membranes: Lysis kinetics and atomic force microscopy probing. *Biophys J*. 2003; 85: 2746-59.
310. Franz V, Loi S, Muller H, Bamberg E and Butt HH. Tip penetration through lipid bilayers in atomic force microscopy. *Colloid Surface B*. 2002; 23: 191-200.
311. Chen X, Kis A, Zettl A and Bertozzi CR. A cell nanoinjector based on carbon nanotubes. *P Natl Acad Sci USA*. 2007; 104: 8218-22.
312. Vakarelski IU, Brown SC, Higashitani K and Moudgil BM. Penetration of living cell membranes with fortified carbon nanotube tips. *Langmuir*. 2007; 23: 10893-6.
313. Tschumperlin DJ, Oswari J and Margulies SS. Deformation-induced injury of alveolar epithelial cells. *American Journal of Respiratory and Critical Care Medicine*. 2000; 162: 357–62.
314. Kamal A and Goldstein LSB. Connecting vesicle transport to the cytoskeleton. *Current Opinion in Cell Biology*. 2000; 12: 503–8.
315. Rodionov VI, Gyoeva FK, Tanaka E, Bershadsky AD, Vasiliev JM and Gelfand VI. Microtubule-Dependent Control of Cell-Shape and Pseudopodial Activity Is Inhibited by the Antibody to Kinesin Motor Domain. *J Cell Biol*. 1993; 123: 1811-20.
316. Goldman RD, Khuon S, Chou YH, Opal P and Steinert PM. The function of intermediate filaments in cell shape and cytoskeletal integrity. *J Cell Biol*. 1996; 134: 971-83.
317. Helfand BT, Chang L and Goldman RD. Intermediate filaments are dynamic and motile elements of cellular architecture. *Journal of cell science*. 2004; 117: 133-41.
318. Guilak F. Compression-induced changes in the shape and volume of the chondrocyte nucleus. *J Biomech*. 1995; 28: 1529–41.
319. Stewart-Hutchinson PJ, Hale CM, Wirtz D and Hodzic D. Structural requirements for the assembly of LINC complexes and their function in cellular mechanical stiffness. *Exp Cell Res*. 2008; 314: 1892-905.
320. Caille N, Thoumine O, Tardy Y and Meister JJ. Contribution of the nucleus to the mechanical properties of endothelial cells. *Journal of Biomechanics*. 2002; 35: 177-87.
321. Dahl KN, Engler AJ, Pajerowski JD and Discher DE. Power-law rheology of isolated nuclei with deformation mapping of nuclear substructures. *Biophys J*. 2005; 89: 2855-64.
322. Guilak F, Tedrow JR and Burgkart R. Viscoelastic properties of the cell nucleus. *Biochem Bioph Res Co*. 2000; 269: 781-6.
323. Costa KD and Yin FCP. Analysis of indentation: Implications for measuring mechanical properties with atomic force microscopy. *J Biomech Eng-T Asme*. 1999; 121: 462-71.
324. Shroff SG, Saner DR and Lal R. Dynamic Micromechanical Properties of Cultured Rat Atrial Myocytes Measured by Atomic-Force Microscopy. *Am J Physiol-Cell Ph*. 1995; 269: C286-C92.
325. Nagayama M, Haga H, Takahashi M, Saitoh T and Kawabata K. Contribution of cellular contractility to spatial and temporal variations in cellular stiffness. *Exp Cell Res*. 2004; 300: 396-405.
326. Watanabe N and Mitchison TJ. Single-Molecule Speckle Analysis of Actin Filament Turnover in Lamellipodia. *Science*. 2002; 295: 1083-6.
327. Saarikangas J, Zhao H and Lappalainen P. Regulation of the Actin Cytoskeleton-Plasma Membrane Interplay by Phosphoinositides. *Physiological Reviews*. 2010; 90: 259-89
328. Porter KR, Fonte V and Weiss G. Scanning Microscope Study of Topography of Hela-Cells. *Cancer Res*. 1974; 34: 1385-94.
329. Python JL, Wilson KO, Snook JH, Guo B and Guilford WH. The viscoelastic properties of microvilli are dependent upon the cell-surface molecule. *Biochem Bioph Res Co*. 2010; 397: 621-5.
330. Hutter JL and Bechhoefer J. Calibration of Atomic-Force Microscope Tips. *Review of Scientific Instruments*. 1993; 64: 1868-73.
331. Matzke R, Jacobson K and Radmacher M. Direct, high-resolution measurement of furrow stiffening during division of adherent cells. *Nat Cell Biol*. 2001; 3: 607-10.

332. Carl P, Kwok CH, Manderson G, Speicher DW and Discher DE. Forced unfolding modulated by disulfide bonds in the Ig domains of a cell adhesion molecule. *P Natl Acad Sci USA*. 2001; 98: 1565-70.
333. Brugues J, Maugis B, Casademunt J, Nassoy P, Amblard F and Sens P. Dynamical organization of the cytoskeletal cortex probed by micropipette aspiration. *P Natl Acad Sci USA*. 2010; 107: 15415-20.
334. DeMali KA and Burridge K. Coupling membrane protrusion and cell adhesion. *Journal of Cell Science*. 2003; 116: 2389-97.
335. Haase K and Pelling AE. Resiliency of the plasma membrane and actin cortex to large-scale deformation. *Cytoskeleton*. 2013: n/a-n/a.
336. Kasas S, Wang X, Hirling H, et al. Superficial and deep changes of cellular mechanical properties following cytoskeleton disassembly. *Cell Motil Cytoskel*. 2005; 62: 124-32.
337. Remmerbach TW, Wottawah F, Dietrich J, Lincoln B, Wittekind C and Guck J. Oral Cancer Diagnosis by Mechanical Phenotyping. *Cancer Res*. 2009; 69: 1728-32.
338. Zwerger M, Ho CY and Lammerding J. Nuclear Mechanics in Disease. *Annual Review of Biomedical Engineering, Vol 13*. 2011; 13: 397-428.
339. Zhang WJ, Kai K, Choi DS, et al. Microfluidics separation reveals the stem-cell-like deformability of tumor-initiating cells. *P Natl Acad Sci USA*. 2012; 109: 18707-12.
340. Bukoreshtliev NV, Haase K and Pelling AE. Mechanical cues in cellular signalling and communication. *Cell Tissue Res*. 2013; 352: 77-94.
341. Mahaffy RE, Shih CK, MacKintosh FC and Kas J. Scanning probe-based frequency-dependent microrheology of polymer gels and biological cells. *Phys Rev Lett*. 2000; 85: 880-3.
342. Radmacher M, Fritz M, Kacher CM, Cleveland JP and Hansma PK. Measuring the viscoelastic properties of human platelets with the atomic force microscope. *Biophys J*. 1996; 70: 556-67.
343. Kirmizis D and Logothetidis S. Atomic force microscopy probing in the measurement of cell mechanics. *Int J Nanomed*. 2010; 5: 137-45.
344. Haase K and Pelling AE. The role of the actin cortex in maintaining cell shape. *Communicative and Integrative Biology*. 2013; 6.
345. Moreno-Flores S, Benitez R, Vivanco MD and Toca-Herrera JL. Stress relaxation and creep on living cells with the atomic force microscope: a means to calculate elastic moduli and viscosities of cell components. *Nanotechnology*. 2010; 21.
346. Zhou EH, Trepat X, Park CY, et al. Universal behavior of the osmotically compressed cell and its analogy to the colloidal glass transition. *P Natl Acad Sci USA*. 2009; 106: 10632-7.
347. Trickey WR, Baaijens FPT, Laursen TA, Alexopoulos LG and Guilak F. Determination of the Poisson's ratio of the cell: recovery properties of chondrocytes after release from complete micropipette aspiration. *Journal of Biomechanics*. 2006; 39: 78-87.
348. Haase K and Pelling AE. Resiliency of the plasma membrane and actin cortex to large-scale deformation. *Cytoskeleton (Hoboken)*. 2013; 70: 494-514.
349. Berro J, Michelot A, Blanchoin L, Kovar DR and Martiel JL. Attachment conditions control actin filament buckling and the production of forces. *Biophys J*. 2007; 92: 2546-58.
350. Murrell MP and Gardel ML. F-actin buckling coordinates contractility and severing in a biomimetic actomyosin cortex. *P Natl Acad Sci USA*. 2012; 109: 20820-5.
351. Maloney JM, Nikova D, Lautenschlager F, et al. Mesenchymal Stem Cell Mechanics from the Attached to the Suspended State. *Biophys J*. 2010; 99: 2479-87.
352. McBeath R, Pirone DM, Nelson CM, Bhadriraju K and Chen CS. Cell shape, cytoskeletal tension, and RhoA regulate stem cell lineage commitment. *Dev Cell*. 2004; 6: 483-95.
353. Erickson GR, Northrup DL and Guilak F. Hypo-osmotic stress induces calcium-dependent actin reorganization in articular chondrocytes. *Osteoarthr Cartilage*. 2003; 11: 187-97.
354. Hoffmann EK and Dunham PB. Membrane mechanisms and intracellular signalling in cell volume regulation. *Int Rev Cytol*. 1995; 161: 173-262.
355. Ofek G, Wiltz DC and Athanasiou KA. Contribution of the Cytoskeleton to the Compressive Properties and Recovery Behavior of Single Cells. *Biophys J*. 2009; 97: 1873-82.
356. Chang YC, Nalbant P, Birkenfeld J, Chang ZF and Bokoch GM. GEF-H1 couples nocodazole-induced microtubule disassembly to cell contractility via RhoA. *Molecular Biology of the Cell*. 2008; 19: 2147-53.

357. Al-Rekabi Z, Haase K and Pelling AE. Microtubules mediate changes in membrane cortical elasticity during contractile activation. *Exp Cell Res*. 2014; 322: 21-9.
358. Wiggan O, Shaw AE, DeLuca JG and Bamburg JR. ADF/Cofilin Regulates Actomyosin Assembly through Competitive Inhibition of Myosin II Binding to F-Actin. *Dev Cell*. 2012; 22: 530-43.
359. Wang LL, Xue LX, Yan HX, Li J and Lu YC. Effects of ROCK inhibitor, Y-27632, on adhesion and mobility in esophageal squamous cell cancer cells. *Mol Biol Rep*. 2010; 37: 1971-7.
360. Arber S, Barbayannis FA, Hanser H, et al. Regulation of actin dynamics through phosphorylation of cofilin by LIM-kinase. *Nature*. 1998; 393: 805-9.
361. Guigas G, Kalla C and Weiss M. Probing the nanoscale viscoelasticity of intracellular fluids in living cells. *Biophys J*. 2007; 93: 316-23.
362. Larsen TH, Dalen H, Boyle R, Souza MM and Lieberman M. Cytoskeletal involvement during hypo-osmotic swelling and volume regulation in cultured chick cardiac myocytes. *Histochem Cell Biol*. 2000; 113: 479-88.
363. Byfield FJ, Aranda-Espinoza H, Romanenko VG, Rothblat GH and Levitan I. Cholesterol depletion increases membrane stiffness of aortic endothelial cells. *Biophys J*. 2004; 87: 3336-43.
364. Tse JM, Cheng G, Tyrrell JA, et al. Mechanical compression drives cancer cells toward invasive phenotype. *P Natl Acad Sci USA*. 2012; 109: 911-6.
365. Shieh AC, Koay EJ and Athanasiou KA. Strain-dependent recovery behavior of single chondrocytes. *Biomech Model Mechan*. 2006; 5: 172-9.
366. Cole RW, Jinadasa T and Brown CM. Measuring and interpreting point spread functions to determine confocal microscope resolution and ensure quality control. *Nat Protoc*. 2011; 6: 1929-41.
367. Beyer H. *Handbuch der Mikroskopie*. 2nd ed. ed.: VEB Verlag Technik, 1985.
368. Motulsky H. *Fitting Models to Biological Data Using Linear and Nonlinear Regression: A Practical Guide to Curve Fitting: A Practical Guide to Curve Fitting*. Oxford University Press, 2004.
369. Haase K and Pelling AE. Resiliency of the plasma membrane and actin cortex to large-scale deformation. *Cytoskeleton*. 2013.
370. Guilak F. Compression-induced changes in the shape and volume of the chondrocyte nucleus. *Journal of biomechanics*. 1995; 28: 1529-41.
371. Fedorchak GR, Kaminski A and Lammerding J. Cellular mechanosensing: Getting to the nucleus of it all. *Prog Biophys Mol Biol*. 2014; 5: 00051-0.
372. Dahl KN and Kalinowski A. Nucleoskeleton mechanics at a glance. *Journal of Cell Science*. 2011; 124: 4.
373. Sims JR, Karp S and Ingber DE. Altering the cellular mechanical force balance results in integrated changes in cell, cytoskeletal and nuclear shape. *Journal of Cell Science*. 1992; 103: 1215.
374. Guolla L, Bertrand M, Haase K and Pelling AE. Force transduction and strain dynamics in actin stress fibres in response to nanonewton forces. *Journal of Cell Science*. 2012; 125: 603-13.
375. Iyer KV, Pulford S, Mogilner A and Shivashankar GV. Mechanical Activation of Cells Induces Chromatin Remodeling Preceding MKL Nuclear Transport. *Biophys J*. 2012; 103: 1416-28.
376. Holaska JM. Emerin and the nuclear lamina in muscle and cardiac disease. *Circ Res*. 2008; 103: 16-23.
377. Sullivan T, Escalante-Alcalde D, Bhatt H, et al. Loss of A-type lamin expression compromises nuclear envelope integrity leading to muscular dystrophy. *The Journal of cell biology*. 1999; 147: 913.
378. Lammerding J, Schulze PC, Takahashi T, et al. Lamin A/C deficiency causes defective nuclear mechanics and mechanotransduction. *Journal of Clinical Investigation*. 2004; 113: 370-8.
379. Coffinier C, Jung HJ, Nobumori C, et al. Deficiencies in lamin B1 and lamin B2 cause neurodevelopmental defects and distinct nuclear shape abnormalities in neurons. *Mol Biol Cell*. 2011; 22: 4683-93.
380. Rowat AC, Lammerding J and Ipsen JH. Mechanical properties of the cell nucleus and the effect of emerin deficiency. *Biophys J*. 2006; 91: 4649-64.
381. Brandt A, Papagiannouli F, Wagner N, et al. Developmental control of nuclear size and shape by Kugelkern and Kurzkern. *Curr Biol*. 2006; 16: 543-52.
382. Pilot F, Philippe JM, Lemmers C, Chauvin JP and Lecuit T. Developmental control of nuclear morphogenesis and anchoring by charleston, identified in a functional genomic screen of Drosophila cellularisation. *Development*. 2006; 133: 711-23.

383. Vergnes L, Peterfy M, Bergo MO, Young SG and Reue K. Lamin B1 is required for mouse development and nuclear integrity. *Proc Natl Acad Sci U S A*. 2004; 101: 10428-33.
384. Mazumder A and Shivashankar G. Emergence of a prestressed eukaryotic nucleus during cellular differentiation and development. *Journal of The Royal Society Interface*. 2010; 7: S321-S30.
385. Pajerowski JD, Dahl KN, Zhong FL, Sammak PJ and Discher DE. Physical plasticity of the nucleus in stem cell differentiation. *Proceedings of the National Academy of Sciences*. 2007; 104: 15619.
386. Swift J, Ivanovska IL, Buxboim A, et al. Nuclear Lamin-A Scales with Tissue Stiffness and Enhances Matrix-Directed Differentiation. *Science*. 2013; 341: 975-+.
387. Janmey PA and Miller RT. Mechanisms of mechanical signaling in development and disease. *Journal of Cell Science*. 2010; 124: 9-18.
388. Chen CS. Mechanotransduction - a field pulling together? *Journal of Cell Science*. 2008; 121: 3285-92.
389. Lammerding J, Dahl KN, Discher DE and Kamm RD. Nuclear mechanics and methods. *Methods in cell biology*. 2007; 83: 269-94.
390. Tremblay D, Andrzejewski, L., Leclerc, A. & Pelling, A.E. . Actin and Microtubules Play Distinct Roles in Governing the Anisotropic Deformation of Cell Nuclei in Response to Substrate Strain. *Cytoskeleton*. 2013.
391. Rosato DV, Rosato MG and Schott NR. *Plastics Engineering, Manufacturing & Data Handbook*. Kluwer Academic Pub, 2001.
392. Pelling AE, Dawson DW, Carreon DM, et al. Distinct contributions of microtubule subtypes to cell membrane shape and stability. *Nanomedicine: Nanotechnology, Biology and Medicine*. 2007; 3: 43-52.
393. Yuen FLY, Zak G, Waldman SD and Docoslis A. Morphology of fibroblasts grown on substrates formed by dielectrophoretically aligned carbon nanotubes. *Cytotechnology*. 2008; 56: 9-17.
394. Samson F, Donoso JA, Heller-Bettinger I, Watson D and Himes RH. Nocodazole action on tubulin assembly, axonal ultrastructure and fast axoplasmic transport. *Journal of Pharmacology and Experimental Therapeutics*. 1979; 208: 411.
395. Martins RP, Finan JD, Guilak F and Lee DA. Mechanical Regulation of Nuclear Structure and Function. *Annu Rev Biomed Eng*. 2012; 14: 431-55.
396. Chalut KJ, Hopfler M, Lautenschlager F, et al. Chromatin Decondensation and Nuclear Softening Accompany Nanog Downregulation in Embryonic Stem Cells. *Biophys J*. 2012; 103: 2060-70.
397. Toth KF, Knoch TA, Wachsmuth M, et al. Trichostatin A-induced histone acetylation causes decondensation of interphase chromatin. *Journal of Cell Science*. 2004; 117: 4277-87.
398. Galiova G, Bartova E, Raska I, Krejci J and Kozubek S. Chromatin changes induced by lamin A/C deficiency and the histone deacetylase inhibitor trichostatin A. *Eur J Cell Biol*. 2008; 87: 291-303.
399. Guilluy C, Osborne LD, Van Landeghem L, et al. Isolated nuclei adapt to force and reveal a mechanotransduction pathway in the nucleus. *Nat Cell Biol*. 2014; 16: 376-81.
400. Ailenberg M and Silverman M. Trichostatin A - histone deacetylase inhibitor with clinical therapeutic potential - is also a selective and potent inhibitor of gelatinase A expression. *Biochem Bioph Res Co*. 2002; 298: 110-5.
401. Nikolova V, Leimena C, McMahon AC, et al. Defects in nuclear structure and function promote dilated cardiomyopathy in lamin A/C-deficient mice. *Journal of Clinical Investigation*. 2004; 113: 357-69.
402. Broers JLV, Peeters EAG, Kuijpers HJH, et al. Decreased mechanical stiffness in LMNA-/- cells is caused by defective nucleo-cytoskeletal integrity: implications for the development of laminopathies. *Hum Mol Genet*. 2004; 13: 2567-80.
403. Shin JW, Spinler KR, Swift J, Chasis JA, Mohandas N and Discher DE. Lamins regulate cell trafficking and lineage maturation of adult human hematopoietic cells. *P Natl Acad Sci USA*. 2013; 110: 18892-7.
404. Eckersley-Maslin MA, Bergmann JH, Lazar Z and Spector DL. Lamin A/C is expressed in pluripotent mouse embryonic stem cells. *Nucleus-Austin*. 2013; 4: 53-60.
405. Pajerowski JD, Dahl KN, Zhong FL, Sammak PJ and Discher DE. Physical plasticity of the nucleus in stem cell differentiation. *P Natl Acad Sci USA*. 2007; 104: 15619-24.
406. Smith ER, Zhang XY, Capo-Chichi CD, Chen XW and Xu XX. Increased Expression of Syne1/Nesprin-1 Facilitates Nuclear Envelope Structure Changes in Embryonic Stem Cell Differentiation. *Dev Dynam*. 2011; 240: 2245-55.

407. Chien S, Li S and Shyy JYJ. Effects of mechanical forces on signal transduction and gene expression in endothelial cells. *Hypertension*. 1998; 31: 162-9.
408. Tidball JG, Albrecht DE, Lokensgard BE and Spencer MJ. Apoptosis Precedes Necrosis of Dystrophin-Deficient Muscle. *Journal of Cell Science*. 1995; 108: 2197-204.
409. Colussi C, Gurtner A, Rosati J, et al. Nitric oxide deficiency determines global chromatin changes in Duchenne muscular dystrophy. *Faseb J*. 2009; 23: 2131-41.
410. Grigoriev I, Borisy G and Vorobjev I. Regulation of microtubule dynamics in 3T3 fibroblasts by Rho family GTPases. *Cell Motil Cytoskel*. 2006; 63: 29-40.
411. Heggeness MH, Wang K and Singer SJ. Intracellular distributions of mechanochemical proteins in cultured fibroblasts. *Proceedings of the National Academy of Sciences*. 1977; 74: 3883.
412. Harada T, Swift J, Irianto J, et al. Nuclear lamin stiffness is a barrier to 3D migration, but softness can limit survival. *J Cell Biol*. 2014; 204: 669-82.
413. Helin K and Dhanak D. Chromatin proteins and modifications as drug targets. *Nature*. 2013; 502: 480-8.
414. Fedorova E and Zink D. Nuclear architecture and gene regulation. *Bba-Mol Cell Res*. 2008; 1783: 2174-84.
415. Wang X, Fan JW, Zhang M, Sun ZC and Xu GZ. Gene Expression Changes under Cyclic Mechanical Stretching in Rat Retinal Glial (Muller) Cells. *Plos One*. 2013; 8.
416. dos Santos CC, Han B, Andrade CF, et al. DNA microarray analysis of gene expression in alveolar epithelial cells in response to TNF alpha, LPS, and cyclic stretch. *Physiol Genomics*. 2004; 19: 331-42.
417. Li Y, Pan H and Huard J. Isolating stem cells from soft musculoskeletal tissues. *Journal of visualized experiments: JoVE*. 2010.
418. Furumai R, Komatsu Y, Nishino N, Khochbin S, Yoshida M and Horinouchi S. Potent histone deacetylase inhibitors built from trichostatin A and cyclic tetrapeptide antibiotics including trapoxin. *P Natl Acad Sci USA*. 2001; 98: 87-92.
419. Yoshida M, Kijima M, Akita M and Beppu T. Potent and Specific-Inhibition of Mammalian Histone Deacetylase Both Invivo and Invitro by Trichostatin-A. *J Biol Chem*. 1990; 265: 17174-9.
420. Abramoff MD, Magelhaes PJ and Ram SJ. Image Processing with ImageJ. *Biophotonics international*. 2004; 11: 36-42.
421. Haase K and Pelling AE. The role of the actin cortex in maintaining cell shape. *Commun Integr Biol*. 2013; 6: 9.
422. Ferko MC, Bhatnagar A, Garcia MB and Butler PJ. Finite-element stress analysis of a multicomponent model of sheared and focally-adhered endothelial cells. *Ann Biomed Eng*. 2007; 35: 208-23.
423. Nguyen BV, Wang QG, Kuiper NJ, El Haj AJ, Thomas CR and Zhang ZB. Biomechanical properties of single chondrocytes and chondrons determined by micromanipulation and finite-element modelling. *Journal of The Royal Society Interface*. 2010; 7: 1723-33.
424. Slomka N, Oomens CWJ and Gefen A. Evaluating the effective shear modulus of the cytoplasm in cultured myoblasts subjected to compression using an inverse finite element method. *J Mech Behav Biomed*. 2011; 4: 1559-66.
425. Barreto S, Clausen CH, Perrault CM, Fletcher DA and Lacroix D. A multi-structural single cell model of force-induced interactions of cytoskeletal components. *Biomaterials*. 2013; 34: 6119-26.
426. Charras GT and Horton MA. Determination of cellular strains by combined atomic force microscopy and finite element modeling. *Biophys J*. 2002; 83: 858-79.
427. Charras GT, Williams BA, Sims SM and Horton MA. Estimating the sensitivity of mechanosensitive ion channels to membrane strain and tension. *Biophys J*. 2004; 87: 2870-84.
428. Sen S, Engler AJ and Discher DE. Matrix Strains Induced by Cells: Computing How Far Cells Can Feel. *Cell Mol Bioeng*. 2009; 2: 39-48.
429. Hemsley AL, Hernandez D, Mason C, Pelling A and Veraitch F. Precisely delivered nanomechanical forces induce blebbing in undifferentiated mouse embryonic stem cells. *Cell Health and Cytoskeleton*. 2011; 3: 23-34.
430. Carl P, Kwok C, Manderson G, Speicher D and Discher DE. Forced unfolding modulated by disulfide bonds in the Ig domains of a Cell adhesion molecule. *Mol Biol Cell*. 2000; 11: 113a-a.
431. Hertz H. {Über} die {B} erührung fester elastischer {K} örper. *J für die reine u angew Math*. 1882; 92.